

WELDING PROCESSES



Edited by **Radovan Kovacevic**

WELDING PROCESSES

Edited by **Radovan Kovacevic**

Welding Processes

<http://dx.doi.org/10.5772/2884>

Edited by Radovan Kovacevic

Contributors

J. Zhou, H.L. Tsai, Hitoshi Ozaki, Muneharu Kutsuna, Kelvii Wei Guo, Ikhwan Naim Md Nawi, Jalil Ali, Mohamed Fadhali, Preecha P. Yupapin, Abdel-Monem El-Batahgy, Junjie Ma, Fanrong Kong, Blair Carlson, Radovan Kovacevic, Zhiguo Gao, Jauhari Tahir Khairuddin, Jamaluddin Abdullah, Zuhailawati Hussain, Indra Putra Almanar, Farag Soul, Nada Hamdy, Miroslav Mijajlović, Dragan Milčić, Yoji Ogawa, Marek Stanisław Węglowski, Wei Jie Zhang, Yu Kang Liu, Yu Ming Zhang, Riyadh Mohammed Ali Hamza, P. S. Wei, Clébio Domingues da Silveira-Júnior, Morgana Guilherme de Castro, Letícia Resende Davi, Flávio Domingues das Neves, Verediana Resende Novais, Paulo César Simamoto-Júnior

Published by InTech

Janeza Trdine 9, 51000 Rijeka, Croatia

Copyright © 2012 InTech

All chapters are Open Access distributed under the Creative Commons Attribution 3.0 license, which allows users to download, copy and build upon published articles even for commercial purposes, as long as the author and publisher are properly credited, which ensures maximum dissemination and a wider impact of our publications. After this work has been published by InTech, authors have the right to republish it, in whole or part, in any publication of which they are the author, and to make other personal use of the work. Any republication, referencing or personal use of the work must explicitly identify the original source.

Notice

Statements and opinions expressed in the chapters are those of the individual contributors and not necessarily those of the editors or publisher. No responsibility is accepted for the accuracy of information contained in the published chapters. The publisher assumes no responsibility for any damage or injury to persons or property arising out of the use of any materials, instructions, methods or ideas contained in the book.

Publishing Process Manager Viktorija Zgela

Typesetting InTech Prepress, Novi Sad

Cover InTech Design Team

First published November, 2012

Printed in Croatia

A free online edition of this book is available at www.intechopen.com

Additional hard copies can be obtained from orders@intechopen.com

Welding Processes, Edited by Radovan Kovacevic

p. cm.

ISBN 978-953-51-0854-2

Contents

Preface IX

Section 1 Laser Welding 1

Chapter 1 **Hybrid Laser-Arc Welding 3**
J. Zhou and H.L. Tsai

Chapter 2 **Dissimilar Metal Joining of Zinc Coated Steel
and Aluminum Alloy by Laser Roll Welding 33**
Hitoshi Ozaki and Muneharu Kutsuna

Chapter 3 ***In situ* Reaction During Pulsed Nd:YAG Laser Welding
SiC_p/A356 with Ti as Filler Metal 55**
Kelvii Wei Guo

Chapter 4 **Nd:YAG Laser Welding
for Photonics Devices Packaging 75**
Ikhwan Naim Md Nawj, Jalil Ali,
Mohamed Fadhali and Preecha P. Yupapin

Chapter 5 **Laser Beam Welding of Austenitic Stainless
Steels – Similar Butt and Dissimilar Lap Joints 93**
Abdel-Monem El-Batahgy

Chapter 6 **Mitigating Zinc Vapor Induced Weld Defects in Laser
Welding of Galvanized High-Strength Steel by Using
Different Supplementary Means 117**
Junjie Ma, Fanrong Kong, Blair Carlson and Radovan Kovacevic

Section 2 Numerical Modeling of Welding Processes 139

Chapter 7 **Numerical Modelling to Understand
Cracking Phenomena During Laser-GMA
Hybrid Welding Nickel-Base Superalloys 141**
Zhiguo Gao

- Chapter 8 **Development of a Comprehensive Process Model for Hybrid Laser-Arc Welding** 165
Fanrong Kong and Radovan Kovacevic
- Chapter 9 **Principles and Thermo-Mechanical Model of Friction Stir Welding** 191
Jauhari Tahir Khairuddin, Jamaluddin Abdullah, Zuhailawati Hussain and Indra Putra Almanar
- Chapter 10 **Numerical Simulation of Residual Stress and Strain Behavior After Temperature Modification** 217
Farak Soul and Nada Hamdy
- Chapter 11 **Analytical Model for Estimating the Amount of Heat Generated During Friction Stir Welding: Application on Plates Made of Aluminium Alloy 2024 T351** 247
Miroslav Mijajlović and Dragan Milčić
- Section 3 Sensing of Welding Processes** 275
- Chapter 12 **Visual Analysis of Welding Processes** 277
Yoji Ogawa
- Chapter 13 **Monitoring of Arc Welding Process Based on Arc Light Emission** 305
Marek Stanisław Węglowski
- Chapter 14 **Real-Time Measurement of Three Dimensional Weld Pool Surface in GTAW** 333
Wei Jie Zhang, Yu Kang Liu and Yu Ming Zhang
- Section 4 General Topics in Welding** 367
- Chapter 15 **Optimized Stud Arc Welding Process Control Factors by Taguchi Experimental Design Technique** 369
Riyadh Mohammed Ali Hamza
- Chapter 16 **The Physics of Weld Bead Defects** 395
P. S. Wei
- Chapter 17 **Welding Techniques in Dentistry** 415
Clébio Domingues da Silveira-Júnior, Morgana Guilherme de Castro, Letícia Resende Davi, Flávio Domingues das Neves, Verediana Resende Novais and Paulo César Simamoto-Júnior

Preface

Despite the wide availability of literature on welding processes, a need exists to regularly update the engineering community on advancements in joining techniques of similar and dissimilar materials, in their numerical modeling, as well as in their sensing and control. In response to InTech's request to provide undergraduate and graduate students, welding engineers, and researchers with updates on recent achievements in welding, a group of 34 authors and co-authors from 14 countries representing five continents have joined to co-author this book on welding processes, free of charge to the reader.

This book is divided into four sections: Laser Welding; Numerical Modeling of Welding Processes; Sensing of Welding Processes; and General Topics in Welding.

The first section, Laser Welding, includes six chapters covering topics ranging from an extensive overview of the physics of hybrid laser-arc welding, to welding of dissimilar materials, aluminum matrix composite, photonics devices, stainless steel, and high-strength galvanized steels.

The second section, Numerical Modeling of Welding Processes, includes five chapters focused on numerical modeling of hybrid laser-arc welding, friction stir welding, and modeling of residual stresses and distortions with an overview of techniques designed to mitigate residual stresses during welding.

The third section, Sensing of Welding Processes, includes three chapters focused on applying high-speed imaging to the study of fusion welding processes, using arc light emission to monitor the welding process, and measuring in real time the free surface of a molten pool in GTAW (gas tungsten arc welding).

The final section, General Topics in Welding, includes three chapters focused on optimization of stud arc welding process parameters, weld bead defects, and welding techniques in dentistry.

It is our firm belief that the material presented in this book will appeal to a broad audience of readers interested in recent advancements in hybrid laser-arc welding,

autogenous laser welding, friction stir welding, numerical modeling of different welding processes, and real-time sensing of the welding processes.

Radovan Kovacevic, Ph.D., FAWS, FSME, FASME

Herman Brown Chair in Engineering

Professor of Mechanical Engineering

Director of the Research Center for Advanced Manufacturing

and Center for Laser-aided Manufacturing

Southern Methodist University, Dallas, TX,

USA

Laser Welding

Hybrid Laser-Arc Welding

J. Zhou and H.L. Tsai

Additional information is available at the end of the chapter

<http://dx.doi.org/10.5772/50113>

1. Introduction

Hybrid laser-arc welding has received increasing interest in both academia and industry in last decade^{1,2}. As shown in Fig. 1, hybrid laser-arc welding is formed by combining laser beam welding and arc welding. Due to the synergic action of laser beam and welding arc, hybrid welding offers many advantages over laser welding and arc welding alone³⁻⁶, such as high welding speed, deep penetration⁷, improved weld quality with reduced susceptibility to pores and cracks⁸⁻¹⁶, excellent gap bridging ability¹⁷⁻²², as well as good process stability and efficiency, as shown in Fig. 2.

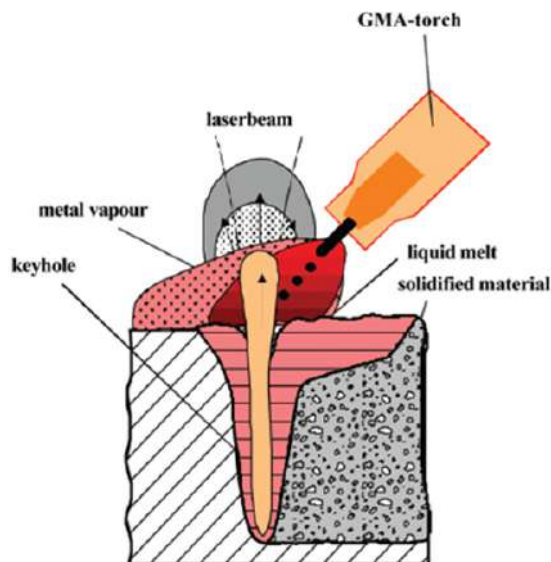


Figure 1. Schematic sketch of a hybrid laser-arc welding process.

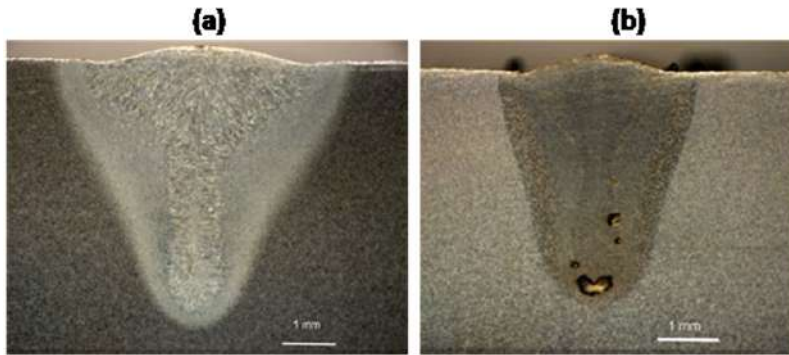


Figure 2. Comparison between (a) a laser weld and (b) a hybrid laser-arc weld in 250 grade mild steel.

Development of the hybrid laser-arc welding technique can be divided into three stages¹. The concept of hybrid laser welding was first proposed by Steen *et al.*^{3, 23, 24} in the late seventies. In their studies, a CO₂ laser was combined with a tungsten inert gas (TIG) arc for welding and cutting applications. Their tests showed clear benefits of combining an arc and a laser beam in the welding process, such as a stabilized arc behavior under the influence of laser radiation; a dramatic increase in the speed of welding of thin metal sheets; and an increase in penetration depth compared with laser welding. Japanese researchers continued Steen's effort and developed various methods and corresponding devices for laser-arc welding, cutting, and surface treatment. However, these efforts did not advance this joining technique into engineering applications particularly because laser welding itself was not yet an economic and viable joining technique at that time²⁵. In the second stage of the development of the hybrid laser-arc welding technique, the observed influence of the arc column behavior by laser radiation was used to improve the efficiency of arc welding processes, which leads to the laser-enhanced arc welding technology¹. A characteristic feature of this technology was that only a low-intensity laser beam was needed, i.e., the required laser power was small compared to the arc power. For TIG welding, Cui and Decker²⁶⁻²⁸ demonstrated that a low-energy CO₂ laser beam with a power of merely 100 W could facilitate arc ignition; enhance arc stability; improve weld quality; and increase welding speed due to a reduced arc size and higher arc amperages. However, despite such reported improvements of the arc welding process through laser support, there were neither subsequent extensive investigations of this subject nor known industrial applications of the laser-enhanced arc welding technology. The third stage of hybrid welding technology started in the early 1990s with the development of combined welding processes using a high-power laser beam as the primary and an additional electric arc as the secondary heating source²⁹⁻³⁷. At that time, although the continuous wave CO₂ laser welding process was already well established in industry, it had some known disadvantages, e.g., high requirements of edge preparation and clamping; fast solidification leading to material-dependent pores and cracks; as well as the high investment and operating costs for the laser equipment. Additionally, some welding applications of highly practical interest could not be

solved satisfactorily by the laser welding process alone, e.g., joining of tailored blanks in the automotive engineering; welding of heavy plates in shipbuilding industry; as well as high speed welding of crack-susceptible materials. In searching for suitable solutions, the hybrid laser welding was developed into a viable joining technique with significant industrial acceptance during the last decade.

According to the combination of various heating sources used, hybrid welding can be generally categorized as: (1) laser-gas tungsten arc (GTA) welding; (2) laser-gas metal arc (GMA) welding; and (3) laser-plasma welding²⁵. Since laser welding offers deep penetration, primary heating sources commonly used in hybrid welding are CO₂, Nd:YAG, and fiber lasers. The first two types of lasers are well established in practice and used for various hybrid welding process developments. While the fiber laser is still in development for industrial applications, it seems to be a future primary heating source for hybrid welding due to its high beam quality. The secondary heating sources used in hybrid welding are mainly electric arcs. Dedicated processes can be divided into GMA welding with consumable electrodes and GTA welding with non-consumable tungsten electrodes. In GMA welding, the arc is burning between a mechanically supplied wire electrode and the workpiece. The shielding gas used in GMA welding was found to have significant effects on arc shape and metal transfer^{38,39}. Hence, GMA welding can be subdivided into metal inert-gas (MIG) and metal active-gas (MAG) welding according to the type of shielding gas used. In GTA welding, a chemically inert gas, such as argon or helium, is often used. A special form of this is the plasma arc welding (PAW), which produces a squeezed arc due to a special torch design and results in a more concentrated arc spot.

In hybrid welding, laser and arc are arranged preferably in a way that they can compensate and benefit from each other during the welding process, which implies the creation of a common interaction zone with changed characteristics in comparison to the laser welding and the arc welding alone. In contrast to this is the arrangement in which laser and arc are serving as two separate heating sources during the welding process. Several configurations have been proposed. In a parallel arrangement, there is a distance in either the vertical or horizontal direction along the path between both heating sources. In a serial arrangement, the primary and secondary heating sources are moved along the same welding path with a certain working distance, and the secondary heating source can either lead or follow the primary heating source¹. The first one enables a preheating of the region to be welded. It can increase the efficiency of the laser welding process because materials to be welded are locally preheated and energy losses through heat conduction are reduced. In comparison, the second one often acts like a short-time post-heat treatment of the weld that can change the weld microstructure favorably. There exists a key difference between parallel and serial process arrangement. In a serial arrangement, additional energy is dissipated within the weld seam region, whereas in the parallel arrangement, the heat flow is reduced only across the weld seam. The option to move the working area temporally enables flexibility in influencing the cooling rates in order to avoid defects.

In the hybrid laser-arc welding process, the workpiece is first heated up and melted due to the laser irradiation. The plasma arc between the consumable electrode and the workpiece continues to heat up and melt the base metal and the droplets generated at the electrode tip periodically detach and impinge onto the workpiece. Then a cavity with large depth-to-width ratio called keyhole was formed in the weld pool under the dynamical interaction of laser irradiation, plasma arc and filler droplets. An externally supplied shielding gas provides the protection of molten metal from exposing to the atmosphere. The successive weld pools create a weld bead and become a part of a welded joint when solidified. The numbers of process parameters are greatly increased in the hybrid welding, mainly including laser beam parameters, electric power parameters, laser-arc interval, electrode diameter, wire feed speed, welding speed and shielding gas. Bagger and Olsen⁶⁶ reviewed the fundamental phenomena occurring in laser-arc hybrid welding and the principles for choosing the process parameters. Ribic *et al.*⁶⁷ reviewed the recent advances in hybrid welding with emphases on the physical interactions between laser and arc, and the effects of the combined laser-arc heat source on the welding process.

Current understanding of hybrid laser-arc welding is primarily based on experimental observations. Hybrid laser-arc welding is restricted to specific applications, predominantly the joining of thick section plain carbon steels. In order to expand the applications of this joining technique and optimize the processes for its current applications, fundamental understanding of the transport phenomena and the role of each parameter becomes critical. Numerical investigations were often carried out for this purpose. Ribic *et al.*⁶⁷ developed a three-dimensional heat transfer and fluid flow model for laser-GTA hybrid welding to understand the temperature field, cooling rates and mixing in the weld pool. Kong and Kovacevic⁶⁸ developed a three-dimensional model to simulate the temperature field and thermally induced stress field in the workpiece during the hybrid laser-GTA process. Mathematical models have also been developed to simulate the weld pool formation and flow patterns in hybrid laser-GMA welding by incorporating free surfaces based on the VOF method. Generally, the typical phenomena in GMA welding such as droplets impingement into the weld pool, electromagnetic force in the weld pool and the typical phenomena in laser beaming welding such as keyhole dynamics, inverse Bremsstrahlung absorption and Fresnel absorption were considered in these models. Surface tension, buoyancy, droplet impact force and recoil pressure were considered to calculate the melt flow patterns. In the following, fundamental physics, especially transport phenomena involved in hybrid laser-arc welding will be elaborated.

2. Fundamentals of hybrid laser-arc welding

Since hybrid laser-arc welding involves laser welding, arc welding and their interactions as well, complicated physical processes like metal melting and solidification; melt flow; keyhole plasma formation; arc plasma formation and convection are typically involved, which results in very complex transport phenomena in this welding process⁴⁰. As known,

transport phenomena in welding, such as heat transfer; melt flow; and plasma flow, can strongly affect both metallurgical structures and mechanical properties of the weld⁴¹⁻⁴⁵. In the following, transport phenomena in hybrid welding will be discussed and particular attentions are given to 1) arc plasma formation and its effect on metal transfer and weld pool dynamics; 2) laser-induced plasma formation and laser-plasma interaction; 3) recoil pressure and other possible mechanisms contributing to keyhole formation and dynamics; 4) the interplay among various process parameters; and 5) plasma - filler metal - weld pool interactions.

Due to the different natures of heat and mass transfer mechanisms in metal and plasma, different models are developed to study the fundamental physics in hybrid laser-arc welding. One is for the metal region containing base metal, electrode, droplets, and arc plasma. The other is for the keyhole region containing laser-induced plasma. There is a free surface (liquid/vapor interface) separating these two regions. For the metal region, continuum formulation is used to calculate the energy and momentum transport⁴⁰. For the keyhole plasma region, laser-plasma interaction and the laser energy absorption mechanism will be discussed. These two regions are coupled together and the VOF technique is used to track the interface between these two regions⁴⁰.

2.1. Transport phenomena in metal (electrode, droplets, and workpiece) and arc plasma

Differential equations governing the conservation of mass, momentum and energy based on continuum formulation are given below⁴⁶:

Conservation of mass

$$\frac{\partial}{\partial t}(\rho) + \nabla \cdot (\rho \mathbf{V}) = 0 \quad (1)$$

where t is the time, ρ is the density, and \mathbf{V} is the velocity vector.

Conservation of momentum

$$\begin{aligned} \frac{\partial}{\partial t}(\rho u) + \nabla \cdot (\rho \mathbf{V} u) = & \nabla \cdot \left(\mu_l \frac{\rho}{\rho_l} \nabla u \right) - \frac{\partial p}{\partial x} - \frac{u_l}{K} \frac{\rho}{\rho_l} (u - u_s) - \frac{C \rho^2}{K^{0.5} \rho_l} |u - u_s| (u - u_s) \\ & - \nabla \cdot (\rho f_s f_l \mathbf{V}_r u_r) + \nabla \cdot \left(\mu_s u \nabla \left(\frac{\rho}{\rho_l} \right) \right) + \mathbf{J} \times \mathbf{B} \Big|_x \end{aligned} \quad (2)$$

$$\begin{aligned} \frac{\partial}{\partial t}(\rho v) + \nabla \cdot (\rho \mathbf{V} v) = & \nabla \cdot \left(\mu_l \frac{\rho}{\rho_l} \nabla v \right) - \frac{\partial p}{\partial y} - \frac{u_l}{K} \frac{\rho}{\rho_l} (v - v_s) - \frac{C \rho^2}{K^{0.5} \rho_l} |v - v_s| (v - v_s) \\ & - \nabla \cdot (\rho f_s f_l \mathbf{V}_r v_r) + \nabla \cdot \left(\mu_s v \nabla \left(\frac{\rho}{\rho_l} \right) \right) + \mathbf{J} \times \mathbf{B} \Big|_y \end{aligned} \quad (3)$$

$$\begin{aligned} \frac{\partial}{\partial t}(\rho w) + \nabla \cdot (\rho \mathbf{V} w) = \rho g + \nabla \cdot \left(\mu_l \frac{\rho}{\rho_l} \nabla w \right) - \frac{\partial p}{\partial z} - \frac{u_l}{K} \frac{\rho}{\rho_l} (w - w_s) - \frac{C \rho^2}{K^{0.5} \rho_l} |w - w_s| (w - w_s) \\ - \nabla \cdot (\rho f_s f_l \mathbf{V}_r w_r) + \nabla \cdot \left(\mu_s w \nabla \left(\frac{\rho}{\rho_l} \right) \right) + \rho g \beta_T (T - T_0) + F_{drag} + \mathbf{J} \times \mathbf{B} \Big|_z \end{aligned} \quad (4)$$

where u , v and w are the velocities in the x -, y - and z -directions, respectively, and \mathbf{V}_r is the relative velocity vector between the liquid phase and the solid phase. \mathbf{J} is the current field vector and \mathbf{B} is the magnetic field vector. The subscripts s and l refer to the solid and liquid phases, respectively; Subscript 0 represents the reference conditions; p is the pressure; μ is the viscosity; f is the mass fraction; K , the permeability, is a measure of the ease with which fluid passes through the porous mushy zone; C is the inertial coefficient; β_T is the thermal expansion coefficient; g is the gravitational acceleration; and T is the temperature.

Conservation of energy

$$\begin{aligned} \frac{\partial}{\partial t}(\rho h) + \nabla \cdot (\rho \mathbf{V} h) = \nabla \cdot \left(\frac{k}{c_p} \nabla h \right) - \nabla \cdot \left(\frac{k}{c_p} \nabla (h_s - h) \right) - \\ - \nabla \cdot (\rho (\mathbf{V} - \mathbf{V}_s)(h_l - h)) + \frac{|\mathbf{J}|}{\sigma_e} - S_R + \frac{5k_b}{2e} \mathbf{J} \cdot \frac{\nabla h}{c_p} \end{aligned} \quad (5)$$

where h is the enthalpy, k is the thermal conductivity, and c_p is the specific heat. The first two terms on the right-hand side of Eq. (5) represent the net Fourier diffusion flux. The third term represents the energy flux associated with the relative phase motion. σ_e is the electrical conductivity; S_R is the radiation heat loss; k_b is the Stefan-Boltzmann constant; and e is the electronic charge.

The third and fourth terms on the right-hand side of Eqs. (2)-(4) represent the first and second order drag forces of the flow in the mushy zone. The fifth term represents an interaction between the solid and the liquid phases due to the relative velocity. The second term on the right hand side of Eq. (5) represents the net Fourier diffusion flux. The third term represents the energy flux associated with the relative phase motion. All these aforementioned terms in this paragraph are zero except in the mushy zone. In addition, the solid phase is assumed to be stationary ($V_s = 0$).

Conservation of species

$$\frac{\partial}{\partial t}(\rho f^\alpha) + \nabla \cdot (\rho \mathbf{V} f^\alpha) = \nabla \cdot (\rho D \nabla f^\alpha) - \nabla \cdot (\rho D \nabla (f_l^\alpha - f^\alpha)) - \nabla \cdot (\rho (\mathbf{V} - \mathbf{V}_s)(f_l^\alpha - f^\alpha)) \quad (6)$$

where D is a mass diffusivity and f^α is a mass fraction of constitute. Subscript, l and s , represents liquid and solid phase respectively.

2.2. Transport phenomena in laser induced plasma

The vapor inside the keyhole is modeled as a compressible, inviscid ideal gas. No vapor flow is assumed in the keyhole and the energy equation is given in the following form⁴⁷:

$$\begin{aligned} \frac{\partial}{\partial t}(\rho_v h_v) = \nabla \cdot \left(\frac{k_v}{c_v} \nabla h_v \right) + \nabla \cdot (-q_r) + k_{pl} \cdot I_{laser} \cdot (1 - \alpha_{iB,1}) + \\ + \sum_{mr=1}^n k_{pl} I_{laser} \cdot (1 - \alpha_{iB,1}) \cdot (1 - \alpha_{Fr}) \cdot (1 - \alpha_{iB,mr}) \end{aligned} \quad (7)$$

where h_v and ρ_v represent the enthalpy and density of the plasma; k_v and c_v represent the thermal conductivity and specific heat of the plasma. The first term on the right-hand side of Eq. (7) represents the heat conduction term. The second term represents the radiation heat term and q_r stands for the radiation heat flux vector. The fourth term represents energy input from the original laser beam. The last term represents the energy input from multiple reflections of the laser beam inside the keyhole.

2.3. Electrical potential and magnetic field

Arc plasma from GMA welding will not only provide heat to the base metal, but will also exert magnetic force on the weld pool. The electromagnetic force can be calculated as follows⁴⁸:

Conservation of current

$$\nabla \cdot (\sigma_e \nabla \phi) = 0 \quad (8)$$

$$\mathbf{J} = -\sigma_e \nabla \phi \quad (9)$$

where ϕ is the electrical potential. According to Ohm's law, the self-induced magnetic field B_θ is calculated by the following Ampere's law:

$$B_\theta = \frac{\mu_0}{r} \int_0^r j_z r dr \quad (10)$$

where $\mu_0 = 4\pi \times 10^{-7}$ H m⁻¹ is the magnetic permeability of free space. Finally, three components of the electromagnetic force in Eqs. (2)-(4) are calculated via

$$\mathbf{J} \times \mathbf{B} \Big|_x = -B_\theta j_z \frac{x - x_a}{r} \quad (11)$$

$$\mathbf{J} \times \mathbf{B} \Big|_y = -B_\theta j_z \frac{y}{r} \quad (12)$$

$$\mathbf{J} \times \mathbf{B} \Big|_z = -B_\theta j_r \quad (13)$$

2.4. Arc plasma and its interaction with metal zone (electrode, droplets, and weld pool)

In welding, shielding gas is ionized and forms a plasma arc between the electrode and workpiece. In the arc region, the plasma is assumed to be in local thermodynamic equilibrium (LTE)⁴⁹, implying the electron and the heavy particle temperatures are equal. On this basis, the plasma properties, including enthalpy, specific heat, density, viscosity, thermal conductivity and electrical conductivity, are determined from an equilibrium composition calculation⁴⁹. It is noted that the metal vaporized from the metal surface may influence plasma material properties, but this effect is omitted in the present study. It is also assumed that the plasma is optically thin, thus the radiation may be modeled in an approximate manner by defining a radiation heat loss per unit volume⁴⁹. The transport phenomena in the arc plasma and the metal are calculated separately in the corresponding arc domain and metal domain, and the two domains are coupled through interfacial boundary conditions in each time step.

Heat transfer

At the plasma-electrode interface, there exists an anode sheath region⁴⁹. In this region, the mixture of plasma and metal vapor departs from LTE, thus it no longer complies with the model presented above. Since the sheath region is very thin, it is treated as a special interface to take into account the thermal effects on the electrode. The energy balance equation at the surface of the anode is modified to include an additional source term, S_a ,^{50,51} for the metal region.

$$S_a = \frac{k_{eff}(T_{arc}-T_a)}{\delta} + J_a\phi_w - q_{rad} - q_{evap} \quad (14)$$

The first term on the right-hand side of Eq. (14) is the contribution due to heat conduction from the plasma to the anode. The symbol k_{eff} represents the thermal conductivity taken as the harmonic mean of the thermal conductivities of the arc plasma and the anode material. δ is the length of the anode sheath region. T_{arc} is the arc temperature and T_a is the temperature of the anode. The second term represents the electron heating associated with the work function of the anode material. J_a is the current density at the anode and ϕ_w is the work function of the anode material. The third term q_{rad} is the black body radiation loss from the anode surface. The final term q_{evap} is the heat loss due to the evaporation of electrode materials.

Similar to the anode region, there exists a cathode sheath region between the plasma and the cathode. However, the physics of the cathode sheath and the energy balance at the nonthermionic cathode for GMA welding are not well understood⁵⁰⁻⁵⁶. The thermal effect due to the cathode sheath has been omitted in many models and reasonable results were obtained⁵⁰⁻⁵⁴. Thus, the energy balance equation at the cathode surface will only have the conduction, radiation, and evaporation terms.

$$S_a = \frac{k_{eff}(T_{arc}-T_c)}{\delta} - q_{rad} - q_{evap} \quad (15)$$

where k_{eff} is the effective thermal conductivity at the arc-cathode surface taken as the harmonic mean of the thermal conductivities of the arc plasma and the cathode material. δ is the length of the cathode sheath. T_c is the cathode surface temperature.

Force balance

The molten part of the metal is subjected to body forces, such as gravity and electromagnetic force. It is also subjected to surface forces, such as surface tension due to surface curvature, Marangoni shear stress due to temperature difference, and arc plasma shear stress and arc pressure at the interface of arc plasma and metal. For cells containing a free surface, surface tension pressure normal to the free surface can be expressed as⁵⁷

$$p_s = \gamma\kappa \quad (16)$$

where γ is the surface tension coefficient and κ is the free surface curvature.

The temperature-dependent Marangoni shear stress at the free surface in a direction tangential to the local free surface is given by⁵⁸

$$\tau_{Ms} = \frac{\partial\gamma}{\partial T} \frac{\partial T}{\partial s} \quad (17)$$

where s is a vector tangential to the local free surface.

The arc plasma shear stress is calculated at the free surface from the velocities of arc plasma cells immediately adjacent the metal cells

$$\tau_{ps} = \mu \frac{\partial V}{\partial T} \quad (18)$$

where μ is the viscosity of arc plasma.

The arc pressure at the metal surface is obtained from the computational result in the arc region. The surface forces are included by adding source terms to the momentum equations according to the CSF (continuum surface force) model⁵⁷. Using F of the VOF function as the characteristic function, surface tension pressure, Marangoni shear stress, arc plasma shear stress, and arc pressure are all transformed to the localized body forces and added to the momentum transport equations as source terms for the boundary cells. Based on these assumptions, Hu *et al.* has successfully simulated the arc and droplet formation and effects of current density and the type of shielding gas on arc formation in a GMA welding process, as shown in Fig. 3.

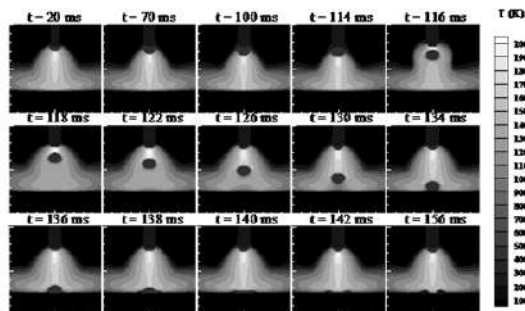


Figure 3. Arc formation in a GMA welding process.

2.5. Laser-induced recoil pressure and keyhole dynamics

In the laser welding process, the laser beam is directed to the metal surface, which first melts the material and produces a small molten pool in the workpiece. The liquid metal is then heated to high temperatures resulting in large evaporation rates. The rapid evaporation creates a large recoil pressure on the surface of the molten layer depressing it downwards. Thus, a cavity with large depth-to-width ratio called keyhole is formed. Many investigators believe that the balance between the recoil pressure and surface tension force determines the shape of the keyhole. So, understanding the formation and behavior of the recoil pressure becomes very important for studying the laser welding process. The recoil pressure results from the rapid evaporation of the liquid metal surface. When the liquid metal on the surface is heated to its boiling point, evaporation begins to occur. There is a very thin layer called Knudsen layer adjacent to the liquid surface where the vapor escaping from the liquid surface is in a state of thermodynamic non-equilibrium, i.e., the vapor molecules do not have a Maxwellian velocity distribution. This occurs when the equilibrium vapor pressure (i.e., the saturation pressure) corresponding to the surface temperature is large compared to the ambient partial pressure of the vapor. Under these conditions the vapor adjacent to the surface is dominated by recently evaporated material that has not yet experienced the molecular collisions necessary to establish a Maxwellian velocity distribution. The Knudsen layer is estimated to be a few molecular mean free paths thick in order to allow for the molecular collisions to occur that bring the molecules into a state of translational equilibrium at the outer edge of the Knudsen layer. The flow field around the Knudsen layer is shown in Fig. 4.

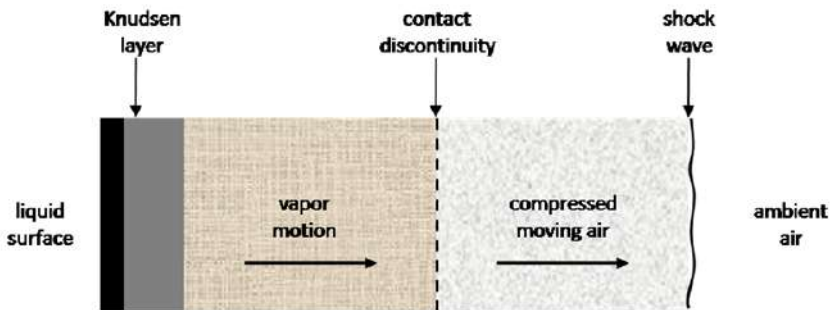


Figure 4. A schematic of the gas dynamic of vapor and air away from a liquid surface at elevated temperature.

Anisimov⁵⁹ and Knight⁶⁰ did the early investigations on the Knudsen layer. Here a kinetic theory approach⁶¹ is used in the present study. The analysis proceeds by constructing an approximate molecular velocity distribution adjacent to the liquid surface. Equations describing the conservation of mass, momentum and energy across the Knudsen layer are developed in terms of this velocity distribution. This gives Eqs. (19) and (20), as given below, for gas temperature, T_K , and density, ρ_K , outside of the Knudsen layer as functions of the liquid surface temperature and the corresponding saturation density, ρ_{sat} .

$$\frac{T_K}{T_L} = \left[\sqrt{1 + \pi \left(\frac{\gamma - 1}{\gamma + 1} \frac{m}{2} \right)^2} - \sqrt{\pi} \frac{\gamma - 1}{\gamma + 1} \frac{m}{2} \right]^2 \quad (19)$$

$$\frac{\rho_K}{\rho_{sat}} = \sqrt{\frac{T_L}{T_K}} \left[\left(m^2 + \frac{1}{2} \right) e^{m^2} \operatorname{erfc}(m) - \frac{m}{\sqrt{\pi}} \right] + \frac{1}{2} \frac{T_L}{T_K} \left[1 - \sqrt{\pi} m e^{m^2} \operatorname{erfc}(m) \right] \quad (20)$$

The quantity, m , is closely related to the Mach number at the outer edge of the Knudsen layer, M_K , and is defined as, $m = u_K / \sqrt{2R_V T_K} = M_K \sqrt{2/\gamma_V}$, where γ_V and R_V are the ratio of specific heats and the gas constant for the vapor, respectively. The value of m depends on the gas dynamics of the vapor flow away from the surface. The gas temperature, pressure and density throughout the vapor region (outside of the Knudsen layer) are uniform. The contact discontinuity, that is, the boundary between vapor and air, is an idealization that results due to the neglect of mass diffusion and heat conduction. The velocity and pressure are equal in these regions, $u_K = u_S$ and $P_K = P_S$, where the subscript, S , denotes properties behind the shock wave. Note that, in general, $T_K \neq T_S$ and $\rho_K \neq \rho_S$.

The thermodynamic state and velocity of the air on each side of the shock wave are related by the Rankine-Hugoniot relations, where the most convenient forms to this application are given by Eqs. (21) and (22). M_K is the Mach number in the vapor, $M_K = u_K / \sqrt{2\gamma_V R_V T_K}$.

$$\frac{P_S}{P_\infty} = 1 + \gamma M_K \sqrt{\frac{\gamma_V R_V T_K}{\gamma_\infty R_\infty T_\infty}} \left[\frac{\gamma_\infty + 1}{4} M_K \sqrt{\frac{\gamma_V R_V T_K}{\gamma_\infty R_\infty T_\infty}} + \sqrt{1 + \left(\frac{\gamma_\infty + 1}{4} M_K \sqrt{\frac{\gamma_V R_V T_K}{\gamma_\infty R_\infty T_\infty}} \right)^2} \right] \quad (21)$$

$$\frac{T_S}{T_\infty} = \frac{P_S}{P_\infty} \left(1 + \frac{\gamma + 1}{\gamma - 1} \frac{P_S}{P_\infty} \right) / \left(\frac{\gamma + 1}{\gamma - 1} + \frac{P_S}{P_\infty} \right) \quad (22)$$

The saturation pressure, P_{sat} , is obtained from Eq. (23), where A , B and C are constants which depend on the material. This is used to obtain the saturation density, $\rho_{sat} = P_{sat} / (R_V T_L)$, assuming an ideal gas.

$$\log(P_{sat}) = -\frac{A}{T_L} - B \log(T_L) + C \quad (23)$$

Eqs. (20)-(23) are solved as a function of T_L using an iterative solution method. The vapor was assumed to be iron in the form of a monatomic gas with a molecular weight of 56, and $\gamma_V = 1.67$. Quantities of particular interest are the recoil pressure, P_r , and rate of energy loss due to evaporation, q_e , and they are given below.

$$P_r = P_K + \rho_K u_K^2, \quad q_e = H_V \rho_K u_K \quad (24)$$

2.6. Laser-plasma interaction and multiple reflections of laser beam in keyhole

In the keyhole, the laser beam is reflected and absorbed multiple times on the keyhole wall. Each time when the laser beam travels inside the keyhole, it will interact with the keyhole plasma. Multiple reflections of the laser beam and its absorption mechanism are critical in determining the energy transfer in laser welding, which are discussed below.

Inverse Bremsstrahlung (IB) absorption

With the continuous heating of the laser beam, the temperature of the metal vapor inside the keyhole can reach much higher than the metal evaporation temperature, resulting in strong ionization, which produces keyhole plasma. The resulting plasma absorbs laser power by the effect of Inverse Bremsstrahlung (IB) absorption. Eqs. (25) and (26) define the IB absorption fraction of laser beam energy in plasma by considering multiple reflection effects⁶²:

$$\alpha_{iB,1} = 1 - \exp\left(-\int_0^{s_0} k_{pl} ds\right) \quad (25)$$

$$\alpha_{iB,mr} = 1 - \exp\left(-\int_0^{s_m} k_{pl} ds\right) \quad (26)$$

here, $\alpha_{iB,1}$ is the absorption fraction in plasma due to the original laser beam; $\alpha_{iB,mr}$ is the absorption fraction due to the reflected laser beam. $\int_0^{s_0} k_{pl} ds$ and $\int_0^{s_m} k_{pl} ds$ are, respectively, the optical thickness of the laser transportation path for the first incident and multiple reflections, and k_{pl} is the plasma absorption coefficient due to inverse Bremsstrahlung absorption⁶³:

$$k_{pl} = \frac{n_e n_i Z^2 e^6 2\pi}{6\sqrt{3} m \varepsilon_0^3 c h \omega^3 m_e^2} \left(\frac{m_e}{2\pi k T_e}\right)^{0.5} \left[1 - \exp\left(-\frac{\omega}{k T_e}\right)\right] \bar{g} \quad (27)$$

where Z is the average ionic charge in the plasma, ω is the angular frequency of the laser radiation, ε_0 is the dielectric constant, k is the Boltzmann's constant, n_e and n_i are particle densities of electrons and ions, h is Planck's constant, m_e is the electron mass, T_e is the excitation temperature, c is the speed of light, and \bar{g} is the quantum mechanical Gaunt factor. For the weakly ionized plasma in the keyhole, the Saha equation⁶³ can be used to calculate the densities of plasma species:

$$\frac{n_e n_i}{n_0} = \frac{g_e g_i}{g_0} \frac{(2\pi m_e k T_e)^{1.5}}{h^3} \exp\left(-\frac{E_i}{k T_e}\right) \quad (28)$$

Fresnel absorption

As discussed before, part of the laser energy will be absorbed by keyhole plasma and part of the laser energy can reach the keyhole wall directly. So, the energy input (q_{laser}) for the keyhole wall consists of two parts: 1) Fresnel absorption of the incident intensity directly from the laser beam ($I_{\alpha,Fr}$) and 2) Fresnel absorption due to multiple reflections of the beam inside the keyhole ($I_{\alpha,mr}$).

$$q_{laser} = I_{\alpha,Fr} + I_{\alpha,mr} \quad (29)$$

$$I_{\alpha,Fr} = I_{laser} \cdot (1 - \alpha_{iB,1}) \cdot \alpha_{Fr}(\varphi_1) \quad (30)$$

$$I_{\alpha,mr} = \sum_{mr=1}^n I_{laser} \cdot (1 - \alpha_{iB,1}) \cdot (1 - \alpha_{Fr}) \cdot (1 - \alpha_{iB,mr}) \cdot \alpha_{Fr}(\varphi_{mr}) \quad (31)$$

where I_{laser} is the incoming laser intensity. We assume the laser beam has in the simplest case a Gaussian-like distribution:

$$I_{laser}(x, y, z) = I_0 \left(\frac{r_f}{r_{f0}}\right)^2 \exp\left(-\frac{2r^2}{r_f^2}\right) \quad (32)$$

where r_f is the beam radius and r_{f0} is the beam radius at the focal position; I_0 is the peak intensity. α_{Fr} is the Fresnel absorption coefficient and can be defined it in the following formula⁶⁴:

$$\alpha_{Fr}(\varphi) = 1 - \frac{1}{2} \left(\frac{1 + (1 - \varepsilon \cos \varphi)^2}{1 + (1 + \varepsilon \cos \varphi)^2} + \frac{\varepsilon^2 - 2\varepsilon \cos \varphi + 2 \cos^2 \varphi}{\varepsilon^2 + 2\varepsilon \cos \varphi + 2 \cos^2 \varphi} \right) \quad (33)$$

where φ is the angle of incident light with the normal of keyhole surface, n is the total number incident light from multiple reflections, \vec{l} is the unit vector along the laser beam radiation direction and \vec{n} is unit vector normal to the free surface. ε is a material-dependent coefficient.

2.7. Radiative heat transfer in laser-induced plasma

When an intense laser beam interacts with metal vapor, a significant amount of the laser radiation is absorbed by the ionized particles. The radiation absorption and emission by the vapor plume may strongly couple with the plume hydrodynamics. This coupling, shown on the right-hand side of Eq. (7), will affect the plasma laser light absorption and radiation cooling terms. The radiation source term $\nabla \cdot (-\mathbf{q}_r)$ is defined via

$$\nabla \cdot \mathbf{q}_r = k_a(4\pi I_b - \int_{4\pi} I d\Omega) \quad (34)$$

where k_a , I_b and Ω denote the Planck mean absorption coefficient, blackbody emission intensity and solid angle respectively. For the laser-induced plasma inside the keyhole, the scattering effect is not significant compared with the absorbing and emitting effect. So it will not lead to large errors to assume the plasma is an absorbing-emitting medium. The radiation transport equation (RTE) has to be solved for the total directional radiative intensity I^{65} :

$$(\mathbf{s} \cdot \nabla)I(\mathbf{r}, \mathbf{s}) = k_a(I_b - I(\mathbf{r}, \mathbf{s})) \quad (35)$$

where \mathbf{s} and \mathbf{r} denote a unit vector along the direction of the radiation intensity and the local position vector. The Planck mean absorption coefficient is defined in the following⁶⁵:

$$k_a = \left(\frac{128}{27} k \right)^{0.5} \left(\frac{\pi}{m_e} \right)^{1.5} \frac{Z^2 e^6 \bar{g} n_e n_i}{h \sigma c^3 T_v^{3.5}} \quad (36)$$

where n_i and n_e represent the particle density of ions and electrons, T_v is the temperature of the plasma, Z stands for the charge of ions, e is the proton charge and m_e is the mass of electrons.

2.8. Tracking of free surfaces

The algorithm of volume-of-fluid (VOF) is used to track the moving free surface⁴⁸. The fluid configuration is defined by a volume of fluid function, $F(x,y,z,t)$, which is used to track the location of the free surface. This function represents the volume of fluid per unit volume and satisfies the following conservation equation:

$$\frac{dF}{dt} = \frac{\partial F}{\partial t} + (\mathbf{V} \cdot \nabla)F = 0 \quad (37)$$

When averaged over the cells of a computing mesh, the average value of F in a cell is equal to the fractional volume of the cell occupied by the fluid. A unit value of F means a cell full of fluid and a zero value indicates a cell containing no fluid. Cells with F values between zero and one are partially filled with fluid and identified as surface cells.

3. Results and discussions

Based on the aforementioned scientific principles governing the hybrid laser-arc welding process, Zhou *et al.*^{40,69,70} have successfully developed mathematical models to simulate the transport phenomena like heat and mass transfer, melt flow; energy transport in keyhole plasma, etc. in both pulsed and three-dimensional moving hybrid laser-MIG welding. Detailed discussions are given in the following sections.

3.1. Two-dimensional hybrid laser-MIG welding

In this study, the base metal is assumed to be a stainless steel 304 containing 100 ppm of sulfur. The laser energy is assumed to be in the Gaussian distribution and the divergence of the laser beam is negligible because the focus length of the laser beam is less than 3mm. The laser power and beam radius at the focus are 1800 W and 0.2 mm respectively. The laser power is turned on at $t = 0$ s and shut down at $t = 15$ ms. To simulate the MIG process, droplet is assumed to be spherical and is generated in a steady manner. The diameter of filler droplet is assumed to be 0.35 mm, its initial speed is 0.5 m/s right above the weld surface, its initial temperature is 2400 K, and its generation frequency is 1000 Hz. The droplet is assumed to be fed into the keyhole from the top. Droplet generation and formation are actually related to wire size and wire feed speed. Further information can be found in Ref. [13].

Fig. 5 shows the comparison of the cross-sectional view of a hybrid laser-MIG weld and a laser weld. As shown, there is a "pore" in the laser weld, which is due to the rapid solidification in laser welding. Detailed discussion on the formation of porosity in the weld can be found in Ref. [14]. It is also noticed that there are some "undercuts" near the top edge of the laser weld which is one of the major disadvantages of laser welding. In hybrid laser-MIG welding, the reason why there is no pore found in the final weld was believed to be mainly due to the addition of filler metal in the process. The momentum and energy carried by the filler droplets greatly impact the fluid flow and heat transfer in the weld pool and the shape of the solidified weld pool as well. The overall effect depends on the droplet size, droplet generation frequency and droplet generation duration as well. With an optimal operation window, a weld with desired shape and quality can be achieved in hybrid laser-MIG welding. In addition, it is found that the additional heat input from the arc in hybrid laser welding is transferred to the weld pool mainly in the region near the top of the weld, which makes the top portion of the weld wider than that in laser welding. It is further found the undercuts frequently observed in laser welding are eliminated and the shape of the final weld can be modified by the extra filler metal coming from the MIG process. However, the penetration depth in hybrid welding is noticed to be almost the same as that in laser welding, which means the penetration depth in hybrid laser-arc welding mainly depends on the laser power used, but not the arc power.

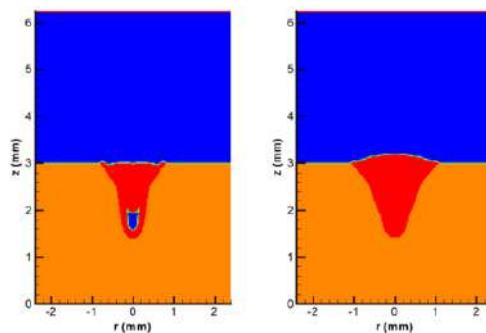


Figure 5. Comparison of weld bead shape between laser welding and hybrid laser-MIG welding.

3.2. Interaction between filler droplets and weld pool

Fig. 6 shows typical interactions between droplets and weld pool in hybrid laser-arc welding. The corresponding distributions of temperature, sulfur concentration, and melt flow velocity are given in Figs. 7, 8 and 9, respectively. Since only the interaction between filler droplets and weld pool is concerned in this discussion, the keyhole formation process is ignored which can be found in Ref. [14]. As shown in Fig. 6, after the laser is shut off at $t = 15.0$ ms, the laser-induced recoil pressure decreases quickly. Under the action of surface tension and hydrostatic pressure, the molten metal near the keyhole shoulder has tendency to "fill up" the keyhole. At about $t = 17.5$ ms, the first droplet impinges onto the liquid metal at the bottom of the keyhole. The downward momentum carried by the droplet causes the droplet liquid to flow downward and outward along the keyhole wall, which can be seen clearly by the sulfur composition shown in Fig. 8. Under the action of hydrostatic force and surface tension, the liquid along the keyhole wall has a tendency to flow downward along the keyhole wall. So the upward flow caused by the filler droplet impingement will be weakened. So when the subsequent droplets falls into the keyhole, the liquid level in the center of the keyhole rises, as shown in Fig. 6 at $t = 21.5$ ms. For the first several droplets, the filler metal mainly diffuses along the longitude direction. Only the first droplet can spread out along the solid-liquid interface driven by the downward momentum. However, as more and more droplets impinge into the weld pool, a vortex is created, which helps the filler metal to diffuse outwards in the latitude direction, as shown in Fig. 8.

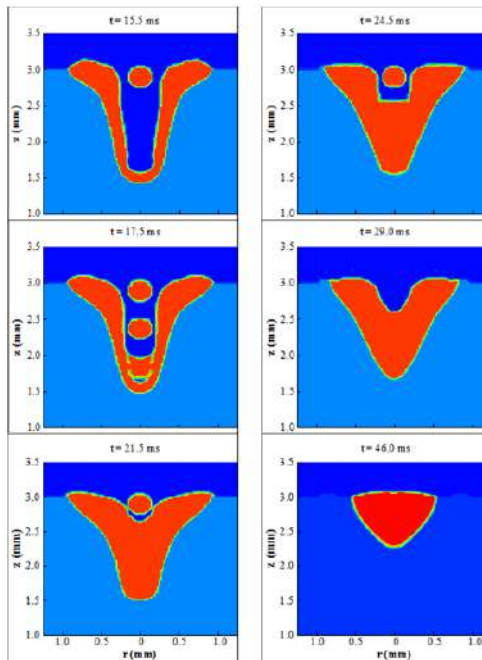


Figure 6. Droplet and weld pool interaction in hybrid laser welding.

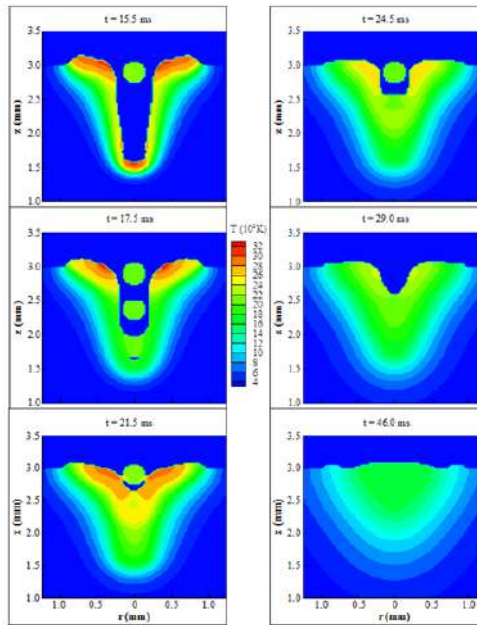


Figure 7. The corresponding temperature distributions as shown in Fig. 6.

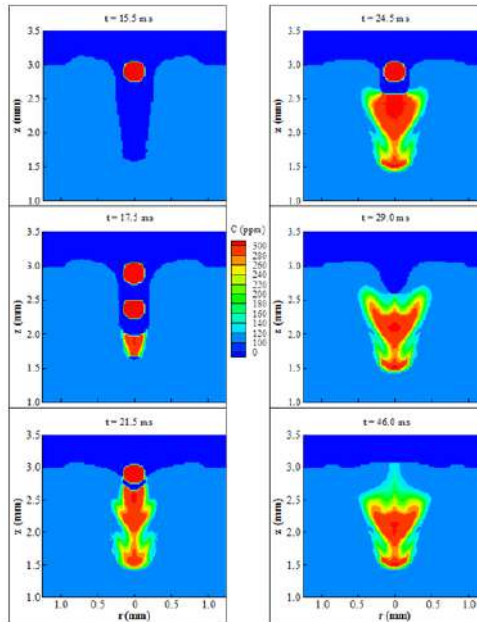


Figure 8. The corresponding sulfur concentration distributions as shown in Fig. 6

As shown in Fig. 9, there is an anticlockwise vortex in the middle waist of the keyhole. As mentioned before, the liquid on the shoulder of the keyhole has a tendency to fill back along the keyhole wall. When the droplets impinge into the keyhole, the outer liquid layer along the keyhole wall has the same flow direction as the filler metal. So the flow direction of the liquid metal here remains downward. Since the liquid is incompressible, the downward flow will push up some amount of liquid upward. The kinetic energy of the fluid flow in the center will be transferred into the potential and kinetic energy of the outward flow. So the downward momentum becomes smaller and smaller and finally it changes its direction. As shown in Fig. 9 at $t = 21.5$ ms, the flow direction changes from downward to outward at the bottom of the vortex and then bounds upward on the solid keyhole wall. During the upward flow process along the solid-liquid interface of the keyhole wall, the kinetic energy is transferred into the potential energy and the velocity becomes smaller and smaller. Finally the flow direction is changed to be inward by the back-filling momentum from the liquid on the shoulder of the keyhole. As droplets continue to drip into the keyhole, more and more downward momentum is added into the center of the keyhole, the vortex affected zone is enlarged and the strength of the vortex is enhanced, which helps the filler metal to distribute outward along with the vortex flow, as shown in Fig. 8. At $t = 24.5$ ms, the diffusion zone of filler metal is much larger compared with that at $t = 21.5$ ms. Since the latitude diffusion of filler metal has a close relationship with the vortex, the evolution of the vortex can be deduced from the shape of the diffusion zone of the filler metal in the final fusion zone. Moreover, at $t = 24.5$ ms, the downward velocity of the liquid in the center is quite large, the mass from droplets is not enough to compensate the downward mass flow in the center of the keyhole, which leaves the liquid surface decrease here.

After $t = 25.0$ ms, no droplet will be added into the keyhole. The fluid near the center of the keyhole is bounced back under the action of hydrostatic force and surface tension force. As shown at $t = 29.0$ ms in Fig. 9, the liquid in the keyhole starts to flow inward and downward, which causes the size of the keyhole to become smaller and smaller. Finally the keyhole will be filled, as shown at $t = 49.0$ ms in Fig. 6. During the backfill process, the vortex becomes weaker and weaker. So the diffusion of filler metal is not improved much in the latitude direction, which can be found by comparing those figures at $t = 29.0$ ms and at $t = 46.0$ ms in Fig. 5.9. Moreover, from the distribution of filler metal at $t = 46.0$ ms as shown in Fig. 8, it can be concluded that during the backfill process, majority of the filling metal comes from the upper shoulder of the keyhole because only a little of the filler metal is located near the center of the keyhole, which is brought here by the bouncing flow. As shown in Fig. 7, the filler droplet also brings some heat into the weld pool, which will delay the solidification process. Since the diffusion of filler in the fusion zone is greatly limited by the solidification, the delayed solidification will give more time for the filler to diffuse. After the termination of droplets, the heat input carried by droplets also decreases. Due to heat loss to the base metal through conduction and to the surroundings through radiation and convection, the size of the molten pool becomes smaller and smaller as a result of solidification. At $t = 46.0$ ms, the melt flow in the weld pool is almost diminished and the temperature distribution is more uniform than before, as shown in Figs. 9 and 7, respectively. The shape and composition of the weld will not change much comparing with the completely solidified one.

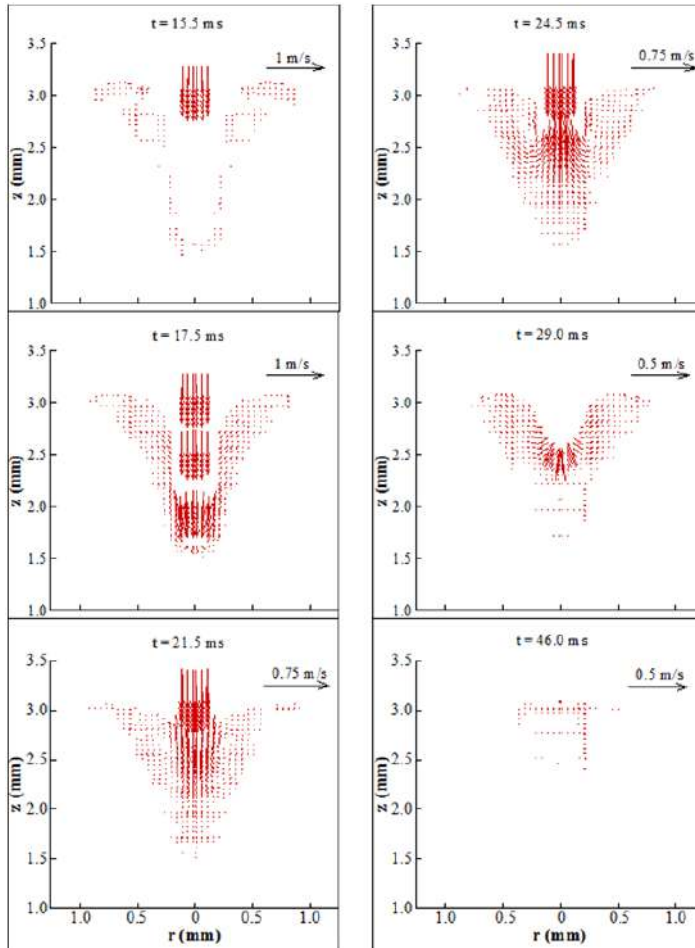


Figure 9. The corresponding velocity distributions as shown in Fig. 6.

3.3. Modification of composition by adding filler metal

Since crack sensitivity of the weld is believed to be strongly related with the composition of the weld pool, adding filler metal with anti-crack elements into the weld pool in hybrid laser welding can thus improve the weld bead quality. However, the effect depends greatly on the diffusion process in the weld pool. In the following, the effects of factors such as droplet size, droplet generation frequency, impingement velocity of the droplet and its lasting duration on the diffusion process are discussed by changing the condition of one specific parameter, while keeping the rest of the parameters unchanged. If not specially mentioned, the welding condition is defined as follows: the droplet diameter is 0.35 mm, its initial velocity is 0.5 m/s, the generation frequency is 1000 HZ and the duration of droplet feeding is 10.0 ms which starts at $t = 15.0$ ms and ends at $t = 25.0$ ms.

3.3.1. Effect of droplet size on the diffusion process in hybrid laser welding

Three studies are carried out with a droplet size of 0.3 mm, 0.35 mm and 0.4 mm respectively. As shown in Fig. 10, with the increase of droplet size, the latitude diffusion of filler metal is enlarged. From the previous discussions on the diffusion process, the latitude diffusion of the filler metal is found to be closely related to the vortex in the weld pool. The strength and the affected zone of the vortex depend on the downward momentum carried by droplets, which is the product of droplet mass and velocity. As the droplet size increases, the downward momentum increases, which will lead to a stronger vortex. So the diffusion zone is enlarged outward, especially in the middle depth of the keyhole where the vortex is located. This is clear shown by comparing those figures for $d = 0.30$ mm and $d = 0.35$ mm in Fig. 10. Meanwhile, larger downward momentum from larger droplet also leads to a strong bouncing flow near the center of keyhole after termination of droplet feeding, which helps filler metal to diffuse into the upper layer in the final weld, as shown in Fig. 10 for $d = 0.40$ mm. Moreover, larger droplet size brings more filler metal into the keyhole. The heat input carried by droplets also increases, which helps delay the solidification of the fusion zone. Thus, the filler metal has more time to diffuse into the weld pool before its solidification. More filler metal also helps to increase the filler concentration in the final weld. However, larger droplets also lead to some negative effects on the diffusion of filler metal near the center of the weld zone. After the termination of droplet feeding, the melt surface near the center of the keyhole will continue to go down due to the larger hydrodynamic pressure caused by the downward momentum. This will lead to a deep hole there. During the backfill process of this hole, some metal from the upper part of the keyhole may flow into the bottom part of this hole. Since the concentration of filler metal in the upper part of keyhole is very low, it leaves a low diffusion zone of filler metal in the center of the final weld, as shown in Fig. 10 for $d = 0.40$ mm.

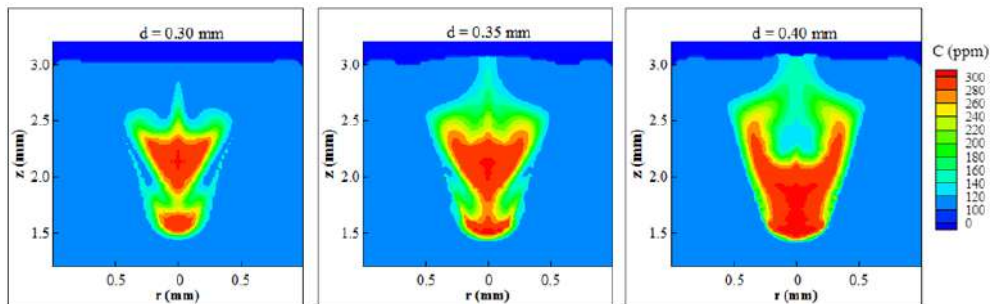


Figure 10. Effect of droplet size on diffusion process in hybrid laser welding.

3.4. Effect of droplet generation frequency on diffusion of filler metal in fusion zone

In the hybrid laser welding process, the droplet is generated at a specific frequency that is controlled by the wire feed rate. The effect of droplet generation frequency on diffusion of

filler metal in the fusion zone is shown in Fig. 11. In the study, the droplet generation frequency is 500 HZ, 667 HZ and 1000 HZ, which corresponds to the generation of one droplet every 2.0 ms, 1.5 ms and 1.0 ms. As shown, the diffusion of filler metal in the weld pool is improved with the increase of generation frequency. This can be interpreted through the above analysis on the interaction between the droplets and weld pool. As mentioned before, the latitude diffusion of filler is mainly through the vortex flow induced by the impingement of droplets. With the increase of generation frequency, more droplets fall into the weld pool per unit time, which results in higher downward momentum per unit time. So the vortex in the weld pool is enhanced, which helps the filler metal diffuse in the latitude direction. Meanwhile, the total amount of filler metal added into the weld pool also increases with higher generation frequency, which also helps increase the concentration of filler metal in the final weld and increase the diffusion time, as mentioned before. Furthermore, the longitude distribution of filler metal is found to be improved with higher generation frequency. As shown, in the case $f = 500$ HZ, there exists a low filler metal concentration zone in the lower part of the keyhole due to the weak strength of the vortex in the weld pool and a long delay time between the droplet generation. When frequency increases to 1000 HZ, the size of this zone is greatly reduced.

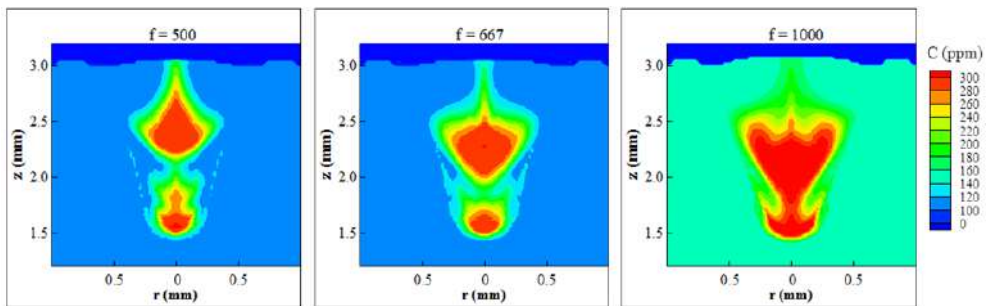


Figure 11. Effect of droplet generation frequency on diffusion process in hybrid laser welding.

3.5. Effect of droplet generation duration on diffusion of filler metal in fusion zone

In hybrid laser welding, the termination of droplet generation can be achieved through the control of removal of the filler wire. The effect of controlling the droplet generation duration on metal diffusion in the weld pool is investigated. As shown in Fig. 12, three cases are carried out with droplet generation duration at 5.0 ms, 10.0 ms and 15.0 ms, respectively. For short duration of 5.0 ms, the vortex induced by the downward momentum of the droplet is not completely developed because of lower downward momentum, which leads to poor latitude distribution of filler metal. In this case, most of the filler metal is located in the lower part of the keyhole. During the backfill process, the bounced flow is not strong enough to push the filler metal upward to the upper part of the keyhole. The keyhole is filled with the base metal liquid where no filler metal exists. So the longitude filler diffusion is also poor with a short duration of droplet generation.

With the increase of the duration length to 10.0 ms, more filler metal will fall into the keyhole. The vortex in the weld pool is enhanced with the increased downward momentum which improves the latitude diffusion. Meanwhile, the droplets are distributed along the entire depth of the keyhole, which leads to better longitude distribution of filler metal. Moreover, the total amount of filler metal also increases with the increase of duration, which also helps the diffusion of filler metal in the fusion zone, as mentioned before. So both the longitude and latitude diffusion of filler metal are improved, as shown. However, with a further longer droplet generation to 15.0 ms, the downward momentum is accumulated due to the continuous impingement of the droplets into the weld pool, which leads to a deep hole in the weld pool. During the backfill process of this hole, the filler metal is mainly located in the bottom, which cannot bounce back in time before the base metal fluid from the upper shoulder arrives at the bottom of this hole, which leaves a low diffusion zone of filler metal in the center of final weld, as shown in Fig. 12.

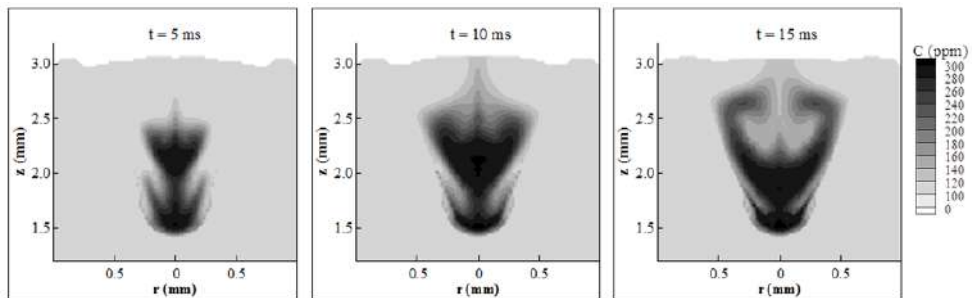


Figure 12. Effect of droplet impingement duration on diffusion process in hybrid laser welding.

3.6. Three-dimensional hybrid laser-MIG welding

Fig. 13 shows a schematic sketch of a three-dimensional hybrid laser-MIG welding. In this study, the laser power is 2.0 kW and the laser beam radius is 0.2 mm and the focal plane is on the top surface of the base metal. The laser beam is started at $x = 3.75$ mm. The laser beam begins to move after being held for 20.0 ms for the keyhole to reach a certain depth. The welding speed is 2.5 cm/s and the arc power is 1 kW. Droplet begins to fall onto the base metal at $t = 20.0$ ms and the radius of the droplet is 0.25 mm. The droplet feeding frequency is 86 Hz and its initial speed is 30 cm/s. The distance between arc center and laser beam center is 1 mm. Fig. 14 is the side-view (at $Y = 0$) of the hybrid laser welding process showing a sequence of a droplet impinging onto the weld pool at different times. Fig. 15 shows the corresponding sulfur concentration distribution during the hybrid welding process, indicating the mixing process in the welding. Fig. 16 shows the corresponding velocity distributions in the weld pool. As shown in Fig. 15, the filler droplet did not mix well with the base metal in this case. Most of the droplet is just stacking on the top of the weld coupon and only small amount of the filler metal is diffused into the base metal near the solid-liquid interface. The poor mixing may have been caused by the relative long distance between the laser beam and MIG arc

center. The filler droplet is impinging into the weld pool where only a small amount of liquid metal exists. Since the temperature of this part of liquid metal is low, due to the quick solidification process there, the liquid metal there solidifies very quickly. The droplet flowing downward does not have enough time to flow around and exchange the momentum and mix with the base metal before it solidifies, as shown in Fig. 16. Therefore, most of the filler metals are just stacking on top surface of the base metal.

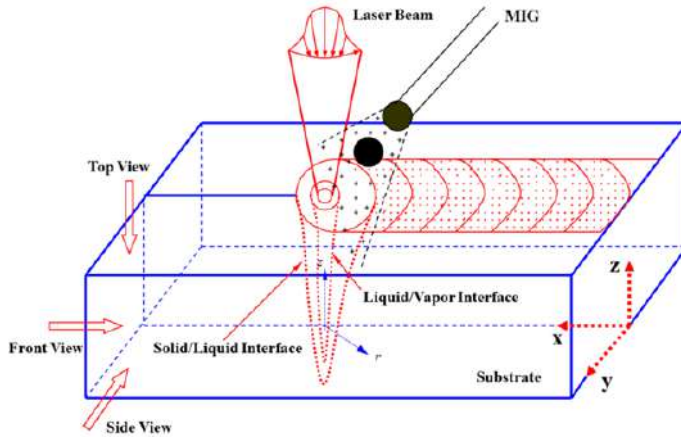


Figure 13. Schematic sketch of 3-D hybrid laser keyhole welding.

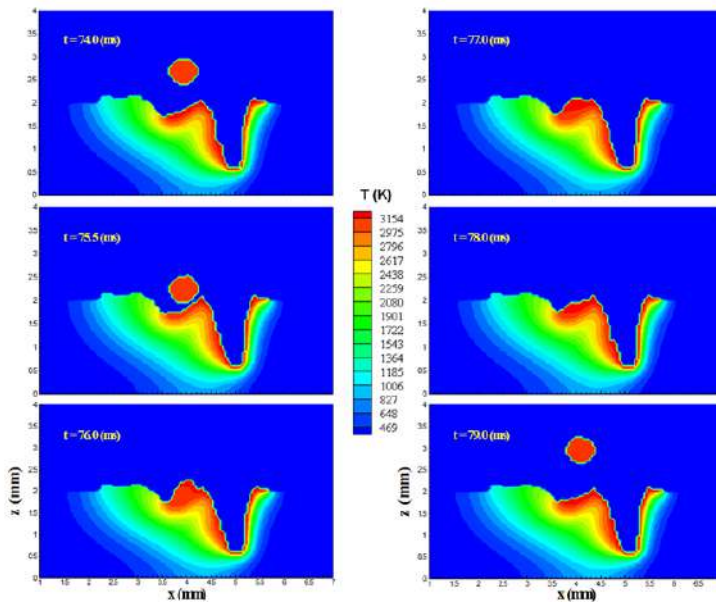


Figure 14. A typical sequence showing the impinging process and temperature distributions in 3-D moving hybrid laser keyhole welding.

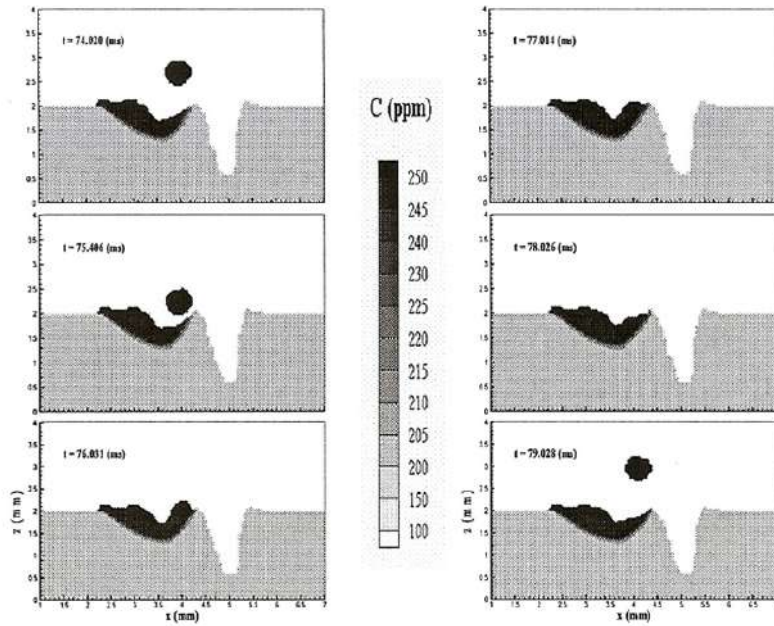


Figure 15. The corresponding sulfur concentration distributions as shown in Fig. 14.

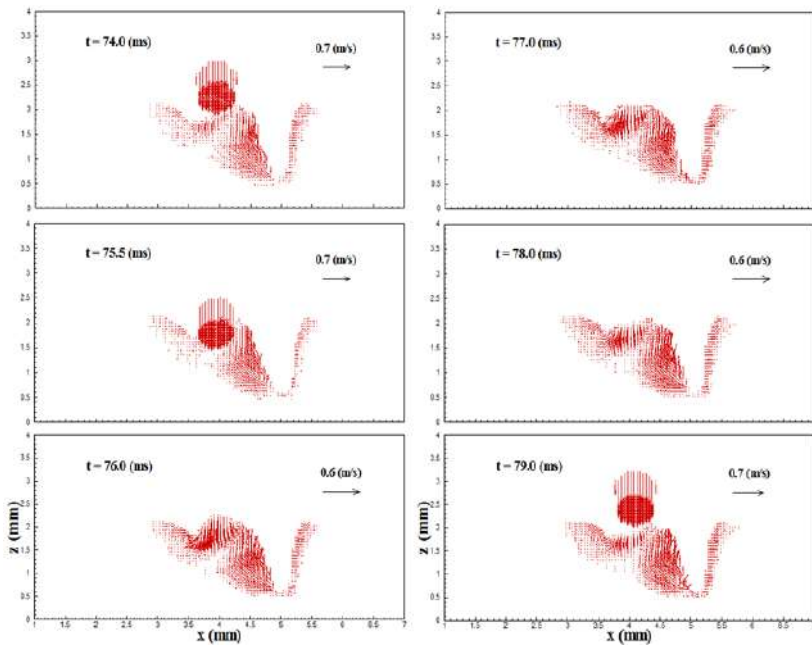


Figure 16. The corresponding velocity distributions as shown in Fig. 14.

There are a lot of process parameters which can affect the mixing of filler droplets into the weld pool in three-dimensional hybrid laser-arc welding. These include laser-arc distance, laser and arc powers, welding speed, wire feed speed and filler droplet size, etc. In the following study, the effect of laser-arc distance on diffusion is conducted by decreasing the laser-arc distance to 0.6 mm. Fig. 17 shows the mixing process during the welding. As shown, the droplet is now mixing with the base metal much better than in the previous case. In this case, since the laser-arc distance is decreased, the filler droplet can impinge into a region in the weld pool where there exists a lot of liquid metal with strong velocity and high temperature. This strong velocity liquid metal flow will interact with the impinging droplets, creating a strong momentum exchange between the droplets and weld pool, which can force the droplet to flow in all directions. Hence, a better mixing can be achieved. Also, in this case, there are more hot liquid metals in the droplet-weld pool interaction zone, thus creating relatively longer time for the droplet to mix and diffuse into the base metal. Hence, a better mixing of droplets into the weld pool is achieved.

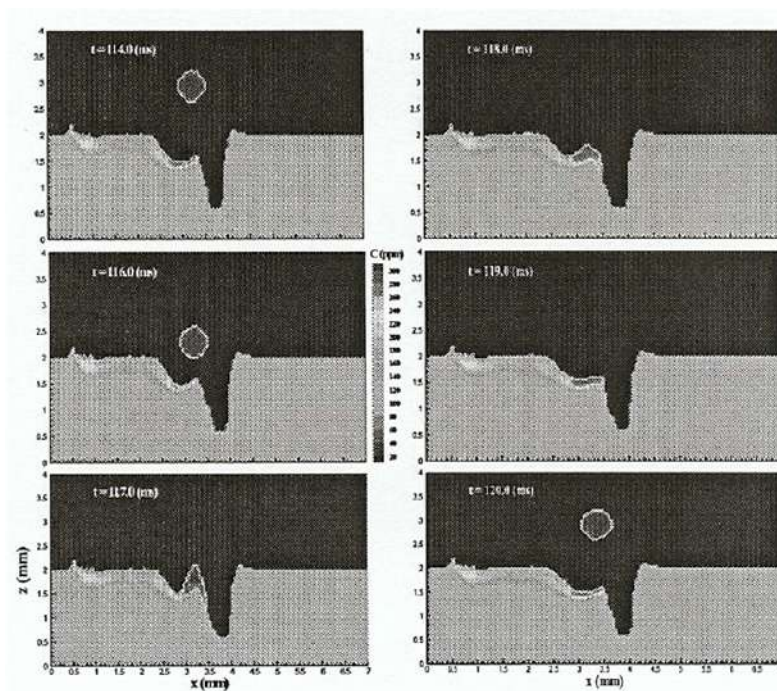


Figure 17. Diffusion process in 3-D hybrid laser keyhole welding with shorter laser-arc distance.

4. Future trends

Although hybrid laser-arc welding has been under investigation and development and gaining increasing acceptance in recent years, good understanding of the underlying physics remains a challenge. For example, the interaction between the laser and the arc has

been observed to enhance arc stability and push the arc towards the laser keyhole, resulting in a deeper penetration. However, the origin of this synergistic interaction between the arc and laser plasma is not well understood. Measuring the distributions of electron temperatures and densities in the plasma can provide a better understanding of the laser-arc interaction⁹. Porosity formation is believed to be strongly related to the keyhole collapse process. Hence, better understanding of keyhole stability and dynamics through experimental and theoretical studies would be beneficial. Hybrid welding is known to produce welds with desirable widths and depths, but the maximum gap tolerance and weld penetration for various welding conditions have not been quantified. In the future, advanced mathematical modeling of the heat transfer and fluid flow will enable accurate predictions of weld profile and cooling rates in the welding process, which is critical in understanding the evolution of weld microstructures and residual stress formation in welds. Thus, the hybrid welding process can be optimized to obtain quality welds with no cracking, no brittle phase and less thermal distortion. Better sensing and process control of the hybrid welding process would also be helpful in expanding its applications⁶⁷.

Author details

J. Zhou

Department of Mechanical Engineering, Pennsylvania State University, The Behrend College, USA

H.L. Tsai

*Department of Mechanical and Aerospace Engineering,
Missouri University of Science and Technology, USA*

5. References

- [1] Tusek, J., and Suban, M., 'Hybrid welding with arc and laser beam', *Science and Technology of Welding and Joining*, 4(5), 308-311, 1999.
- [2] Mahrle, A., and Beyer, E., 'Hybrid laser beam welding – Classification, characteristics, and applications', *Journal of Laser Applications*, 18(3), 169-180, 2006.
- [3] Steen, W.M., 'Arc-augmented laser processing of materials' *J. Appl. Phys.*, 51, 5636–5641, 1980.
- [4] Campana, G., Fortunato, A., Ascari, A., Tani, G., and Tomesani, L., 'The influence of arc transfer mode in hybrid laser-MIG welding', *J. Mater. Process. Technol.*, 191, 111–113, 2007.
- [5] Casalino, G., 'Statistical analysis of MIG-laser CO₂ hybrid welding of Al–Mg alloy', *J. Mater. Process. Technol.*, 191, 106–110, 2007.
- [6] Hu, B., and Richardson, I.M., 'Microstructure and mechanical properties of AA7075(T6) hybrid laser/GMA welds', *Material Science Engineering A*, 459, 94-100, 2007.
- [7] Feng, Z.L., *Processes and mechanisms of welding residual stress and distortion*, Woodhead Publishing Ltd, Cambridge, England, 2005.
- [8] Metzbowler, E.A., Denney, P.E., Moon, D.W., Feng, C.R., and Lambrakos, S.G., 'Thermal analysis and microhardness mapping in hybrid laser welds in a structural steel', *Materials Science Forum*, 426-432, 4147-4152, 2003.

- [9] Ribic, B., Palmer, T.A., and Debroy, T., 'Problems and issues in laser-arc hybrid welding', *International Materials Reviews*, 54(4), 223-244, 2009.
- [10] G. Song, L. M. Liu and P. C. Wang: *Material Science Engineering A*, 429, 312-319, 2006.
- [11] Nonn, A., Dahl, W., and Bleck, W., 'Numerical modelling of damage behaviour of laser-hybrid welds', *Engineering Fracture Mechanics*, 75, 3251-3263, 2008.
- [12] Pinto, H., Pyzalla, A., Hackl, H., and Bruckner, J., 'A Comparative Study of Microstructure and Residual Stresses of CMT-, MIG- and Laser-Hybrid Welds', *Materials Science Forum*, 524-525, 627-632, 2006.
- [13] Zhang, J. X., Xue, Y., and Gong, S. L., 'Residual welding stresses in laser beam and tungsten inert gas weldments of titanium alloy', *Science and Technology of Welding & Joining*, 10, 643-646, 2005.
- [14] Liu, L.M., Song, G., and Wang, J.F.,", *Materials Science Forum*, 488-489, 361-364, 2005.
- [15] Liu, L.M., Song, G., Liang, G.L., and Wang, J.F, 'Pore formation during hybrid laser tungsten inert gas arc welding of magnesium alloy AZ31B – mechanism and remedy', *Material Science and Engineering A*, 390, 76-80, 2005.
- [16] Katayama, S., Uchiumi, S., Mizutani, M., Wang, J., and Fujii, K., 'Penetration and porosity prevention mechanism in YAG laser-MIG hybrid welding', *Welding International*, 21, 25-31, 2007.
- [17] Fellman, A., and Kujanpaa, V., 'The effect of shielding gas composition on welding performance and weld properties in hybrid CO₂ laser-gas metal arc welding of carbon manganese steel', *Journal of Laser Applications*, 18, 12-20, 2006.
- [18] Kim, T., Suga, Y., and Koike, T., 'Welding of thin steel plates by hybrid welding process combined TIG arc with YAG laser', *JSME International Journal Series A*, 46A, 202-207, 2003.
- [19] Kim, Y. P., Alam, N., and Bang, H. S., 'Observation of hybrid (cw Nd:YAG laser + MIG) welding phenomenon in AA5083 butt joints with different gap conditions', *Science and Technology of Welding & Joining*, 11(3), 295-307, 2006.
- [20] Murakami, K., Mitooka, Y., Hino, M., Iogawa, H., Ono, H., and Katayama, S., "", *J. Japn. Inst. Met.*, 70, 134-137, 2006.
- [21] Qin, G. L., Lei, Z., and Lin, S. Y., 'Effects of Nd:YAG laser + pulsed MAG arc hybrid welding parameters on its weld shape', *Science and Technology of Welding & Joining*, 12(2), 79-86, 2007.
- [22] Swanson, P. T., Page, C. J., Read, E., and Wu, H. Z., 'Plasma augmented laser welding of 6 mm steel plate', *Science and Technology of Welding & Joining*, 12(2), 153-160, 2007.
- [23] Eboo, M., Steen, W.M., and Clarke, J., 'Arc-augmented laser welding', *Advances in Welding Processes*, Proc. of the 4th Int. Conf., Harrogate, UK, 257-265, 1978.
- [24] Steen, W. M., and Eboo, M., 'Arc augmented laser welding', *Metal Construction*, 11, 332-335, 1979.
- [25] Bagger, C., and Olson, F.O., 'Review of laser hybrid welding', *Journal of Laser Applications*, 17(1), 2-14, 2005.
- [26] Cui, H., Decker, I., and Ruge, J., 'Wechselwirkungen zwischen WIGSchweißlichtbogen und fokussiertem Laserstrahl', *Proc. of the Conference Laser'89*, Springer, Berlin, 577-581, 1989.

- [27] Finke, B. R., Stern, F., and Decker, I., 'Auswirkungen eines unterstützenden Laserstrahls auf den WIG-Schweißprozess,' *DVS-Ber.*, 135, 149–152, 1991.
- [28] Cui, H., Decker, I., Pursch, H., Ruge, J., Wendelstorf, J., and Wohlfahrt, H., 'Laserinduziertes Fokussieren des WIG-Lichtbogens', *DVS-Ber.*, 146, 139–143, 1992.
- [29] Dilthey, U., Lüder, F., and Wieschemann, A., 'Expanded capabilities in the welding of aluminium alloys with the laser-MIG hybrid process', *Aluminium*, 75, 64–75, 1999.
- [30] Graf, T., and Staufer, H., 'Laser hybrid process at Volkswagen', *International Institute of Welding*, IIW-Doc. XII-1730-02, 1999.
- [31] Jokinen, T., Vihervä, T., Riikonen, H., and Kujanpää, V., 'Welding of ship structural steel A36 using a Nd:YAG laser and gas metal arc welding', *Journal of Laser Applications*, 12, 185–188, 2000.
- [32] Höfemann, M., Fersini, M., Szinyur, J., Haferkamp, H., and Cordini, P., 'Laser-GMA-hybrid welding of zinc-coated steel for hydroforming applications', *Proc. of the 1st Int. WLT-Conf. on Lasers in Manufacturing*, Munich, Germany, 466–472, 2001.
- [33] Dilthey, U., and Keller, H., 'Prospects in laser GMA hybrid welding of steel', *Proc. of the 1st Int. WLT-Conf. on Lasers in Manufacturing*, Munich, Germany, 453–465, 2001.
- [34] Waltz, C., Seefeld, T., and Sepold, G., 'Laser-GMA welding and its influence on bead geometry and process stability', *Proc. of the 1st Int. WLT-Conf. on Lasers in Manufacturing*, Munich, Germany, 444–452, 2001.
- [35] Shibata, K., Sakamoto, H., and Iwase, T., 'Laser-MIG hybrid welding of aluminium alloys', *Proc. of the 1st Int. WLT-Conf. on Lasers in Manufacturing*, Munich, Germany, 436–443, 2001.
- [36] Jokinen, T., Jernström, P., Karhu, M., Vanttaja, I., and Kujanpää, V., 'Optimisation of parameters in hybrid welding of aluminium alloy', *Proc. Of the 1st Int. Symp. on High Power Laser Macroprocessing*, Proc. SPIE 4831, 307–312, 2003.
- [37] Ishide, T., Tsubota, S., and Watanabe, M., 'Latest MIG, TIG Arc-YAG laser hybrid welding systems for various welding products', *Proc. of the 1st Int. Symp. on High Power Laser Macroprocessing*, 2003 Proc. SPIE 4831, 347–352, 2003.
- [38] Hyatt, C. V., Magee, K. H., Porter, J. F., Merchant, V. E., and Matthews, J. R., 'Laser-assisted gas metal arc welding of 25-mm-thick HY-80 plate', *Welding Journal Symposium*, Miami, FL, U. S.A, 163s–172s, 2001.
- [39] Fellman, A., Jernström, P., and Kujanpää, V., 'The effect of shielding gas composition in hybrid welding of carbon steel', *Proceedings 9th NOLAMP, Conference on Laser Materials Processing in the Nordic Countries*, Trondheim, Norway, 103–112, 2003.
- [40] Zhou, J., and Tsai, H.L., 'Modeling of transport phenomena in hybrid laser-MIG keyhole welding', *International Journal of Heat and Mass Transfer*, 51, 4353–4366, 2008.
- [41] Page, C. J., Devermann, T., Biffin, J., and Blundell, N., 'Plasma augmented laser welding and its applications', *Science and Technology of Welding & Joining*, 7(1), 1–10, 2002.
- [42] S. M. Joo, Y. P. Kim, C. S. Ro, H. S. Bang and J. U. Park, " , *Adv. Nondestr. Eval.*, 270–273, 2383–2388, 2004.
- [43] Graf, T., and Staufer, H., 'Laser-hybrid welding drives VW improvements', *Welding Journal*, 82, 42–48, 2003.

- [44] Ono, M., Shinbo, Y., Yoshitake, A., and Ohmura, M., 'Welding properties of thin steel sheets by laser-arc hybrid welding: laser-focused arc welding', *Proc. 1st Int. Symp. on High-power laser macroprocessing*, Osaka, Japan, 369–374, 2002.
- [45] Song, G., Liu, L. M., Chi, M. S., and Wang, J. F., 'Investigations of Laser-TIG Hybrid Welding of Magnesium Alloys', *Materials Science Forum*, 488–489, 371–375, 2005.
- [46] Chiang, K.C., Tsai, H.L., 'Shrinkage-induced fluid flow and domain change in two-dimensional alloy solidification', *Int. J. Heat and Mass Transfer*, 35, 1763-1769, 1992.
- [47] Zhou, J., Tsai, H.L., and Wang, P.C., 'Transport Phenomena and Keyhole Dynamics during Pulsed Laser Welding', *ASME Journal of Heat Transfer*, 128(7), 680-690, 2006.
- [48] Wang, Y., 'Modeling of three-dimensional gas metal arc welding process', *Ph.D. Thesis*, University of Missouri-Rolla, 1999.
- [49] Lowke, J.J., Kovitya, P., and Schmidt, H.P., 'Theory of free-burning arc columns including the influence of the cathode', *J. Phys. D: Appl. Phys.*, 25, 1600-1606, 1992.
- [50] Haidar, J., 'A theoretical model for gas metal arc welding and gas tungsten arc welding', *J. Appl. Phys.*, 84, 3518-3529, 1998.
- [51] Haidar, J., Lowke, J.J., 'Predictions of metal droplet formation in arc welding', *J. Appl. Phys. D: Appl. Phys.*, 29, 2951-2960, 1996.
- [52] Haidar, J., 'An analysis of the formation of metal droplets in arc welding', *J. Phys. D: Appl. Phys.*, 1233-1244, 1998.
- [53] Haidar, J., 'Prediction of metal droplet formation in gas metal arc welding. II.', *J. Appl. Phys.*, 84, 3530-3540, 1998.
- [54] Haidar, J., 'An analysis of heat transfer and fume production in gas metal arc welding. III.', *J. Appl. Phys.*, 85, 3448-3459, 1998.
- [55] Lowke, J.J., Kovitya, P., and Schmidt, H.P., 'Theory of free-burning arc columns including the influence of the cathode', *J. Phys. D: Appl. Phys.*, 25, 1600-1606, 1995.
- [56] Zhu, P., Lowke, J.J., Morrow, R., 'A unified theory of free burning arcs, cathode sheaths and cathodes', *J. Phys. D: Appl. Phys.*, 25, 1221-1230, 1992.
- [57] Brackbill, J.U., Kothe, D.B., and Zemach, C., 'A continuum method for modeling surface tension', *J. of Computational Physics*, 100, 335-354, 1992.
- [58] Fan, H.G., and Kovacevic, R., 'Droplet formation, detachment, and impingement on the molten pool in gas metal arc welding', *Metall. Trans.*, 30B, 791–801, 1999.
- [59] Anisimov, S.I., 'Vaporization of metal absorbing laser radiation', *Soviet Physics, JETP* 27 (1), 182-183, 1968.
- [60] Knight, C.J., 'Theoretical modeling of rapid surface vaporization with back pressure', *AIAA J.*, 17(5) 519-523, 1979.
- [61] Kanouff, M.P., Kassinos, A., Noble, D.R., and Schunk, P.R., 'Laser spot weld modeling using an ALE finite element method', Sandia National Laboratories Report.
- [62] Kaplan, A., 'A model of deep penetration laser welding based in calculation of the keyhole profile', *J. Phys. D: Appl. Phys.*, 27, 1805-1814, 1994.
- [63] Duley, W., *Laser welding*, John Wiley & Sons, 1999.
- [64] Ducharme, R., Williams, K., Kapadia, P., Dowden, J., Steen, B., and Glowacki, M., 'The laser welding of thin metal sheets: an integrated keyhole and weld pool model with supporting experiments', *J. Phys. D: Appl. Phys.*, 27, 1619-1627, 1994.

- [65] Ho, J.R., Grigoropoulos, C.P., Humphrey, J.A.C., 'Gas dynamics and radiation heat transfer in the vapor plume produced by pulsed laser irradiation of aluminum', *J. Appl. Phys.*, 79, 7205-7215, 1996.
- [66] Bagger, C., Olsen, F.O., 'Review of hybrid laser welding', *J. Laser Appl.*, 17, 2-14, 2005.
- [67] Ribic, B., Palmer, T.A., DebRoy, T., 'Problems and issues in laser-arc hybrid welding', *Int. Mater. Rev.*, 54 (4), 223-244, 2009.
- [68] Kong, F. and Kovacevic, R., '3D Finite Element Modeling of the Thermally Induced Residual Stress in the Hybrid Laser/Arc Welding of Lap Joint', *Journal of Materials Processing Technology*, 941-950, 2010.
- [69] Zhou, J., Zhang, W. H., Tsai, H. L., Marin, S. P., Wang, P. C., and Menassa, R., 'Modeling the transport phenomena during hybrid laser-MIG welding process', *Proceedings IMECE'03, ASME International Mechanical Engineering Congress & Exposition*, Washington, DC, IMECE2003-41763, 1-8, 2003.
- [70] Zhou, J., and Tsai, H. L., 'Investigation of mixing and diffusion processes in hybrid spot laser – MIG keyhole welding', *Journal of Physics D: Applied Physics*, 42, 1-15, 2009.

Dissimilar Metal Joining of Zinc Coated Steel and Aluminum Alloy by Laser Roll Welding

Hitoshi Ozaki and Muneharu Kutsuna

Additional information is available at the end of the chapter

<http://dx.doi.org/10.5772/48242>

1. Introduction

Nowadays, the car industry has targets to improve fuel consumption due to the problems of the global environment. For example, in the Corporate Average Fuel Economy, CAFE, which was approved in the U. S. Congress in July 2011, attaining the average fuel efficiency of 54.5 mpg (23.2 km/l) by 2025 is called for (Yamamoto, 2012). In addition, it's obliged to improve the average fuel efficiency to 35.5 mpg (15.1 km/l) by 2017. This is a significant increase compared with the present 27.5 mpg (11.7 km/l) which have been fixed for the past 11 years. Hence, the further weight reduction of cars has become imperative.

On the other hand, the weight of vehicle which influences the fuel consumption directly is increasing owing to a rise of safety awareness of automobile user's, tightening of safety standards, and diversification and sophistication of needs. Therefore, the car industry has conflicting targets of the low fuel consumption by "lightening car body" and "safety improvement". Additionally these targets should be achieved in together. Then, a "hybrid body structure" concept has been proposed.

In this concept, high strength steel and light alloy are arranged in the right places of the car body. For instance, by using high strength steel for pillars, a lightening with improving strength is achieved. In addition, by using aluminum alloys for the bonnet, the door panel, and the trunk lid, a further lightening is achieved. In order to make this "hybrid body structure", the welding technology for joining of steel to aluminum with high reliability and productivity is required. However, it's difficult to join steel to aluminum by conventional fusion welding.

Generally, in respect to dissimilar metal joining by the fusion welding, because of melting and alloying largely both metals, intermetallic compound layer formed at joint interface grows thick; oxide film is formed; hot cracking is generated. Consequently, high joint

strength can not be gotten. Moreover, when melting point of both metals has large difference, burn-through occurs in the metal of lower melting point (Nishimoto et al., 2005).

In order to solve these problems, many studies of the dissimilar metal joining have been conducted such as resistance welding (Okita, 2004), laser welding (Katayama, 2004), explosive welding (Satou, 2004), friction stir welding (Okamura & Aota, 2004; Katoh & Tokisue, 2004), and diffusion bonding (Ohashi, 2004). As a result, solid-phase bonding is mainly put to practical use. However, higher productivity, joint strength and flexibility are needed to expand the coverage of application of the dissimilar metal joints. Since laser welding has advantages such as local heat input, short process time and high flexibility compared with other welding processes, there has been considerable research on the welding of steel and aluminum. In the recent, the studies of keyhole welding (Torkamany, et al., 2010), laser welding-brazing (Dharmendra, et al., 2011), dual-beam YAG laser welding (Yan, et al., 2010), and thermal cycle during laser welding (Fan, et al., 2011) are carried out.

Then, the welding process of steel and aluminum which have been regarded as difficult, Laser Roll Welding has been developed for joining of dissimilar metals by M. Kutsuna, M. Rathod and A. Tsuboi in 2002. This welding is a hybrid welding process, as shown in Fig.1, combined high-temperature heating by a 2.4 kW CO₂ laser with pressurizing by a pressure roller. It's registered as Japanese Patents No. 3535152 and No. 3692135.

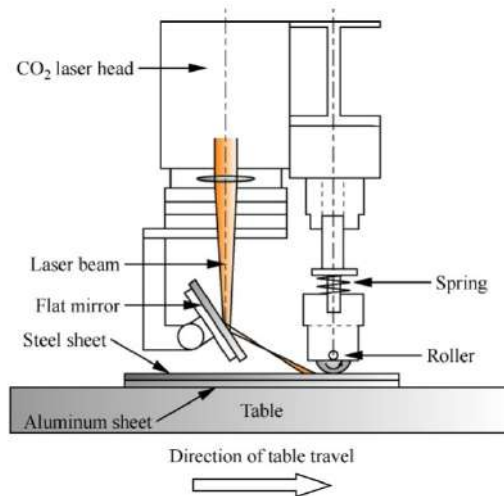


Figure 1. Schematic diagram of Laser Roll Welding process

Fig.2 shows Fe-Al phase diagram (Massalski, et al., 1986). In this figure, there are various intermetallic compounds, hereafter, called as IMC's, and they are grouped as Fe-rich compounds, FeAl and Fe₃Al, and Al-rich compounds, FeAl₂, Fe₂Al₅ and FeAl₃. M. Yasuyama et al. (1996) have shown the mechanical properties of these IMC's. Vickers hardness of cast IMC's is shown in Table 1, and mechanical properties by compressive test are shown in Fig.3.

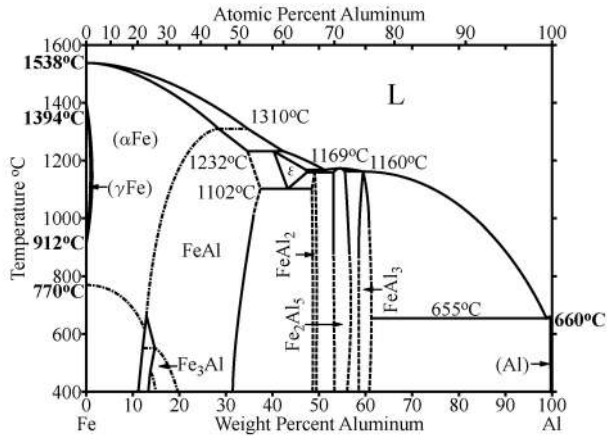


Figure 2. Fe-Al binary equilibrium diagram

	Vickers hardness
FeAl ₃	892
Fe ₂ Al ₅	1013
FeAl	470
Fe ₃ Al	330

Table 1. Vickers hardness of Fe-Al intermetallic compounds

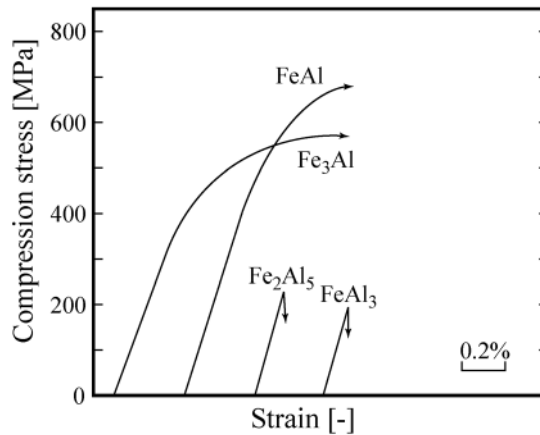


Figure 3. Stress-strain curves in compressive test of Fe-Al intermetallic compounds

While Al-rich IMC's are hard and brittle, Fe-rich IMC's show slight ductility and high strength. These brittle IMC's constitute barriers to the dissimilar metal welding of steel to

aluminum. Kutsuna et al. thought if the thickness of brittle IMC layer is minimized and the formation of more ductile IMC's is promoted, high reliable joints are able to be obtained. Therefore, they developed the Laser Roll Welding process. In this process, since the thermal cycle for joining can be shortened by laser heating, the formation of the brittle IMC's can be easily controlled. Furthermore, good contact of a steel sheet and an aluminum sheet and rapid heat transfer from the steel sheet to the aluminum sheet are conducted by the pressure roller.

Kutsuna et al. produced Laser Roll Welding equipment experimentally, and conducted basic studies of the welding of low carbon steel to aluminum alloy (Rathod & Kutsuna, 2003, 2004). As a result, when the IMC layer thickness was from 4 to 8 μm , failure of base metal sheet was obtained after tensile shear test of specimen.

Until now, it's found that Laser Roll Welding has two types of welding mechanisms. The combination of iron and aluminum is that of metals with large difference in their melting points (Ozaki & Kutsuna, 2007). The combination of titanium and aluminum also corresponds to this category (Ozaki et al., 2008). In this case, only the metal with a higher melting point is heated up to an elevated temperature for avoid the formation of brittle IMC's. For example, in the case of steel to aluminum joint, steel is heated up to 1200 °C, because the max formation temperature of Fe_2Al_5 is 1169 °C. The interlayer is formed and cooled rapidly to minimize the thickness of brittle IMC's.

The other is a combination of metals with eutectic reaction at a lower temperature than melting point. For instance, the combination of titanium and iron falls into this type (Ozaki et al., 2007). In this case, the eutectic reaction occurs at a lower temperature, about 1085 °C, than melting points of both metals. The interlayer of the eutectic phase, $\beta\text{-Ti}$ and TiFe , is formed at the interface.

In this way, uncoated materials have been mainly used in the previous study of Laser Roll Welding. However, coated materials such as zinc coated steel have not investigated enough yet. In this chapter, Laser Roll Welding of zinc coated steel and 6000 series aluminum alloy was conducted, and the weldability was investigated. Two types of zinc coated steel were used. One is hot-dip galvanized steel called as GI, the other is hot-dip galvanized steel called as GA. The former is used mainly in Europe, the latter is in Japan. Then, the influences of process parameters, such as welding speed and roll pressure, on the formation of intermetallic compound layer and the change of zinc coated layer have been investigated to get sound joints with these galvanized steel. Furthermore, the effects of process parameters on joint performance have been also discussed.

2. Experimental procedure

2.1. Materials used

As materials, two types of zinc coated steel and A6000 series aluminum alloy, Al-0.5Mg-1.0Si, were used for joining. The zinc coated steels were hot-dip galvanized steel, hereafter,

called as GI, and hot-dip galvanized steel, hereafter, called as GA, respectively. The dimension of the zinc coated steel sheets were 125 x 180 x 0.55 mm and that of the A6000 series aluminum alloy sheet, hereafter, called as A6000, was 125 x 180 x 1 mm. The zinc coating weight of the GI sheet was 60 g/m² and the GA was 45 g/m².

The surface of the steel sheets was coated with graphite by using a graphite spray to increase the absorption rate of laser beam. The thickness of the coating layer was approximately 10 μm. The faying surface of the steel sheets was only degreased with ethanol alcohol. The faying surface of the A6000 sheet was wire-brushed, polished by emery paper #600 and cleaned by ethanol before welding. Then, to remove the oxide film on aluminum alloy sheet, the surface of the aluminum alloy was spread with flux, KAlF₄:K₂AlF₅·H₂O, 17-25 wt%, with particle size of 15 to 21 μm.

The setup of specimens is shown in Fig.4. A zinc coated steel sheet is placed as a top plate; an A6000 sheet is placed as a bottom with 3 mm width overlapping.

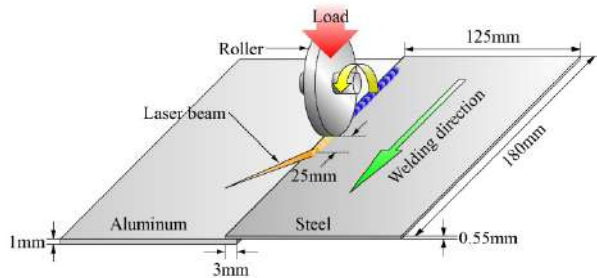


Figure 4. Setup of specimens in Laser Roll Welding

Laser type	CO ₂ laser (Pulse mode)
Laser peak power	2.0 kW
Duty cycles	75%
Frequency	150 Hz
Beam spot size	Minor axis : 2.5 mm Major axis : 3.5 mm
D _{LR}	25 mm
Welding speed	3.3 ~ 15.0 mm/s
Overlapped width	3 mm
Roll pressure	100 ~ 175 MPa
Shielding gas	Ar : 25 l/min

D_{LR}: Distance between Laser beam spot and Roller

Table 2. Process parameters for Laser Roll Welding

2.2. Process parameters

In this study, to investigate the effect of the welding condition on the joint properties of two types of zinc coated steel and aluminum alloy by Laser Roll Welding, welding speed and roll pressure were varied. Process parameters are shown in Table 2.

Pulsed laser was used by controlling a 2.4 kW CO₂ laser with continues wave. Laser peak power, duty cycles and frequency were constant 2.0 kW, 75 % and 150 Hz respectively. These parameters have been optimized in the previous study. Beam spot shape was an quasi-elliptical with major axis of 3.5 mm and minor axis of 2.5 mm. Distance between the center of laser beam spot and the pressurizing axis of roller was 25 mm. Welding speed was varied from 3.3 to 15.0 mm/s. Overlapped width was 3 mm, and laser beam was irradiated the center of overlap. The roller is mounted with a calibrated compression spring for applying predetermined roll pressure. The roll pressure was calculated by assuming that the contact area between the roller and the steel sheet surface was a rectangle of 15 mm². Roll pressure was varied from 100 to 175 MPa. For the sake of the protection of condenser lens and the oxidation prevention of Laser Roll Welded joints, argon gas with flow rate of 25 l/min was used.

2.3. Evaluation method of Laser Roll Welded joints

After welding, Laser Roll Welded specimens were cut across the lap joint seam for macrostructure and microstructure observation. Etching with 3% nital was made for observation of the interface layer. Hardness test and electron-probe microanalysis (EPMA) were conducted to analyze the interface layer and to identify the IMC present.

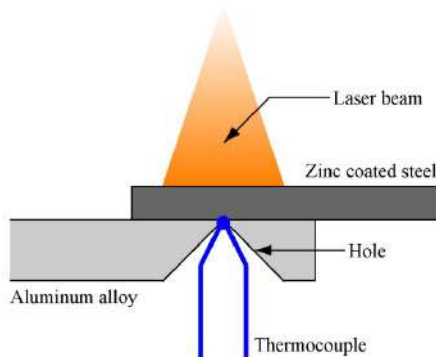


Figure 5. Schematic diagram of measurement method for thermal cycle at weld interface

Thermal cycle was measured using a Pt-PtRh thermocouple with a diameter of 0.3 mm. As shown in Fig.5, a cone-shaped hole of 2 mm in diameter was drilled at the center of the overlap width in the aluminum sheet. The hole was used for placing thermocouple at the lower surface of the steel sheet. In addition, tensile shear test and Erichsen cupping test were carried out to investigate the mechanical properties of welded joint. The specimens with 20 mm width were used for tensile shear test and with 77 mm square for Erichsen cupping test.

3. Experimental results and discussions

3.1. Bead appearance and cross-section of Laser Roll Welded joints

Bead appearance of Laser Roll Welded specimen with the welding speed of 8.3 mm/s and roll pressure of 150 MPa are shown in Figs.6-7. Top bead is shown in Fig.6, and bottom bead is in Fig.7. Furthermore, cross-section of the weld bead is shown in Fig.8. In these figures, (a) shows GI/A6000 joint and (b) shows GA/A6000, respectively.

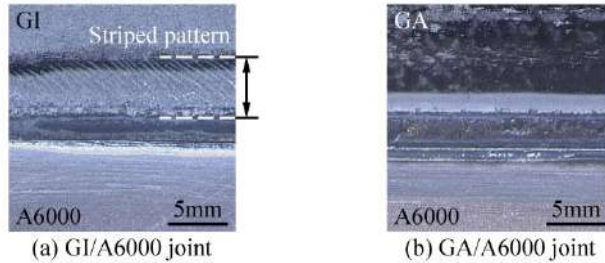


Figure 6. Top bead appearance of GI/A6000 and GA/A6000 Laser Roll Welded joints

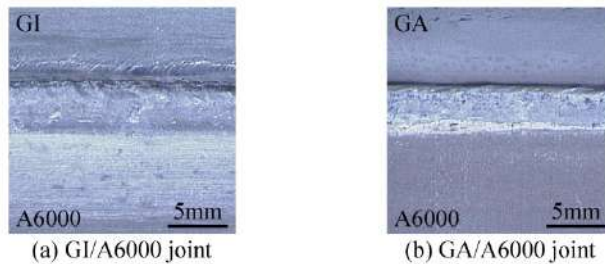


Figure 7. Bottom bead appearance of GI/A6000 and GA/A6000 Laser Roll Welded joints



Figure 8. Macro cross-section of GI/A6000 and GA/A6000 Laser Roll Welded joints

As shown in Fig.6, both of the bead turned black due to the effect of the graphite spray and the laser heating. In Fig.6 (a), striped pattern is observed on the GI sheet near the weld bead. This is the first time this striped pattern has been observed in the past study of Laser Roll Welding, the pattern seems to be unique to this welding of galvanized steel sheet. A GI sheet has galvanized layer, which exists as a thin layer at the surface of steel sheet. Thus it's thought that the pattern was caused by the laser heating and the roller pressure. On the other hand, the striped pattern doesn't exist on the GA sheet as

shown in Fig.6 (b). This is because the coated layer of a GA sheet is alloyed zinc with iron.

As shown in Figs.7-8 (a), partial melting and spreading of molten aluminum alloy on the GI sheet occurs in the A6000 sheet. The GI sheet was heated by laser, and the heat transferred to A6000 sheet by the contact of GI and A6000 sheets. Hence A6000 sheet was supposed to be melted. In contrast, molten A6000 alloy doesn't spread on the GA sheet.

In order to compare the wettability of the GI sheet with that of the GA sheet, bonding width was measured from the cross-section of the weld bead as shown in Fig.9 (a). Effect of the welding speed and the roll pressure on the bonding width of GI/A6000 and GA/A6000 joints are shown in Fig.9 (b) and (c), respectively.

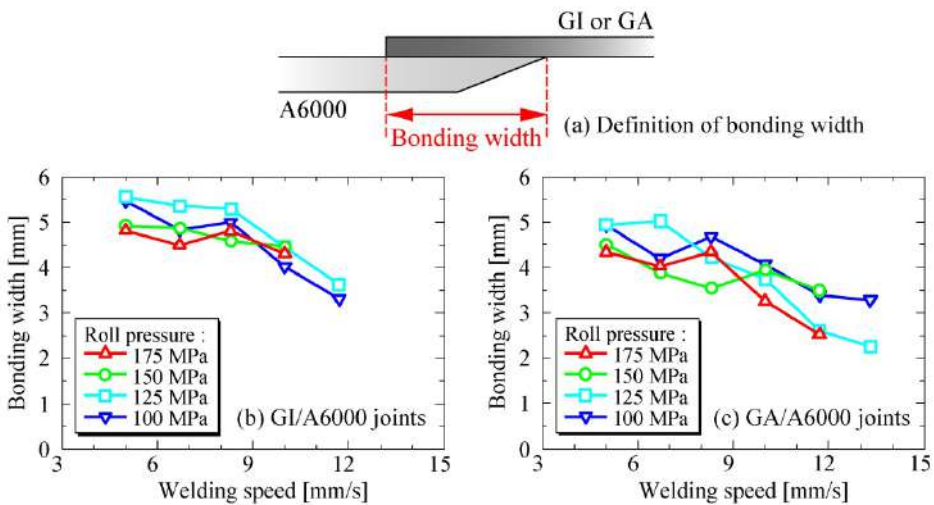


Figure 9. Effect of welding speed on bonding width at different roll pressures

It's common with Fig.9 (b) and (c) that the bonding width decreased as the welding speed is increased from 5.0 to 11.7 mm/s. This is because heat input decreases as the welding speed increased; the meltage of A6000 sheet also decreased. On the whole, the bonding width of GA/A6000 joints is narrower than that of GI/A6000. For example, the width with the welding speed of 8.3 mm/s and roll pressure of 150 MPa of GI/A6000 joint is 4.6 mm, and that of GA/A6000 is 3.5 mm. This is considered to be produced from the difference in the wettability of the surface of the GI and GA sheet.

3.2. Microstructures at weld interface

Interface microstructures of GI/A6000 joint with welding speed of 6.7 mm/s and roll pressure of 150 MPa are shown in Fig.10.

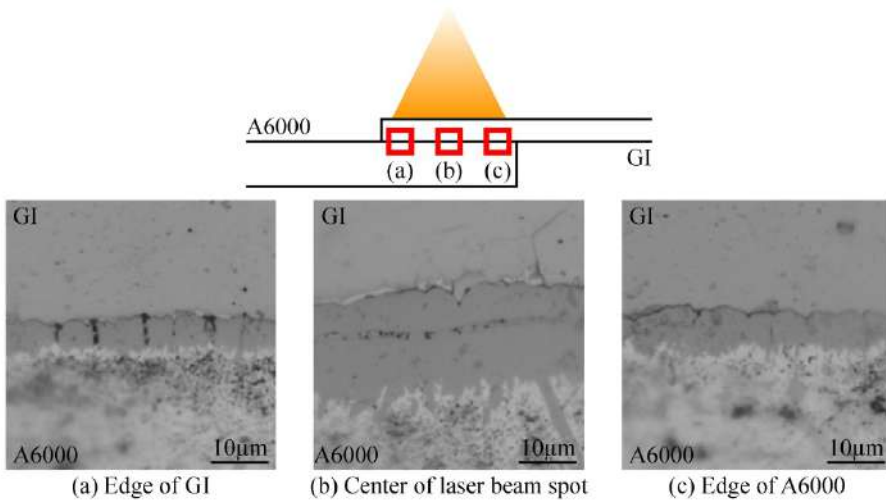


Figure 10. Microstructures at joint interface of GI and A6000 sheet

IMC layer was confirmed at the joint interface between the GI and the A6000 sheet. The IMC layer at the edge of the GI sheet is shown in Fig.10 (a), at the center of the laser beam spot is shown in (b) and at the edge of the A6000 sheet is shown in (c). The IMC layer thicknesses in each place were $4.1\ \mu\text{m}$, $13.0\ \mu\text{m}$, and $4.9\ \mu\text{m}$ respectively. Therefore, the thickness right under the center of laser beam spot was the thickest. Due to the high energy density near the center of the beam spot of the CO_2 laser used, it's thought that the area under the center of the beam spot is heated the highest temperature and cooled the slowest speed.

Interface microstructures of GA/A6000 joint with welding speed of $8.3\ \text{mm/s}$ and roll pressure of $150\ \text{MPa}$ are shown in Fig.11. IMC layer was also observed at the interface between the GA and the A6000 sheet. In addition, the thickness right under the center of laser beam spot was the thickest, and this was the same as that of the case of GI/A6000 joint.

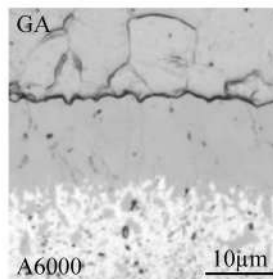


Figure 11. Microstructure at joint interface of GA and A6000 sheet

3.3. Electron-probe microanalysis (EPMA) of interlayer

As the optical microscope doesn't reveal the details of the IMC layers, EPMA of iron, aluminum and zinc across joint interface were made to identify IMC's and existence of zinc. The results for GI/A6000 and GA/A6000 joints at different welding speeds with roll pressure of 150 MPa are shown in Figs.12-13. Bottom pictures show the SEM images of the IMC layer. In these figures, the EPMA results with the welding speed of 8.3 mm/s are shown in (a), with the welding speed of 10.0 mm/s are shown in (b).

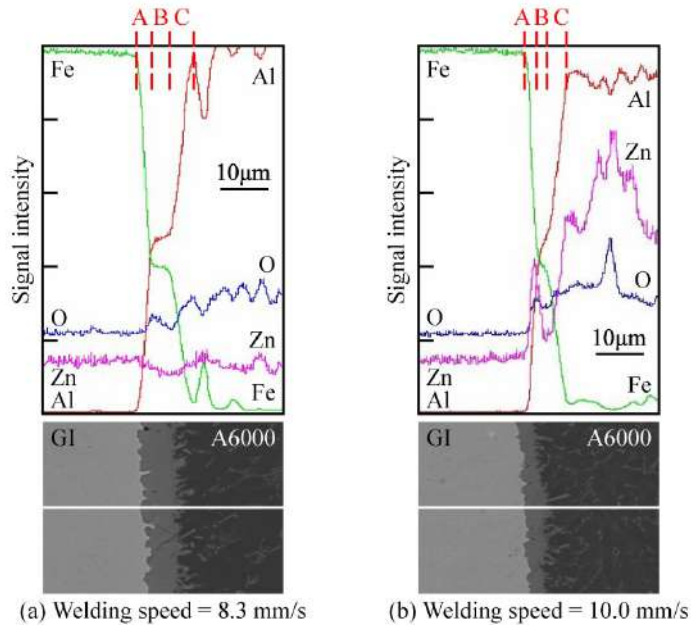


Figure 12. Results of EPMA at interlayer of GI/A6000 joints

From EPMA results of iron, aluminum and zinc across interface, IMC's and existence of zinc were identified. At the center of these EPMA results which are shown by the layer A to C in Fig.12 as an example, the signal intensity of Fe and Al has changed similarly. At the layer A, the intensity of Fe decreases rapidly, and Al rises. At the layer B, the IMC's are observed as stepped lines. At the layer C, the intensity of Fe decreases further and Al rises. From the estimation of composition from stepped lines at the layer B, it's suggested that main IMC's were brittle FeAl_3 and Fe_2Al_5 .

When the welding speed is increased to 10.0 mm/s, zinc can be seen in aluminum alloy. From this result, it's thought that zinc tends to diffuse into aluminum when the welding speed becomes more than 10.0 mm/s. This reason is considered as follows.

Most of the zinc layer is vaped by the laser heating from the faying surface of the GI sheet at slow welding speeds. On the other hand, at fast welding speeds, the diffusion amount of

the zinc into aluminum alloy by the roll pressure is larger than the evaporation amount of the zinc by the laser heating.

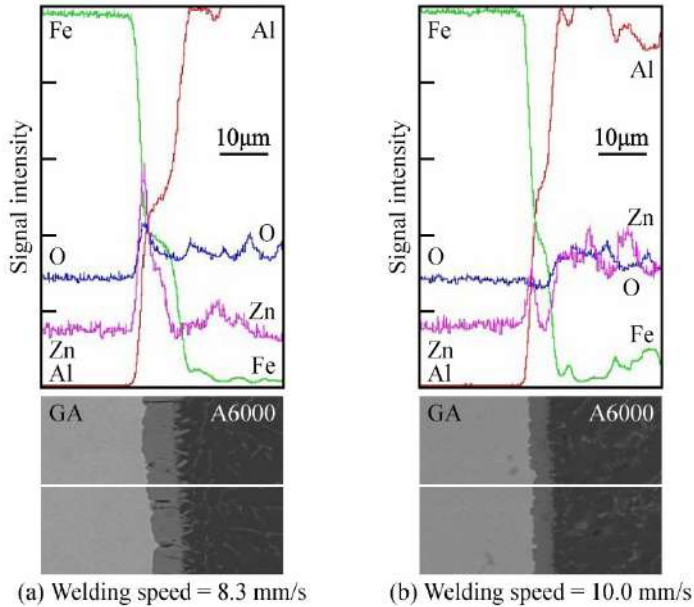


Figure 13. Results of EPMA at interlayer of GA/A6000 joints

As shown in Fig.13 (a), the zinc line has higher peak than any other zinc line at the interface of the GA sheet side. This is because the zinc on GA sheet surface exists as Fe-Zn alloy. Then it's suggested that zinc was hard to be evaporated by the laser heating, and a lot of zinc was remained at the interface of the GA sheet side.

3.4. Vickers hardness measurements

From the EPMA results, it was presumed that main IMC's were brittle FeAl_3 and Fe_2Al_5 . However, in order to obtain further evidence, Vickers hardness measurement was conducted. SEM image of GI/A6000 and GA/A6000 weld interface after the measurement with welding speed of 8.3 mm/s and roll pressure of 150 MPa are shown in Fig.14 (a) and (b), respectively.

Indentation size became small in order of the base metal of A6000, zinc coated steel, and the IMC layer. In particular, the indentation size of the IMC layer is much smaller than that of both base metals. As shown in Fig.14 (a), the Vickers hardness of the base metal of the GI, the A6000, and the IMC layer were 137 Hv, 94 Hv and 940 Hv on average respectively. The results show a large difference between IMC layer hardness and the surrounding base metals. The IMC hardness was about 10 times more than the A6000 base metal and 7 times more than the GI base metal. In the same way, as shown in Fig.14 (b), the Vickers hardness

of the base metal of the GA, the A6000, and the IMC layer were 141 Hv, 97 Hv and 857 Hv on average respectively, the IMC layer was the hardest. Because the hardness of these IMC layers are between 892 Hv of FeAl_3 and 1013 Hv of Fe_2Al_5 according to Table 1, it's thought that FeAl_3 and Fe_2Al_5 are mainly formed at the interface as above.

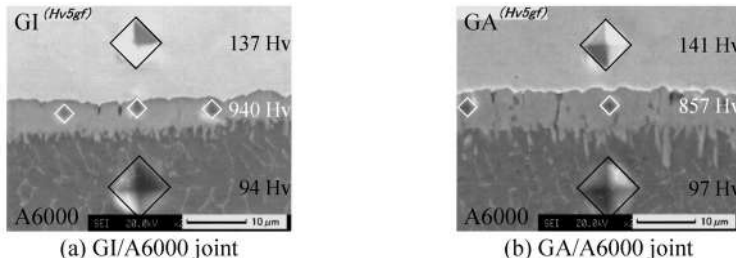


Figure 14. Results of Vickers hardness measurement at joint interface

3.5. Effect of welding speed on thickness of intermetallic compound layer

Effect of the welding speed on the IMC layer thickness of GI/A6000 and GA/A6000 joints at different roll pressure are shown in Fig.15 (a) and (b), respectively. The thicknesses were measured right under the center of the laser beam spot.

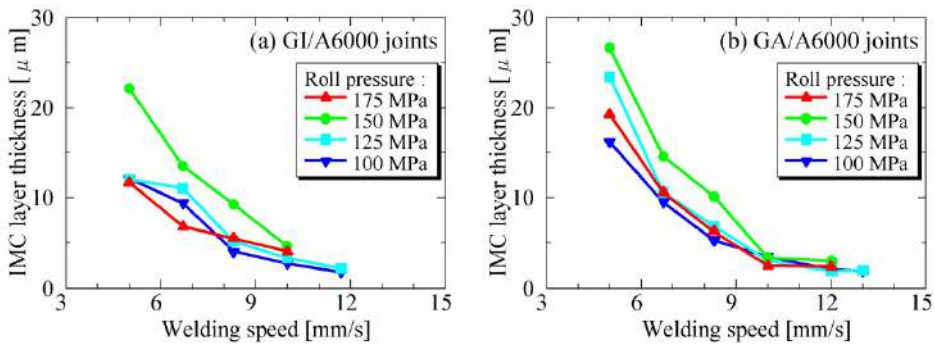


Figure 15. Effect of welding speed on IMC layer thickness of Laser Roll Welded joints interface

The IMC layer thickness decreases significantly as the welding speed is increased from 5.0 to 11.7 mm/s regardless of the roll pressure as shown in Fig.15 (a) and (b). This is because heat input decreases as the welding speed is increased. Therefore, this result indicates that the IMC layer thickness could be suppressed by heat input as was mentioned in previous study of Laser Roll Welding of steel to aluminum alloy.

3.6. Effect of roll pressure on thickness of intermetallic compound layer

Effect of the roll pressure on the IMC layer thickness of GI/A6000 and GA/A6000 joints at constant welding speed of 8.3 mm/s is shown in Fig.16.

The IMC layer thickness of both joints increases as the roll pressure is increased from 100 to 150 MPa. This is because increment of the roll pressure augments the contact between the zinc coated steel and A6000 sheet in this region. In contrast, the IMC layer thickness decreases as the roll pressure is increased from 150 to 175 MPa. This reason is considered as follows.

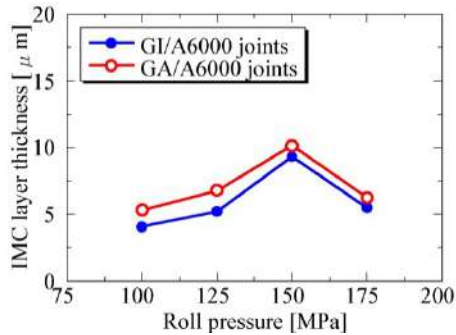


Figure 16. Effect of roll pressure on IMC layer thickness of Laser Roll Welded joints interface

The zinc coated steel and the A6000 sheet contact most widely at roll pressure of 150 MPa. However, when the roll pressure becomes more than 150 MPa, the steel sheet might be curved greatly by high roll pressure. Thus, it's thought that the contact area between the zinc coated steel and the A6000 sheet is narrowed in this region.

3.7. Effect of types of zinc coated steel on thickness of intermetallic compound layer

As shown in Fig.16, the IMC layer thickness of GA/A6000 joints is thicker than that of GI/A6000. This difference is attributed to the evaporation of zinc on the surface of each zinc coated steel sheets.

The boiling point of aluminum, iron and zinc are 2477 °C, 2887 °C and 906 °C respectively, that of zinc is far below those of aluminum and iron. Hence, the zinc on the surface of zinc coated steel sheet is melting, heat of fusion of 7.12 kJ/mol, and evaporating, heat of vaporization of 113.4 kJ/mol (The Japan Institute of Metals, 2004), in the process of Laser Roll Welding. However, because of the zinc on the surface of the GA sheet exists as Fe-Zn alloy, it's hard to be evaporated by the laser heating. Thus, laser energy is little-used for the zinc evaporation, and heat is conducted to A6000 sheet. On the other hand, the zinc on the surface of the GI sheet is easier to be evaporated than that of the GA. Therefore, it's thought that more laser energy for the zinc evaporation is used, and the heat conduction to A6000 sheet decreases.

3.8. Discussion of formation of intermetallic compound layer by thermal cycle at weld interface

Thermal cycle at the weld interface was measured to discuss about the effects of the welding speed and the roll pressure on the IMC layer thickness of Laser Roll Welded joints. The

results of GI/A6000 and GA/A6000 joints at constant roll pressure of 150 MPa is shown in Fig.17 (a) and (b), respectively.

When the welding speed increases from 5.0 to 11.7 mm/s, different thermal cycles were obtained as shown in Fig.17 (a) and (b). Then, in order to quantitative the shape of these thermal cycles, peak temperature and holding time more than 500 °C were focused on.

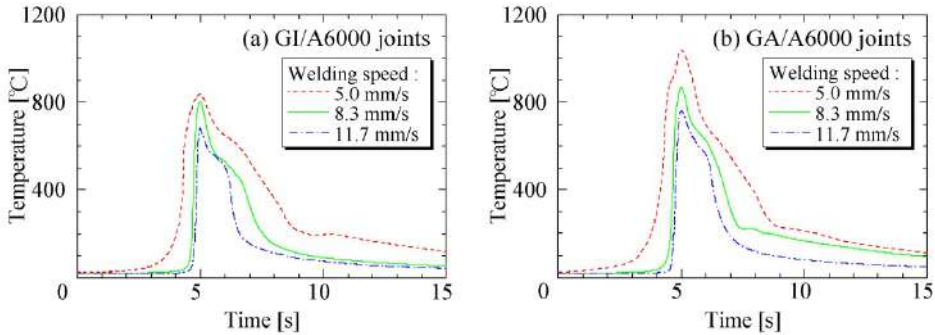


Figure 17. Effect of welding speed on interface thermal cycles of Laser Roll Welded joints

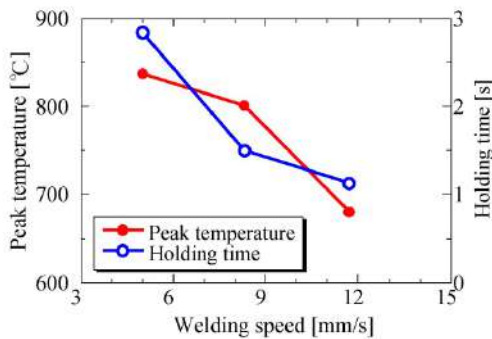


Figure 18. Effect of welding speed on peak temperature and holding time more than 500 °C at interface of GI/A6000 joints

The peak temperature and the holding time more than 500 °C of the thermal cycles in Laser Roll Welding of the GI and the A6000 at different welding speeds are shown in Fig.18. When the welding speed is increased from 5.0 to 11.7 mm/s, the peak temperature decreases from 850 to 680 °C, and the holding time more than 500 °C shortens from 2.8 to 1.1 sec at the weld interface. Hence the reduction of the IMC layer thickness by the increment of welding speed was attributed to the decline of the peak temperature and the shortening of the holding time. The similar results were obtained in Laser Roll Welding of the GA and the A6000.

When the welding speed is slow, there is excessive heat input and the cooling rate is slow. This provides surplus time for the formation of a thick interlayer containing a large amount of the Al-rich brittle IMC's. When the welding speed is fast, there is suitable heat and time

for melting of the aluminum and the diffusion process to take place. Therefore, it's thought that the change of the thermal cycle at the interface affect the formation of the IMC layer when the welding speed is varied.

In addition, when Fig.17 (a) is compared with (b), the peak temperatures of GA/A6000 joints are higher than those of GI/A6000. This fact caused the formation of thicker IMC layer in GA/A6000 joints than in GI/A6000 as shown in Fig.16.

Effect of the roll pressure on the interface thermal cycles of GA/A6000 joints at constant welding speed of 8.3 mm/s is shown in Fig.19. Thermal cycles are shown in Fig.19 (a) and the peak temperature and the holding time more than 500 °C of them are in (b). The reason of the changing of IMC layer thickness by the increment of the roll pressure as shown in Fig.16 is considered by using Fig.19.

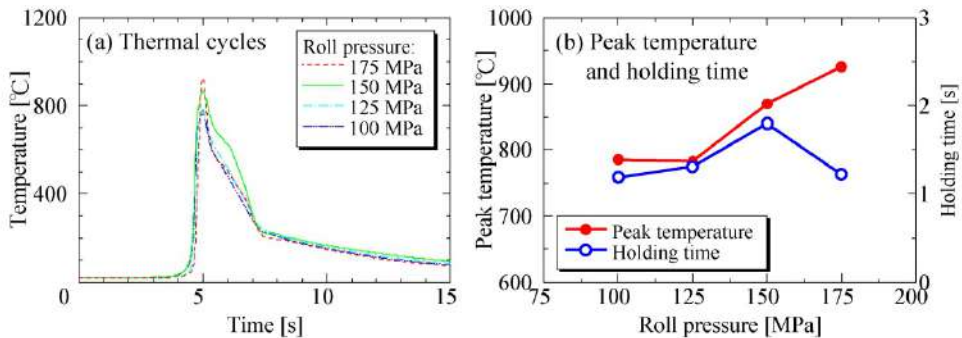


Figure 19. Effect of roll pressure on interface thermal cycles of GA/A6000 joints

From 100 to 150 MPa, the peak temperature and the holding time increase as the roll pressure is increased in Fig.19. Hence the IMC layer thickness increased as the roll pressure is increased in Fig.16. This is because increment of the roll pressure augments the contact between zinc coated steel and A6000 sheet in this region as above. In contrast, from 150 to 175 MPa, the peak temperature rises, but holding time shortens as the roll pressure is increased in Fig.19. It's supposed that this tendency caused the decrement of IMC layer thickness as the roll pressure is increased at high region in Fig.16.

3.9. Results of tensile shear test

Tensile shear test was conducted to investigate the influence of the welding conditions on the weldability. The tensile shear specimens were prepared by cutting the welded specimen with 20 mm width.

Fig.20 shows the tensile shear specimen after testing of GI/A6000 joints. Failure in base metal of the GI sheet is shown in Fig.20 (a), and failure in interface is shown in (b). It's

found that the base-metal-failure specimen failed far from the weld bead as shown in Fig.20 (a).

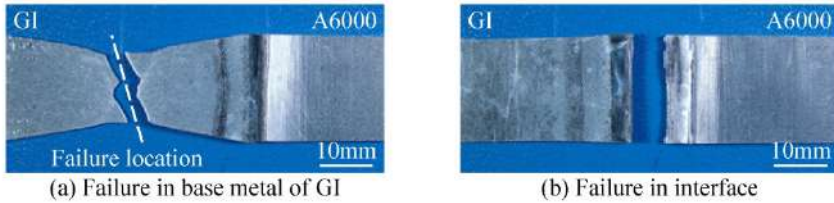


Figure 20. Tensile shear specimen after testing of GI/A6000 Laser Roll Welded joints

Results of tensile shear test of GI/A6000 and GA/A6000 joints at various welding speed with the roll pressure of 150 MPa is shown in Fig.21 (a) and (b), respectively. Here the tensile shear strength was converted into the tensile shear load per millimeter of weld length, N/mm, as adopted by Peyre et al. (2007) and Sasabe et al. (2007). Failure in the base metal of the zinc coated steel sheet is shown as a circle in the figure, and failure in interface is shown as a solid mark.

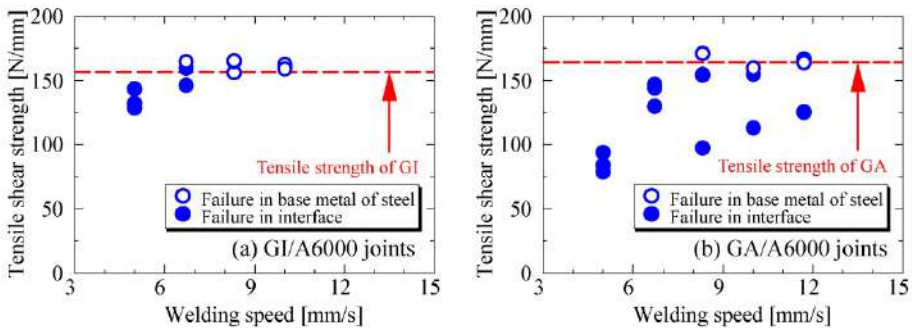


Figure 21. Effect of welding speed on tensile shear strength for Laser Roll Welded joints

When the welding speed is between 6.7 and 10.0 mm/s, the tensile shear strength shows high, and there are many specimens failed in the base metal. This result indicates that the IMC layer thickness is appropriate at these welding speeds. As shown in Fig.21 (a), specimens failed in the base metal could be obtained from 6.7 to 10.0 mm/s. In this region, the IMC layer thickness was less than 10 μm , and failure of specimen occurred in the base metal of the steel sheet. Therefore, it's thought that the IMC layer thickness should be less than 10 μm to get a good joint. As shown in Fig.21 (b), specimens failed in base metal were confirmed when the IMC layer thickness was less than 10 μm . This result corresponded to the articles by other researchers (Bruckner, 2005; Furukawa, 2005).

Additionally, when Fig.21 (a) is compared with (b), the tensile shear strength of GA/A6000 joints is lower than those of GI/A6000. There are three points which can be considered as this reason.

The first is the bonding width of GA/A6000 joints was narrower than that of GI/A6000 as shown in Fig.9. Therefore, when tensile shear load was applied to the joints with narrow bonding width, the load concentrated to the weld. The second is the IMC layer thickness of GA/A6000 joints was thicker than that of GI/A6000 as shown in Fig.16. Moreover, the IMC layers were mainly composed of Al-rich brittle IMC's from the results of the EPMA and the Vickers hardness. The third is the residual zinc at the interface of GA/A6000 joints influenced the tensile shear strength. From the results of the EPMA, a lot of zinc was remained as Fe-Zn alloy layers at the interface of GA sheet side. The zinc coated layer of the GA sheet is formed from the steel side in order of Γ -phase ($\text{Fe}_3\text{Zn}_{10}$), Γ_1 - ($\text{Fe}_5\text{Zn}_{21}$), δ - (FeZn_7) and ζ - (FeZn_{13}) (The Iron and Steel Institute of Japan, 1982). Since each phase has a difference in generation speed, the Γ -phase is thin and alloy layers are composed mostly of δ - and ζ -. Their phases are hard and brittle. Therefore, the interface of the GA/A6000 joints is weaker than that of the GI/A6000.

The maximum tensile shear strength of GI/A6000 joint, 162 N/mm, was obtained at the welding speed of 8.3 mm/s and the roll pressure of 150 MPa. This strength is equal to the tensile strength of the GI sheet, 157 N/mm, and 63% of the A6000 sheet, 256 N/mm. On the other hand, the maximum strength of GA/A6000 joint, 160 N/mm, was obtained at the welding speed of 10.0 mm/s and the roll pressure of 100 MPa. This strength is equal to the tensile strength of the GA sheet, 164 N/mm, and 62% of the A6000 sheet, 256 N/mm.

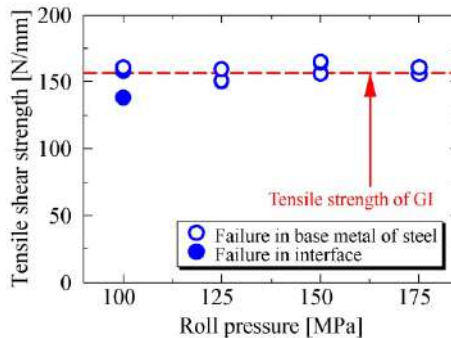


Figure 22. Effect of roll pressure on tensile shear strength for GI/A6000 joints

In addition, results of tensile shear test at various roll pressure with welding speed of 8.3 mm/s is shown in Fig.22. All specimens were failure in the base metal of the GI sheet except for the roll pressure 100 MPa. It's considered that the IMC layer thickness is less than 10 μm at these roll pressures as shown in Fig.16. Therefore, it seems that there is little influence of the roll pressure on the tensile shear strength.

3.10. Discussion of relation between intermetallic compound layer thickness and tensile shear strength

From the above results, it has become clear that there is a close relation to the IMC layer thickness to the tensile shear strength also in Laser Roll Welding of zinc coated steel and aluminum alloy. There, the relationship between the IMC thickness and the tensile strength was discussed about all joints in this experiment. Effect of the IMC layer thickness on the tensile shear strength of GI/A6000 and GA/A6000 joints with different welding speed and roll pressure is shown in Fig.23 (a) and (b), respectively.

As above, only when the IMC layer thickness was less than 10 μm , the base-metal-failure specimens were obtained. When the IMC layer thickness is from 4 to 6 μm , high tensile shear strength could be obtained. When the IMC layer is thicker than 6 μm , the tensile strength is decline. This is because the increment of the brittle IMC's at the joint interface might lead to weaken of the welded joint, and the joint isn't able to resist a heavy load.

On the other hand, when the IMC layer is thinner than 4 μm , the tensile strength also declines. In this case, due to low heat input might lead to incomplete welding at the joint interface. As shown in Fig.9, the bonding width is decreased by the decrement of the heat input.

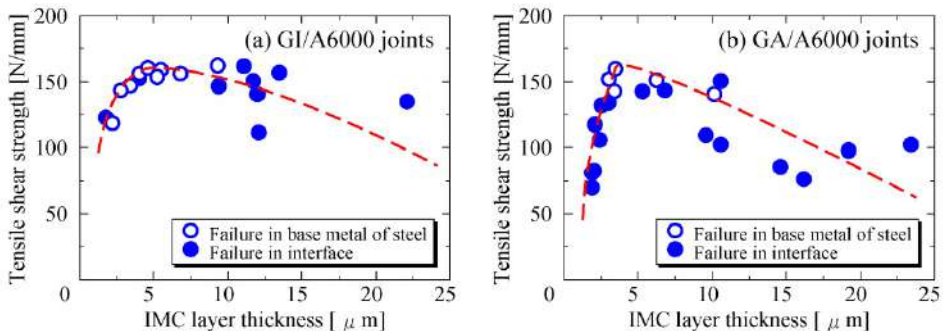


Figure 23. Effect of IMC layer thickness on tensile shear strength for Laser Roll Welded joints

3.11. Results of Erichsen cupping test

Finally, in order to investigate the formability of GI/A6000 and GA/A6000 joints, Erichsen cupping tests were carried out. The specimens were prepared by cutting the welded joints with the welding speed of 8.3 mm/s and roll pressure of 150 MPa into 77 mm square. A punch is pushed into the specimen. When the specimen is failed somewhere, the cupping height is evaluated as Erichsen value.

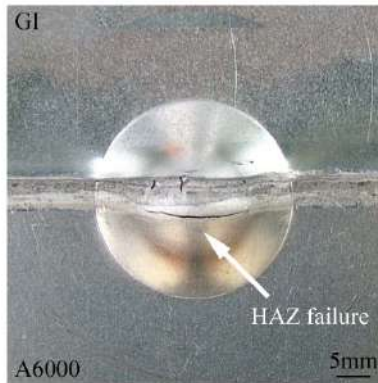


Figure 24. Erichsen cupping test specimen after testing of GI/A6000 joint

The Erichsen cupping test specimen after testing of GI/A6000 joint is shown in Fig.24. The specimen was failed at HAZ of the A6000 sheet side and the Erichsen value was 7.9 mm. With the GI base metal, the Erichsen value was 11.9 mm; with the A6000 base metal, the value was 8.6 mm. Therefore, this value was 92% of the base metal of A6000 sheet. In contrast, the specimen of GA/A6000 joint was failed at interface and the value was 3.6 mm. The same tendency was seen in the tensile shear test.

4. Conclusions

The present study is focused on the dissimilar metal joining of zinc coated steel and aluminum alloy by Laser Roll Welding. The following conclusions can be drawn.

1. The IMC layer was observed at the interface of all welded joints. It was suggested that most of the IMC's are brittle FeAl_3 and Fe_2Al_5 from the results of EPMA and Vickers hardness measurement. As the welding speed was faster than 10.0 mm/s, zinc was confirmed in aluminum alloy.
2. Increase in the welding speed led to decrease the bonding width and the IMC layer thickness at the joint interface. When the roll pressure was increased, the IMC thickness at the pressure of 150 MPa was the thickest. The IMC layer thickness of GA/A6000 joints was thicker than that of GI/A6000 on the whole.
3. Increase in the welding speed led to lowering of the peak temperature and shortening of the holding time more than 500 °C at the interface. The peak temperature at the roll pressure of 175 MPa was the highest, and the holding time at the pressure 150 MPa was the longest. The peak temperature of GA/A6000 joints was higher than that of GI/A6000 at the same welding condition.
4. When the IMC layer was less than 10 μm , failure of specimen occurred at the base metal of zinc coated steel in tensile shear test. The joint properties of GI/A6000 joints were better than those of GA/A6000 from the results of tensile shear test and Erichsen cupping test.

5. The welding speed influenced the joint performance such as the IMC layer thickness and the tensile shear strength to a greater degree than the roll pressure in Laser Roll Welding.

Author details

Hitoshi Ozaki
Graduate School of Engineering, Mie University, Japan

Muneharu Kutsuna
Advanced Laser Technology Research Center Co., Ltd., Japan

Acknowledgement

The authors would like to thank Mr. S. Nakagawa and Mr. K. Miyamoto from Research Center, Nissan Motor Co., Ltd. for their support in this research.

5. References

- Bruckner, J. (2005). Cold Metal Transfer Has a Future Joining Steel to Aluminum. *Welding Journal*, Vol.84, No.6, pp.38-40, ISSN 0043-2296
- Dharmendra, C., Rao, K. P., Wilden, J. & Reich, S. (2011). Study on Laser Welding-brazing of zinc Coated Steel to Aluminum Alloy with a Zinc Based Filler. *Material Science and Engineering A*, Vol.528, pp.1497-1503, ISSN 0921-5093
- Fan, J., Thomy, C. & Vollertsen, F. (2011). Effect of Thermal Cycle of the Formation of Intermetallic Compounds in Laser Welding of Aluminum-Steel Overlap Joints. *Physics Procedia*, Vol.12, pp.134-141, ISSN 1875-3892
- Furukawa, K. (2005). Welding Process of Iron-Aluminum. *Welding Technology*, Vol.53, No.8, pp.94-102, ISSN 0387-0197
- Katayama, S. (2004). Laser Welding of Aluminum Alloys and Dissimilar Metals. *Journal of Light Metal Welding & Construction*, Vol.42, No.1, pp.16-25, ISSN 0368-5306
- Katoh, K. & Tokisue, H. (2004). Dissimilar Friction Welding of Aluminum Alloys to Other Materials. *Journal of Light Metal Welding & Construction*, Vol.42, No.2, pp.11-18, ISSN 0368-5306
- Massalski, T. B. (1986). *Binary Alloy Phase Diagrams Volume 1*, American Society for Metals, p.148, ISBN 0871702614, Ohio
- Nishimoto, K., Atagi, K., Fujii, H. & Katayama, S. (2005). Laser Pressure Welding of Dissimilar Metals Welding. *Proceedings of the 63rd Laser Materials Processing Conference*, pp.133-138, ISBN 4947684585, May, 2005
- Ohashi, O. (2004). Diffusion Bonding of Aluminum to Different Metals. *Journal of Light Metal Welding & Construction*, Vol.42, No.2, pp.19-23, ISSN 0368-5306

- Okamura, H. & Aota, K. (2004). Joining of Dissimilar Materials with Friction Stir Welding, *Journal of Light Metal Welding & Construction*, Vol.42, No.2, pp.1-10, ISSN 0368-5306
- Okita, T. (2004). Resistance Welding of Aluminum Alloys to Dissimilar Metals. *Journal of Light Metal Welding & Construction*, Vol.42, No.1, pp.2-15, ISSN 0368-5306
- Ozaki, H., Hayashi S. & Kutsuna M. (2008). Laser Roll Welding of Dissimilar Metal Joint of Titanium to Aluminum Alloy. *Quarterly Journal of Japan Welding Society*, Vol.26, No.1, pp.24-30, ISSN 0288-4771
- Ozaki, H., Ichioka R. & Kutsuna M. (2007). Laser Roll Welding of Dissimilar Metal Joint of Low Carbon Steel and Titanium. *Quarterly Journal of Japan Welding Society*, Vol.25, No.1, pp.173-178, ISSN 0288-4771
- Ozaki, H. & Kutsuna M. (2007). Laser Roll Welding of Dissimilar Metal Joint of Low Carbon Steel to Aluminum Alloy Using 2kW Fiber Laser. *Quarterly Journal of Japan Welding Society*, Vol.25, No.4, pp.473-479, ISSN 0288-4771
- Peyre, P., Sierra, G., Deschaux-Beaume, F., Stuart, D. & Fras, G. (2007). Generation of Aluminum-steel Joints with Laser-induced Reactive Wetting. *Material Science and Engineering A*, Vol.444, pp.327-338, ISSN 0921-5093
- Rathod, M. & Kutsuna M. (2003). Laser Roll Bonding of A5052 Aluminum Alloy and SPCC Steel. *Quarterly Journal of the Japan Welding Society*, Vol.21, No.2, pp.282-294, ISSN 0288-4771
- Rathod, M. J. & Kutsuna M. (2004). Joining of Aluminum Alloy 5052 and Low-Carbon Steel by Laser Roll Welding. *Welding Journal*, Vol.83, No.1, pp.16s-26s, ISSN 0043-2296
- Sasabe, S., Iwase, T., Matsumoto, T., Hattori, Y. & Miono, T. (2007). Dissimilar Metal Joining of Aluminum Alloys to Steel by using Newly-developed Hot-dip Aluminized Steel Sheet. *Journal of Light Metal Welding & Construction*, Vol.45, No.2, pp.23-33, ISSN 0368-5306
- Satou, D. (2004). Aluminum Clad of Explosive Welding. *Journal of Light Metal Welding & Construction*. Vol.42, No.1, pp.26-30, ISSN 0368-5306
- The Iron and Steel Institute of Japan (1982). *Iron and Steel Handbook Vol. 6 (3rd Edition)*, Maruzen, pp.421-434, Tokyo
- The Japan Institute of Metals (2004). *Metals Data Book (Revised 4th Edition)*, Maruzen, p.11, ISBN 4621073672, Tokyo
- Torkamany, M., Tahamtan, S. & Sabbaghzadeh, J. (2010). Dissimilar Welding of Carbon Steel to 5754 Aluminum Alloy by Nd:YAG Pulsed Laser. *Materials and Design*, Vol.31, pp.458-465, ISSN 0261-3069
- Yamamoto, S. (2012). Welding in the World –Picking up from Foreign Magazine. *Welding Technology*, Vol.60, No.3, (2012), p. 75, ISSN 0387-0197
- Yan, S., Hong, Z., Watanabe, T. & Jingguo, T. (2010). CW/PW Dual-beam YAG Laser Welding of Steel/Aluminum Alloy Sheets. *Optics and Lasers in Engineering*, Vol.48, pp.732-736, ISSN 0143-8166

Yasuyama, M., Ogawa, K. & Taka, T. (1996). Spot welding of aluminum and steel sheet with insert of aluminum clad steel sheet – Part 1. *Quarterly Journal of Japan Welding Society*, Vol.14, No.2, pp.314-320, ISSN 0288-4771

***In situ* Reaction During Pulsed Nd:YAG Laser Welding SiC_p/A356 with Ti as Filler Metal**

Kelvii Wei Guo

Additional information is available at the end of the chapter

<http://dx.doi.org/10.5772/46087>

1. Introduction

As aluminum matrix composites are generally low-cost and exhibit higher specific strength, high wearability, and good design performance property and functionality. They are widely applied in aerospace-flight, aviation structure, and automobile and in the heat resistant-wearable parts of engine [1-4]. Hence, a great deal of contemporary research effort is focusing upon their development and applications, typically on the discontinuously reinforced aluminum matrix composites like matrix with particle, short fiber, whisker and so forth. Additionally, a great deal of attention has also been drawn into the investigation of their secondary processing technologies like machining, joining and plastic forging. Welding is an important process for joining these materials. There has extensive effort to be devoted to developing appropriate process for joining the similar or dissimilar composites in literatures [2-4]. These processes can be mainly categorized as: (i) fusion welding like arc welding, shielding gas welding, laser welding and electron beam welding, *etc.*; and (ii) solid-state welding like soldering, explosive welding, friction welding and diffusion welding, *etc.* However, there still exist many problems in joining of the discontinuously reinforced aluminum matrix composites using conventional arc-welding processes and those high energy density welding methods like: laser welding and electron beam (EB) welding. These problems include: (i) the formation of poor weldment and the unsatisfactory properties of welded joints – mainly due to the high viscosity and poor flowability of the liquid welding pool causing mixing difficulty of the composite base material with filler materials; (ii) the occurrence of micro-segregation or inhomogeneous distribution of the reinforcement phases of SiC_p, Al₂O_{3p}, AlN and *etc.*, and whiskers like SiC_w – typically owing to the rejection by their solidification front in the welding pool as cooling down, which subsequently prompts for many micro and macro defects in the weld and very poor

properties of the welded joints; (iii) the formation of aluminum carbide – mainly as a result of harmful interfacial reaction between aluminum matrix and reinforcement phases; and (iv) *so on*. A typical example of the interfacial reaction likely to have pernicious effects on the mechanical and chemical behavior of the composite is $4Al + 3SiC \rightarrow Al_4C_3 + 3Si$. This is owing to: (a) the formation of brittle and weak aluminum carbide Al_4C_3 in the interfacial reaction sacrifices the reinforcement-materials in the composite; and (b) the unstable aluminum carbide in wet environments causes corrosion of the composite because of its rapid hydrolysis *etc*.

Aiming at developing or improving the conventional welding technique, this paper studies the technique of welding the stir-cast aluminum matrix composite $SiC_p/A356$ by Nd:YAG laser welding with pure titanium as filler. This study has been specifically concerned on the *in situ* reinforcement effect of Ti on the microstructures of laser welded joints, which have been analyzed by means of Scanning Electron Microscope (SEM), Transmission Electron Microscope (TEM) and Electron Diffusion X-ray analysis (EDX) *etc*. The study aims at providing some ground works for further studies in this field.

2. Experimental material and process

2.1. Experimental material

Stir-cast $SiC_p/A356$ aluminum matrix composite, reinforced with 20 % volume fraction SiC particle of 12 μm mean size, was used as the welding specimens. The tensile strength of such specimens was 240 MPa and their solid-liquid phase transformation temperature was in the range of 562.6~578.3 °C. Figure 1 showed their corresponding microstructure while Table 1 tabulated the chemical composition of the A356 matrix alloy. Pure titanium was used as the filler metal.

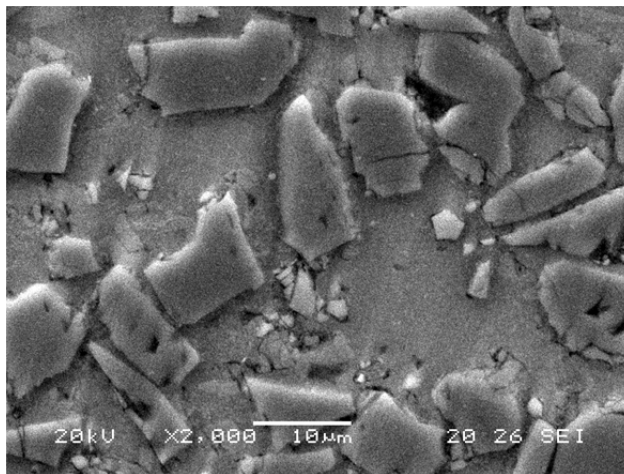


Figure 1. Microstructure of $SiC_p/A356$ aluminum matrix composite

Composition (Wt %)			
Si	Mg	Ti	Al
6.5~7.5	0.3~0.5	0.08~0.2	Bal.

Table 1. Composition of A356

2.2. Experimental process

The stir-cast aluminum matrix composite specimens were individually wire-cut to the size of 3 mm × 10 mm × 35 mm (Fig. 2). The quench-hardened layer induced by wire-cut and the oxide on the surfaces of specimens were polished away by 400 # emery cloth. The pure titanium filler was then machined to depth 3 mm × width 10 mm × thickness of 0.15 mm, 0.3 mm, 0.45 mm, 0.5 mm, 0.6 mm and 0.75 mm, respectively. The specimens were then mounted into a clamping device on the platform of a GSI Lumonics Model JK702H Nd:YAG TEM₀₀ mode laser system, and their welding surfaces were properly cleaned by acetone and pure ethyl alcohol so as to remove any possible contaminant. The prepared pure titanium filler was also thoroughly cleaned and carefully sandwiched between the two composite specimens in the clamp. Thereafter, specimens were welded immediately by the Nd:YAG laser with wavelength of 1.06 μm, defocused distance of 10 mm so as to give a focus spot diameter of approximately 1.26 mm, laser fluence energy 2 J, frequency 25 Hz, and pulse duration 4 ms. In the welding, the relative moving speed of the laser and the welding pieces (i.e. feedrate) was set at 300 mm/min

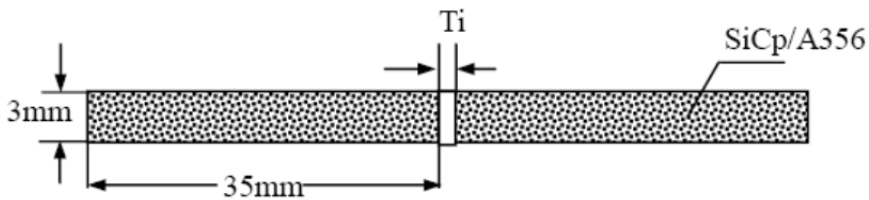


Figure 2. Schematic illustration of laser welding with Ti filler

Tensile strength of the joint was performed by a MTS Alliance RT/30 electron-mechanical material testing machine with a straining velocity of 0.5mm/min. The cross-section of welded joints was wire-cut for optical microscope investigation, and Scanning Electron Microscope (SEM) and Transmission Electron Microscope (TEM) analyses. SEM was used to analyze in detail the microstructure at the weld joints and the fractured tensile test-pieces of the joints. Optical microscope was used for observing the structure of a large area. TEM and Electron Diffusion X-ray analysis (EDX) were used to analyze the interface between the newly-formed phases and aluminum matrix, the distribution of chemical elements and spectra at the joints. The Nd:YAG laser with the similar setting conditions and feedrate was also used to weld the aluminum matrix composite specimens without any filler.

3. Results and discussion

3.1. Microstructures and properties of welded joints

The microstructure of the *in situ* reinforcement of Ti by Nd:YAG laser welding with 0.3 mm thick Ti filler was shown in Fig. 3. Appearance of *in situ* reinforcement particles distributed uniformly in the welded joint was seen. It also showed the disappearing of the drawbacks like incomplete fusion and pernicious phase Al₄C₃. These subsequently resulted in higher tensile strength (Table 2) of the joint. Comparatively, the reinforcement particles distributed more compactly than that of parent composite (cf. Fig. 1 and Fig. 3). The relatively more highly compacting reinforcement particles improved distinctly the properties of welded joints. The presence of Ti effectively improved the flowability of the liquid welding pool and the newly formed *in situ* reinforcement particles (Fig. 3) replaced those initial reinforcement particles (Fig. 1). Those dimples appeared in the SEM of the corresponding fractured surface (Fig. 4) suggested that: (i) the new-formed reinforcement particles had been perfectly wet; and (ii) the harmful composite structure of the initial welding viz. reinforcement/Ti/reinforcement had been changed to the state of reinforcement/matrix/reinforcement. XRD pattern of the fractured surface (Fig. 5) of the weld joint did not give sign of any harmful phase or brittle phase of Al₄C₃. This suggested the occurrence of effective interface transfers between reinforcement particles and matrix in the laser welded joint that subsequently provided favorable welding strength (Table 2). By the newly formed *in situ* reinforcement particles as detected by EDX (Table 3) and the intensity spectra shown in Fig. 5, the newly-formed reinforcement particle in the weld was identified as TiC.

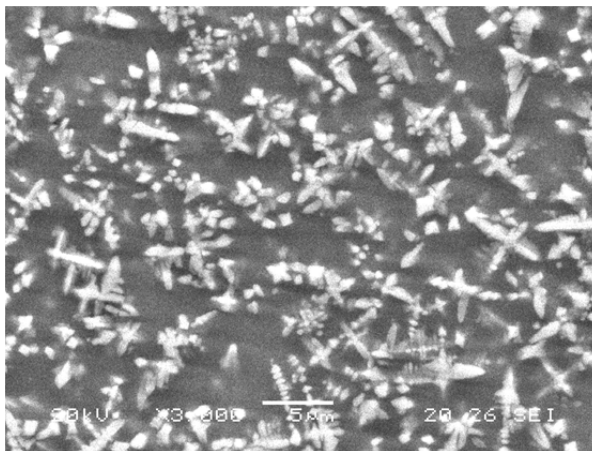


Figure 3. Microstructure of *in situ* reinforcement by laser welding with 0.3 mm thick Ti filler

Thickness of Ti filler (mm)	0.00	0.15	0.3	0.45	0.60	0.75
Mean strength (MPa)	76-91	126-135	168-180	143-160	107-113	79-96

Table 2. Mean tensile strength of laser welded specimens with various Ti filler thicknesses

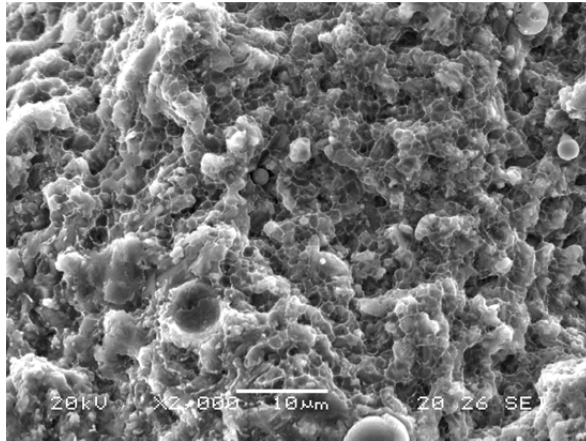


Figure 4. Fractograph of the laser welded joint with 0.3 mm thick Ti filler

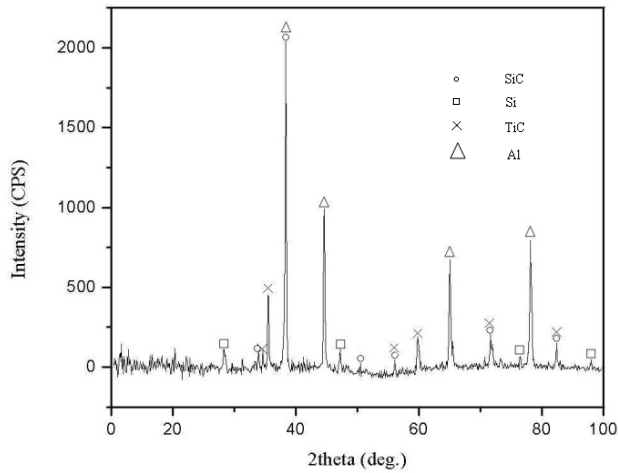


Figure 5. XRD pattern of the fracture surface for laser welding with 0.3 mm thick Ti filler

Element	Ti	Si	Al
Wt (%)	81.84	4.42	Bal.

Table 3. EDX analysis of newly-formed particle in the laser weld with 0.3 mm thick Ti filler



Figure 6. Macro-structure of the laser welded joint with 0.3 mm thick Ti filler

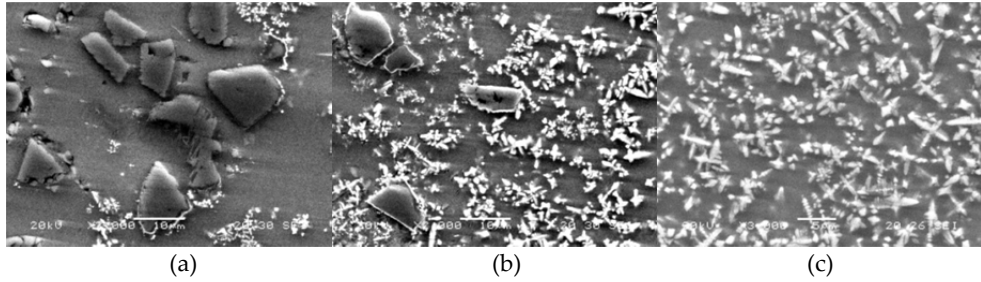


Figure 7. Microstructures of the different areas in the laser weld with 0.3 mm thick Ti filler
(a) Area A (b) Area B (c) Area C

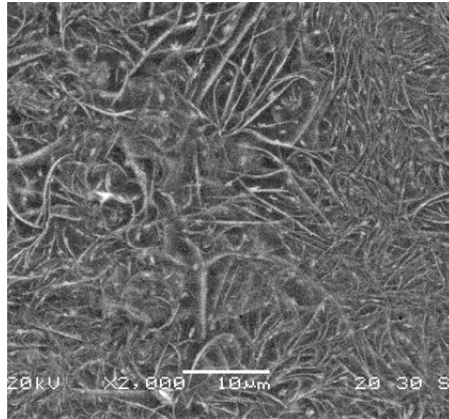
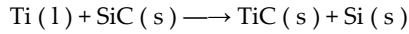


Figure 8. Microstructure of the weld with no-filler

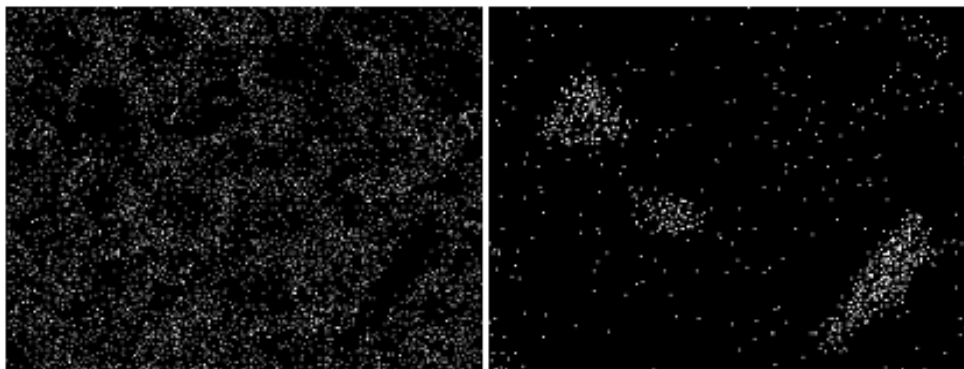
Figure 6 illustrates the macro-structure of welded joint with Ti filler. Basically, the weld consisted of three main areas, namely: the *in situ* reinforcement area A, the two transitional areas B and C, and the no-*in situ* reinforcement area D. Their individual microstructures were shown in Fig. 7. The microstructures indicated the initial reinforcement SiC particles were completely replaced by the newly-formed *in situ* reinforcement TiC particles that mainly resulted in the formation of the *in situ* reaction area A (Fig. 7a). In the area B, the newly-formed *in situ* reinforcement TiC particles and the initial reinforcement SiC particles were coexistent (Fig. 7b). In the area C, very little newly-formed *in situ* reinforcement TiC particles were found (Fig. 7c). In the area D, there only existed the initial reinforcement particles SiC (Fig. 1). It was found that the typical pernicious acicular Al₄C₃ microstructure had been effectively alleviated in the welded area. Hence, it improved markedly the properties of the welded joints and their achievable tensile strength was up to 180 MPa (Table 2) that was about 75 % of the strength of SiCp/A356. The microstructure (Fig. 8) of the traditional Nd:YAG laser welding with no-filler showed that there were lots of pernicious acicular Al₄C₃ in the weld, which led to lower weld joint tensile strength (Table 2), i.e. only as high as 91 MPa (that was about 37.9 % of its parent SiCp/A356).

3.2. Element distribution in the transition area

Figure 9 illustrates the element distribution of the area B in the weld as shown in Fig. 6 and Fig. 7b. It showed the newly-formed *in situ* reinforcement particles were around the initial reinforcement SiC particles which offered a high density nucleus area for the nucleation of *in situ* TiC. The stirring effect in the welding pool by laser irradiation and the initial reinforcement SiC particles would be replaced by the newly-formed *in situ* TiC (cf. Figs 9b and 9c) following the chemical reaction process of:



(a)



(b)

(c)

Figure 9. Element distribution of B area in the weld; (a) micrograph of the area B (b) Ti element face distribution (c) Si element surface distribution

According to the free energy for forming the SiC, TiC and Al₄C₃ carbides as elaborated in Fig. 10 of literatures [5, 6, 7], the free energy required to form TiC was much lower than that for Al₄C₃ when the reaction temperature was above 800 °C. The affinity between Ti and C in the Nd:YAG laser welding was therefore greater than that of Al and C. The chemical reaction between Ti and SiC in the welding pool would subsequently take precedence over the reaction between Al and SiC and thus resulted in restraining the formation of the pernicious acicular Al₄C₃.

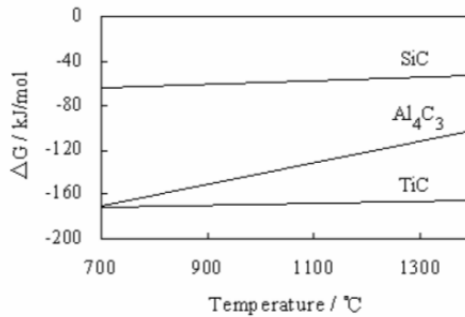


Figure 10. Free energy of formation of several metallic carbides [5, 6, 7]

3.3. Influence of Ti filler thickness

The microstructures of *in situ* reinforcement with various thicknesses of Ti filler were illustrated in Fig. 11 and its corresponding fractographs were shown in Fig. 12. It illustrated that the amount of the formed *in situ* TiC was distinctly increased with the increase in the thickness of Ti filler. Test indicated that maximum strength of welded joints (Table 2) was achieved at Ti filler thickness 0.3 mm (Figs. 3 and 4). This was because the newly-formed *in situ* reinforcement particles TiC were uniformly distributed in the weld and the initial irregular (mostly in hexagonal shape as shown in Fig. 1) reinforcement SiC particles in the weld were no longer observed (Fig. 3). Moreover, the pernicious acicular Al₄C₃ was successfully restrained (Figs 3 and 7a). At the thickness of Ti filler below 0.3 mm, there was little sign of the newly-formed *in situ* reinforcement TiC particles to be observed (Fig. 11a) and a number of pernicious acicular Al₄C₃ were formed in the weld. When the thickness of Ti filler was just beyond 0.3 mm, the properties of the joints tended to become poorer again (Fig. 12b). This was because the input energy was mainly used for melting the Ti filler and resulted in the coexistence of coarse columnar crystals and fine equiaxed crystals (Fig. 11b). When the thickness of Ti filler was further increased (Fig. 11c), the percentage of liquid Ti in the welding pool would also be increased. Subsequently, the weld zone would form coarser columnar crystals, as displayed in the SEM micrograph of Fig. 11c, after the resolidification of the melt. From the phase diagram (Fig. 13) of Ti-Al binary system [8], it can be anticipated that increasing the content of Ti would lead to the intermetallic compounds like TiAl and Ti₃Al, *etc.*, to be

formed during the Nd:YAG laser welding. As illustrated by the XRD pattern of the fractured surface of a laser weld joint with the thicker Ti filler in Fig. 14, there were some distributing brittle intermetallic compounds like TiAl and Ti₃Al to be detected. Available literature [9] has demonstrated that TiAl and Ti₃Al are the harmful intermetallic compounds in the weld and tend to decrease obviously the strength of welded joints. Such harmful effect may follow the chemical reaction of: $5\text{Ti}[\text{Al}] + 3\text{Al}[\text{Ti}] + \text{SiC}[\text{s}] \rightarrow \text{TiC}[\text{s}] + \text{Si}[\text{Al}] + \text{Al}[\text{Ti}] + (\text{TiAl} + \text{Ti}_3\text{Al})$. Hence, too thick of the Ti filler led to: (i) the appearance of the large block of columnar crystals in the microstructure (Fig. 15); and (ii) the new-formed reinforcement TiC to be replaced by the melted/re-solidified Ti and subsequently only the melted/re-solidified Ti existing in the weld. Results (Figs 3, 7 and 11) indicated that there existed an optimal thickness of Ti filler in the individually set parameters in the Nd:YAG laser welding of SiC_p/A356. With the optimal thickness of Ti filler, the initial reinforcement particles SiC distributed in the aluminum matrix composite SiC_p/A356 would offer a highly dense nucleus area for the *in situ* TiC nucleation. This would effectively alleviate the forming of intermetallic compounds like TiAl and Ti₃Al in the weld. It was in this manner that ultimately created favorable condition to provide relatively superior strength of the welded joint to that of conventional laser welding.

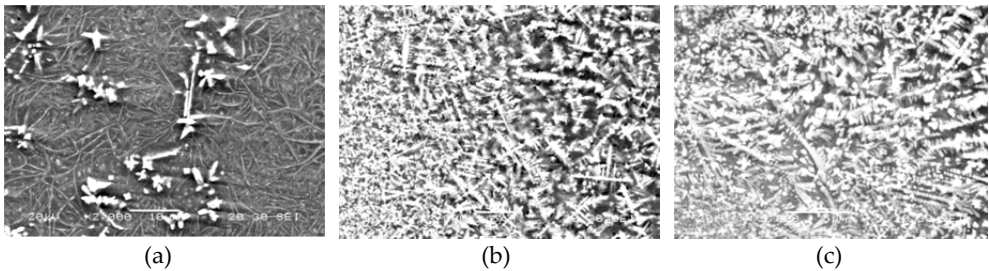


Figure 11. Microstructures in the A area with various thicknesses of Ti filler; (a) $\delta=0.15$ mm (b) $\delta=0.45$ mm (c) $\delta=0.60$ mm

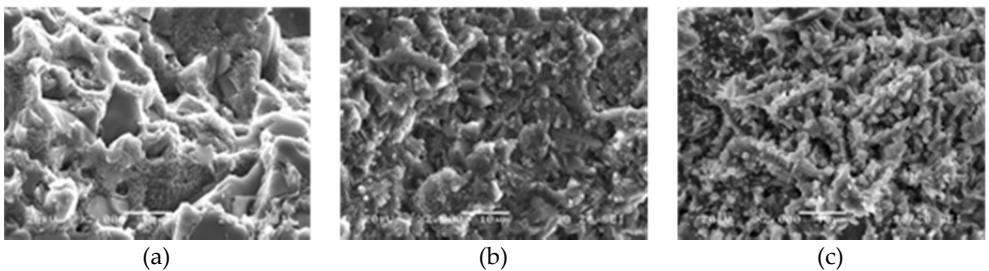


Figure 12. Fractographs of welded joints with various thicknesses of Ti filler; (a) $\delta=0.15$ mm (b) $\delta=0.45$ mm (c) $\delta=0.60$ mm

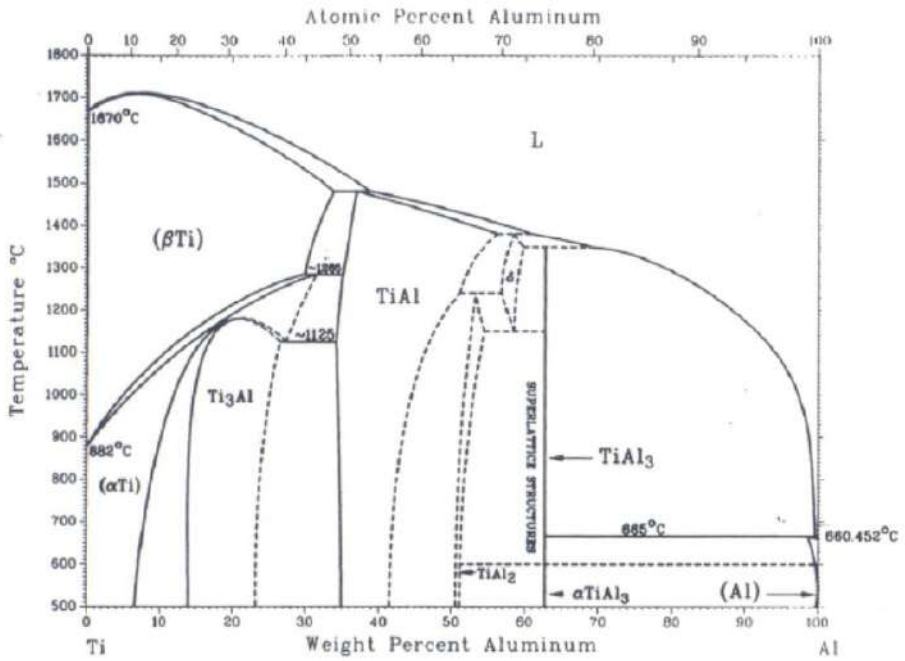


Figure 13. Binary phase diagram of Ti–Al [8]

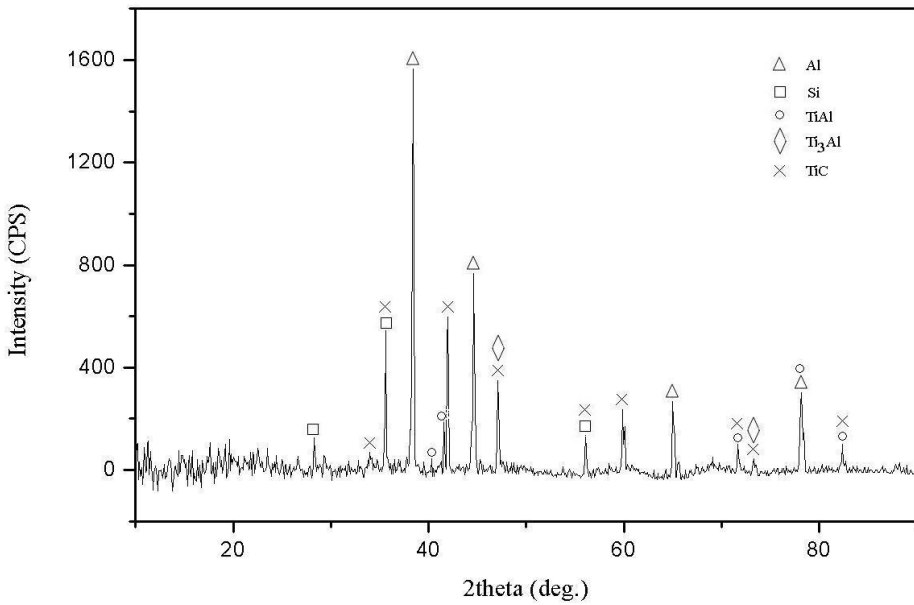


Figure 14. XRD pattern of fracture surface ($\delta=0.6$ mm)

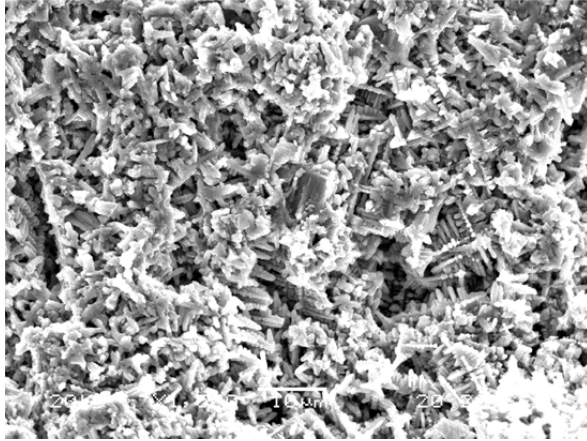


Figure 15. Columnar crystals in the laser weld with 0.6 mm thick Ti filler

3.4. TEM of the interface between *in situ* reinforcement particle TiC and matrix

The interface between *in situ* reinforcement particle TiC and the matrix was analyzed by the TEM micrograph displayed in Fig. 16. It demonstrated a clear interface between the newly-formed *in situ* reinforcement particle TiC and matrix. This clearly distinct interface (Fig. 16) suggested the occurrence of prominent *in situ* reaction to integrate the reinforcement particle with matrix (cf. Figs 4 and 16), and the high probability of successfully transferring load from the matrix to TiC and vice versa. It also gives indication that the aluminum matrix composite SiC_p/A356 would be welded satisfactorily by Nd:YAG laser.

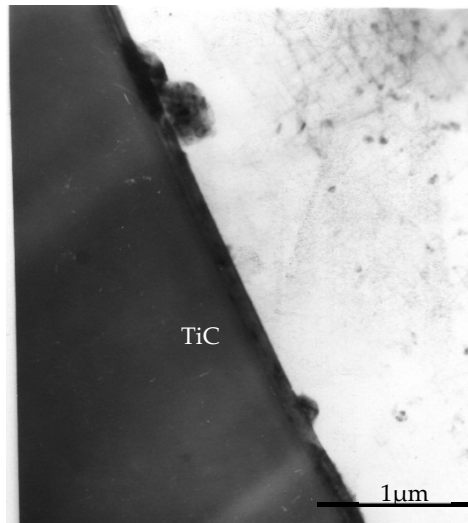


Figure 16. TEM of interface between *in situ* TiC reinforcement and the matrix for laser welding with 0.3 mm Ti filler

4. Microstructure evolution during the welding

4.1. Temperature field of laser welding

The heat is assumed to be released instantaneously at time $t=0$ on the surface of the substrate. This causes a temperature rise in the material as follows [10-12]:

$$T - T_0 = \frac{Q}{\rho c (4\pi\alpha t)^{\frac{3}{2}}} \exp\left(\frac{-R^2}{4\alpha t}\right) \quad (1)$$

where ρ is the material density, C is specific heat, α is thermal diffusivity, λ is thermal conductivity, Q is the input energy.

When temperature distribution is quasi-steady state:

$$T - T_0 = \frac{q_0}{2\pi\rho c\alpha R} \exp\left(-\frac{v}{2\alpha}(R+x)\right) \quad (2)$$

During the Nd:YAG laser welding, q_0 can be expressed as

$$q_0 = \eta(N(f,v)) \times \frac{P}{\frac{\pi D^2}{4} \times PD} = \eta(N(f,v)) \times \frac{4P}{\pi D^2 \times PD} \quad (3)$$

Where

$\eta(N(f,v))$ is the coefficient of laser welding input energy, which is direct proportional to number of overlaps or pulse frequency. With number of overlaps increasing, or pulse frequency increasing with constant the feed-rate, $\eta(N(f,v))$ will be increased synchronously. With the velocity (feedrate) increasing, number of overlaps with the constant pulse frequency will be decreased correspondingly led to lower heat input, $\eta(N(f,v))$ will be decreased accordingly.

Eq. (2) can be rewritten as:

$$T - T_0 = \frac{2 \times \eta(N(f,v)) \times P}{\pi^2 D^2 \rho c \alpha R \times PD} \exp\left(-\frac{v}{2\alpha}(R+x)\right) \quad (4)$$

Define $\xi = \frac{1}{2\pi\rho c\alpha}$, then Eq. (4) can be written as:

$$T - T_0 = \frac{\xi \times \eta(N(f,v)) \times P}{\frac{\pi D^2}{4} \times PD \times R} \exp\left(-\frac{v}{2\alpha}(R+x)\right) \quad (5)$$

$$\text{Define } q = \frac{P}{\frac{\pi D^2}{4} \times PD}, \quad (6)$$

then Eq. (6) can be written as

$$T - T_o = \frac{\xi \times \eta (N(f, v)) \times q}{R} \exp\left(-\frac{v}{2\alpha}(R+x)\right) \quad (7)$$

4.2. Simulation model

4.2.1. Equations for temperature distribution

Using energy balance, a differential equation can be obtained for the steady temperature distribution in a homogeneous isotropic medium, that is

$$\frac{\partial}{\partial x} \left(K_x \frac{\partial \theta}{\partial x} \right) + \frac{\partial}{\partial y} \left(K_y \frac{\partial \theta}{\partial y} \right) + \frac{\partial}{\partial z} \left(K_z \frac{\partial \theta}{\partial z} \right) = -q^B \quad (8)$$

Where the boundary conditions are $\theta|_{s_1} = \theta_e, K_s \frac{\partial \theta}{\partial x}|_{s_2} = q^s$.

For

$$\pi = \int_V \left\{ K_x \left(\frac{\partial \theta}{\partial x} \right)^2 + K_y \left(\frac{\partial \theta}{\partial y} \right)^2 + K_z \left(\frac{\partial \theta}{\partial z} \right)^2 \right\} d_V - \int_V \theta q^s d_V - \int_{s_2} \theta^s q^s d_s \quad (9)$$

After Eq. 9 is discrete for the element, and according to $\delta \pi = \sum_{e=1}^n \delta \pi_e = 0$, it will be obtained

$$\overline{K} \overline{\theta} = \overline{\theta}_s + \overline{\theta}_B - \overline{C} \theta + \overline{K}^c (\theta_c - \overline{\theta}^s) + \overline{K}^r (\theta_r - \overline{\theta}^s) \quad (10)$$

where S: isothermal boundary, B: the heat-input, c: the conductive and r: the irradiative.

4.2.2. Hypothesis and mesh

Based on the situations during the laser welding and mainly focused on the temperature distribution, it is supposed that the laser resource is considered as a Gaussian distribution. Also, on the basis of specimen size wire-cut, the calculating size is set as 25 mm (x) × 20 mm (y) × 3 mm (z), the schematic of its finite element (FE) mesh is shown in Fig. 17. Moreover, Ti filler is considered as a section of the substrate with the different properties to ignore the effect of gap between the Ti filler and the substrate.

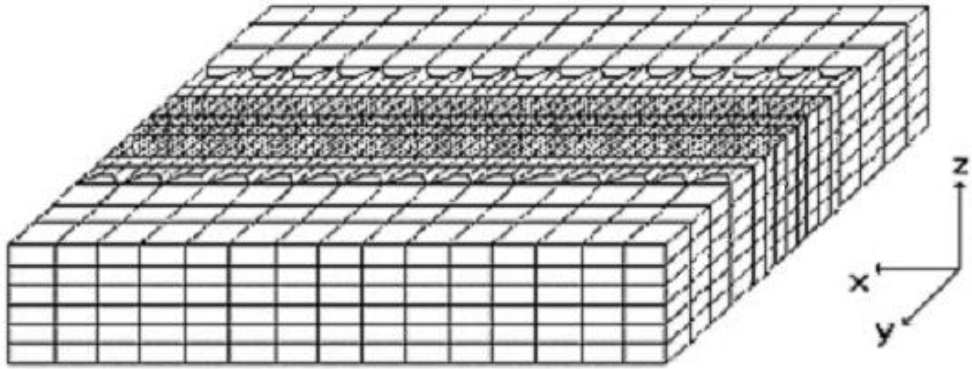


Figure 17. FE mesh for 3D numerical analysis

4.2.3. Temperature distribution

The simulated results are shown in Fig. 18 to Fig. 23. It shows that the temperature without Ti filler is same as the traditional laser welding. Simultaneously, due to the heat input into the substrates directly, without the additional heat resource for melting Ti filler, the peak of temperature (heat input) is relatively higher to form the weld. As a result, increasing the heat input into the substrate will decrease the tensile strength of the welded joint and wide the heat affected zone (HAZ) resulted in lower properties in the succedent practical applications (Table 2 and Fig. 19). Furthermore, a large amount of coarser acicular Al_4C_3 distributed in the fracture surface as shown in Fig. 19, which decreased the tensile strength of the welded joints seriously.

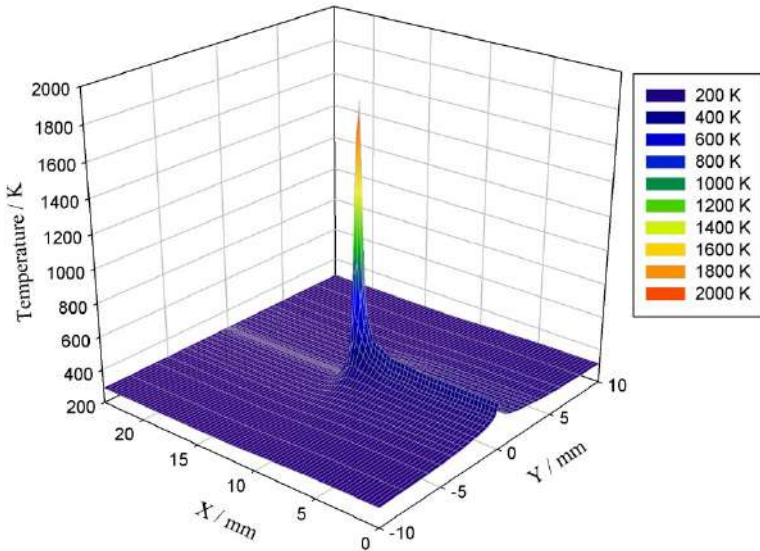


Figure 18. Temperature distribution without Ti filler

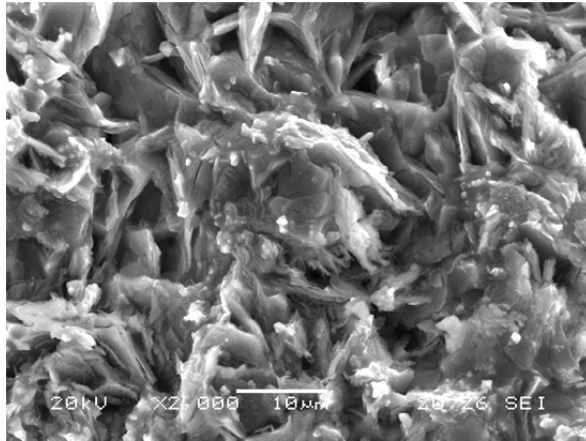


Figure 19. Fractograph of the laser welded joint without Ti filler

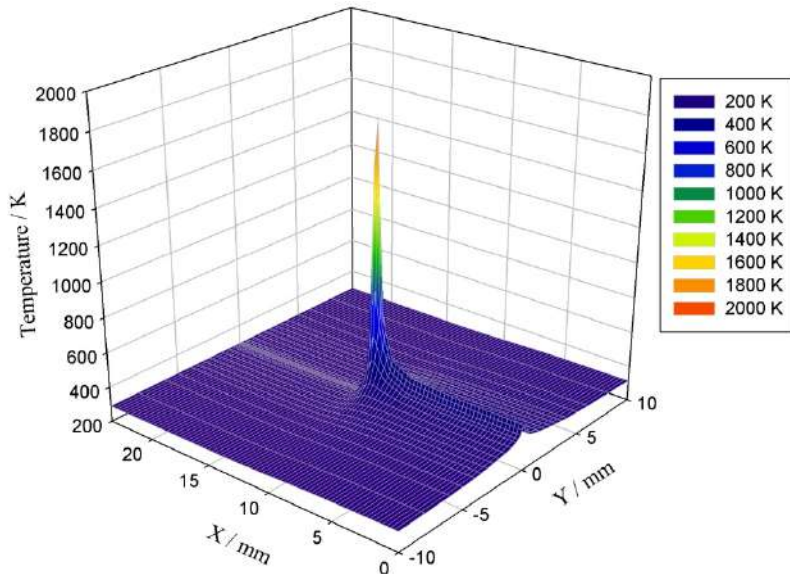


Figure 20. Temperature distribution with Ti filler

Figure 20 shows the temperature field of laser welding SiC_p/A356 with Ti filler. Considering the Ti melting and *in situ* reaction in the welding pool as an endothermic reaction, the welding temperature decreases and will be lower than that of laser welding directly (cf. Figs. 18 and 20), and its temperature field is distributed more smoothly with *in situ* reaction than that of laser welding without Ti filler as shown in Fig. 21. Also, the width of HAZ is decreased to some extent (Fig. 21b). Furthermore, it shows that according to the real effect of laser beam diameter, the thickness of Ti filler is about 0.3 mm will be optimal for *in situ* welding which conformed to the experimental results as shown in Table 2.

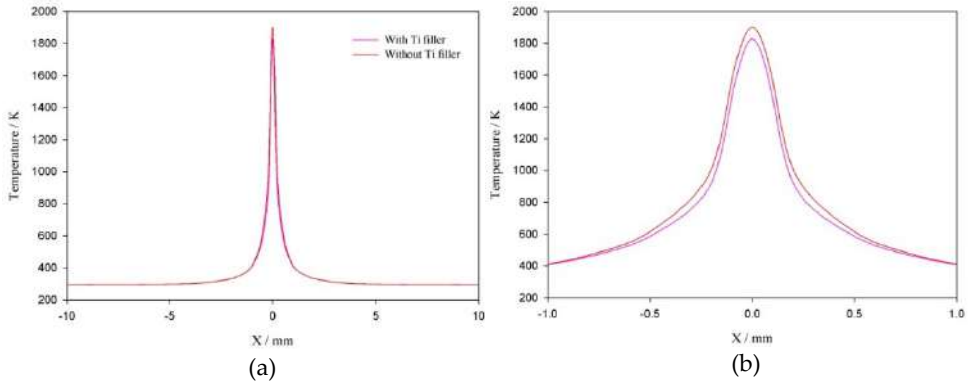


Figure 21. Temperature distribution of central heating on XOZ plane
 (a) Temperature distribution on XOZ plane (b) Magnification of (a)

In addition, the effect of Ti on the temperature distribution on the central line is shown in Fig. 22. It illustrates that the peak of the temperature is changed distinctly. Because of the sandwiched Ti between the substrates and *in situ* endothermic reaction, the temperature of substrate ahead of laser resource is lower than that of without Ti filler. Moreover, the temperature at the succedent distance is increased or accumulated a little bit due to the different conductive coefficient between Ti and substrate. On the other side, its corresponding trend of the temperature behind the laser resource (resolidification) is same as that of without Ti filler except for a peak appearance induced by more serious exothermic potential during the crystallization.

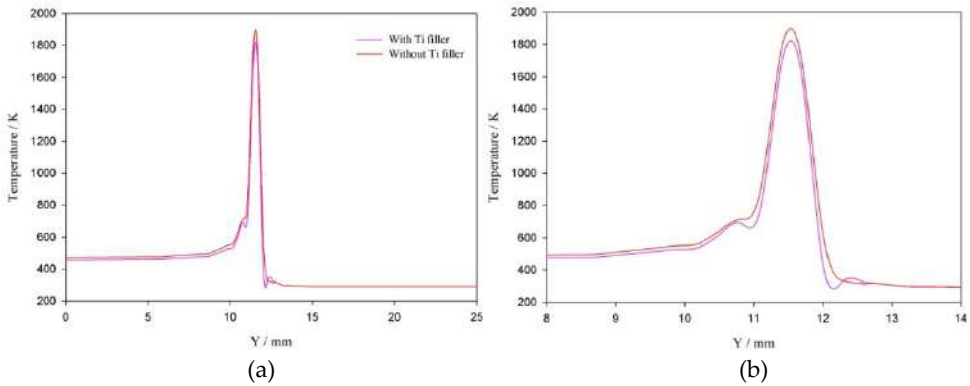


Figure 22. Temperature distribution of central line on YOZ plane
 (a) Temperature distribution on YOZ plane (b) Magnification of (a)

Figure 23 shows the temperature distribution when Ti filler is thick. The peak of temperature is decreased obviously and leads to the welding failure.

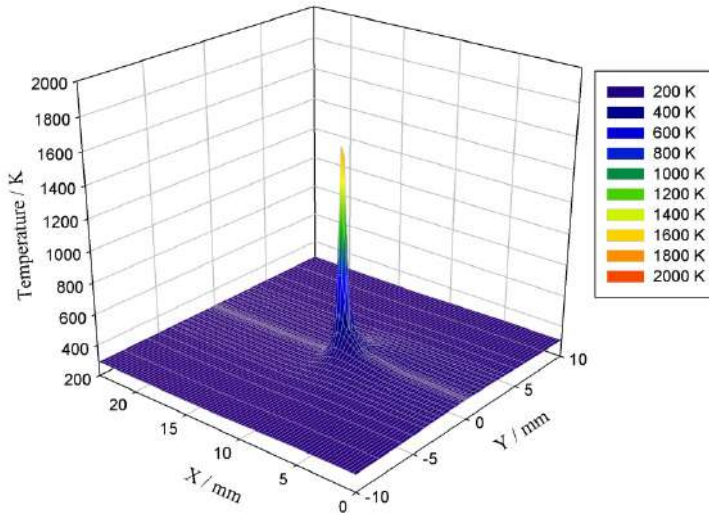


Figure 23. Temperature distribution with thick Ti filler

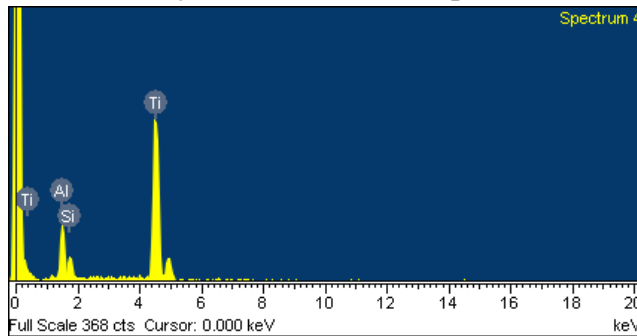
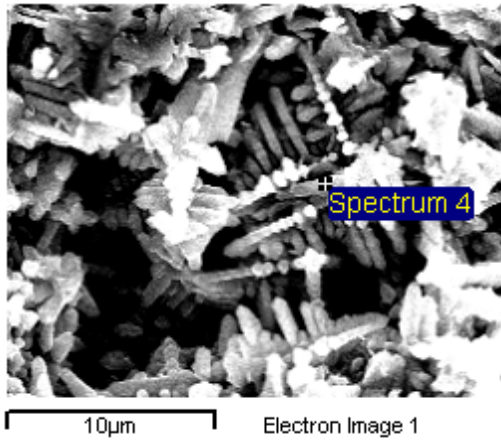


Figure 24. Microstructure and EDX of laser weld with thick Ti filler

Figure 24 shows the microstructure of laser welded joint with thick Ti filler and its corresponding energy dispersive X-ray spectroscopy (EDX) results. It can be observed that a large number of columnar Ti crystallization is distributed in the weld. From Figs. 23 and 24, it elucidates that with the increase of Ti thickness, the heat input into the substrate is decreased and most of energy is used for melting Ti led to the insufficient *in situ* reaction and stirring in the welding pool resulted in lower properties of welded joints.

Furthermore, in order to verify the temperature field, noncontact thermometer (model AZ9881) was used to measure the spot temperature on-line. The measured temperature results are shown in Fig. 25. It shows that the measured results agree well with the simulated results.

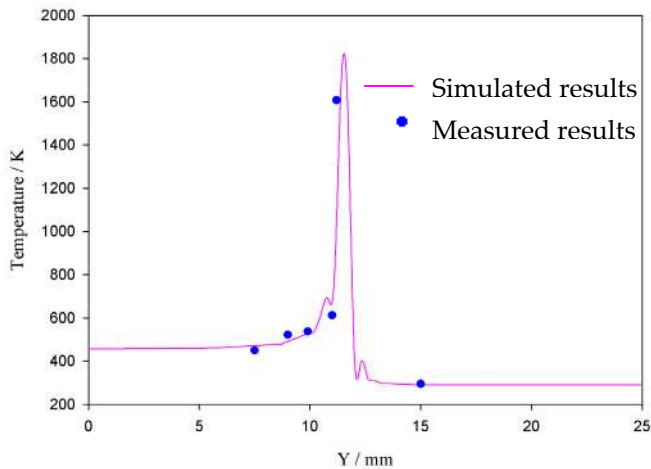


Figure 25. Surface temperature distribution in the processing center

4.3. Microstructure evolution simulation

According to the temperature calculation, the simulation of the evolution of the microstructure based on thermodynamic equilibria, diffusion [5, 6, 7] was shown in Fig. 26. It showed that during the welding pool solidification, the *in situ* reinforcement particles TiC would be formed around the initial reinforcement SiC particles. With the increase of cooling time, the initial reinforcement SiC particles would be replaced by the newly-formed *in situ* reinforcement particles TiC. It was well matched with the results shown in Figs. 7 and 9.

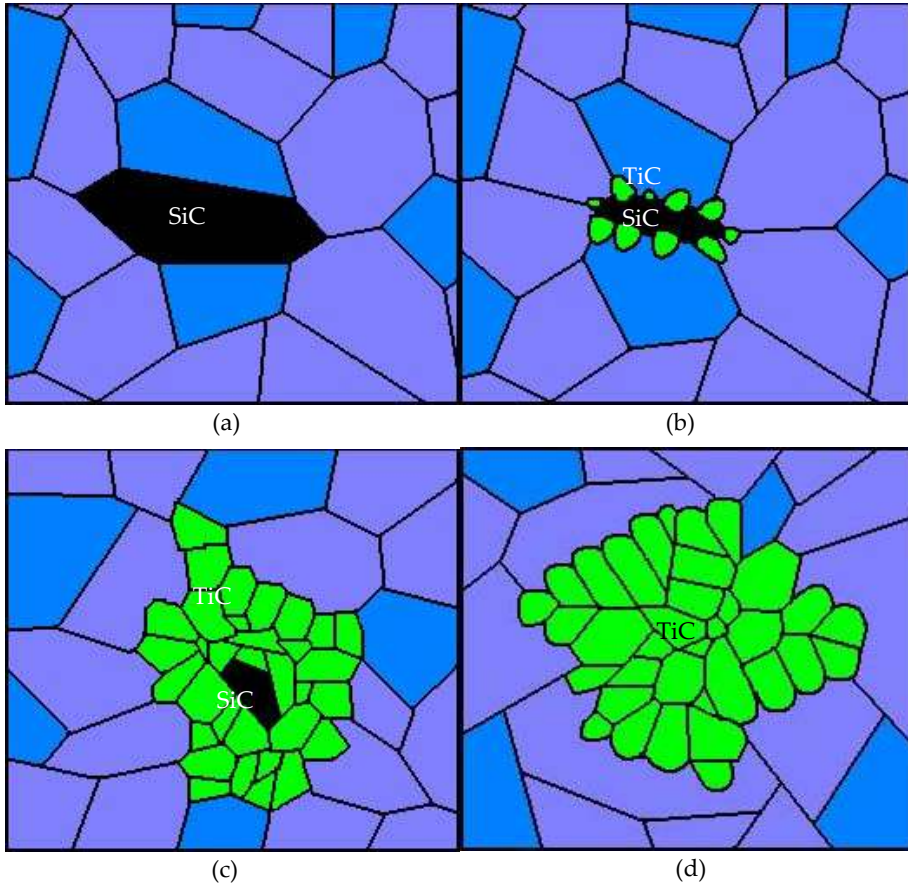


Figure 26. Simulation on microstructure evolution
 (a) Initial (b) Start of solidification (c) Middle of solidification (d) End of solidification

5. Conclusions

The use of titanium as a filler metal in Nd:YAG laser welding of SiC_p/A356 provided beneficial *in situ* reinforcement effect. The effect of *in situ* reinforcement of the Ti filler allowed the newly-formed reinforcement TiC particles to distribute uniformly in the weld that subsequently resulted in successfully welding the SiC_p/A356 composite. Moreover, the typical pernicious interfacial reaction microstructure such as Al₄C₃ was effectively restrained from the interface between aluminum matrix and reinforcement particles in the Nd:YAG laser welding of SiC_p/A356 with Ti filler. Furthermore, according to the temperature calculation, the evolution of the microstructure was simulated based on thermodynamic equilibria, diffusion. Results were well matched with the corresponding experiments.

Author details

Kelvii Wei Guo

MBE, City University of Hong Kong, Hong Kong, China

Acknowledgement

The work is supported by a RGC general research fund (GRF) (Grant No.:9041503.) and a Strategic Research Grant (SRG) from City University of Hong Kong (Grant No.: 7002287.)

6. References

- [1] J. M. Go´mez de Salazar, M. I. Barrena: Dissimilar Fusion Welding of AA7020/MMC Reinforced with Al_2O_3 Particles. Microstructure and mechanical properties. *Materials Science and Engineering A* 2003; 352(1-2): 162-168.
- [2] W. Guo, M. Hua, H. W. Law and J. K. L. Ho: Liquid-Phase Impact Diffusion Welding of SiCp/6061Al and Its Mechanism. *Materials Science and Engineering: A*, 2008, 490, (1-2), 427-437.
- [3] W. Guo, M. Hua, and J. K. L. Ho: Study on Liquid-Phase-Impact Diffusion Welding SiCp/ZL101. *Compos. Sci. Technol.*, 2007, 67, (6), 1041-1046.
- [4] L. M. Marzoli, A. V. Strombeck, J. F. Dos Santos, C. Gambaro, L. M. Volpone: Friction Stir Welding of an AA6061/ Al_2O_3 /20p Reinforced Alloy. *Composites Science and Technology* 2006; 66(2): 363-371.
- [5] D. A. Porter, K. E. Easterling: *Phase Transformations in Metals and Alloys*, 2nd. Cheltenham: Nelson Thornes, 2001.
- [6] R. Riedel: *Handbook of Ceramic Hard Materials*. New York: Wiley-VCH, Weinheim, 2000.
- [7] R. Boyer, G. Welsch, E. W. Collings: *Materials Properties Handbook: Titanium Alloys*. Materials Park, Ohio: ASM International, 1994.
- [8] J. R. Davis: *ASM Specialty Handbook – Aluminum and Aluminum Alloys*. Materials Park, Ohio: ASM International, 1993. p.557.
- [9] S. Mall, T. Nicholas: *Titanium Matrix Composites – Mechanical Behavior*. Lancaster, Pa.: Technomic Pub. Co. Inc., 1998.
- [10] W. M. Steen: *Laser Material Processing*, 3rd ed. London: Springer-Verlag; 2003.
- [11] K. W. Guo: Influence of In Situ Reaction on the Microstructure of SiCp/AlSi7Mg Welded by Nd:YAG Laser with Ti Filler. *J. Materials Engineering and Performance*, 2010, 19, 52-58.
- [12] A.F. Mills: *Heat and Mass Transfer*. P. R. Donnelly & Sons Company; 1995.

Nd:YAG Laser Welding for Photonics Devices Packaging

Ikhwan Naim Md Nawwi, Jalil Ali, Mohamed Fadhali and Preecha P. Yupapin

Additional information is available at the end of the chapter

<http://dx.doi.org/10.5772/50656>

1. Introduction

The state-of-the art of the pulsed Nd:YAG laser spot welding for photonics device packaging has been introduced by Marley (Marley, 2002), which utilizes the laser for high precision joining and alignment. The advantages of laser welding over conventional fusion welding processes include precise welds with a high aspect ratio, narrow heat affected zone (HAZ), very little thermal distortion, ease of automation, high welding speed, enhanced design flexibility, clean, high energy density, low heat input and an efficient process (Zhou & Tsai, 2008; Kazemi & Goldak, 2009). One of the key features of laser welding is the ability to weld without filler materials and it offers distinct advantages (Pang et al., 2008). Laser welding is a liquid-phase fusion process. It joins metals by melting the interfaces and resulting the mixing of liquid molten metal. Then, it solidifies on the removal of the laser beam irradiation (Ready, 1997). Photonics devices used for telecommunications of military applications are usually required to operate for a long life of operation in fields with potentially humid, corrosive and mechanically turbulent environments. Therefore, long term reliability in such hostile operating conditions requires strong fixing of the aligned components and hermetic sealing of the photonics devices inside metal hybrid housings (Fadhali et al., 2007a). It is worth to mention that 60% to 80% of the photonics devices modules cost are due to the coupling and packaging processes. Therefore, understanding the effective packaging technique is very important to produce efficient and reliably packaged photonics devices. Moreover, care must be taken to assemble functional packages because only packages that can be manufactured reliably at competitive costs will survive in the business world. For photonics packaging applications, most of the welds are of butt or lap joints which require the weld penetration depth to be larger than the bead width. Moreover, for miniature packages that contain some sensitive coupling components, the penetration depth should be large enough to achieve a strong attachment (Fadhali et al.,

2007a, 2007b, 2007c, 2007d, 2008). At the same time, the bead width should be small to minimize the HAZ and hence prevent the damage to the sensitive optical components. The desired material for this application requires a low thermal conductivity or a higher electrical resistivity (Dawes, 1992). The lower the thermal conductivity of a material the more likely it is to absorb laser energy. For this reason, several weldable grades of steel and stainless steel are ideal for laser welding. The low carbon austenitic stainless steel (300 series steel) which has carbon level less than 0.1% produces good quality welds and reliable weld performance (Fadhali et al., 2007a; Naim et al., 2009). Hence, in this chapter, a stainless steel 304 is utilized as a base material for laser welding. It has been reported that other types of stainless steel were studied by other researchers. For instance, Mousavi and Sufizadeh investigated stainless steel 321 and 630 (Mousavi & Sufizadeh, 2008), while Beretta et al. studied stainless steel 420 (Beretta et al., 2007), for the application of pulsed Nd:YAG laser welding. Whilst a great deal of effort has been focused on developing processing systems there is an urgent need to understand the strength of the weldment. It is the aim of this chapter to examine the strength of a stainless steel 304 welded joint. Despite the pulsed Nd:YAG laser welding has been widely used in microelectronic and photonics packaging industry, a full understanding of various phenomena involved is still a matter of trials and speculations.

2. Mathematical model of penetration depth of a spot weld

Penetration depth of laser spot welding is one of the vital parameters that contributes to a good laser spot micro welding outcome. Practical penetration depth measurements are time consuming and laborious like cutting the samples in order to obtain the weld cross section. Thus, this section shows a theoretical model to estimate penetration depth inside the welded samples by controlling laser parameters or to predict the laser parameters at the required penetration depth. Figure 1 illustrates the penetration depth on a welding specimen. The 1-Dimensional model is developed base on the heat conduction and energy balance equations (Naim et al., 2010).

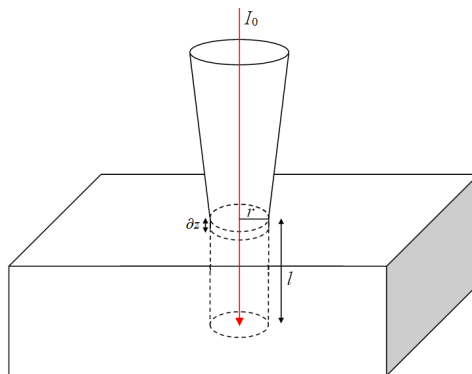


Figure 1. Illustration of the penetration depth of the focused laser beam on a welding specimen.

Applying the energy balance equation at the laser spot gives (Naim et al., 2010),

$$(1-R)I_0 = \rho L_m \frac{\partial l}{\partial t} - K \left(\frac{\partial T}{\partial z} \right)_{z=0} \quad (1)$$

Here I_0 is laser power density, L_m is latent heat of fusion, R is material reflectivity, ρ is material density, K is thermal conductivity, $\partial T / \partial z$ is temperature gradient at the welding front, l is the penetration depth, t is irradiation time and $\partial l / \partial t$ is penetration velocity. To determine the penetration velocity which is the change of penetration depth with time, the temperature gradient at the welding front should first be determined. The temperature distribution inside the target material is governed by the 1-Dimension heat conduction equation given as (Naim et al., 2010),

$$\frac{1}{\alpha} \frac{\partial T}{\partial t} = \frac{\partial^2 T}{\partial z^2} \quad (2)$$

where, α is thermal diffusivity. Equation (2) can be rewritten as

$$-\frac{1}{\alpha} \frac{\partial l_p}{\partial t} \frac{dT}{dz} = \frac{d^2 T}{dz^2} \quad (3)$$

The boundary conditions are taken as,

$$z=0, T=T_m \text{ and at } z \rightarrow \infty, T=T_0.$$

The maximum attainable temperature is the melting temperature of the material, T_m . Substituting these boundary conditions into Equation (3) and the solution for temperature distribution inside the material as

$$\frac{T-T_0}{T_m-T_0} = \exp \left[-\frac{1}{\alpha} \left(\frac{dl}{dt} \right) z \right] \quad (4)$$

The temperature gradient at the welding front can be obtained using Equation (4),

$$\left(\frac{dT}{dz} \right)_{z=0} = -\frac{1}{\alpha} \left(\frac{dl}{dt} \right) (T_m - T_0) \quad (5)$$

Substituting Equation (5) into the energy balance equation,

$$(1-R)I_0 = \rho L_m \left(\frac{dl}{dt} \right) + \rho c \frac{dl}{dt} (T_m - T_0) \quad (6)$$

From Equation (6), the welding velocity can be rewritten as,

$$\frac{dl}{dt} = \frac{(1-R)I_0}{\rho [L_m + c(T_m - T_0)]} \quad (7)$$

Integrating Equation (7) gives,

$$l = \frac{(1-R)Pt}{\pi r_o^2 \rho [L_m + c(T_m - T_0)]} \quad (8)$$

Here P is the laser peak power, t is the irradiation time or pulse duration and r is the laser beam radius. From Equation (8), one can observe that penetration depth is proportional to laser peak power and pulse duration as well as the material reflectivity.

Figure 2 illustrates the penetration depth versus peak power and pulse duration. Any changes of either peak power or pulse duration gives the same influence to the penetration depth. This is in agreement with the fact that the penetration depth increases linearly with both the peak powers and pulse durations. The penetration depth increases linearly with an increase of laser peak power. The higher laser peak power means more laser energy is absorbed into the welding material. When a higher laser energy is absorbed, it will produce a deeper melting pool. After solidification, the melting pool produces deeper weld or penetration depth. The trend is similar for variation of pulse duration. Higher pulse duration means longer heating duration. This will provide more time for laser beam to penetrate into the welding material. Thus, a deeper penetration depth will be produced. From Figure 3, it can be summarized that the penetration depth decreases significantly with laser spot radius. This is because the laser power density, I is proportional to $1/r^2$ and the power density will drop significantly as the laser spot radius increases. Laser power density determines the quantity of energy applied on welding material at a specific time. Higher power density will produce a deeper penetration depth.

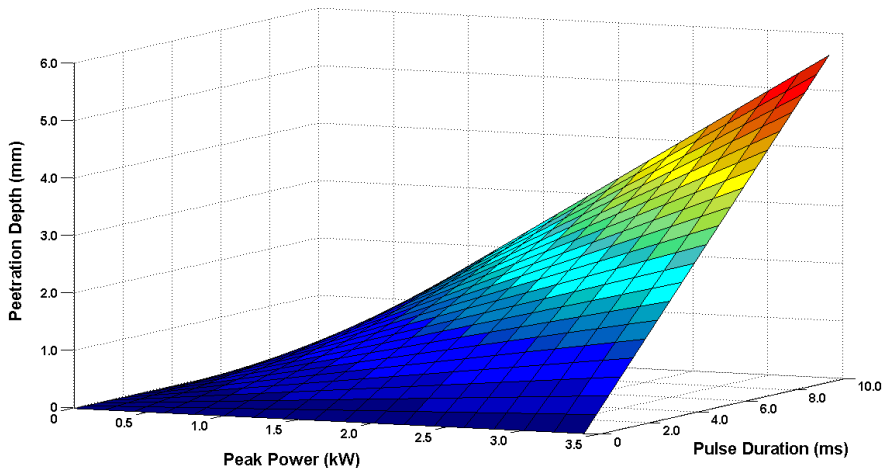


Figure 2. Penetration depth versus peak power and pulse duration.

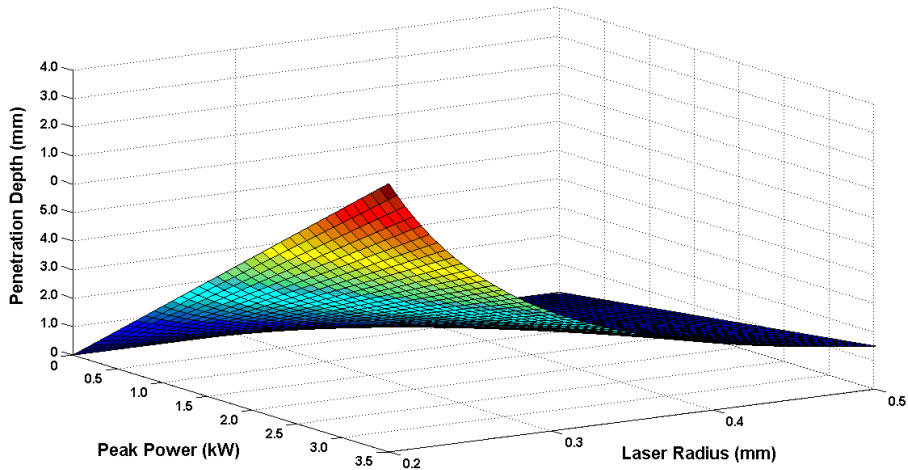


Figure 3. Penetration depth versus peak power and laser beam radius.

3. Mathematical model of laser beam power penetration

In order to produce a spot weld, a laser beam is incident on a specimen surface. The incident laser beam will be absorbed by the specimen depending on the material absorption coefficient. Thus, the absorbed laser beam heats up the specimen surface, raising its temperature. It will melt the specimen and produce a weld when it solidifies. The laser beam penetration in welding material has been derived using the continuity equation (Naim et al., 2010). It is assumed that laser beam penetrates the material based on a cylindrical coordinate. Figure 4 illustrates the laser beam power penetration in stainless steel specimen.

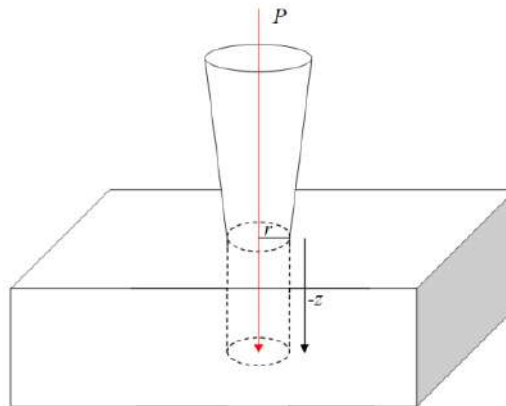


Figure 4. Laser beam power penetration in stainless steel specimen.

The laser beam power penetration is derived from a continuity equation given as (Naim, 2010),

$$\frac{\partial P}{\partial t} - k\nabla P = 0 \quad (9)$$

In cylindrical coordinate, Equation (9) then becomes,

$$\frac{\partial P}{\partial t} = k \left(\frac{\partial^2 P}{\partial r^2} + \frac{1}{r} \frac{\partial P}{\partial r} + \frac{\partial^2 P}{\partial z^2} \right) \quad (10)$$

Here $P=P(r,z,t)$ is the laser beam power penetration, r is the laser spot radius, z is the depth, k is the thermal conductivity and t is time. To solve this equation, let $P = RZT = R(r)Z(z)T(t)$ and the solutions are given by,

$$T = c_1 e^{-\mu^2 kt}, \quad (11)$$

$$R = c_2 J_0(\mu r) + c_3 Y_0(\mu r), \quad (12)$$

$$\text{and } Z = c_4 e^{\mu z} + c_5 e^{-\mu z} \quad (13)$$

where c_1, c_2, c_3, c_4, c_5 and μ are the unknown constants and determined by the boundary conditions, J_0 is first order of Bessel function and Y_0 is second order of Bessel function. Equation (10) can be solved by using Equations (11), (12) and (13) giving,

$$P(r, z, t) = [c_1 e^{-\mu^2 kt}] [c_2 J_0(\mu r) + c_3 Y_0(\mu r)] [c_4 e^{\mu z} + c_5 e^{-\mu z}] \quad (14)$$

Let $A = c_1 = c_2 = c_3 = c_4 = c_5$ as the incident laser beam peak power and μ is the material absorption coefficient. In this calculation, only first order of Bessel function is considered. It is also assumed that the laser beam propagates only directing into the material which is $-z$ direction. Equation (14) can be written as,

$$P(r, z, t) = A e^{-k\mu^2 t} [J_0(\mu r)] [e^{-\mu z}] \quad (15)$$

For stainless steel material, the absorption coefficient, μ is 0.3 (Kazemi & Goldak, 2009) and the laser beam peak power used in this consideration is 3.5kW. Equation (15) then specified as,

$$P(r, z, t) = 3500 e^{-0.3^2 kt} [J_0(0.3r)] [e^{-0.3z}] \quad (16)$$

Equation (16) provides the time dependent laser beam penetration. The laser beam penetration is computed for its radius and depth. Figure 5 shows the profile of applied peak power versus the depth of specimen and laser spot radius. The peak power 3.500kW decreases exponentially with depth of stainless steel material and decreases according to the first order of Bessel function in terms of the spot radius. The peak power incident on the surface is 3.500kW at the centre of laser spot target, but decreases to 3.0248 kW at the spot radius of 0.25mm. Peak power reduces to 0.1743kW at the centre and 0.1506kW at spot radius of 0.25mm for a depth of 1.00mm. At the laser spot radius of 2.00mm, the laser beam is almost fully penetrated with only peak power of 0.0087kW at the centre of the penetration.

Figure 6 illustrates the time dependent laser beam penetration for stainless steel material. According to the illustration, the peak power reduces exponentially for both depth and time. From observation, laser beam peak power decreases faster through the depth rather than through the time, relatively. This is explained by Equation (16) which states penetrated laser beam is based on absorption coefficient through the depth is -0.03 m but only -0.0009 m through time. At a depth of 2.00 mm and time of 4.0 ms, the peak power is 0.0002 kW. At this point, laser beam is almost fully penetrated. On the interface between stainless steel material and laser beam spot, laser beam penetration can be illustrated by Figure 7 at certain time. As discussed before, laser beam penetration decreases according to the first order of Bessel function with the spot radius and exponentially with time. At the central of the interface, the peak power is 3.5 kW and it reduces to 0.0026 kW after 8.0 ms. At laser spot radius of 0.25 mm, the laser beam penetration is 3.0248 kW and it reduces to 0.0023 kW after 8.0 ms where the laser beam is about to fully absorbed by the stainless steel material.

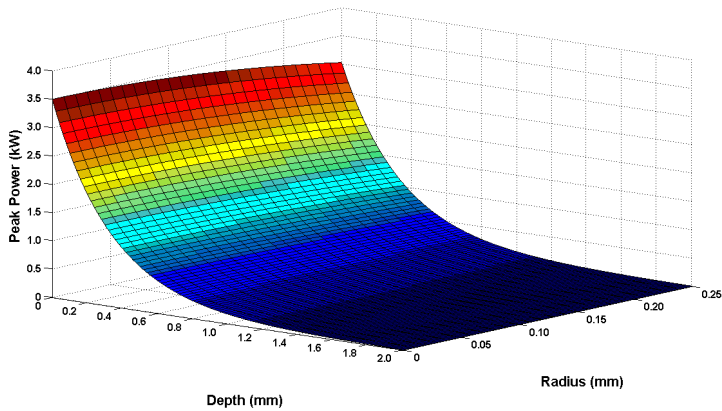


Figure 5. Peak power versus depth and radius for stainless steel with absorption coefficient, $\mu=0.3$ and $t=1$ ms.

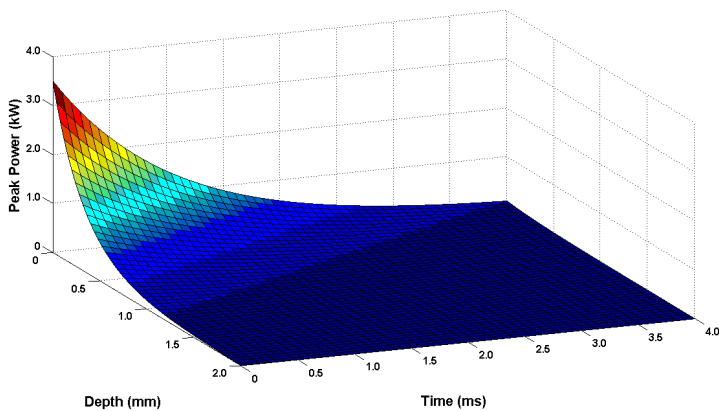


Figure 6. Peak power versus depth and time for stainless steel with absorption coefficient, $\mu=0.3$ at the centre of penetration.

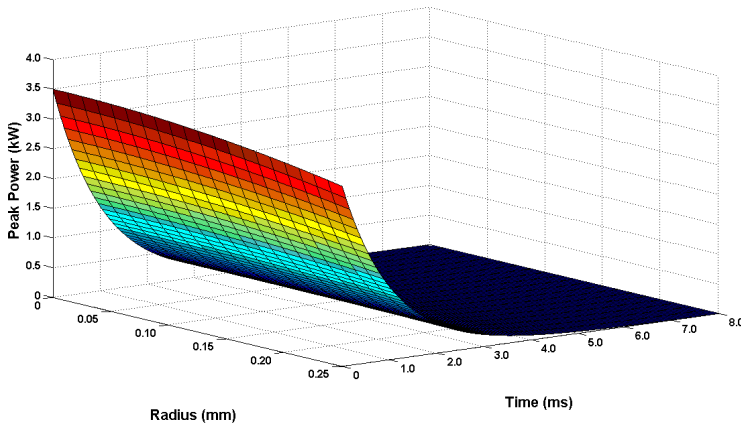


Figure 7. Peak power versus radius and time for stainless steel with absorption coefficient, $\mu=0.3$ at the welding front.

4. Analysis of the pulsed Nd:YAG laser spot weld

The profiles for the penetration depth and bead width produced by the pulsed Nd:YAG laser beam are depicted in Figure 8 and Figure 9. The weld dimensions (weld penetration depth and bead width) for different laser beam peak powers are illustrated in Figure 10. The results display an increase in penetration depth and bead width with an increase in the laser beam peak power. The deepest penetration depth produced is 1.31 mm and the largest bead width is 0.57 mm when laser beam peak power is set at 3.5 kW. When laser beam peak power is reduced to 0.5 kW, the reading of penetration depth and the bead width are only 0.36 mm and 0.24 mm. The linear gradients of penetration depth and bead width are 0.301 and 0.10, respectively. These values show the laser beam peak power is almost 3 times more effective on the penetration depth rather than the bead width. This suggests that the laser beam peak power is a reliable parameter to control the desired penetration depth. It is observed in Figure 10 that the penetration depth and bead width increases when the pulse duration is increased. From the Figure 11, linear gradient of penetration depth and bead width are 0.0039 and 0.035, respectively. Only slight difference is noted and this means that the pulse duration has no significant effect either on penetration depth or bead width. As compared with the effect of laser peak power, the pulse duration is a much more better parameter to control the desired bead width.

Laser beam can be defocused by moving the focus point position forward or backward from the specimen surface. Figure 12 depicts that the penetration depth decreases significantly when the laser beam focus point position is moved from 0 to 4.0 mm with respect to the specimen surface. After 4.0 mm, the penetration depth decreases gradually until 6.0 mm and there is no penetration depth that can be traced after 6.0 mm. Otherwise, when the focus point position is moved forward or backward, the bead width increases. But after 6.00 mm, there is no more bead width and only the sign of burning can be observed on the welding

surface. As the focus point position is moved forward or backward from the specimen surface, the laser spot size increases. This will reduce the intensity of the laser beam which is given by, $I_0 = P / \pi r^2$. Here, P is the laser beam peak power and r is the laser spot radius. It indicates that the intensity of laser beam is negatively proportional with r^2 . Hence, the laser beam does not have sufficient intensity to penetrate the material. As illustrated in Figure 13, it is observed that the penetration depth and bead width changes with the laser beam incident angle. As the laser beam incident angle increases, the laser spot becomes elliptical and wider. Hence the bead width also becomes elliptical and wider. The wider laser spot will reduce the intensity of the laser beam. This will result in a decrease of the penetration depth. However, when the laser beam incident angle is increased, the reflectivity of material surface drops due to the influence of light polarization. When the reflectivity drops, it will transport more laser energy into the welding material. Hence, it will increase the penetration depth. It can be seen that when weld penetration depth at angle of incidence of 45 degrees is much higher than that at 25 degrees. But, even though the reflectivity of the material surface drops greatly at 65 degrees, the penetration depth is only 0.82 mm because laser beam is less intense due to the significant increases in the laser spot area for a slight increase of the incident angle. In Figure 14, it can be seen that the penetration depth increases slightly with the number of shots. The penetration depth for the first and seventh pulse shots are 0.91 mm and 1.11 mm. When the first shot is applied it produces a shallow concave hole on the specimen surface. This is due to the material ablation produced by laser pulse pressure when it strikes the material surface. Then, when the second shot is given, it is able to go towards the bottom of the concave hole. The second shot weld penetration depth is similar to the first shot but with an increase in the depth of the concave hole. The first and seventh shot produce 0.52 mm and 0.57 mm of bead width. The difference is relatively small because the same laser beam parameters are used for each shot.

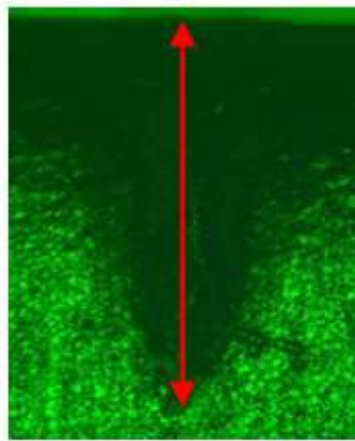


Figure 8. Cross-section of a spot weld produced by 2.5kW laser beam peak power and 2.5ms pulse duration. The penetration depth is labelled by the vertical line.

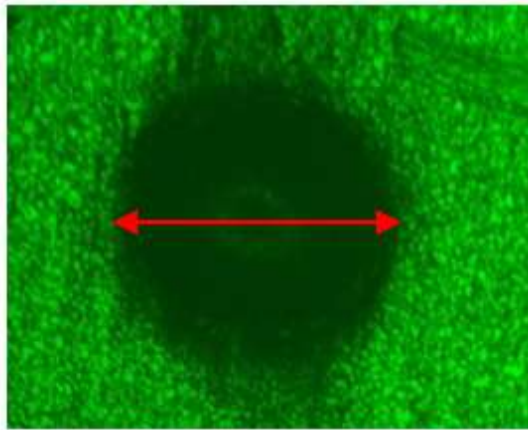


Figure 9. Figure 9. Top view of a spot weld produced by 2.5kW laser peak power and 2.5ms pulse duration. The bead width is labelled by the horizontal line.

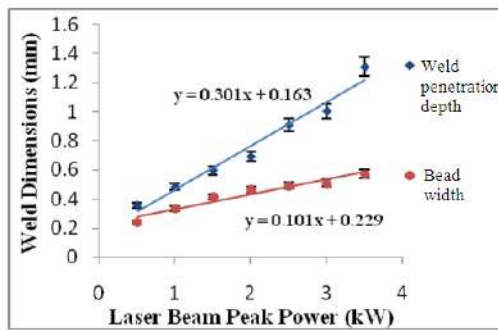


Figure 10. Characteristics of a spot weld dimensions as a function of laser peak powers conducted by 2.5 ms pulse duration with laser beam incidence is vertical in respect to the surface normal.

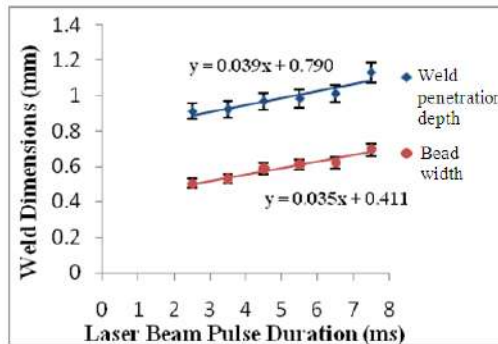


Figure 11. Characteristics of a spot weld dimensions as a function of laser pulse durations conducted by 2.5 kW laser peak power with wavelength of 1064 nm.

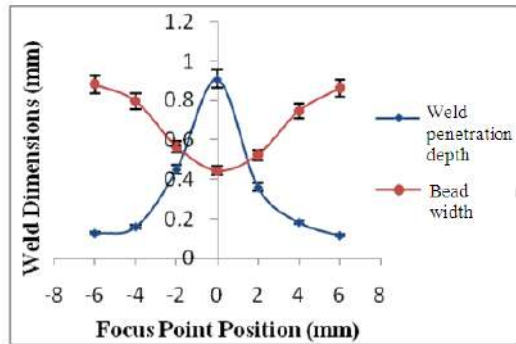


Figure 12. Characteristics of a spot weld dimensions when Nd:YAG laser spot is positioned forward and backward from the stainless steel 304 surface with 2.5 kW laser peak power and 2.5 ms pulse duration.

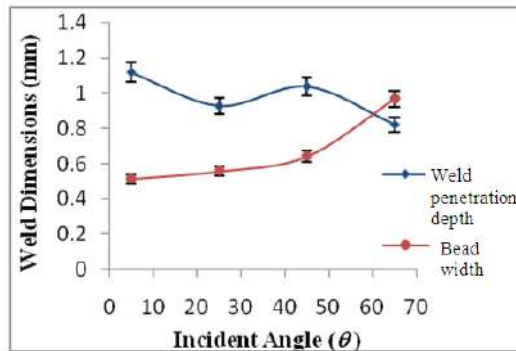


Figure 13. Characteristics of a spot weld dimensions when Nd:YAG laser spot incident angle is varied with respect to the stainless steel 304 surface normal by employing 2.5 kW laser peak power and 2.5 ms pulse duration.

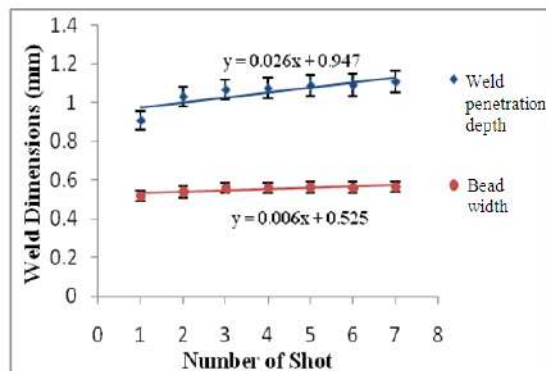


Figure 14. Spot weld produced by 2.5 kW laser peak power, 2.5 ms pulse duration with laser beam incidence is vertical in respect to the surface normal and laser focus point is on the stainless steel 304 surface, while the laser beam shot numbers are varied.

5. The strength analysis of a welding joint

In this section, the strength test of a welding joint of a single spot welding is discussed for stainless steel 304. A test is also executed for a seam welding which is produced by shooting the laser pulses continuously along the 10.0 ± 0.1 mm stainless steel 304 interfaces. The strength for seam welding of stainless steel 304 is also compared to an Invar™, which is a commercial welding material for photonics device packaging. A Unitek Miyachi LW10E ultra compact pulsed Nd:YAG laser with wavelength of $1.064 \mu\text{m}$ is employed to produce a weld joint. The energy per pulse output is in the range of 1 to 20 J, laser beam peak power is up to 3.5 kW and pulse duration ranging from 0.3 ms to 10.0 ms. However, in this investigation, only 3.5 kW laser beam peak power and 6.5 ms pulse duration is employed. This parameter is chosen because it produces a deepest penetration depth on stainless steel 304 which is 1.2 mm (Nawi et al., 2011). The penetration depth is important and should be large enough to achieve a strong attachment. The welding base material used is a stainless steel 304 sheet with a thickness of 1.0 ± 0.1 mm. The experimental setup to produce a weld consists of a laser source, fiber optics delivery system, and focusing lenses with focal length of 100.00 mm as illustrated in Figure 14.

The optical fiber cables transmit the laser beam to the welding focusing lenses inside the lens housing. The laser welding system is also equipped with an aiming diode laser beam, which simplifies positioning of the laser spot on the stainless steel sheet. A spot weld and a seam weld are produced with two types of joint; butt joint and lap joint, as illustrated in Figures 15(a) and 15(b). The strength of the weld joints is conducted by pulling the joint materials using INSTRON Series IX/s Automated Materials Tester System. The crosshead speed utilized for pulling the joint is set to 0.2 mm/min. The strength for a weld joint is determined by measuring the applied load during the test.

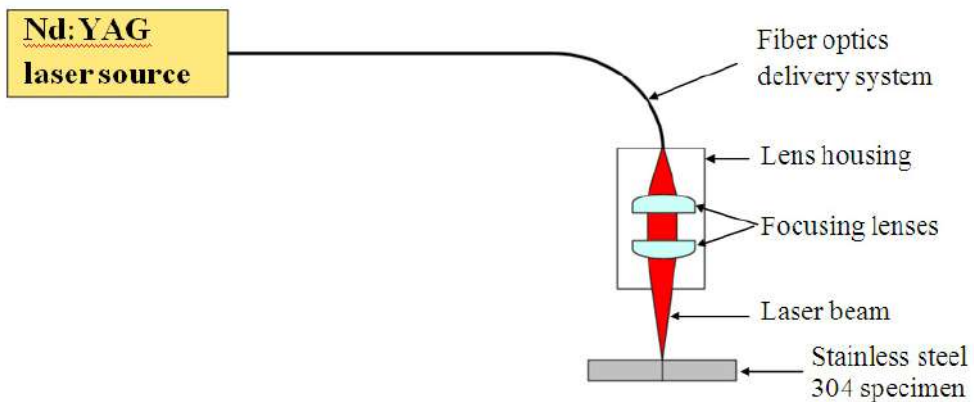


Figure 15. Nd:YAG laser experimental setup to produce a spot weld on stainless steel 304 specimen.

The element composition of stainless steel 304 and welded stainless steel 304 are examined by using Energy Dispersive X-ray (EDX) technique. The stainless steel 304 consists of iron (Fe) 69.59wt%, chromium (Cr) 18.33wt% and nickel (Ni) 12.08wt%. Figure 16 shows the element composition for stainless steel 304 changes when it is welded by Nd:YAG laser beam and it is now comprising of iron (Fe) 68.83wt%, chromium (Cr) 17.10wt% and nickel (Ni) 14.08wt%. It is observed that there are no changes in the elemental composition before and after welding of stainless steel 304. The applied load for the test and the pulling displacement for spot and seam welding are shown in Figure 17 and Figure 18, respectively. Maximum applied load is considered as the strength of the weld joint. Figure 16 illustrates maximum load for butt and lap joint which are 0.2296 kN and 0.0691 kN with a pulling displacement of 0.43 mm and 0.40 mm, respectively.

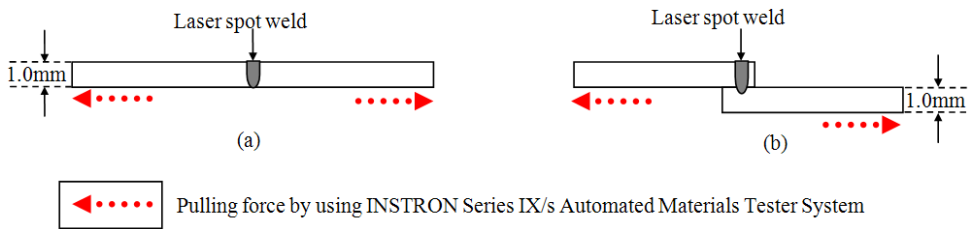


Figure 16. Configuration of the (a) butt joint and (b) lap joint, for stainless steel 304 with a thickness 1.0 ± 0.1 mm.

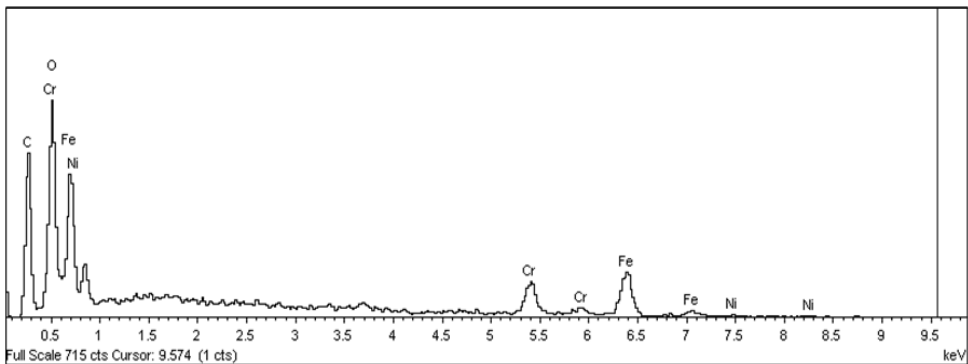


Figure 17. EDX analysis for the elemental composition of welded stainless steel 304.

The Invar™ maximum load is recorded as 0.3760 kN with 0.43 mm pulling displacement. The outcome indicates that the butt joint produces much stronger attachment than the lap joint. The stronger attachment is contributed by a larger volume of welded stainless steel at the joint interfaces as shown in Figure 19(a). For lap joint, the thickness of the stainless steel 304 becomes double as the upper and lower stainless steel sheets are overlapped. If

the laser beam produces insufficient penetration depth, thus only a small volume of welded stainless steel 304 is produced at the interfaces of the joint as shown in Figure 19(b). This will lead to a weaker joint. But, the penetration depth can be increased by controlling the laser beam parameters such as laser beam peak power and pulse duration. Hence, it will increase the strength of a lap joint. In terms of welding materials comparison, the commercial welding material, Invar™, provides more robust joint than stainless steel 304. Figure 18 indicates the seam welding maximum load for butt joint is 2.6339 kN with 0.62 mm pulling displacement. Lap joint recorded the maximum load of 1.0466 kN at 0.49 mm. This implies that the butt joint of a seam welding provides a much stronger attachment than the lap joint similar with the case of a single spot weld. Figure 18 also indicates between the butt joint pulling displacement of 0.48 mm and 0.72 mm, there are no significant changes in the joint strength because each point along the seam welding has the similar maximum strengths but it is not achieved simultaneously depending on its geometry.

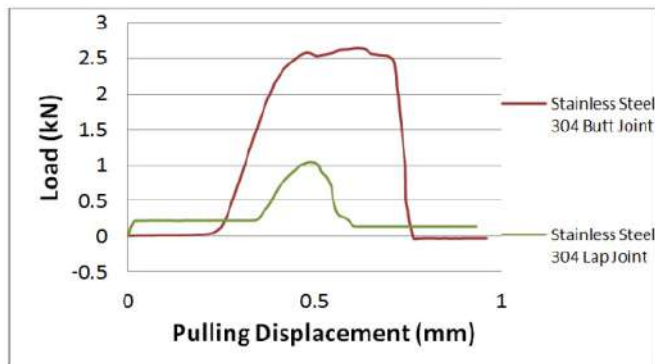


Figure 18. Strength profile of a single spot weld produced on stainless steel 304 and Invar™ by using 3.5 kW Nd:YAG laser beam peak power and 6.5 ms pulse duration.

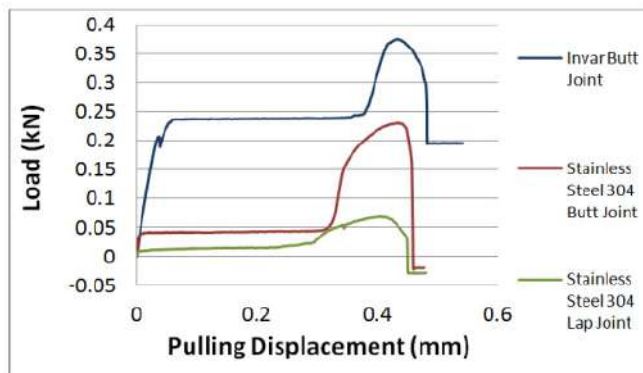


Figure 19. Strength profile of a seam weld produced on a stainless steel 304 along 10.0 ± 0.1 mm joint interfaces.

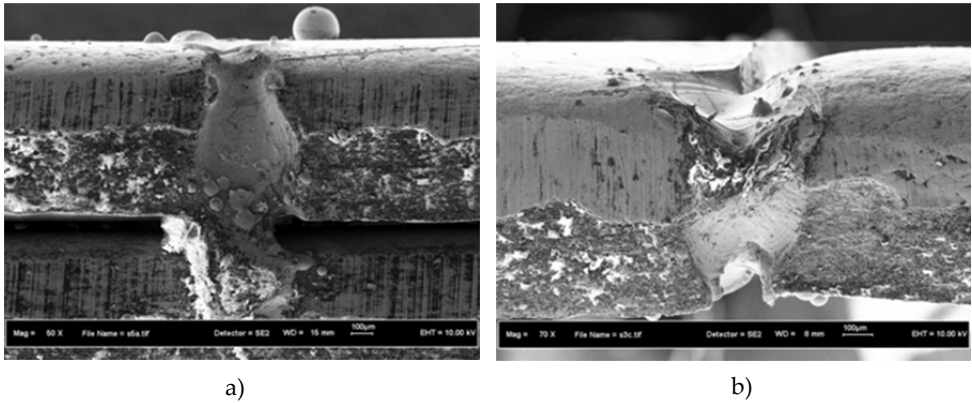


Figure 20. FESEM micrographs of a stainless steel 304 spot weld joint; (a) butt joint and (b) lap joint, produced by 3.5 kW laser beam peak power and 6.5 ms laser pulse duration.

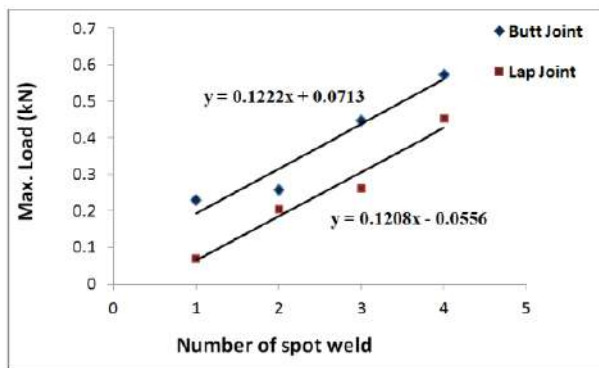


Figure 21. The strength comparison between butt joint and lap joint for variation number of spot weld.

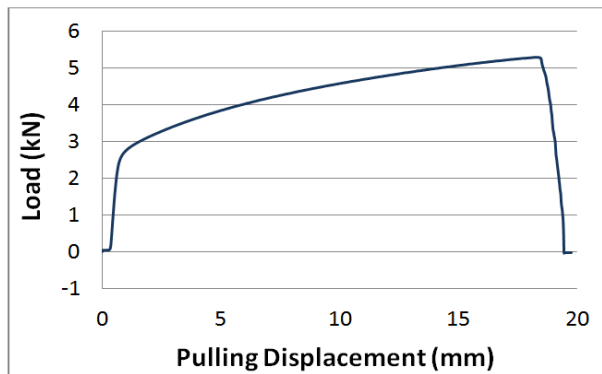


Figure 22. The strength of a stainless steel 304 with 1.0 ± 0.1 mm thickness and 10.0 ± 0.1 mm width.

In miniature assemblies, only a small number of laser spot weld is used for an attachment because of the relative small parts (Fadhali et al., 2007a, 2007b, 2007c, 2007d, 2008). The strength on the number of laser spot welding up to four spots is investigated for butt joint and lap joint. Then, the maximum strength for both joint types is compared. Figure 20 illustrates that the strength increases when the number of spots increases for butt and lap joint. A linear relationship is obtained from both joints strength against the number of spots and it has equal gradient which are 0.122 and 0.120, respectively. This suggests there is no significant difference in the influence of number of spots on the strength for both types of joint. The strength of stainless steel 304 is shown in Figure 21. It produces a strength of 5.2866 kN with 18.23 mm pulling displacement. The strength of stainless steel 304 is almost twice stronger than the seam welded stainless steel 304. Thus the welded material cannot attain the strength of the base material itself. The pulling displacement indicates that the elastic modulus of stainless steel 304 is much more greater than the welded stainless steel 304.

6. Conclusion

In conclusion, it is shown that the penetration depth and bead width increase when the laser beam peak power, pulse duration and number of shot are increased. It is found that the laser peak power is more effective to produce the deeper penetration depth rather than the bead width. Otherwise, the laser beam pulse duration is an accurate parameter to control if the desired bead width is required rather than the penetration depth. As the focus point positions are placed forward and backward from the stainless steel 304 specimen surface, the laser spot size increases. This leads to the reduction of the laser beam intensity. Hence, the penetration depth decreases. The increase of the laser spot size will increase the bead width. When the laser beam incident angle is varied, the bead width also changes due to the widening of the laser spot size. The penetration depth depends on the both widening laser spot size and material surface reflectivity that drops due to the influence of light polarization. The penetration depth increases slightly with the number of shots due to the material ablation produced by laser pulse pressure when it strikes the specimen surface. For welding joint strength, a butt joint produces much stronger attachment than a lap joint. The stronger attachment is contributed by a larger volume of welded stainless steel 304 at the joint interfaces. It is observed that each point along the seam welding has a similar maximum strengths but it is not achieved simultaneously. The similar gradient obtained in a linear relationship suggests that there is no significant difference in the influence of number of spots on the butt and lap joint strength. The commercial welding material, Invar™, provides more robust joint rather than stainless steel 304. The welded stainless steel 304 cannot attain the strength and elastic modulus of the stainless steel 304 itself. From the strength test results, it is found that stainless steel 304 is a good candidate to be used as a welding material for photonics device packaging by using pulsed Nd:YAG laser welding technique.

Author details

Ikhwan Naim Md Nawi

Centre of Foundation Studies & Faculty of Applied Sciences, Universiti Teknologi MARA, Malaysia

Jalil Ali

Universiti Teknologi, Malaysia

Mohamed Fadhali

Physics Department, Faculty of Science, Ibb University, Yemen

Preecha P. Yupapin

King Mongkut's Institute of Technology Ladkrabang, Bangkok, Thailand

7. References

- Beretta, J.R.; Rossi, W.; Neves, M.D.M.; Almeida, L.A. & Vieira, N.D. (2007). Pulsed Nd:YAG laser welding of AISI 304 and 420 Stainless Steel. *Journal of Optical Lasers Engineering*, Vol. 45, pp. 960-966.
- C. Dawes, C. (1992). *Laser welding: A practical guide*. Woodhead Publication Ltd., England.
- Fadhali, M.; Zainal, J.; Munajat, Y.; Ali, J. & Rahman, R. (2007a). Reliable pigtailling of photonic devices employing laser microwelding. *Journal Engineering and Applied Science*, Vol. 2, pp. 1724-1728.
- Fadhali, M.; Zainal, J.; Munajat, Y.; Ali, J. & Rahman, R. (2007b). Investigation of the application of Nd:YAG laser welding to couple photonic devices and packaging. *Lasers Engineering*, Vol. 17, pp. 273-286.
- Fadhali, M.; Zainal, J.; Munajat, Y.; Ali, J. & Rahman, R. (2007c). Laser diode pigtailling and packaging using Nd:YAG laser welding technique. *Jurnal Komunikasi Fisika Indonesia*, Vol. 5, pp. 203-208.
- Fadhali, M.; Zainal, J.; Munajat, Y.; Ali, J. & Rahman, R. (2007d). Analysis of laser microwelding applied for photonic devices packaging. *Journal Solid State Science and Technology Letter*, Vol. 14, pp. 18-19.
- Fadhali, M. (2008). Efficient coupling and reliable packaging of photonic devices using laser welding technique. *Ph.D Thesis: Universiti Teknologi Malaysia*, Skudai, Johor, Malaysia.
- Kazemi, K & Goldak, J.A. (2009). Numerical simulation of laser full penetration welding. *Computer Material Science*, Vol. 44, pp. 841-849.
- Marley, C. (2002). Laser welding photonics devices: Proper design guidelines enable users to achieve high-precision alignment requirements. *Industrial Laser Solutions for Manufacturing*, 2002.
- Mousavi, S.A.A. & Sufizadeh, A.R. (2008). Metallurgical investigations of pulsed Nd:YAG laser welding of AISI 321 and AISI 630 stainless steels. *Journal of Material Design*, Vol. 15, pp. 44-49.
- Naim, I.; Saktioto, T.; Fadhali, M.; Ali, J.; & Yupapin, P.P. (2009). An investigation of a pulsed Nd:YAG laser welding technique. *Proceedings of IEEE-Regional Symposium on Micro and Nanoelectronics*, pp. 274-280, Kelantan, Malaysia, August 10-12, 2009.

- Naim, I.; Saktioto, T.; Hamdi, M.; Fadhali, M.; Ali, J.; & Yupapin, P.P. (2010). Penetration depth estimation for stainless steel 304L using Nd:YAG laser spot micro welding. Proceedings of 2nd Topical Meeting on Lasers and Optoelectronics, Vol. 1, pp. 278-288, Terengganu, Malaysia, March 13-15, 2010.
- Nawi, I.N.; Saktioto; Fadhali, M.; Hussain, M.S.; Ali, J. & Yupapin, P.P. (2011). A Reliable Nd:YAG Laser Welded Stainless Steel 304 for Photonics Device Packaging. *Procedia Engineering*, Vol. 8, pp. 380-385.
- Pang, M.; Yu.G.; Wang, H.H. & Zheng, C.Y. (2008). Microstructure study of laser welding cast nickel-based superalloy K418. *Journal of Material Processing Technology*, Vol. 207, pp. 271–275.
- Ready, J.F. (1997). *Industrial applications of lasers*. New York: Academic Press.
- Zhou, J. & Tsai, H.L. (2008). Modeling transport phenomena in hybrid laser-MIG keyhole welding. *International Journal of Heat and Mass Transfer*, Vol. 51, pp. 4353-4366.

Laser Beam Welding of Austenitic Stainless Steels – Similar Butt and Dissimilar Lap Joints

Abdel-Monem El-Batahgy

Additional information is available at the end of the chapter

<http://dx.doi.org/10.5772/48756>

1. Introduction

1.1. Laser beam welding of similar butt joints of austenitic stainless steels

Because of its inherent corrosion resistance, austenitic stainless steels, known as 300 series, have become cost-effective, staple materials for long-term applications in many industrial sectors including gas, petroleum, petrochemicals, fertilizers, food processing, and pulp industries as well as power generating plants. They have found also widespread use for manufacturing of chemical installations including stationary pressure tanks and tanks for transport of liquid and compressed gases, pipelines of high diameter in water power plants, for manufacturing of ships for transport of chemicals and installations of drilling rigs, etc. Thick-section stainless steels are widely used in the components and structures for nuclear power plants.

For all applications of austenitic stainless steels, welding is of considerable importance since it is widely used in components' manufacturing. In comparison with ferritic steels, lower thermal conductivity and higher thermal expansion coefficient of austenitic stainless steels results in larger thermal distortions and internal stresses of the welded parts, which increase susceptibility of the weld to hot cracks.

Another possible welding problem of austenitic stainless steels is sensitization that occurs at 900-1400°F (482-760°C) during cooling after welding where chromium carbides form along the austenite grains and causes depletion of chromium from the grains resulting in decreasing the corrosion protective passive film.

In this concern, austenitic stainless steels poses distinct challenges when it is joined with gas tungsten arc welding (GTAW) due higher possibility of carbide precipitation and distortion in comparison with laser welding. In other words, joining austenitic stainless steels with

GTAW can be tricky, but with a laser, it can be done successfully. Previous studies of the weldability of stainless steels indicate that the basic condition for ensuring high quality of welded joints and reducing thermal distortions to minimum is reducing the heat input of welding that is ensured only by laser welding.

CO₂ laser beam welding with a continuous wave, which is widely used for stainless steels components, is a high energy density and low heat input process. The result of this is a small heat-affected zone (HAZ), which cools very rapidly with very little distortion, and a high depth-to-width ratio for the fusion zone.

The heat flow and the fluid flow in the weld pool can significantly influence the temperature gradients, the cooling rates and the solidification structure. In addition, the fluid flow and the convective heat transfer in the weld pool are known to control the penetration and shape of the fusion zone [1].

Generally, laser beam welding involves many variables; laser power, welding speed, defocusing distance and type of shielding gas, any of which may have an important effect on heat flow and fluid flow in the weld pool. This in turn will affect penetration depth, shape and final solidification structure of the fusion zone. Both the shape and microstructure of the fusion zone will considerably influence the properties of the weldment.

There are many reports [2-4] that deal with the shape and solidification structure of the fusion zone of laser beam welds in relation to different laser parameters. However, the effect of all influencing factors of laser welding has up to now not been extensively researched. More work is required for understanding the combined effect of laser parameters on the shape and microstructure of the fusion zone.

The present investigation is concerned with laser power, welding speed, defocusing distance and type of shielding gas and their effects on the fusion zone shape and final solidification structure of some austenitic stainless steels.

1.2. Experimental procedure

Three types of commercial austenitic stainless steels, 304L, 316L and 347, were used. Their chemical composition and mechanical properties are given in Table 1. The thickness of both 304L and 316L steels was 3 mm while that of 347 steel was 5 mm.

Base metal										TS	YS	Elong.
	Cr	Ni	Mn	C	Si	P	S	Mo	Cb	(MPa)	(MPa)	(%)
304L	18.2	8.5	1.7	0.025	0.35	0.03	0.01	0.20	0.01	235	309	32
316L	16.5	10.5	1.9	0.02	0.38	0.02	0.01	2.27	0.01	556	317	31
347	17.7	9.7	1.8	0.04	0.40	0.03	0.01	0.25	0.35	577	345	39

Table 1. Chemical composition (wt%) and mechanical properties of the used base metals

Both bead-on-plate and autogenous butt weld joints were made using a carbon dioxide laser capable of producing a maximum output of 5 kW in the continuous wave mode. Bead-on-plate was made on plates with 3 mm thickness while autogenous butt weld joints were made on plates with 3 and 5 mm thickness. Specimens with machined surfaces were prepared as square butt joints with dimensions of 125x150 mm and were held firmly using fixture to prevent distortion

The laser beam welding parameters investigated are summarized in Table 2. Combinations of laser power (P) of 2-5 kW and speed (S) of 0.5-3 m/min resulted in nominal heat in nominal heat inputs (HI) ranging from 0.04 to 0.48 kJ/mm. The defocusing distance (D_d) was in the range of -5 to 3 mm. Shielding was made using either argon or helium gas.

Weld joint/ Thickness (mm)	P (kW)	S (m/min)	HI (kJ/mm)	D_d (mm)	Shielding gas/ Flow rate(l/min)
BOP / 3	2	3	0.04	0.0, -1.0, -2.0,-3.0, -4.0,-5.0, +1.0,+2.0, +3.0	argon / 15
Butt / 3	3	0.5, 1, 2, 3	0.36, 0.18, 0.09, 0.06	0.0	argon / 15
Butt / 3	4	0.5, 1, 2, 3	0.48, 0.24, 0.12, 0.08	0.0	argon / 15
Butt / 3	4	3	0.08	0.0, -0.2, -0.4, -0.6	argon/15
Butt / 3	4	3	0.08	0.0, -0.2	helium / 15
Butt / 5	5	1, 2, 3	0.3, 0.15, 0.1	0.0, -0.2, -0.4	argon/15

Table 2. Welding parameters used

After welding, the specimens were visually inspected then, sectioned transverse to the welding direction. The shape and microstructure of the fusion zone were examined using optical microscopy. Micro-compositional analysis of welds was performed using an electron probe micro-analyzer (EPMA) at an accelerating voltage of 25 kV.

Mechanical tests including tensile, bending and hardness measurements of butt welds having complete penetration were performed according to relevant standards. The data reported are the average of three individual results.

1.3. Results and discussion

1.3.1. Macrostructure of laser beam welds

1.3.1.1. Effect of laser power

The effect of heat input as a function of laser power, $HI = P/S$, was clarified using type 304L and type 316L steels. Both welding speed and defocusing distance were kept constant at 3 m/min and zero respectively.

The penetration depth increased sharply with increasing laser power from 2 to 3 kW as shown in Figure 1. Complete penetration for the 3mm base metal was obtained at laser power equal to or greater than 4 kW. Figure 9 shows an example of a cross section of type 304L steel butt weld made using laser power of 4 kW. The weld bead showed a characteristic of laser welding with dept / width ratio close to 3. No welding cracks or porosity were found in any of the welds, this may be partly due to the good crack resistance of the base metal and the welding conditions provided.

The results indicated also that the development of the weld pool is essentially symmetrical about the axis of the laser beam. Yet, lack of symmetry at the root side was observed particularly at higher welding speed (Figure 2) suggesting an unsteady fluid flow in the weld pool. This is due to the presence of two strong and opposing forces, namely, the electromagnetic and the surface tension gradient forces. At these locations, the electromagnetic force may have overcome the surface tension force, thereby, influencing convective heat transfer. As a result, any local perturbation in the weld pool can cause the flow field to change dramatically, resulting in the observed lack of local symmetry.

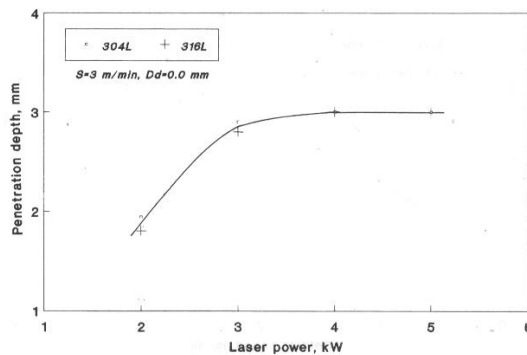


Figure 1. Effect of laser power on penetration depth of types 304L and 316L stainless steel welds.

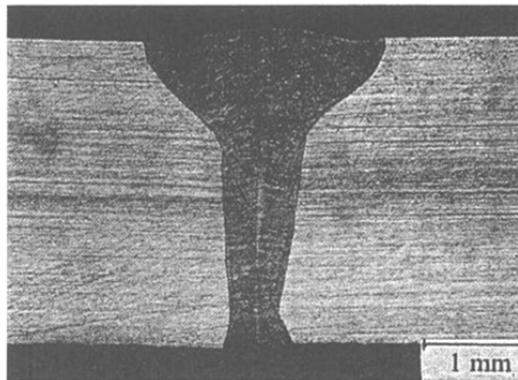


Figure 2. A cross section of type 304L stainless steel weld made using $P=4\text{kW}$, $S=3\text{m/min}$, $D_d=0.0\text{mm}$.

Laser power has a less influence on both weld profile and HAZ width in comparison with its effect on penetration depth. This is in agreement with other researchers work where they pointed out that changing laser power between 3 and 5 kW [5] did not result in any significant change in the size or shape of the weld.

It is expected that similar results concerning the dependence of penetration depth on laser power could be obtained in the case of type 347 steel due to similarity in both physical and mechanical properties. The optimum power for complete penetration with acceptable weld profile for the 5mm base metal thickness was 5 kW at a welding speed of 2 m/min as shown in Figure 3.

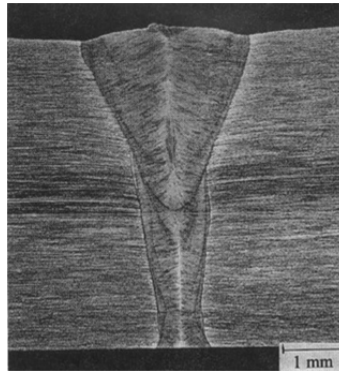


Figure 3. Optimum weld profile of type 347 stainless steel made using $P=5\text{kW}$, $S=2\text{m/min}$, $D_d=-0.4\text{mm}$.

1.3.1.2. Effect of welding speed

The effect of welding speed was investigated at the optimum laser power (4 kW) and zero defocusing distance. Figure 4 shows the relationship between welding speed and fusion zone depth/width ratio for both 304L and 316L base metals. The depth/width ratio increased sharply from 2.1 to 4.1 with the increase in welding speed from 0.5 to 3 m/min.

The dependence of depth/width ratio on welding speed was confirmed at a different laser power (3 kW). A lower welding speed resulted in a considerable increase in the fusion zone size and consequently a decrease in depth/width ratio leading to unacceptable weld profile. Complete penetration with relatively acceptable fusion zone size for the 3mm base metal thickness was obtained at welding speed of 2 m/min as shown in Figure 5. The fusion zone is symmetrical about the axis of the laser beam.

The above results have shown that the laser power and welding speed should be optimized in order to minimize heat input, then a satisfactory weld with reliable quality could be obtained. This reflects one of the most notable features of laser welding compared with other welding processes, which is small heat input.

Turning to the macrographs shown in Figures 5 and 8, complete penetration with relatively acceptable fusion zone profile could be obtained using either 4 kW, 3 m/min (Figure 5) or 3

kW, 2 m/min (Figure 8). However, 4 kW, 3 m/min resulted in a smaller fusion zone size with less inflection at its interface in addition to the high welding speed in this case.

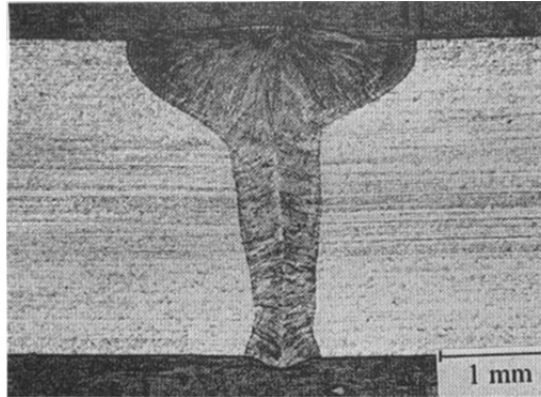


Figure 4. Influence of welding speed on weld depth/width ratio of types 304L and 316L stainless steels.

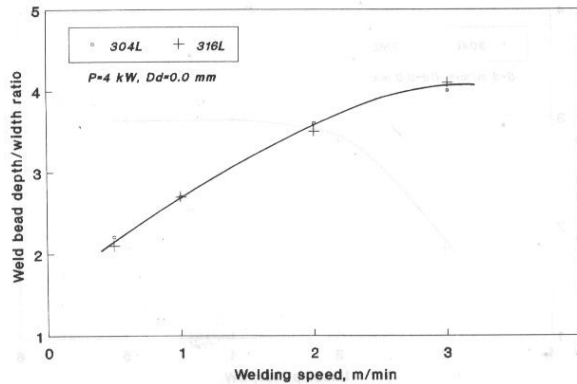


Figure 5. A cross section of type 304L stainless steel weld made using $P=3kW$, $S=2m/min$, $D_d=0.0mm$.

At high welding speed, attenuation of beam energy by plasma is less significant. This results in relatively more exposure of the laser beam on the sample surface. Consequently, the depth/width ratio would be increased and the fusion zone size would be minimized.

1.3.1.3. Effect of defocusing distance

Defocusing distance, focus position, is the distance between specimen surface and the optical focal point. In order to study its effect on both penetration depth and weld profile, bead-on-plate was made with changing defocusing distance between -5 and 3 mm. Low laser power (2 kW) and high welding speed (3 m/min) were selected to obtain incomplete penetration.

Examples of weld cross sections of type 304L steel made using different defocusing distances are shown in Figure 6. No cracking or porosity was observed in all welds. The penetration depth is considerably decreased with changing defocusing distance from zero (Figure 6-b) to either minus (Figure 6-a) or plus (Figure 6-c) values as a result of decreasing laser beam density.

The relationship between defocusing distance and penetration depth of both 304L and 316L steels is summarized in Figure 7. The penetration depth decreased from 1.9 to 1.6 mm on changing the defocusing distance from zero to either -1 or 1mm. Then, the penetration depth decreased sharply to about 0.2 mm on changing the defocusing distance to more negative (-5 mm) or positive (4 mm) values.

These results indicated that the most effective range of defocusing distance to get maximum penetration with acceptable weld profile lies between zero and -1 mm. In order to obtain the optimum value, complete penetration butt welds were made using previously obtained optimum laser power (4 kW) and optimum welding speed (3 m/min). The most acceptable weld profile was obtained at defocusing distance of -0.2 mm for 3 mm thickness where weld bead depth/width ratio is maximum and fusion zone size is minimum with a slight taper configuration as shown in Figure 8. However, the optimum defocusing distance to attain acceptable weld profile for 5 mm thickness was -0.4 mm (Figure 3). The smooth curved and symmetrical fusion zone interface shown in Figures 3 and 8 suggests that the driving forces for fluid flow in the weld pool, buoyancy and surface tension gradient, augment each other, resulting in a coherent flow field.

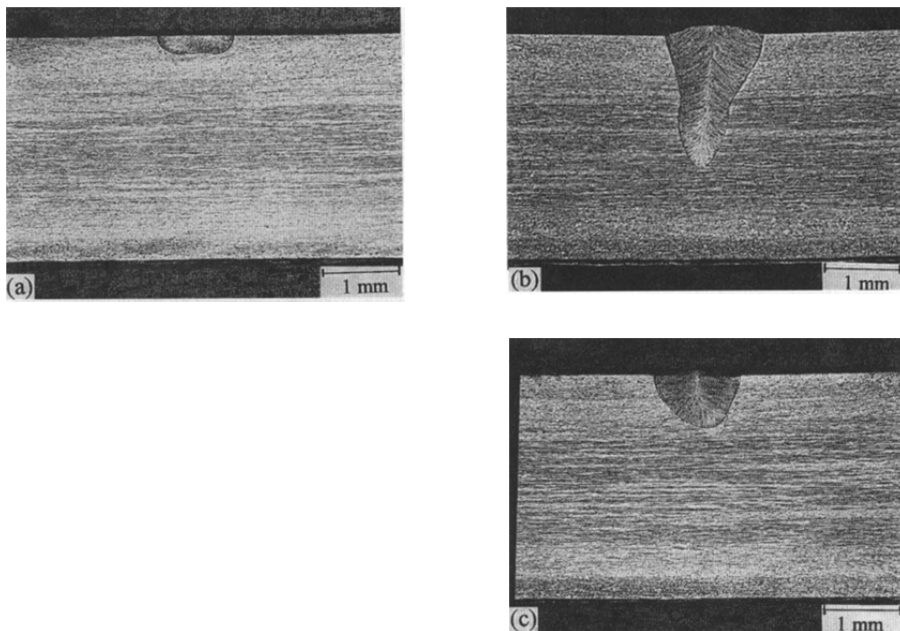


Figure 6. Cross section of type 304L stainless steel welds made using $P=2\text{kW}$, $S=3\text{m/min}$ with different defocusing distances. (a) $D_d=-3.0\text{mm}$, (b) $D_d=0.0\text{mm}$, (c) $D_d=+2.0\text{mm}$.

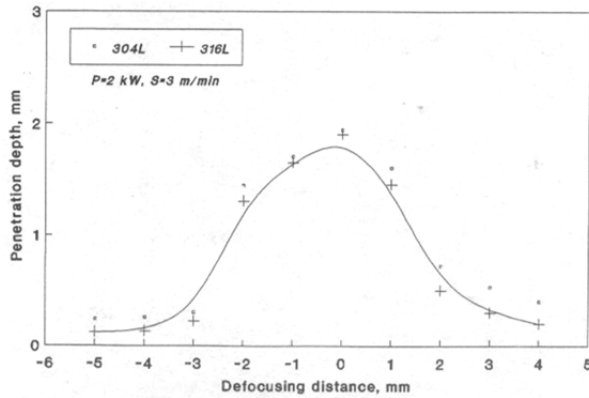


Figure 7. Relationship between defocusing distance and penetration depth of types 304L and 316L stainless steels.

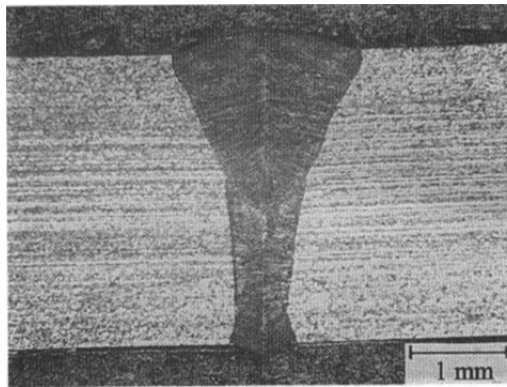


Figure 8. A cross section of type 304L stainless steel weld made using $P=4\text{kW}$, $S=3\text{m/min}$, $D_a=-0.2\text{mm}$.

1.3.1.4. Effect of type of shielding gas

In all previous experiments, argon was used as a shielding gas. For comparison, argon was replaced by helium while other laser parameters were kept constant. Weld profile is remarkably improved where fusion zone interfaces are almost parallel to each other as shown in Figure 9.

In general, when the laser beam interacts with the workpiece, a hole is drilled through the thickness of the material. This hole or cavity is filled with a plasma and surrounded by molten metal, thus, the high energy density of the focused beam could be lost easily. This plasma effect was reduced as a result of the higher ionization potential of helium then, the weld profile was improved.

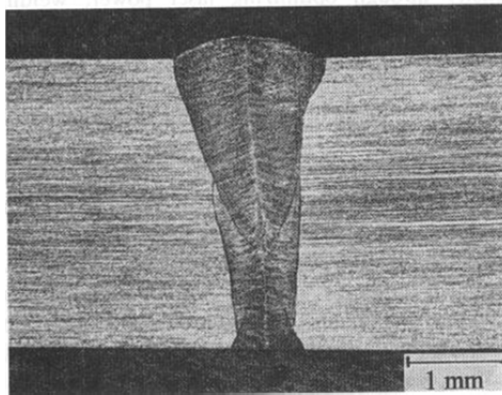


Figure 9. Optimum weld profile of type 304L stainless steel obtained using helium as a shielding gas instead of argon with the same laser parameters as of Figure 15.

1.3.2. Microstructure of laser beam welds

Microstructures of type 304L steel weld metals made using two different welding speeds, 1 and 3 m/min, with same laser power, 4 kW, are shown in Figure 10. The noticeable feature is the highly directional nature of the microstructure around the axis of the laser beam. This is due to solidification of the weld metal at high cooling rate compared to that of conventional GTA welding [6]. It can also be noticed that the higher the welding speed, the finer the dendritic structure (Figure 10-b). This is attributed to an increase in both solidification and cooling rates due to low heat input resulted from high welding speed.

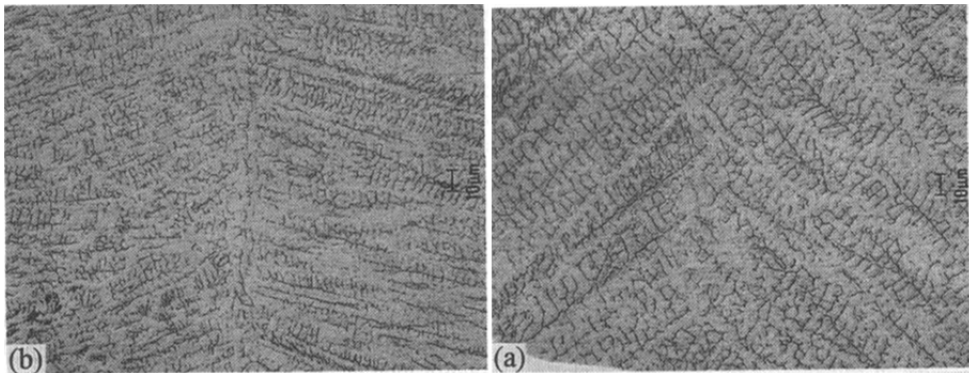


Figure 10. Optical micrographs of weld metals of type 304L stainless steel made using $P=4\text{kW}$ with different welding speeds. (a) $S=1\text{m/min}$, (b) $S=3\text{m/min}$.

Concerning the effect of laser power, the higher the laser power, the coarser is the dendritic structure due to decreasing cooling rate. However, the effect of laser power was relatively less than that of welding speed.

The microstructures of all laser beam welds were always austenite with a few percent of delta-ferrite at the dendritic boundaries. The existence of delta-ferrite was confirmed by both colour etching and electron probe microanalysis (EPMA). The amount of delta-ferrite was estimated using Cr and Ni equivalents [7] of weld metal chemical composition. Based on the Schaeffler diagram, about 2 or 3 vol% ferrite was expected to exist in the austenitic matrix. It should be reported that no weld solidification cracking was observed in any of the welds evaluated.

Under normal weld solidification conditions, the solidification mode in austenitic stainless steels is primarily a function of composition, with a shift from primary ferrite to primary austenite accomplished by reducing the Cr_{eq}/Ni_{eq} ratio below 1.5 [8].

However, Suutala [2], Vitek and David [9], and Lippold [10] have illustrated that the boundary between primary austenite and primary ferrite solidification is not just a function of weld metal composition, but is a function of the growth rate.

The subject results are consistent with the modified Suutala diagram [11] for predicting microstructure and cracking of austenitic stainless steels under rapid weld solidification conditions encountered during laser welding. All the steels tested exhibited a Cr_{eq}/Ni_{eq} ratio greater than 1.7, the value suggested by the modified Suutala diagram as the demarcation of crack susceptibility. Consequently, it can be deduced that all welds concerned in this investigation were solidified as mixed mode of primary and massive austenite. The transition in primary solidification from ferrite to austenite could be attributed to weld pool undercooling as a result of extremely high solidification growth rate [12-15].

The results are also in agreement with Lippold [12] work where he pointed out that cracking in austenitic stainless steel welds is avoided as the proportion of primary ferrite in the mixed mode solidification increases.

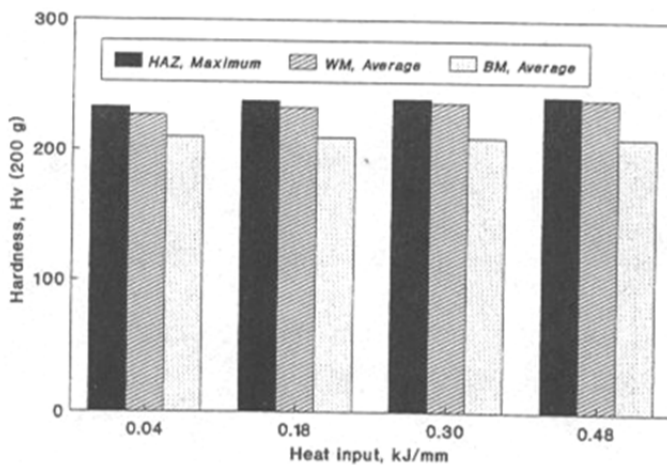


Figure 11. Hardness profiles of base metal, HAZ and weld metal of type 304L stainless steel as a function of heat input.

1.3.3. Mechanical properties

Tensile test results of all laser butt welds with complete penetration showed that failure has taken place in the base metal. The bending test at room temperature showed no cracks in all joints as a result of high ductility.

Typical hardness profiles of the base metal, HAZ and weld metal of type 304L steel as a function of heat input are shown in Figure 11. No significant difference between hardness of the base metal and that of weld metal or HAZ was obtained. Hardness of both weld metal and HAZ was slightly higher than that of the base metal regardless of heat input. These results were also valid for the other two base metals. This is expected because mechanical properties of steel, in general, are based on its microstructure.

2. Laser beam welding of austenitic stainless steel in lap joints with zn-coated carbon steel

2.1. Introduction

Because of its excellent corrosion resistance, austenitic stainless steel has found widespread use in the paper making equipment includes pressure vessels, storage tanks, piping, hopper, bins, chutes and structural components. For all of these applications, attachments such as access platforms, catwalks, stiffeners, column supports, stairways, washers and pipe hangers are welded to the outside surfaces of the equipment. Zn-coated carbon steel is often specified for these attachments due to its good corrosion resistance and lower cost. Lap weld joints of Zn-coated steel to austenitic stainless steel are used also in other fields such as plate-tube joints, radiators, washing machines as well as some components in the aeronautic field [16].

Although welding of Zn-coated steel to austenitic stainless steel is a common practice, it presents serious problems concerning with weld zone porosity and LME cracking of austenitic stainless steel base metal due to zinc vaporization. These welding problems have been studied in the case of conventional metal arc welding processes [17]. It is reported that joining gaps between the sheets to be lap welded are adjusted in order to enable the degasification of zinc vapour.

On the other hand, laser butt and lap weld joints of both similar and dissimilar materials are being used in many industrial applications. The fraction of laser welding in all industrial applications is about 15-25% which varies from country to country [18-20]. The most notable features of laser welding compared with other conventional welding processes are the high weld quality and high welding speed. This together with its low heat input makes laser a most hopeful candidate for thin sheet metal welding.

However, similar problems as in conventional metal-arc-welding of Zn-coated steel to austenitic stainless steel are expected also in case of laser beam welding. Therefore, more work is required for understanding these problems and the factors affecting them.

This investigation has been concerned with CO₂ laser welding of austenitic stainless steel in lap joints with Zn-coated carbon steel. The focus was made on weld joint quality in terms of weld profile, porosity in the weld zone and liquid metal embrittlement (LME) cracking of the austenitic stainless steel base metal. The influence of type and flow rate of shielding gas, gap between the sheets and zinc removal prior to welding was clarified. Quality of weld joints was evaluated as a function of weld zone shape, porosity and LME cracking of austenitic stainless steel base metal.

2.2. Experimental procedure

Commercial types of ASTM A36, 0.7 mm thick carbon steel sheet coated with 10 μm zinc on both sides and ASTM A240 Type 304L, 1mm thick stainless steel sheet were used for dissimilar lap joints. Table 3 shows their chemical composition and mechanical properties.

Base Metal	C	Mn	Si	S	P	Cr	Ni	YS (N/mm ²)	UTS (N/mm ²)	Elong (%)
Zn-coated	0.04	0.35	0.26	0.01	0.02	-	-	245	377	27
304L	0.04	1.70	0.35	0.01	0.03	18.2	8.5	359	558	32

Table 3. Chemical composition (wt%) and mechanical properties of used base metals

Pairs of these dissimilar steel sheets of 150x150 mm were welded with an overlap of 50 mm and with weld bead at the middle of the overlap. Zn-coated steel sheet was upper-most and the joint was clamped 15 mm on both sides of the weld line along its entire length. Configurations of laser lap weld specimen are shown in Figure 12. All specimens were ultrasonically cleaned to remove dirt and oil prior to welding.

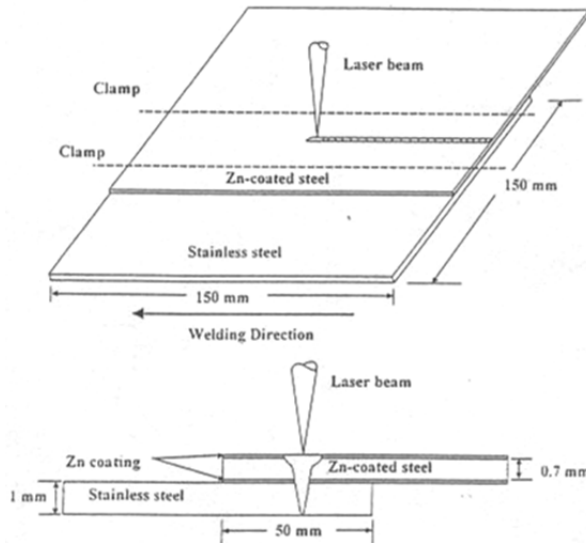


Figure 12. Configuration of the used laser lap weld specimen.

Welding was performed using CO₂ laser with a maximum output of 3 kW operated in multi-mode. The beam was focused using a parabolic mirror with 150 mm focal length. Laser beam welding parameters used are summarized in Table 4. Optimizing laser power, welding speed and focal point position is of considerable importance for the weld quality in terms of fusion zone size and profile. In order to clarify the influence of shielding gas, gap between the sheets and pre-weld zinc removal on weld quality, laser power, welding speed, and defocusing distance (focal point position) were optimized and kept constant at 2.5 kW, 3 m/min, and 0.1 mm below specimen surface respectively. Shielding was done using argon or helium with flow rate of 15–30 l/min. Prescribed gap ranging from 0.025 to 0.3 mm was introduced between the sheets along the clamped areas of the welding fixture. Pre-weld zinc removal from the weld area was done by grinding.

P (KW)	S (m/min)	Dd (mm)	Shielding gas	Gap between Sheets (mm)	Zinc removal prior to Welding
			Type Flow rate (l/min)		
2.5	3	-0.1	Argon 15 ~ 30	No	No
2.5	3	-0.1	Helium 15 ~ 30	No	No
2.5	3	-0.1	Argon 15	0.025 ~ 0.3	No
2.5	3	-0.1	Helium 15	0.025 ~ 0.3	No
2.5	3	-0.1	Argon 15	No	Yes
2.5	3	-0.1	Helium 15	No	Yes

Table 4. Laser welding parameters

P: Laser power, S: Welding speed, Dd: Defocusing distance

Working distance: 10 mm at Dd = 0.0 mm, Nozzle diameter: 4mm

After welding, the specimens were subjected to non-destructive testing including visual and dye penetrant test methods then, sectioned transverse to the welding direction. Three sections of each seam weld were prepared for metallographic examinations using standard technique. Quality of the dissimilar lap joints was evaluated as a function of weld profile, porosity level in fusion zone, LME cracking in austenitic stainless steel base metal. Tensile shear test was carried out for all laser lap welded joints and the data reported are the average of three individual results.

2.3. Results and discussion

2.3.1. Effect of shielding gas

Examples of macrographs laser welds produced using argon and helium as a shielding gas with a flow rate of 15 l/min are shown in Figure 13-a and b respectively. It is clear that non-uniform weld beads with large pores were obtained in both cases. However, wide seam width combined with an increase of the frequency of pores was obtained with argon (Figure 13-a). In other words, the number of pores was much less with using helium as a shielding

gas (Figure 13-b). This means that shielding gas type is an essential factor to improve weld quality since it is used to protect the molten metal against oxidation and blow the plasma away from the beam path.

Generally, when welding zinc coated steel with stainless steel there is a very strong plasma formation due to the low boiling point of zinc (906 °C) and its high vapour pressure, which is about eight orders of magnitude greater than that of Fe [21]. The high vapourization of zinc increases the pressure of the vapour, which is transformed to plasma in the laser beam, to expand further into the free space above the metal surface. This will affect the absorption and fluctuation of the plasma and in practice this is shown as increased splattering and porosity in the weld. This plasma effect was reduced as a result of the higher ionization potential of helium then, weld quality was improved.

With this relatively low flow rate, the process seemed to change swiftly between deep penetration welds and vapour assisted welds. This may be explained by the presence of zinc, which makes the process unstable due to plasma fluctuation as has reported in prior investigation [22]. Consequently, optimized shielding gas flow rate makes the difference between a good or poor weld.

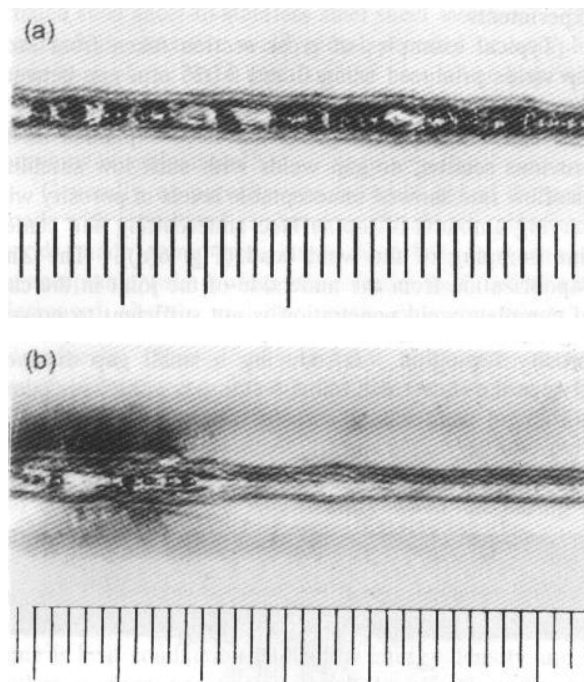


Figure 13. Macrographs of laser welds produced using (a) argon and (b) helium as a shielding gas with 15 l/min flow rate.

With increasing shielding gas flow rate above 15 l/min, the number of pores in seam welds was decreased and weld pool penetration was increased. Examples of macrographs of laser

welds produced using higher flow rate; 30 l/min of argon and helium as a shielding gas are shown in Figure 14. It is obvious that smooth and homogeneous seam welds free from pores were obtained in both cases. The increase in penetration depth obtained in this case is consistent with the expected effect of increased plasma suppression with increased flow rate, i.e. more of the beam was allowed to reach the work-piece. However, there appeared to be a trade-off between plasma suppression effects and weld pool stability with increase shielding gas flow rate.

Turning to shielding gas type, it remarkably affected weld zone profile. Low magnification stereoscopic photographs of cross sections taken from laser welds of Figure 14-a and b are shown in Figure 15-a and b respectively. The use of helium has resulted in complete penetration with higher depth/width ratio and a slight taper configuration which means minimum fusion zone size (Figure 15-b) in comparison with that obtained using argon (Figure 15-a). In other words, helium has a more favorable effect on the molten metal than argon at optimized flow rates, which make the welds more homogeneous and free from pores. A flow rate of 22 l/min for helium was found to be satisfactory in comparison with 30 l/min for argon. These results do conform with prior results of other investigators where they have shown that the weld defects, due to the vapourization of zinc, can be reduced by optimizing shielding gas parameters [23-25].

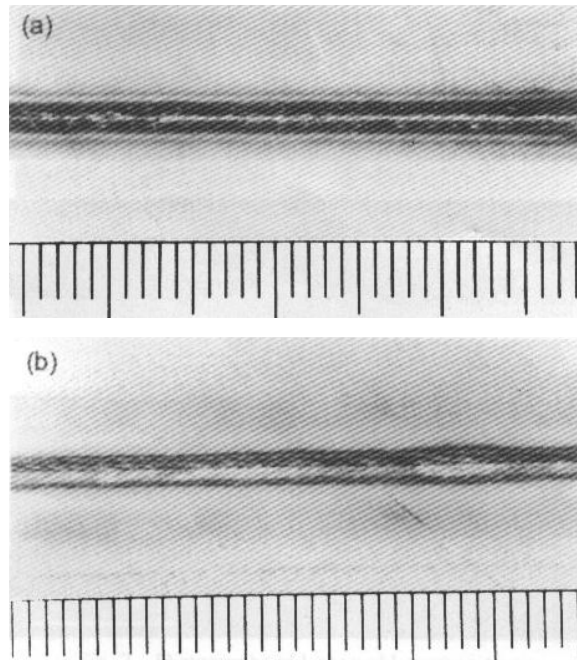


Figure 14. Macrographs of laser welds made using (a) argon and (b) helium as a shielding gas with 30 l/min flow rate.

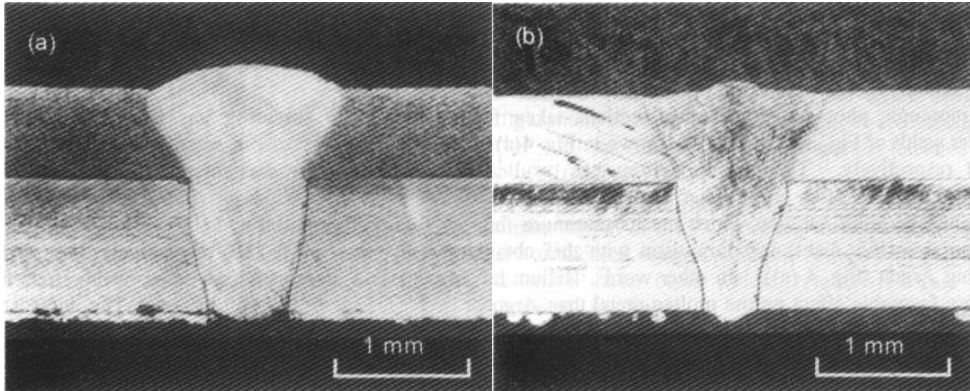


Figure 15. Low magnification stereoscopic photographs of cross sections taken from laser welds of Figure 14

On the other hand, it is found that both type and flow rate of shielding gas have no effect on LME cracking of austenitic stainless steel. Figure 16 shows a typical example of optical micrograph of a cross section taken from lap weld produced using helium with its optimum flow rate; 30 l/min. In spite of obtaining homogeneous, sound, complete penetration and acceptable weld profile with such high flow rate, the noticeable feature is the formation of severe cracking at the stainless steel base metal. These cracking were extended for a distance of about 0.7 mm around both sides of lap weld joints and propagated on grain boundaries. This type of cracking is typical LME cracking of the austenitic stainless steel which occurs above 750°C when it is exposed to molten zinc and tensile stresses. Molten zinc can be produced by the heat of welding and tensile stresses can be generated from the heating and cooling cycles during welding. This cracking type is characterized by extremely rapid crack propagation perpendicular to the applied stress [26]. It should be mentioned also that similar results were obtained for lap weld joints produced using argon gas shielding.

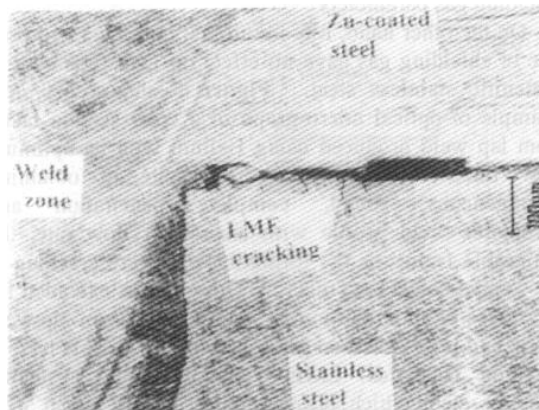


Figure 16. Typical example of optical micrograph of a cross section taken from laser lap weld produced using helium as a shielding gas with its optimum flow rate; 30 l/min.

2.3.2. Effect of gap between the sheets

In the above section, lap welds were made with a good contact, i.e. without a gap between the sheets. In order to clarify its effect on weld joint quality, prescript gap was introduced between the sheets and shielding was done using either argon or helium with its lower flow rate (15 l/min) which resulted in weld porosity in the previous experiments.

Typical examples of cross sections taken from laser lap welds produced using 0.0 and 0.025 mm gap between the sheets in case of helium shielding are shown in Figure 17-a and b respectively. As has been explained in the previous section, no-gap welds with such low shielding gas flow rate showed unacceptable levels of porosity with varying amounts of top surface undercutting and center-line humping of the weld bead (Figure 17-a). The zinc vapourization from the underside of the joint in the case of complete weld penetration is not sufficient to prevent porosity formation. Introducing a small gap distance between the sheets with same welding conditions resulted in a sound weld where porosity was not observed (Figure 17-b). Also, weld profile was remarkably improved where a smooth curved and symmetrical fusion zone interface was obtained.

In other words, acceptable quality for laser lap welds concerning soundness and profile could not be obtained with low shielding gas flow rate and without a gap between the sheets. Once the heat input was sufficient to permit melting through the top sheet, there was explosive ejection of molten weld metal due to vapourization of the zinc layers at the Zn-coated steel sheet-to-stainless steel sheet interface. This resulted in extensive weld metal porosity or complete expulsion of the weld metal in the case of no-gap weld leading to undercutting the top steel sheet, as shown in Figure 17-a. This is in a good agreement with results of previous investigations [27, 28].

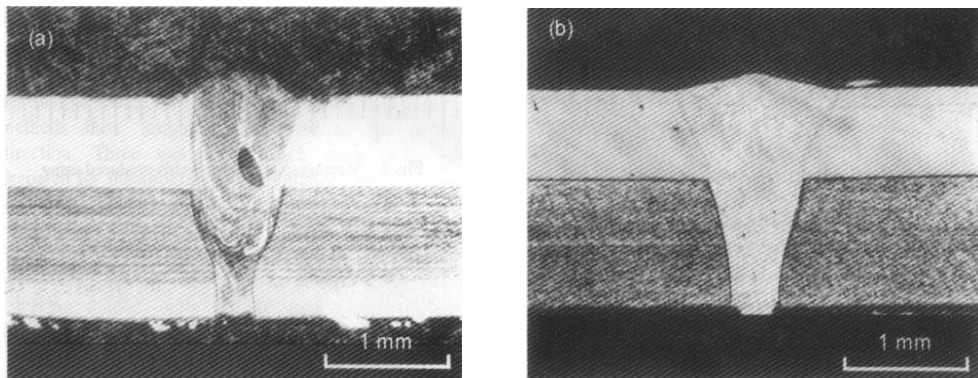


Figure 17. Typical examples of cross sections taken from laser lap welds produced using 15 l/min helium and different gap distances. (a) Gap: 0.0mm, (b) Gap: 0.025mm.

Generally, no porosity was found in any of the welds made with introducing gap between the sheets. However, welds made by gap larger than 0.05 mm showed unacceptable weld profile where weld depth /width ratio decreases sharply and the weld geometry begins to

deteriorate. Photographs of laser weld cross sections produced using 0.1 and 0.3 mm gaps are shown in Figure 18-a and b respectively. A gap distance of 0.1 mm gave a concave top surface, with a relatively low depth/ width ratio (Figure 18-a). The tendency of the molten pool to collapse increased significantly with increasing the gap to higher value. This resulted in remarkable undercut in the welds and excessive drop-through of the weld metal into the gap (Figure 18-b).

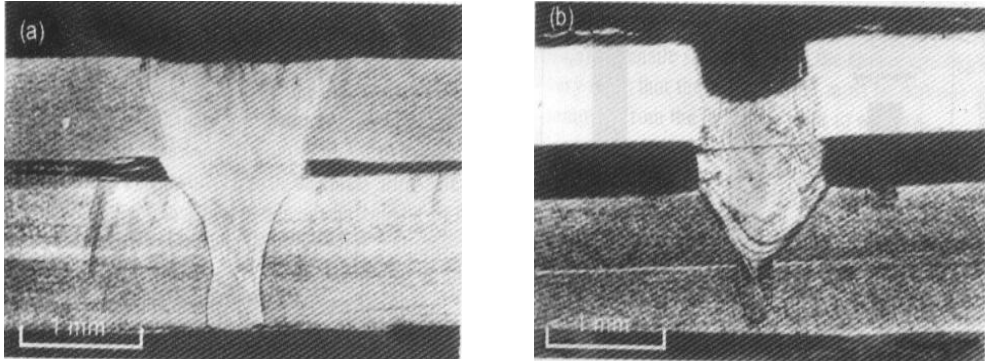


Figure 18. Photographs of cross sections taken from laser lap welds produced using (a) 0.1mm and (b) 0.3mm gap between the sheets.

Generally, there are two mechanisms in laser welding, one is heat conduction under low energy density and the other is deep penetration (keyhole effect) under high energy density. In these experiments, the laser power density when laser beam touched the surface of the top sheet was high enough to melt the metal rapidly and formed the deep penetration. The power density greatly decreased when approached the bottom plate particularly in case of large air gap between both plates that obstructed heat transfer. At this time, the heat transfer was mainly by means of conduction, which could be proved by the weld shape and penetration depth. Based on the weld shape, the fusion lines at both sides of welds were approximately parallel under deep penetration welding conditions, while the fusion line was half circle under heat conduction welding. Consequently, under such experimental conditions, the welding mechanism of lap joints was combination of deep penetration and heat conduction.

Although introducing a small gap between these dissimilar material sheets has resulted in avoiding porosity in weld zone, it has no effect on zinc induced LME cracking in austenitic stainless steel base metal. Figure 19 shows typical example of an optical micrograph of a cross section taken from lap welded joint produced using helium with 15 l/min flow rate and 0.05 mm gap. It is noticed that a sound and uniform weld seam was obtained. However, the most important notice is the formation of LME cracking on grain boundaries of stainless steel base metal as has been explained in the previous section. Cracking were extended for a distance of about 0.5 mm around both sides of lap weld joints. These results of laser welding do conform to other research work concerned with arc welding processes [17].

Generally, the influence of gap between the sheets on weld geometry and quality can be explained using schematic illustrations shown in Figure 20. Since the zinc vapour has no enough access escape route with zero gap, both pores weld with unacceptable profile and LME cracking in stainless steel will be obtained (Figure 20-a). Introducing a small gap between the sheets give the zinc vapour an alternative escape route during welding then, sound and acceptable weld joint will be produced. It should be mentioned that this gap should be limited to an optimum value as has been reported by other researchers [22]. However, the problem is still concerned with LME cracking in austenitic stainless steel base metal around both sides of the joint since it can not be prevented by these measures (Figure 20-b).

2.3.3. Effect of zinc removal prior to welding

The results of the previous two sections confirmed that LME cracking of austenitic stainless steel in laser lap joint with Zn-coated steel is attributed mainly to molten zinc resulted from welding heat. Consequently, this section is concerned with studying this type of cracking as a function of zinc removal prior to welding. In this respect, the effect of both one and two sides grinding of the weld area of Zn-coated sheets was clarified using welding parameters previously resulted in weld zone porosity.

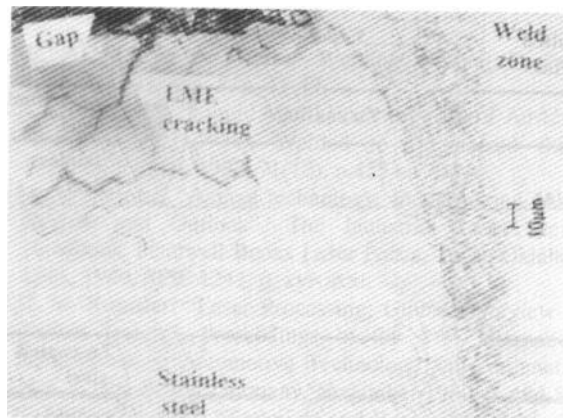


Figure 19. Typical example of optical micrograph of a cross section of lap welded joint produced using 0.05mm gap and 15 l/min helium.

Photographs of laser welds produced without gap between the sheets and with 15 l/min of helium shielding after zinc removal by grinding of weld area from one and two sides are shown in Figure 21-a and b respectively. It can be noticed that removing zinc coating from only one side of Zn-coated sheet was not effective to obtain sound welds since porosity were observed in weld zone (Figure 21-a). In the case of two sides grinding before welding, molten zinc was avoided due to removing of zinc coating then, molten metal was not ejected and this in turn could result in a sound and uniform weld seam (Figure 21-b).

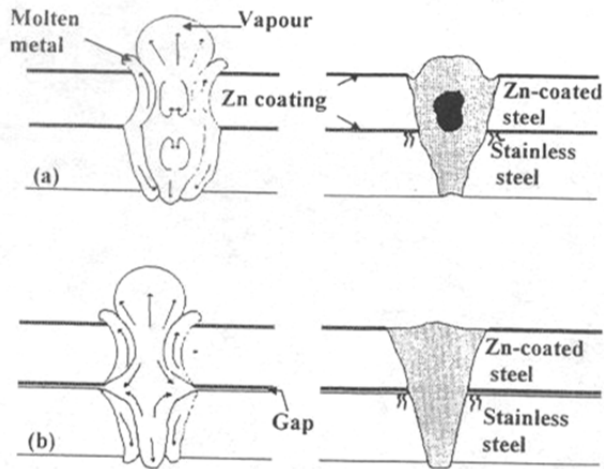


Figure 20. Schematic illustrations showing the effect of introducing a gap between the sheets being welded on weld zone profile, porosity and LME cracking.

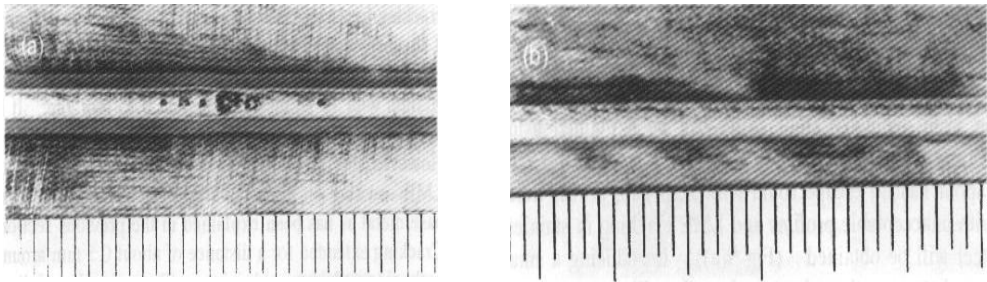


Figure 21. Photographs of laser welds produced using 15 l/min helium shielding and zero gap between the sheets after zinc removal from (a) one side and (b) two sides of the weld area of Zn-coated sheet.

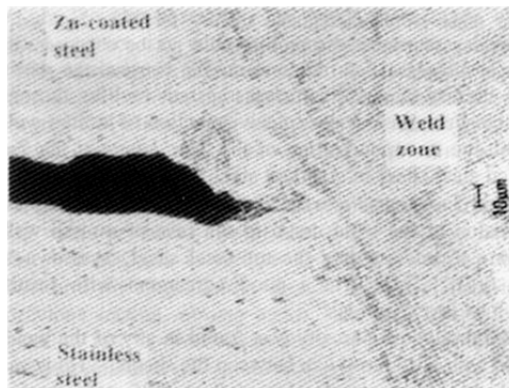


Figure 22. Effect of two sides grinding of weld area of Zinc-coated sheet on LME cracking susceptibility.

In addition, the most important finding in the case of two sides grinding is the disappearance of LME cracking in austenitic stainless steel as shown in Figure 22 that could not be attained in the above two sections. This is due to the complete removal of zinc coatings from the weld area prior to welding.

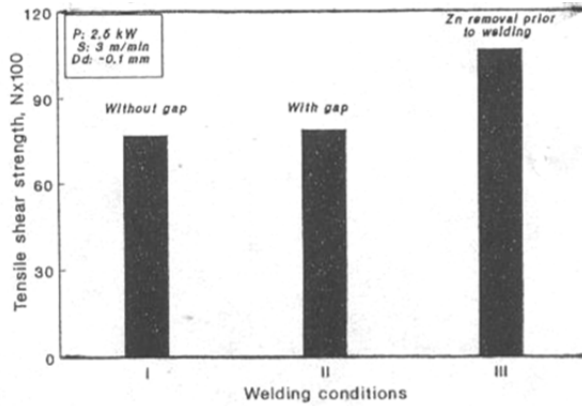


Figure 23. Tensile shear strength of laser lap welded joints as a function of welding conditions used. Welding conditions I, II and III are the optimum conditions used in section 3.3.1, 3.3.2 and 3.3.3, respectively.

Results of tensile shear test of laser lap joints as a function of welding conditions used are shown in Figure 23. Tensile shear strength of joints produced with zinc removal from both sides prior to welding was considerably higher than that of all other joints produced with and without gap regardless of shielding gas type and flow rate. This is attributed to the absence of LME cracking in case of two sides grinding.

Recently, serious industrial incidents of zinc-induced LME cracking in austenitic stainless steel have been reported [29, 30]. The potential for cracking during field welding is certainly greater than the cracking potential in these test specimens. This is due to higher tensile stresses in the case of field welding. Therefore, the removal of galvanized zinc coating prior to welding should be done properly to avoid contamination of austenitic stainless steel with any molten zinc during welding.

3. Conclusion

For CO₂ laser butt welding of similar butt joints of austenitic stainless steels, the following conclusions can be drawn.

- The penetration depth increased with the increase in laser power. However, laser power has a less effect on weld profile.
- Unlike laser power, welding speed has a pronounced effect on size and shape of the fusion zone. Increase in welding speed resulted in an increase in weld depth/width ratio and hence a decrease in the fusion zone size.

- Minimizing heat input and optimizing energy density through optimizing laser power, welding speed, and defocusing distance is of considerable importance for the weld quality in terms of fusion zone size and profile. Helium is more effective than argon as a shielding gas to obtain acceptable weld profile.
- Fusion zone composition was insensitive to change in heat input. However, increase in welding speed and/or decrease in laser power resulted in a finer solidification structure due to low heat input. A dominant austenitic structure with no solidification cracking was obtained for all welds. This could be associated with primary ferrite or mixed mode solidification based on Suutala and Lippold diagrams.
- Mechanical properties, tensile, hardness and bending at room temperature, were not significantly affected by heat input.

For CO₂ laser welding of austenitic stainless steel in lap joints with Zn-coated carbon steel, the following conclusions can be drawn.

- One way to produce sound and uniform laser lap welds of Zn-coated steel with austenitic stainless steel without gap between the sheets is the optimizing shielding conditions. This is of considerable importance for avoiding plasma or preventing porosity and obtaining full penetration without deteriorating the surface quality of the weld. Helium shielding produced noticeably deeper welds while argon exhibited the smoothest top surface. A flow rate of 22 l/min was found to be satisfactory in the case of helium in comparison with 30 l/min for argon.
- The other way to produce sound and homogeneous laser lap welds of these dissimilar materials is the introducing of a small gap (0.025-0.05 mm) between the sheets. Maintaining such gap between the sheets give the zinc vapour an alternative escape route. Smaller gap resulted in pores weld and random instabilities in the weld bead surface while larger gap showed unacceptable levels of drop-through of the weld metal between the sheets.
- To preclude both weld porosity and cracking of the stainless steel by molten zinc in making attachments of Zn-coated steel to 300 series austenitic stainless equipment which in turn will improve tensile shear strength, the choice seems to be very clear that is the zinc coating must be scrupulously removed from the joint area prior to welding.

Recently, new generation of lasers, such as fiber and disk lasers is receiving great attention due to its high efficiency, high power and high beam quality, which can produce an ultra-high peak power density of MW/mm² levels corresponding to a focused electron beam. These features and advantages of fiber and disc lasers are of considerable importance for deep penetration and high speed welding of austenitic stainless steels with thick sections, which are used in some critical applications such as nuclear power plants. It has been reported that such new generation of lasers is promising to be among the desirable heat sources for deep-penetration high speed welding of thick-section austenitic stainless steels [31-34].

In this regard, multi-passes narrow-gap welding of 50mm thick 316L plates has been investigated using 8 kW disk laser where the effect of welding conditions on the weld bead

geometry and welding defects was studied. It is reported that butt joint of 50 mm thick plates with narrow gap could be performed with eight-layers welding at laser power of 6 kW and welding speed of 0.4 m/min. In order to reduce the weld passes further, gas jet assisted laser welding was tried to weld thick 316L plates with a 10 kW fiber laser. The result showed that butt-joint welding of 40 mm plates without filler wire could be carried out at 0.3 m/min welding speed with no porosity or other welding defects. As for 50 mm thick plate, a good weld bead could be obtained with bead-on-plate welding from both sides at 0.2 m/min welding speed [35].

Author details

Abdel-Monem El-Batahgy

Manufacturing Technology Department, Central Metallurgical R & D Institute, Cairo, Egypt

Acknowledgement

The author would like to thank Laser-X Company Ltd., Japan for conducting CO₂ laser beam welding experiments.

4. References

- [1] Zacharia, T.; David, S. A.; Vitek, J. M. & Debroy, T. (1989). *Metall. Trans.* 20 A, 1125.
- [2] Suutala, N. (1983). *Metall. Trans.* 14 A, 191.
- [3] Klimpel, A. & Lisiecki, A. (2007). Laser Welding of Butt Joints of Austenitic Stainless Steel AISI 321. *Journal of Achievements in Materials and Manufacturing Engineering*, 25, 1.
- [4] Curcio, F.; et al. (2006). Welding of Different Materials by Diode Laser. *Journal of Materials Processing and Technology*, 175, 83-89.
- [5] Zacharia, T.; David, S. A.; Vitek, J. M. & Debroy, T. (1989). *Welding Journal*, 68, 12.
- [6] David, S. A.; Vitek, J. M. & Hebble, T. L. (1987). *Welding Journal*. 66, 289.
- [7] Schaeffler, A. L. (1949). *Metal Progr.* 56, 680.
- [8] Kujanpaa, V.; Suutala, N.; Takalo, T. & Moision, T. (1979). *Welding Research Int.* 9, 55.
- [9] Vitek, J. M. & David, S.A. (1982). *ASM Conference Proceedings, Trends in Welding Research in the United States* (ASM, Metals Park, Ohio,) pp.243-258.
- [10] Lippold, J. C. (1985). *Welding Journal*, 64, 127.
- [11] Kotecki, D. & Siewert, T. A. (1992). *Welding Journal* 71, 171.
- [12] Lippold, J. C. (1994), *Welding Journal*. 73, 129.
- [13] Dilthey, U. & Risch, A. (2001). Laser Welding of Stainless Steels and Stainless Low-Alloy Material Combinations, *Welding in the World*, 36, 67-71.
- [14] Elmer, J. W.; Alien, S. M. & Eagar, T. W. (1990). *Recent Trends in Science and Technology*, eds. David S. A. & Vitek J. M. (ASM International, Materials Park, Ohio, pp. 165-170.
- [15] Brooks, J. A. & Thompson, A. W. (1991). *Inst. Met. Reviews*, 36, 16.
- [16] Metzbower, E. A. (1991). Laser Welding, *Naval Engineers Journal*, Vol. 8, p. 41-49

- [17] Bruscato, R. M. (1992). Liquid Metal Embrittlement of Austenitic Stainless Steel When Welded to Galvanized Steel. *Welding Journal*, 71(12), p.455s-459s.
- [18] Belforte, D. A. (1990). Annual technology, Industry, and Market Review and Outlook. *The Industrial Laser Annual Handbook*, Pennwell Books Laser Focus, Tulsa, Oklahoma USA, SPIE 1241, p. xvi-xxxi.
- [19] Roessler, D. M. (1989). Laser Processing-Global Overview and Future Trends. *Proceedings of the 21st International Symposium on Automotive Technology and Automation*, Vol. 1, Wiesbaden, Germany, November 1989, p. 494-516.
- [20] Marinono, G.; et al. (1989). Technical and Economic Comparison of Laser Technology with The Conventional Technologies For Welding. *Proceedings of the 6th Int. Conf. on Laser in Manufacturing*, IFS, May 1989, ISBN 1-85423-047-6, p.105.
- [21] Beyer, E. & Gasser, E. (1987). Plasma Fluctuations in Laser Welding With CW CO₂-Lasers. *Proc. of The 6th Int. Cong. on Appl. Lasers and Electro-Optics, ICALEO '87*, San Diego, California, November 1987, p. 17-23.
- [22] Bagger, C.; Miyamoto, I.; Olsen, F. & Maruo, H. (1992). Process Behaviour During High Power CO₂ Laser Welding of Zinc Coated Steel. *Proceedings of LAMP*, Nagaoka, Japan, June 1992.
- [23] Akhter, R.; Steen, W. M. & Cruciani, D. (1988). Laser Welding of Zinc Coated Steel. *Proc. of The 5th Int. Cong. on Lasers in Manufacturing, LIM 5*, Stuttgart, West Germany, September 1988, p. 195-206.
- [24] Heyden, J.; Nilsson, K. & Magnusson, C. (1989). Laser Welding of Zinc Coated Steel, *Proc. of The 6th Int. Conf. on Lasers in Manufacturing, LIM 6*, May 1989, p. 93-104.
- [25] Graham, M. P.; Hirak, D. M.; Kerr, H. W. & Weckman, D. C. (1994). Nd-YAG Laser Welding of Coated Sheet Steel. *Journal of Laser Applications*, Vol. 6, p. 212-222.
- [26] Stoloff, N. S. (1977). Recent Development in Liquid Metal Embrittlement. *Proceedings Conference on Environment Sensitive Mechanical Behavior*, AIME, Chicago, 1977.
- [27] Nicholas, M. G. & Old, C. F. (1979). Review of Liquid Metal Embrittlement. *Journal of Material Science*, Vol. 14, p. 1-18.
- [28] Tzeng, Y. (2006). Gap-free lap welding of zinc-coated steel using pulsed CO₂ laser. *International Journal of Advanced Manufacturing and Technology*, 29, 287-295.
- [29] Johnson, J. M.; Berry, M. R. & Gutzeit, J. (1982). Zinc Embrittlement of Stainless Steel welds. *Proceedings of AIME Meeting on Embrittlement by Liquid and Solid Metals*, St. Louis, MO, 1982.
- [30] Shinohara, T. & Matsumoto, K. (1982). Welding Cracks of Zn-contaminated Stainless Steel Pipe. *Corrosion Science*, 22(8), p.723-737.
- [31] Thomy, C.; Seefeld, T. & Vollertsen, F. (2005). Proceedings of the Third International WLT-Conference on Lasers in Manufacturing, Munich, Germany, pp.27-32.
- [32] Verhaeghe, G. & Hilton, P. (2005). Proceedings of ICALEO, Miami, USA, pp.264-271.
- [33] Liu, S.; Kutsuna, M. & Xu, G. (2006). Proceedings of ICALEO, Scottsdale, USA, pp.562-568.
- [34] Reem, S. (2006). Proceedings of ICALEO, Scottsdale, USA, pp.586-594.
- [35] Zhang, X.; Ashida, E.; Tarasawa, S.; Anma, Y.; Okada, M.; Katayama, S. & Mizutani, M. (2011). Welding of thick stainless steel plates up to 50 mm with high brightness lasers. *Journal of Laser Applications*, 23, 022002 (2011); <http://dx.doi.org/10.2351/1.3567961>

Mitigating Zinc Vapor Induced Weld Defects in Laser Welding of Galvanized High-Strength Steel by Using Different Supplementary Means

Junjie Ma, Fanrong Kong, Blair Carlson and Radovan Kovacevic

Additional information is available at the end of the chapter

<http://dx.doi.org/10.5772/53562>

1. Introduction

Laser beam welding is a process where a focused laser beam is used as a moving heat source to join pieces of metal. The focused laser beam has a high power density that allows high speed welding, a deep penetration and a narrow heat affect zone (HAZ). There are two distinct types of laser welding modes: a conduction welding mode and a keyhole welding mode. When the laser beam intensity reaches 10^9 W/m², the molten pool starts to evaporate. As the laser intensity increases above 10^{10} W/m², the recoil pressure of the metal vapor pushes the molten metal downward and aside and a deep capillary called the “keyhole” is generated (Dawes, 1992). In the keyhole mode welding process, the keyhole maintains open due to the dynamic balance between the liquid metal surface tension and the pressure of the metal vapor and laser-induced plasma (Bakowski et al., 1984). When the laser radiates on the wall of the keyhole, the laser reflects multiple times on the wall of the keyhole. The laser beam energy is absorbed by Fresnel absorption directly by the walls of the keyhole, and a fraction of the laser energy is absorbed during each reflection (Dowden, 2009). Due to the multiple reflections of the laser beam, the keyhole behaves like an optical black body, making the keyhole mode welding process a highly energy efficient one (Steen, 2003).

Lap joint is the most common type of joint in the automotive assembly application; the traditional car body assembly method in a lap joint configuration uses resistance spot welding. However, the heavy and big spot guns limit the flexibility and accessibility of the welding process (Park et al., 2010); moreover, the localized joints are not particularly strong compared to those acquired by laser welding. On the other hand, the laser welding provides several benefits including a high scanning speed, high strength and low distortion of the joints, and the flexible implementation of the system for the automotive industry. Because of

these advantages, laser welding shows immense potential over the conventional resistance spot welding and has been widely used in the automotive industry in the fabrication of different auto bodies parts (Forrest et al., 2004).

In order to reduce the weight of the vehicles and improve fuel efficiency and safety, the development of lightweight, and high-strength vehicles has prompted an increased use of advanced high strength steels (AHSS) in the automotive industry. These new steel grades include dual phase (DP) steels, transformation-induced plasticity (TRIP) steels, high hole expansion (HHE) steels, complex-phase (CP) steels, martensitic steels (MS), and twinning induced plasticity (TWIP) steels (UltraLight Steel Auto Body- Advanced Vehicle Concepts, 2001). Additionally, these steels are galvanized in order to improve the surface corrosion resistance for automotive parts. However, it is still a great challenge to laser weld of galvanized steels in a zero-gap lap joint configuration. When laser welding of galvanized steels in a zero-gap lap-joint configuration, the zinc coating at the contact interface will vaporize; due to the lower boiling point (906 °C) of zinc as compared to the melting temperature of steel (above 1500 °C), the highly pressured zinc vapor expels the liquid metal out of the weld pool, resulting in blowholes and pores which dramatically decrease the mechanical properties of the weld (Akhter et al., 1988) (Fig. 1).

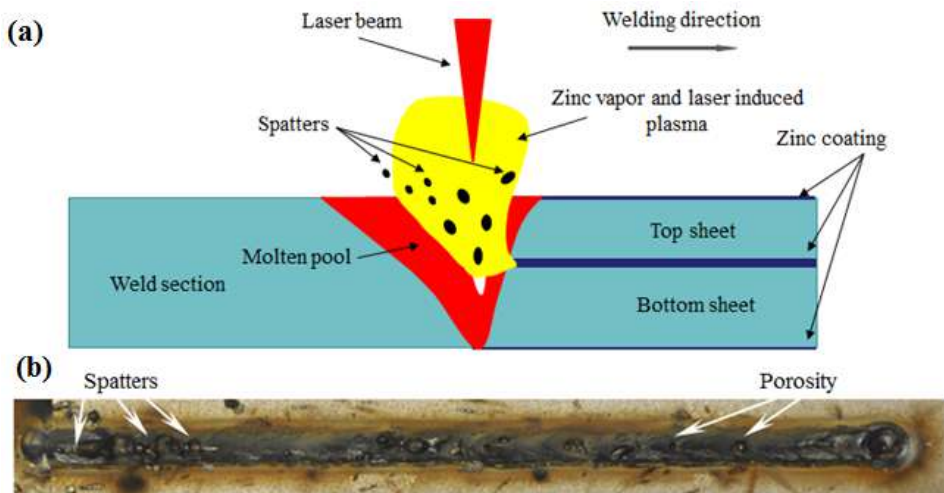
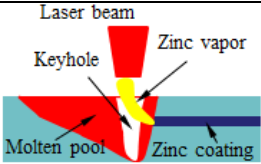

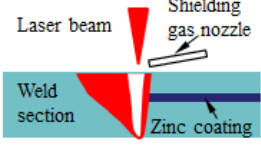
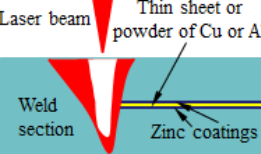
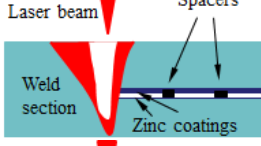
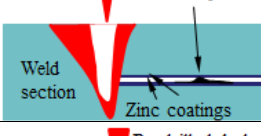
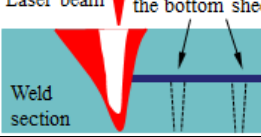
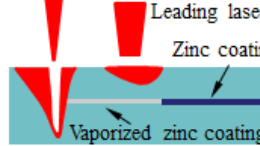


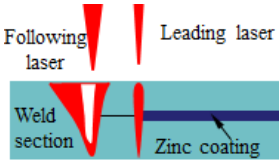
Figure 1. (a) The schematic view of the laser welding of galvanized steel in a zero gap lap-joint configuration and (b) the acquired weld bead with pores

2. Review of the laser welding of galvanized steels in a lap joint configuration

Over the past several decades, industry and academic researchers have been seeking new technologies that will successfully join galvanized steels in a lap joint configuration. Many techniques were proposed, and some are listed in Table 1.

Methods	Schematic	Technical details	Drawbacks
Elongating the laser beam (Fabbro et al., 2006) or using low power / low speed laser welding (Ma et al., 2012)		The zinc vapor was degassed through the keyhole or the enlarged molten pool during welding	
Using pulsed laser welding (Heydon et al., 1989; Kennedy et al., 1989; Norris et al., 1992; Tzeng, 1999; Tzeng, 2006)		Zinc vapor was mitigated in the pulsed laser welding and effectively exhausted through a stable keyhole	Low processing speed or unstable weld qualities that limit the application in production
Using various shielding gas combinations (Berlinger, 1987; Akhter et al., 1990; Ream, 1991; Mitsubishi Co., 1993; Chung et al., 1999; Briand et al., 2008; Yang et al., 2011)		Suppressed the formation of the laser induced zinc plasma or interacted of the zinc vapor with the shielding gas during welding	
Pre-placing a thin metal sheet or powder along the centerline of the weld seam (Dasgupta et al., 2000; Li et al., 2007)		The zinc reacted chemically with the added metal before the steel started to melt	Difficulties will be implemented in production
Applying an appropriate spacer at the faying surfaces (Akhter et al., 1988; Imhoff et al., 1988)		The generated zinc vapor vented out through the gap	
Using a laser to create humps on the bottom sheet to create a gap at the faying surfaces (Gu et al., 2011)		The generated zinc vapor vented out through the gap	The additional pre-welding procedure increases the production cost
Creating vent holes on the bottom steel sheet (Chen et al., 2009)		The generated zinc vapor vented out through the vent holes	
Adding a second laser heat source or splitting the laser beam into two laser beams in order to weld galvanized steel (Loredo et al., 2002; Xie et al., 2001)		The leading laser melted the zinc coating at the interface	Complex equipment that would be difficult to implement in the production environment.

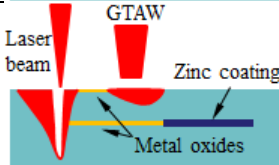
Using a leading beam to cut a slot along the joint line (Iqbal et al., 2010; Milberg et al., 2009)



The leading laser cut the slot through which the zinc vapor was vented out

Moreover, a specific offset is needed between these two heat sources that could limit the application of this welding procedure

Applying gas tungsten arc welding (GTAW) as an auxiliary preheating heat source (Gu et al., 2001; Kim et al., 2008; Yang et al., 2009)



The preheating increased the absorption of the laser beam that contributes to a formation of a stable keyhole through which the zinc vapor is evacuated

Table 1. The alternatives for the welding of galvanized steels in a lap joint configuration

As mentioned above, all of these techniques have some drawbacks that limit their application in the industry. So far, there is no report on a cost-effective, efficient, and easy-to-apply welding procedure that is capable of joining galvanized high-strength steels in a zero-gap lap joint configuration without the material addition or without the assistance of a second heat source. In order to avoid highly pressurized zinc vapor caused weld defects like spatters and blowholes, either the zinc coating should be removed before the steel melts or the vaporized zinc needs to be vented out properly during the welding process. The most direct way of accomplishing this is to mitigate the presence of high pressure zinc vapor during the welding process. In order to achieve this goal several techniques are proposed which will be described in the following sections of this chapter.

3. Low power / low speed laser welding of galvanized steels in a zero-gap lap joint configuration

3.1. Experimental procedure

Ribic et al. (2009) concluded that the generated zinc vapor escapes from the weld pool if the solidification time is longer. A lower welding speed will generate an enlarged weld pool that will require a longer solidification time. An experimental work is presented to show that the effect of zinc vapor on the quality of a weld in a zero-gap lap joint configuration may be successfully mitigated. A fiber laser of 4 kW in power with a focused spot of 0.6 mm in diameter was used as the welding heat source, and a 6-axis high precision robot was used to implement the welding procedure of galvanized steels (see Fig. 2). Pure argon with a flow rate of 30 standard cubic feet per hour (SCFH) was employed as side shielding gas to suppress the laser-induced plasma and to protect the molten material against corrosion. The base material used in this work was galvanized high strength dual phase (DP) steel DP980, whose nominal chemical composition is listed in Table 2 (Burns, 2009). The coupons of galvanized DP980 steel sheets were 1.2 mm and 1.6 mm in thickness, with a zinc coating weight of about 60 g/m².

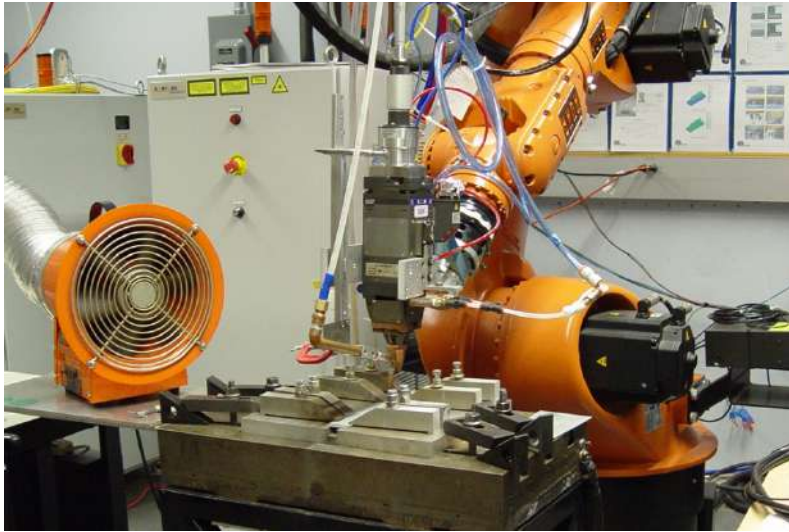


Figure 2. Experimental setup for low power / low speed laser welding

C	Si	Mn	Cr	Mo	Al	Cu	Ni	Fe
0.15	0.31	1.5	0.02	0.01	0.05	0.02	0.01	Balance

Table 2. Chemical composition of galvanized DP980 steel, wt% (Burns, 2009)

3.2. Experimental results for low power / low speed laser welding

The top and bottom views of the weld obtained under a laser power of 2.0 kW and a welding speed of 5 mm/s show an acceptable weld surface quality (see in Fig. 3). A high-speed CCD camera with a frame rate of 4000 fps combined with a green laser with a band pass filter wavelength of 532 nm as the illumination source were used for real time monitoring of the dynamic behavior of the molten pool under different laser welding conditions. The weld pool formed under a relatively low welding speed was larger and relatively stable (see Fig.4a). On the other hand, the molten pool acquired under a higher welding speed shows sever fluctuation, and the high pressured zinc vapor generated at the faying surface jetted into the molten pool causing blowholes (see Fig. 4b). According to Ribic’s work, an enlarged weld pool has a longer solidification time which obviously decreased the probability that the zinc vapor would be trapped in the molten pool under a relatively low welding speed (around 5 mm/s), and a visually acceptable weld quality could be acquired. However, if the welding speed is exceedingly low, the sagging may be generated, which also reduces joint strength. Fig. 5 shows the tensile shear test results of the joints acquired under different welding speeds. A higher failure load was acquired under a lower welding speed. The trapped zinc vapor may result in pores inside the joints which could decrease the failure load with respect to the joints acquired under the same welding conditions but without zinc at the faying surface (see Fig. 5). Although an acceptable quality

of joints could be achieved by this low power / low welding speed procedure, this procedure is not accepted by the industry because of a low productivity.

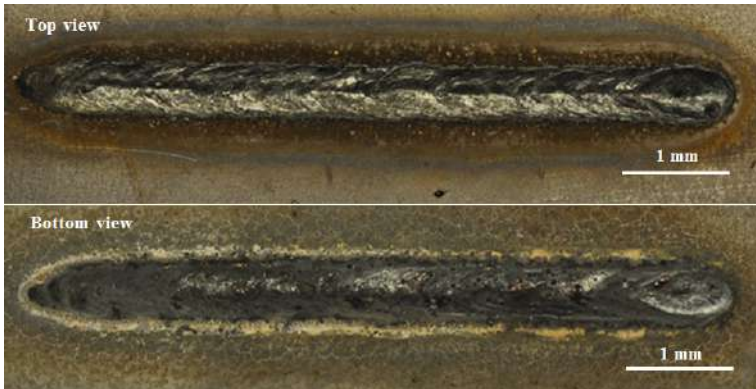


Figure 3. Top and bottom views of the weld obtained under a laser power of 2.0 kW and welding speed of 5 mm/s

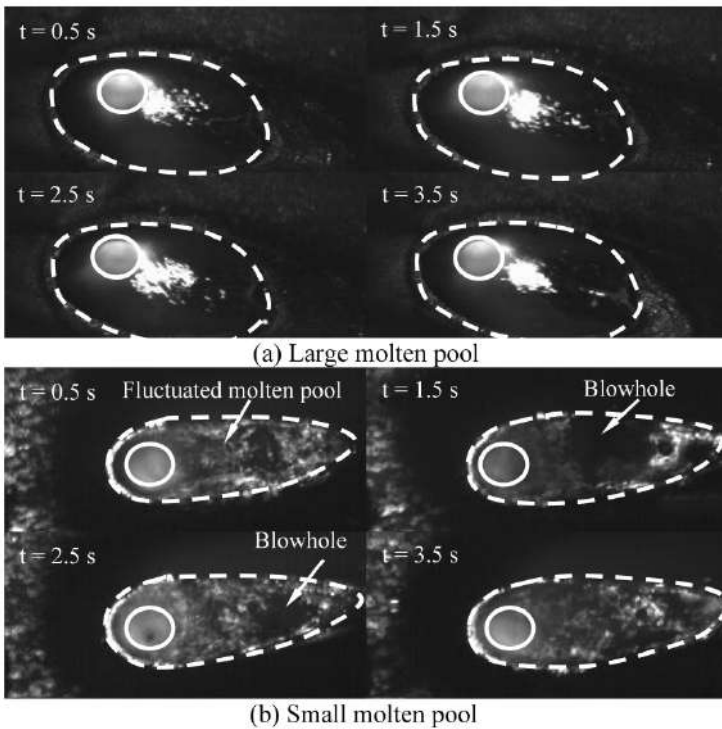


Figure 4. The dynamic behavior of the molten pool acquired under different welding parameters: (a) laser power of 1.5 kW, welding speed of 5 mm/s, and (b) laser power of 4.0 kW, welding speed of 30 mm/s at different time steps during the welding process

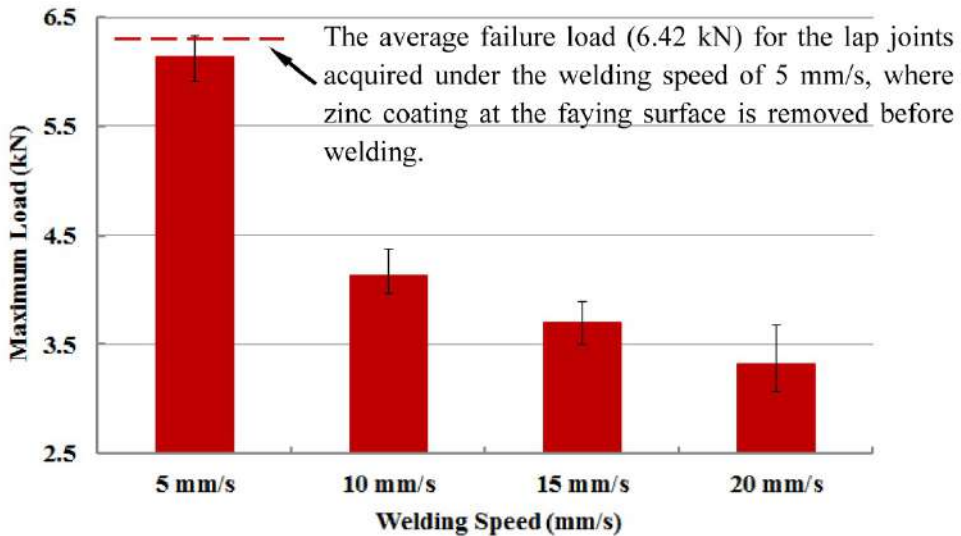


Figure 5. The failure load for tensile shear testing of the DP980 lap joints acquired under different welding speeds and with the laser power of 2.0 kW

4. Two-pass laser welding of galvanized steels in a zero-gap lap joint configuration

4.1. Experimental procedure

In order to improve the production efficiency, the automotive industry requires a welding technique that can join of overlapped galvanized high strength steels successfully under a higher working speed. As discussed previously, if the zinc coating is removed before the steel starts to melt, a much higher welding speed can be achieved. Therefore, a two-pass laser welding process that is capable of successfully joining galvanized steel sheets in a zero-gap lap joint configuration is presented. Fig. 6 shows the schematic view of the two-pass laser welding process. The defocused laser beam shown in Fig. 6a is used to preheat the two overlapped sheets during the preheating pass. Only when the width of the area where the zinc coating is vaporized by preheating is larger than the distance between the zinc boiling isotherms (906 °C), a sound weld could be acquired (see Fig. 6c). The laser power was set at its maximum value of 4.0 kW in order to allow a higher scanning speed. The laser welding speed was set at 60 mm/s in order to acquire a partial penetrated joint that was determined by the preliminary executed experimental trails. The preheating parameters, like the defocused position of the laser beam and the laser scanning speed, are critical in achieving a final weld quality. As shown in Table 3, three levels of defocused off-set distance (26 mm, 44 mm, and 62 mm which corresponds to the defocused diameters of laser beam of about 3 mm, 5 mm, and 7mm, respectively) and four levels of scanning speeds (20 mm/s, 30 mm/s, 40 mm/s, and 50 mm/s) were chosen to optimize the preheating procedure.

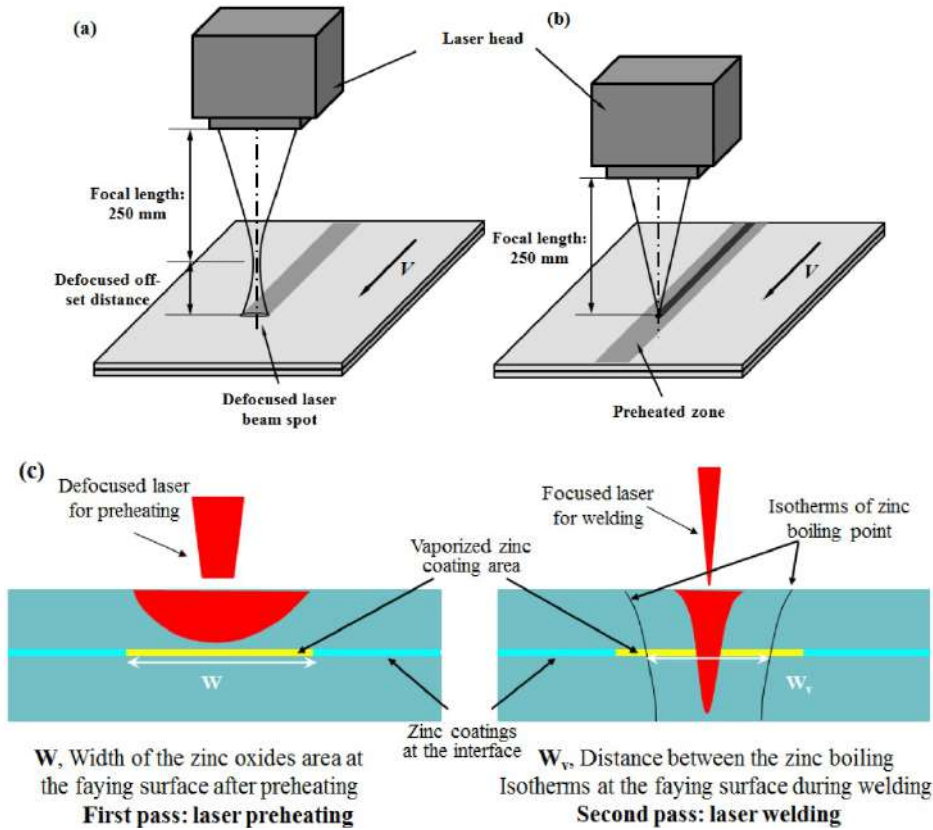


Figure 6. The schematic view of the two-pass welding process: (a) laser preheating, (b) laser welding, and (c) geometrically defined width of zinc coating treated during preheating and welding

Process parameters	Experiment series A				Experiment series B				Experiment series C			
Scanning speed (mm/s)	20	30	40	50	20	30	40	50	20	30	40	50
Defocused off-set distance (mm)	26				44				62			

(Laser preheating and welding power: 4.0 kW, laser welding speed: 60 mm/s)

Table 3. The preheating parameters

4.2. Experimental results for two-pass laser welding

As the defocused off-set distance increased, the defocused laser beam spot became larger, and the laser energy distribution was dispersed. A defocused off-set distance combined with a lower scanning speed generated too much energy that penetrated the top sheet resulting

in spatters and permanent defects which could not be mitigated by the following laser welding pass (see Fig. 7a). A longer defocused off-set distance combined with a higher scanning speed could not vaporize a sufficient amount of zinc coating; the remaining zinc coating at the contact interface caused weld defects (see Fig. 7b). Thus, only for the optimized laser defocused off-set distance and the scanning speed, will a reasonable width of the zinc coating be vaporized (see Fig. 7c). Fig. 8 shows the experimental results for the selected preheating parameters (shown in Table. 3). The optimized preheating parameters that allowed a sound weld are shown in Fig. 8, area A.

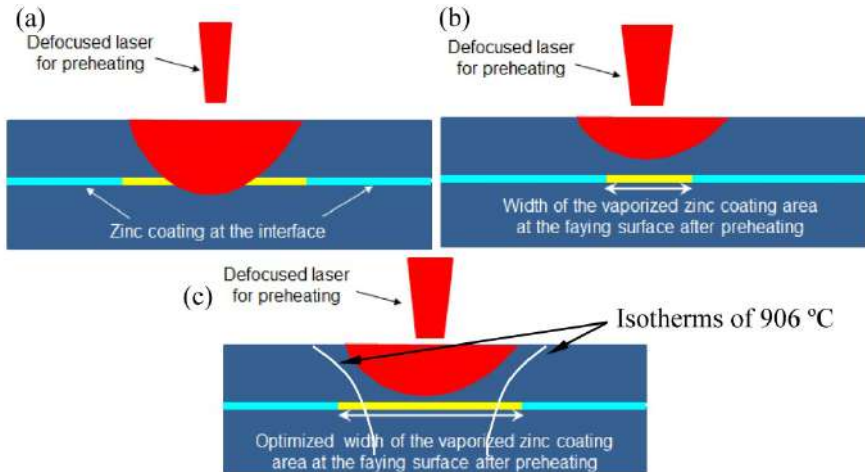


Figure 7. The schematic view of the preheating process: (a) molten pool penetrates the interface, (b) narrow vaporized zinc coating area, and (c) optimized width of the vaporized zinc coating area

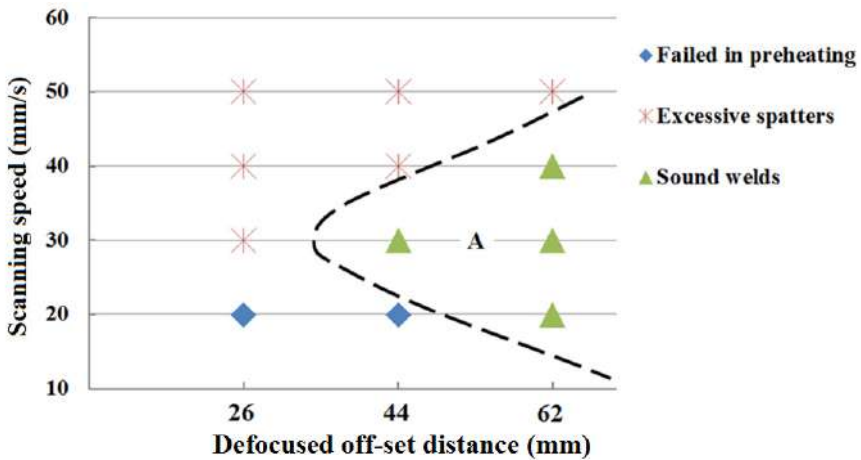


Figure 8. Experimentally determined combinations of defocused off-set distance and scanning speed that result in a good weld quality

Figs. 9 and 10 show the preheated interfaces of the coupons and the cross-sections corresponding to the different locations marked on the preheated interfaces. The zinc coatings far from the preheated zones at the top and bottom sheets are not affected (see Figs. 9b and 10b); the zinc coatings are melted and deformed at the edges of the preheated zone (see Figs. 9c and 10c); and the zinc coatings are vaporized at the center of the preheated zone (see Figs. 9d and 10d).

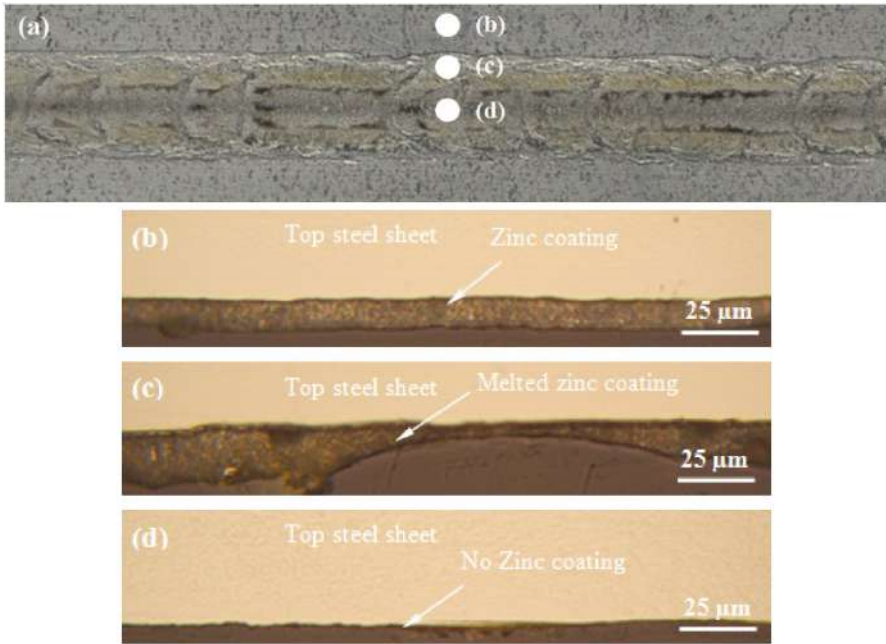


Figure 9. Preheated surface of the top steel sheet obtained with a laser power of 4.0 kW, a 30 mm/s scanning speed, and a 62 mm defocused laser beam off-set distance and the corresponding cross-section at different locations

During the laser preheating pass, the defocused laser beam burns the zinc at the top surface, and melts and partially vaporizes the zinc coatings at the interface of the two overlapped steel sheets, and improves the absorption of the laser beam which results in the formation of a stable keyhole through which any zinc vapor formed at the interface will be vented out (Yang et al., 2009). Fig. 11 shows the top and bottom views of the weld obtained under preheating and welding with a laser power of 4.0 kW, a defocused off-set distance of 62 mm, a scanning speed of 30 mm/s, and a welding speed of 60 mm/s. Fig. 12 shows the weld cross-section of the weld shown in Fig. 11.

The tensile shear test was carried out in order to determine the mechanical strength of the welded joints obtained by the two-pass laser welding procedure. The experimental results demonstrated that the two-pass welded joints were broken in the HAZ of the bottom steel sheet. One of the tensile shear results is shown in Fig. 13. The tensile shear test for the

welded coupons without a zinc coating at the interface was also performed. In order to use the data as a reference, the welded coupons without a zinc coating at the interface had a average failure load value of 5295.88 N which was lower than that of the two-pass welded coupons (6127.58 N). The reason for this difference in results is explained by the fact that the preheating process increased the laser beam absorption of the coupons, which contributed to a stronger (wider) partially penetrated weld joint.

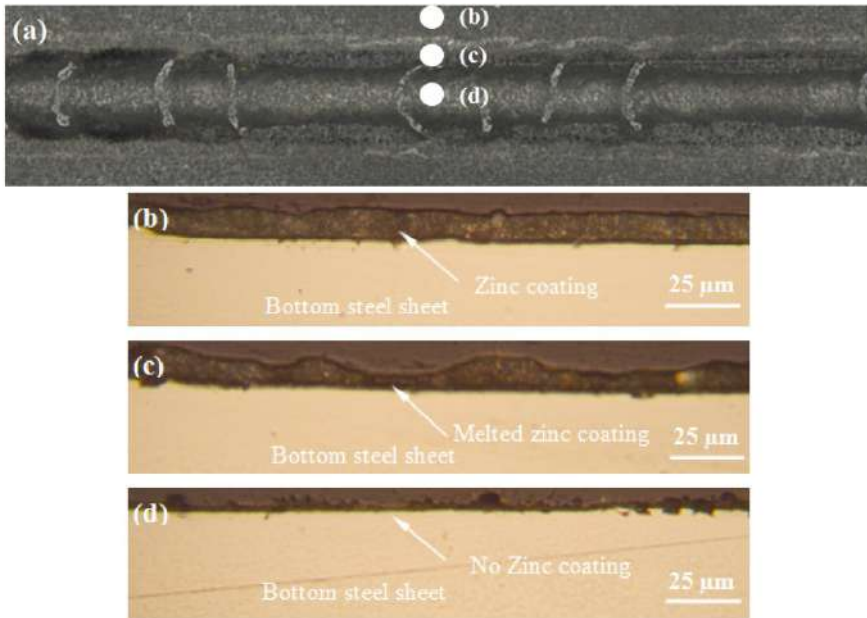


Figure 10. Preheated surface of the bottom steel sheet obtained with a laser power of 4.0 kW, a 30 mm/s scanning speed, and a 62 mm defocused laser beam off-set distance and the corresponding cross-section at different locations

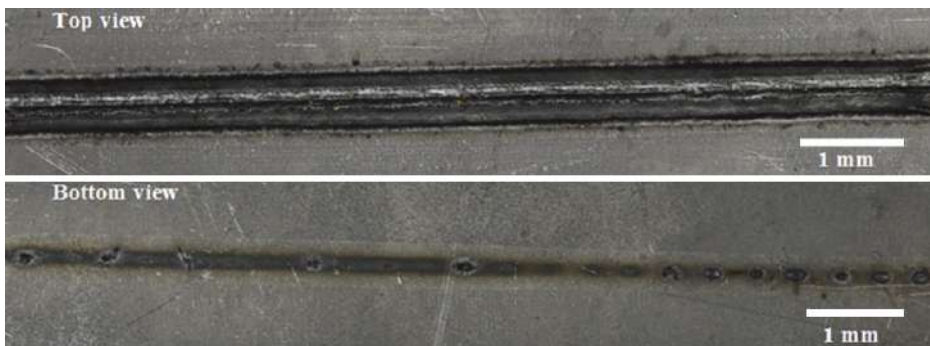


Figure 11. Top and bottom views of weld obtained under a scanning speed of 30 mm/s and a defocused off-set distance of 62 mm (the preheating and welding laser power is 4.0 kW; the welding speed is 60 mm/s)

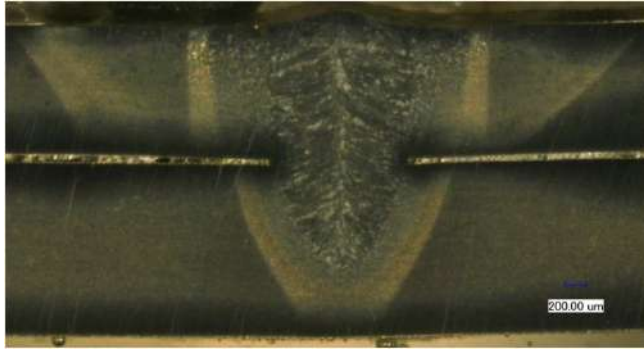


Figure 12. Cross-sectional view of the weld obtained under a scanning speed of 30 mm/s and a defocused off-set distance of 62 mm (the preheating and welding laser power is 4.0 kW; the welding speed is 60 mm/s)

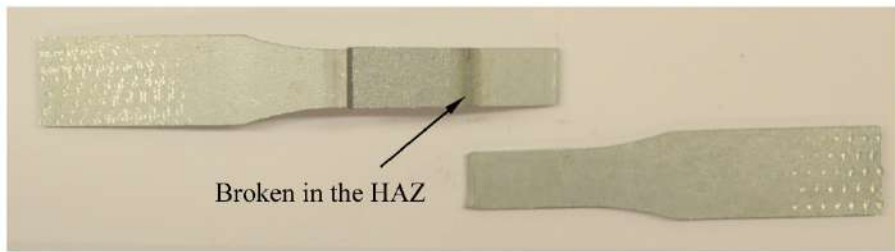


Figure 13. Tensile shear test results of the weld joint obtained under a scanning speed of 30 mm/s, and a defocused laser beam off-set distance of 44 mm (the preheating and welding laser power is 4.0 kW; the welding speed is 60 mm/s)

5. Laser welding of galvanized steels in a lap joint configuration with a pressure wheel

5.1. Experimental procedure

Based on the experimental study performed, it was found that the stability of the laser welding process was sensitive to the clamping conditions. A relatively loose clamp condition resulted in a better weld than a very tight clamp condition. The gap ahead of the weld pool is the key to performing the laser welding of galvanized steel in a lap joint configuration successfully. Moeckel et al. (2003) developed a device for controlling the gap at the faying surface of the overlapped galvanized steel sheets in order to degas the generated zinc vapor during the welding process. The Fraunhofer Institute developed a pressure wheel system which could control the roller clamping force that allows for the controlling of the gap at the faying surface (Fraunhofer Institute website). In order to achieve an overlapped galvanized steel joint with a single laser beam without a pre- and/or post-weld process, a force-controllable pressure wheel (ZM YW50 PW P300 II) is used to control the gap near the laser focused spot during the laser welding. The laser welding of

galvanized steels for a lap joint configuration with a pressure wheel control system is shown in Fig. 14. Fig. 15a shows the close-up of the pressure wheel set-up. The laser head is set-up under a 30° decline with respect to the pressure wheel, and Fig. 15b shows the pressure wheel controller.

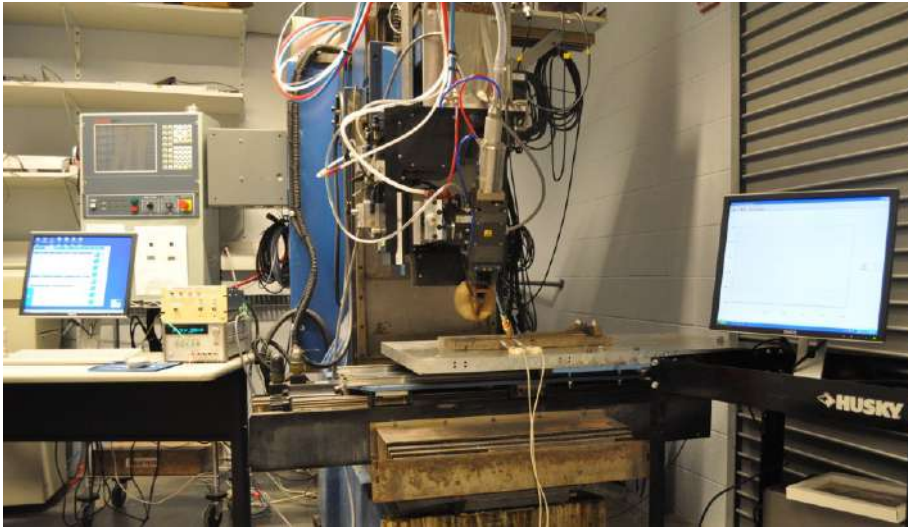


Figure 14. Laser welding of galvanized steel for a lap joint configuration with a pressure wheel control system

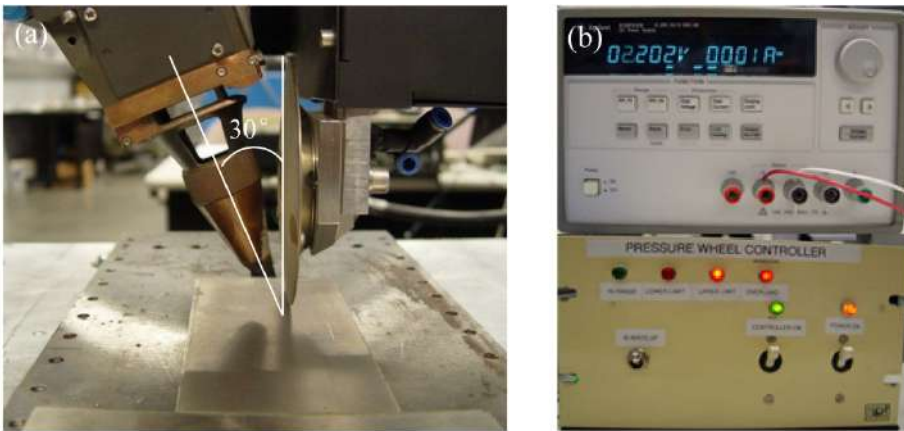


Figure 15. (a) The close-up of pressure wheel set-up and (b) the pressure wheel controller

5.2. Experimental results for laser welding with a pressure wheel

The feasibility of welding galvanized steel sheets in a lap joint configuration by controlling the pressure wheel force during the fiber laser welding process is discussed. Fig. 16 shows

the welds obtained by various levels of pressure wheel force under a laser power of 4.0 kW and a welding speed of 50 mm/s. The corresponding weld cross-sections are shown in Fig. 17. The cross-sections of the welds show that the weld beads are under the angle because the laser head is set-up with an angle of 30° with respect to the pressure wheel (see Fig. 15a). A sound weld was obtained by using a single laser beam with a force-controllable pressure wheel under the optimized force. As shown in Figs. 16 and 17, with an increased pressure wheel force, the weld quality decreased, and lots of spatters and blowholes were generated (see Fig. 16d). An increased pressure wheel force larger than 12N resulted in a decreased gap between the overlapped sheets near the laser focused area; the gap became too narrow to evacuate the generated high pressured zinc vapor. The jet of high pressured zinc vapor generated spatters and blowholes during the welding process.

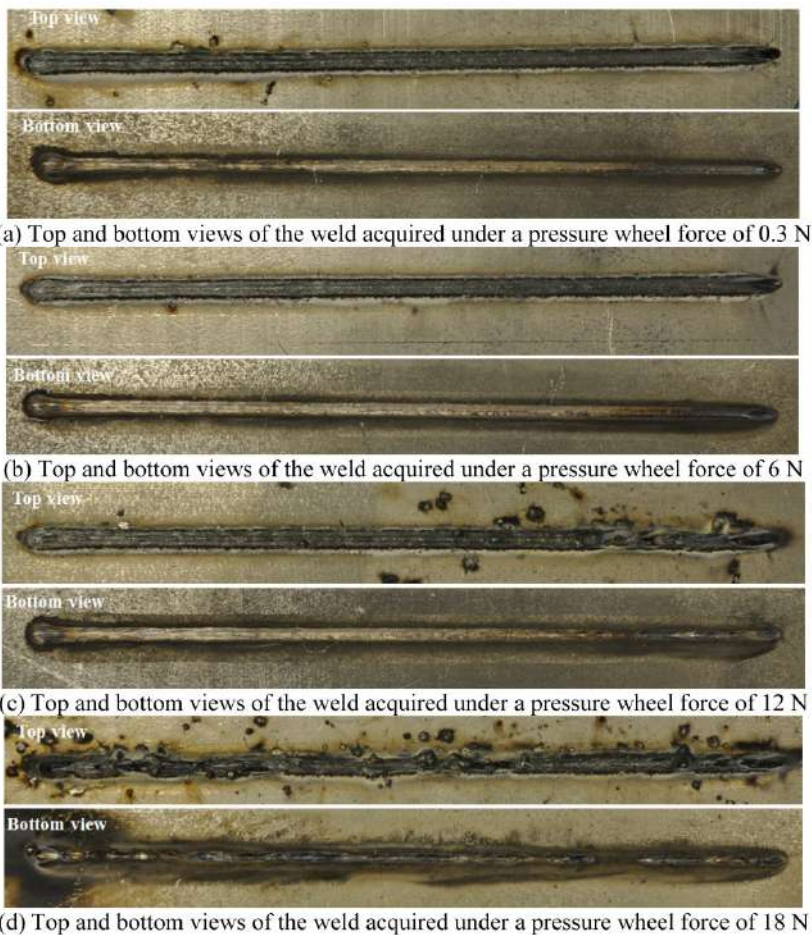


Figure 16. Top and bottom views of the welds acquired by various pressure wheel forces under a laser power of 4.0 kW and a welding speed of 50 mm/s

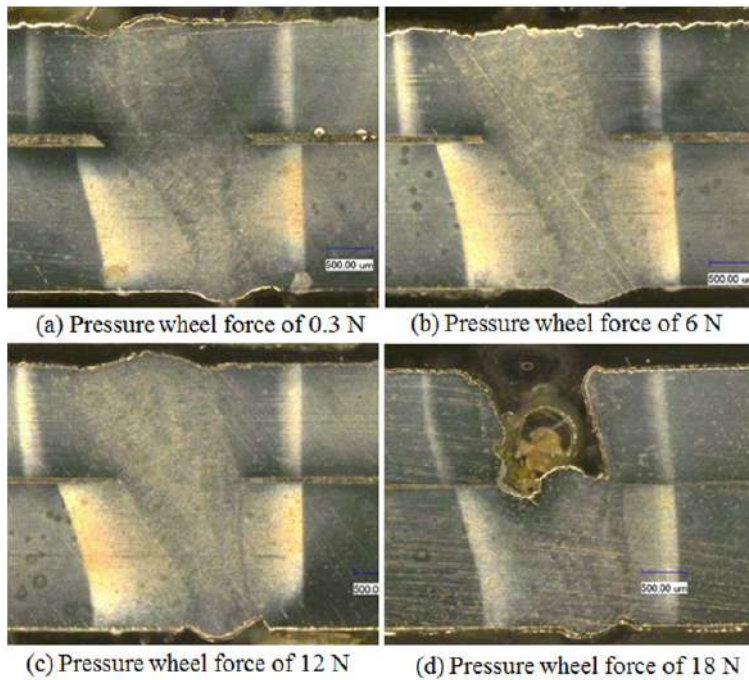


Figure 17. Cross-sectional views of the welds acquired by various pressure wheel forces under a laser power of 4.0 kW and a welding speed of 50 mm/s

Kong et al. (2012) reported that there is a correlation between the optical emission of the plasma and zinc vapor induced welding defects in the laser welding of galvanized steel for an overlapped joint configuration. Therefore, the spectroscopy was used to on-line monitor the laser welding of galvanized steel with a pressure wheel for an overlap joint configuration. The set-up to monitor the optical emission of the plasma in laser welding is shown in Fig. 18.

The emission line intensities detected from plasma during the laser welding of galvanized steel under various pressure wheel forces are shown in Fig. 19. The intensities of the emission lines above the weld pool were much lower when the pressure wheel force is larger than 12 N; while, the intensities of the emission lines were relatively higher when the pressure wheel force is set at 0.3, 6 or 12 N. The reason for this stems from the fact that when welding of galvanized steel under a higher pressure wheel force (18 N), the gap near the focal laser spot became too narrow to evacuate the high pressured zinc vapor; the zinc vapor caused spatters that disturbed the stability of the plasma which affected the intensity of the detected spectrum (Kong et al. 2012). The evolution of iron electron temperature within the laser-induced plasma along the weld bead length is shown in Fig. 20. The iron electron temperature was calculated by using the Boltzmann Plot method expressed by Equation (1) (Kong et al., 2012, Griem, 1997 and Marotta, 1994):

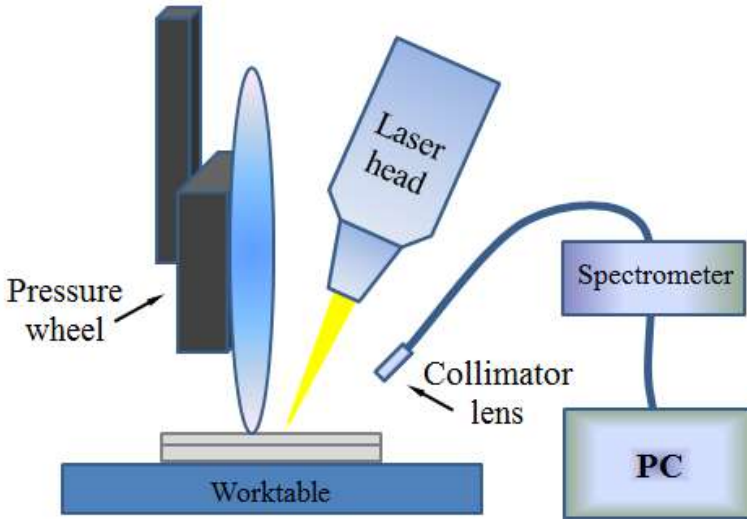


Figure 18. Schematic view of the setup for on-line monitoring the optical properties of plasmas during laser welding

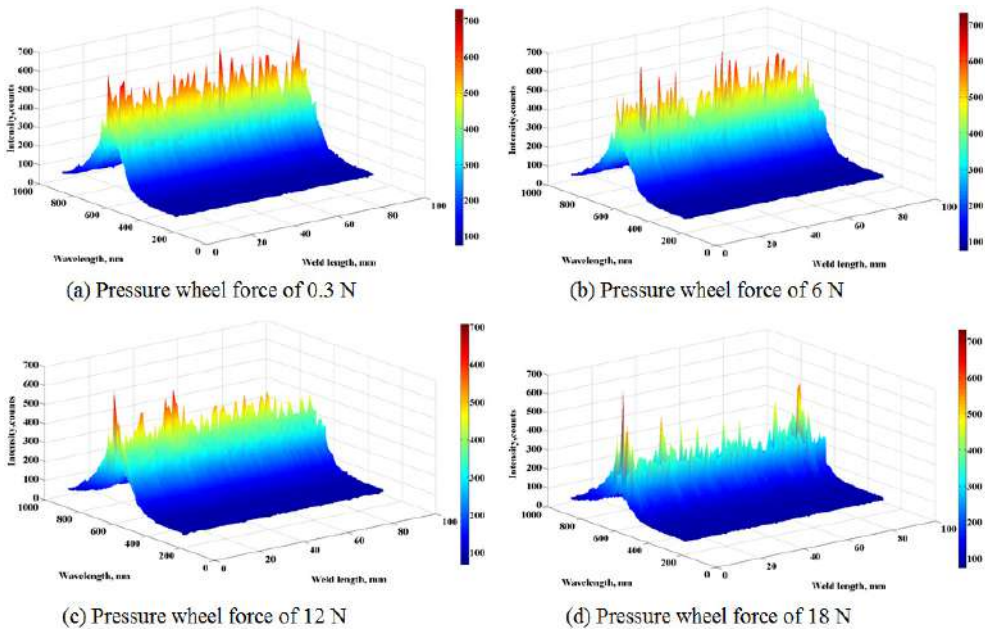


Figure 19. Spectrum of laser induced plasma captured by a spectrometer in the laser welding process by various pressure wheel forces under a laser power of 4.0 kW and a welding speed of 50 mm/s

$$T_e = \frac{E_m(2) - E_m(1)}{k \ln \left[\frac{E_m(1)I(1)A_m(2)g_m(2)\lambda(1)}{E_m(2)I(2)A_m(1)g_m(1)\lambda(2)} \right]} \quad (1)$$

where T_e is the plasma electron temperature, E_m is the energy of the upper state, k is the Boltzmann constant, I_m is the emission line relative intensity, A_m is the transition probability, g_m is the statistical weight, and λ_m is the wavelength.

As shown in Fig. 20, under lower pressure wheel forces (0.3, 6, and 12 N), the electron temperature showed lower intensity and less fluctuation compared to a higher pressure wheel force (18 N). The presence of the zinc vapor induced spatters in the plasma which increased the iron electron concentration which, in turn, increased the iron electron temperature value (Kong et al., 2012).

Thus, there is a correlation between the optical emission of the plasma and zinc vapor induced welding defects during the laser welding; and this optical signal could be further used as feedback for the closed-loop control of the laser welding of galvanized steel with a pressure wheel, which is shown in Fig. 21.

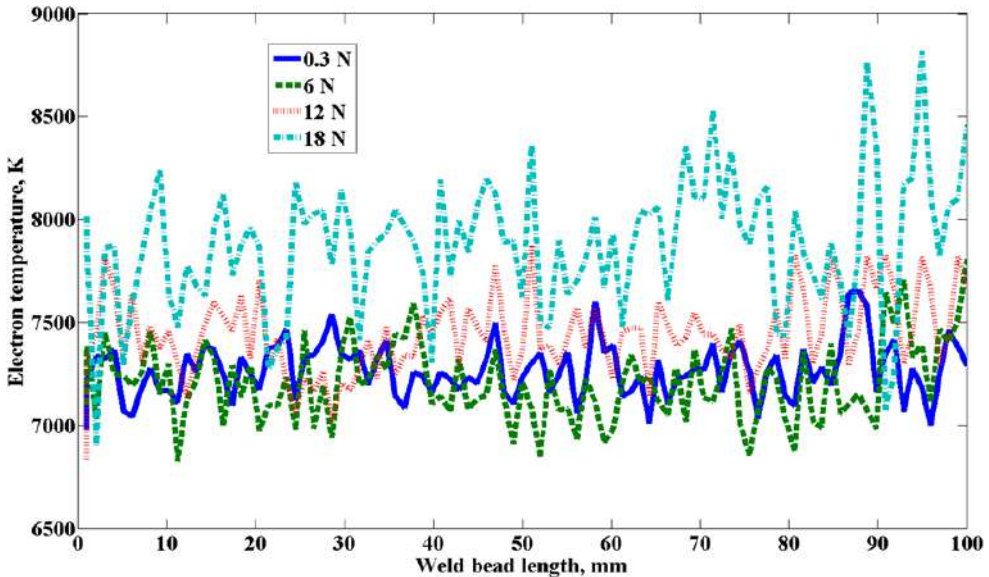


Figure 20. Electron temperatures of iron in laser-induced plasma captured by a spectrometer in the laser welding process by various pressure wheel forces under a laser power of 4.0 kW and a welding speed of 50 mm/s

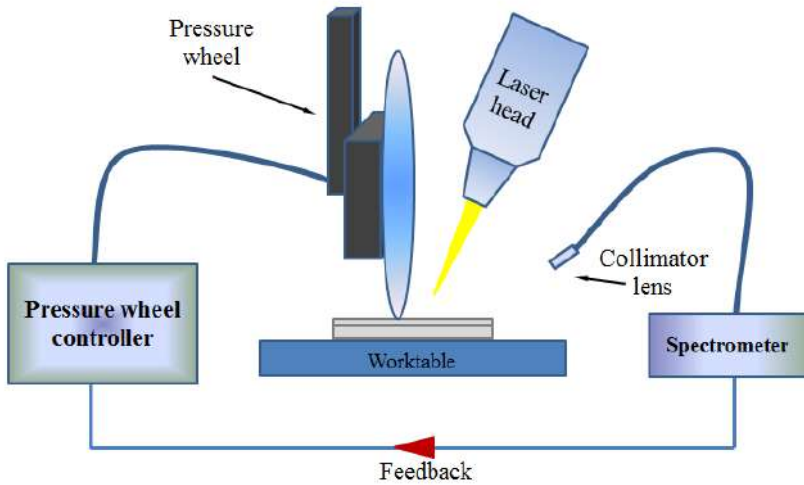


Figure 21. A schematic presentation of a closed-loop control system of the laser welding of galvanized steel by controlling the clamping force

6. Conclusions

In this chapter, issues related to the laser welding of galvanized steels in a zero-gap lap joint configuration are discussed. The authors' recent research results on the laser welding of galvanized steel in a lap joint configuration are reviewed. The different welding procedures, namely, low power / low speed welding, two-pass laser welding and laser welding with a pressure wheel are introduced for the laser welding of galvanized steels in a lap joint configuration. It was found that acceptable weld quality could be achieved by a low power / low welding speed procedure; however, the relatively low welding speed limits its application in the industrial environment. A high quality weld could be obtained by introducing a preheating pass with a defocused laser beam. By using the optical signal acquired during the laser welding process as a feedback signal in the pressure wheel force control, it is possible that a controllable clamping force could be a solution for achieving a good weld quality without using a pre- and post- welding procedure.

Author details

Junjie Ma, Fanrong Kong and Radovan Kovacevic*
Center for Laser-aided Manufacturing, Lyle School of Engineering, Southern Methodist University, Dallas, TX, USA

Blair Carlson
General Motors R&D Center, Warren, MI, USA

* Corresponding Author

Acknowledgement

This work was financially supported by the NSF's Grant No. IIP-1034652.

7. References

- Akhter R., Steen W. M. and Cruciani D. (1988). Laser welding of zinc-coated steel. Proceedings of the 5th International Conference on Lasers in Manufacturing, Stuttgart, West Germany, September 13-14
- Akhter R. and Steen W.M. (1990). The gap model for welding zinc-coated steel sheet. In: Proceedings of the International Conference on Lasers Systems Application in Industry, Torino, Italy, 219-236
- AWS WZC (D19.0-72), Welding Zinc-Coated Steels (1972). American Welding Society.
- Bakowski L., Beyer E., Herziger G. and Poprawe R. (1984). Development and optical absorption properties of a laser induced plasma during CO₂-laser processing. SPIE Proceedings Series 455: 75-80.
- Berlinger G. and Speranza J.J. (1987). U.S. Patent 4,684,779
- Briand F., Chouf K. and Lefebvre P. (2008). Method and installation for laser welding with a N₂/He gas mixture, the N₂/He content being controlled according to the laser power, U.S. patent 7,385,158
- Burns T. Weldability of a dual-phase sheet steel by the gas metal arc welding process. Master Thesis, the University of Waterloo, 2009.
- Chen W., Ackerson P. and Molian P. (2009). CO₂ laser welding of galvanized steel sheets using vent holes. *Materials and Design* (30): 245-251
- Chung B.G., Rhee S. and Lee C.H. (1999). The effect of shielding gas types on CO₂ laser tailored blank weldability of low carbon automotive galvanized steel, *Materials Science and Engineering* 272: 357-362
- Dasgupta A., Mazumder J. and Bembenk M. (2000). Alloying based laser welding of galvanized steel, Proceedings of International Conference on Applications of Lasers and Electro Optics, Dearborn MI.
- Dawes C. Laser welding: a practical guide, Abington publishing, 1992.
- Dowden J. M. The theory of laser materials processing: Heat and mass transfer in modern technology, Springer, 2nd edition, 2009.
- Fabbro R., Coste F., Geobels D. and Kielwasser M. (2006). Study of CW Nd-Yag laser welding of Zn-coated steel sheets. *Journal of physics D: Applied physics* 39:401-409
- Forrest M. G. and Lu F. (2004). Advanced dual beam laser welding of zinc-coated steel sheets in lap joint configuration with zero gap at the interface. 23th International Congress on Applications of Lasers and Electro-Optics, ICALEO.

- Graham M. P., Hirak D. M., Kerr H. W. and Weckman D. C. (1996). Nd: YAG laser beam welding of coated sheet steels using a modified lap joint geometry. *Welding Journal* 75(5): 162-170
- Griem H. R. Principle of plasma spectroscopy. Cambridge Monographs on Plasma Physics. Cambridge University Press, Cambridge, 1997.
- Gu H. and Mueller R. (2001). Hybrid welding of galvanized steel sheet. 20th International Congress on Applications of Lasers & Electro-optics, ICALEO, 130-139
- Gu H. and Shulkin B. (2011). A practical use of humping effect in laser beam welding. *Journal of Laser Applications* 23(1): 1-6
- Gualini M.M.S., Iqbal S. and Grassi F. (2006). Modified dual-beam method for welding galvanized steel sheets in lap configuration. *Journal of Laser Applications* 18(185): 185-191
- Heydon J., Nilsson K. and Magnusson C. (1989). Laser welding of zinc coated steel. In: Proceedings of the 6th International Conference on Lasers in Manufacturing, 93-104
Homepage Fraunhofer - Gesellschaft: [Http://www.fraunhofer.de/en.html](http://www.fraunhofer.de/en.html)
- Imhoff R., Behler K., Gatzweiler W. and Beyer E. (1988). Laser beam welding in car body making. Proceedings of the 5th International Conference on Lasers in Manufacturing, Stuttgart, West Germany, September 13-14
- Iqbal S., Gualini M.M.S. and Rehman A.U. (2010). Dual beam method for laser welding of galvanized steel: Experimentation and prospects. *Optics & Laser Technology* 42(1): 93-98
- Kim C., Choi W., Kim J. and Rhee S. (2008). Relationship between the welding ability and the process parameters for laser-TIG hybrid welding of galvanized steel sheets. *Materials Transactions* 49(1): 179-186
- Kennedy S.C. and Norris I.M. (1989). Nd-YAG laser welding of bare and galvanized steels. SAE Technical Paper Series 890887, International Congress and Exposition, Detroit, MI
- Kong F., Ma J., Carlson B. and Kovacevic R. (2012). Real-time monitoring of laser welding of galvanized high strength steel in lap joint configuration. *Optics & Laser Technology* 44(7): 2186-2196
- Lacroix D., Jeandel G. and Boudot C. (1997). Spectroscopic characterization of laser induced plasma created during welding with a pulsed Nd: YAG laser. *Journal of Physics D: Applied Physics*, 30(10): 6599-6606
- Li X., Lawson S. and Zhou Y. (2007). Novel technique for laser lap welding of zinc coated sheet steels. *Journal of Laser Applications* 19(4): 259-264
- Li X., Lawson S. and Zhou Y. (2008). Lap welding of steel articles having a corrosion resisting metallic coating. U.S. Patent No. 2008/0035615 A1.
- Loredo A., Martin B., Andrzejewski H. and Grevey D. (2002). Numerical support for laser welding of zinc-coated sheets process development, *Applied Surface Science* 195(1-4): 297-303

- Ma J., Kong F. and Kovacevic R. (2012). Finite-element thermal analysis of laser welding of galvanized high-strength steel in a zero-gap lap joint configuration and its experimental verification. *Materials and Design* (36): 348-358
- Marotta A. (1994). Determination of axial thermal plasma temperatures without Abel inversion. *Journal of Physics D: Applied Physics* (27): 268-272
- Mazumder J., Dasgupta A. and Bembek M. (2002). Alloy based laser welding. U.S. patent 6,479,168.
- Milberg J. and Trautmann A. (2009). Defect-free joining of zinc-coated steels by bifocal hybrid laser welding. *Production Engineering. Research and Development* 3(1): 9-15
- Mitsubishi Co. (1993). U.S. Patent 5,618,452
- Moeckel A., Stein H., Jucht H., (2003). Device for degassing laser welded seams Patent no DE 10160156
- Norris I., Hoult T., Peters C., Wileman P., (1992). Material processing with a 3 kW Nd:YAG laser. *Proceedings of Laser Advanced Materials Processing (LAMP)*, Nagaoka, Japan
- Pan Y. and Richardson I. M. (2011). Keyhole behavior during laser welding of zinc-coated steel. *Journal of physics D: Applied physics* 44:045502
- Park H.S. and Choi H.W. (2010). *Digital Laser Welding System for Automobile Side Panel, Laser Welding*, Na, X.D., Stone (Ed.), ISBN: 978-953-307-129-9, InTech.
- Ream S. (1991). Laser welding of zinc-coated steel. In: *Laser applications in materials processing and manufacturing*. Society of Manufacturing Engineering (SME), Southfield, MI
- Ribic B., Palmer T.A. and DebRoy T. (2009). Problems and issues in laser-arc hybrid welding. *Int Mater Rev* 54(4):223-44
- Schmidt M., Otto A., Kägeler C. (2008). Analysis of YAG laser lap-welding of zinc coated steel sheets. *CIRP Annals - Manufacturing Technology*, 57(1): 213-216.
- Steen W. M. *Laser material processing*, 3rd edition, Springer, 2003.
- Tzeng Y.F. (1999). Pulsed Nd:YAG laser seam welding of zinc-coated steel. *Welding J* 78(7): 238s-244s
- Tzeng Y.F. (2006). Gap-free lap welding of zinc-coated steel using pulsed CO₂ laser. *The International Journal of Advanced Manufacturing Technology*, (29)3-4: 287-295
- ULSAB-AVC Body Structure Materials, Technical Transfer Dispatch No. 6, May, 2001.
- Wiese W.L. and Martin G.A. *Wavelengths and transition probabilities for atoms and atomic ions. Part II. Transition Probability*. 1st edition, 1980
- Xie J. and Denney P. (2001). Galvanized steel welding with lasers. *Welding Journal* 80(6): 59-61
- Yang S. and Kovacevic R. (2009). Welding of galvanized dual-phase 980 steel in a zero-gap lap joint configuration. *Welding Journal* 88(8): 168-178

Yang S., Carlson B. and Kovacevic R. (2011). Laser welding of high-strength galvanized steels in a zero-gap lap joint configuration under different shielding conditions. *Welding Journal* 90: 8s-18s

Numerical Modeling of Welding Processes

Numerical Modelling to Understand Cracking Phenomena During Laser-GMA Hybrid Welding Nickel-Base Superalloys

Zhiguo Gao

Additional information is available at the end of the chapter

<http://dx.doi.org/10.5772/47395>

1. Introduction

Laser welding is a highly efficient and precise welding method, which is greatly desired in the automotive, aero and ship building industries. It elucidates some excellence, such as higher depth to width ratio, concentrated heat input, minimal thermal distortion, minimized weld fusion and heat affected zone, reduced post weld rework and possibly joining widely dissimilar materials. But laser welding has also clearly demonstrated some drawbacks. First of all, the cost of laser equipment and maintenance are high. Second, highly reflective materials, such as aluminum, copper and gold, are more difficult to process with some laser sources. Finally, the high welding speed leads to high solidification rate, which in turn induces metallurgical problems, such as cracking, pores and brittle phase structures.

Laser-gas metal arc (GMA) hybrid welding is one of the state-of-the-art technologies and is designed to overcome problems commonly encountered during either laser or arc welding. Hybrid welding offers some additional advantages over mere laser and arc welding. Firstly, the combination of a laser beam and gas metal arc in welding will reduce the propensity for cracking, brittle phase formation and porosity. Secondly, the feeding wire modifies the metallurgy of the weld. Thirdly, the effect of the coupled process exceeds the effects of the laser and arc heat sources taken separately, and the laser beam located in front of the GMA weld pool could suppress hump formation during high travel speed (Claus et al., 2005; Gao et al., 2009; Ribic et al., 2009).

Nickel-base superalloys are extensively used as aeronautical material due to their high temperature properties. However, commonly used types of commercial welding for nickel-

base superalloys have three major hurdles that need to overcome in order to make refurbishment and repair feasible. First, the single crystal nature of nickel-base superalloys is easily lost during welding due to stray grain formation. This phenomenon is called a columnar-to-equiaxed transition (CET). Secondly, polycrystalline nickel-base superalloys are very prone to cracking during welding, and these cracks are mostly thermally induced cracks which originate in the grain boundary in the heat affected zone (HAZ). The combination of welding stress and increased concentration of gamma-prime are thought to be the cause of hot cracks in the HAZ. Finally, on-equilibrium solidification, elemental partitioning and subsequent solid state transformation can yield non-ideal microstructures and will not produce material with the desired properties.

It has been found that the mechanical strengths at elevated temperatures of columnar grains are better than those of gas turbine blades with equiaxed grains. Columnar grains are desirable, and equiaxed grains are treated as casting defects in directionally solidified or single crystal castings. Some researchers have implemented theoretical analyses on the solidification behaviours of nickel-base superalloys. Hunt (1984) and Gäumann et al. (2001) theoretically analyzed stray grain formation to consider the parameter Φ for describing the extent of nucleation and growth for stray grain formation ahead of the advancing solidification front. Φ represents the volume fraction of equiaxed grains and varies from 0 to 1. The value of Φ can be calculated by the following equation:

$$\frac{G^n}{V} = a \left\{ 3 \sqrt[3]{\frac{-4\pi N_0}{3 \ln(1-\Phi)} \frac{1}{n+1}} \right\}^n \quad (1)$$

where G is the thermal gradient, V is the growth velocity, a and n are material constants and N_0 is the nucleation density. $a=1.25 \times 10^6 \text{K}^{3.4} \text{m}^{-1} \text{s}^{-1}$, $n=3.4$ and $N_0=2 \times 10^{15} \text{m}^{-3}$ are used for a similar nickel-base superalloy. When constitutional supercooling is minimal, $\Phi=0$, the weld microstructure is free of stray grains and maintains its single crystal nature. When $\Phi=1$, solidification is equiaxed. A critical value of Φ that corresponds to a stray grain free microstructure is hypothesized to be 0.0066.

Gäumann et al. (2001) derived a criterion based on the G^n/V ratio which states that the microstructure is columnar when the following condition is satisfied everywhere in the weld melt pool.

$$\frac{G^{3.4}}{V} > 2.7 \times 10^{24} \left(\text{K}^{3.4} / \text{m}^{4.4} \text{s} \right) \quad (2)$$

Park et al. (2003) used the degree of constitutional supercooling (CS) at the solidification front as a metric to assess the effects. The basic criterion to avoid CS, which leads to the growth of new grains at the solidification front, is given by:

$$\frac{G}{V} > \left(\frac{G}{V} \right)_{cr} \quad (3)$$

where $(G/V)_{cr}$ is a critical value of G/V , which is proportional to $\Delta T/D_L$ (ΔT is the solidification temperature range, and D_L is the diffusion coefficient of solute in the liquid). In cases where the planar solid/liquid interface breaks down into cellular or dendritic solidification, the theory of CS predicts fairly closely. However, no theory can predict the $(G/V)_{cr}$ for the CET.

Liu and DuPont (2004, 2005) studied the effects of melt-pool geometrical parameters on crystal growth and microstructure development during laser surface melting of single-crystal alloys.

Thanks to the development of welding techniques, much progress has been made to discuss cracking phenomena in the laser join nickel-base superalloys (Egbewande et al., 2010; Hong et al., 2008; Liu et al., 2011). Recently, feasible finite element models were established to provide substantial insights into cracking and how thermal gradient, transient stress and strain were developed in the laser welding process (Dai&Shaw,2001; Hee et al.,2010; Hu&Richardson,2006;Long et al.,2008;Luo et al.,2002; Nishimoto et al., 2002; Wang et al., 2004; Yann et al.,2010 ;Yilbas et al.,2010).

As mentioned previously, albeit laser welding is achieved by rapid heating and rapid cooling, solidification cracking and liquation cracking are prone to be generated in the weld and HAZ. The effect of weld pool shape on the solidification cracking and HAZ cracking susceptibility still remain obscure in many respects for the laser welding. Some experimental conclusions from previous literature have proved that the number of micro cracks at the fusion line in the weld cross-section is reduced with increasing heat input for laser-arc hybrid welding, and cracking might be prevented by adjustment of filler material and heat input for the laser-arc hybrid welding. However, limited information and rationale are available in the literature about how the weld solidification cracking and HAZ crack susceptibility are minimized during laser-arc hybrid welding.

In this chapter, in order to properly explore the capability of the new welding process, i.e. laser-arc hybrid welding, it is necessary to know and understand how laser-arc hybrid welding affects solidification cracking and liquation cracking. A major factor control susceptibility to solidification cracking and liquation cracking are stray grain formation and stress-strain generation during weld pool solidification, respectively. It is important to study and understand stray grain formation and stress-strain generation mechanism during laser-arc hybrid welding, whereas these information are currently scarce in the literature.

2. Solidification cracking and liquation cracking modeling

In this section two kinds of theoretical analysis models are developed to understand cracking phenomena, one is modelling analysis of hybrid laser-arc welding of single-

crystal nickel-base superalloys and the other is modelling analysis HAZ liquation cracking of laser hybrid welding polycrystalline nickel-base alloy and schematic diagram is shown in Fig.1.

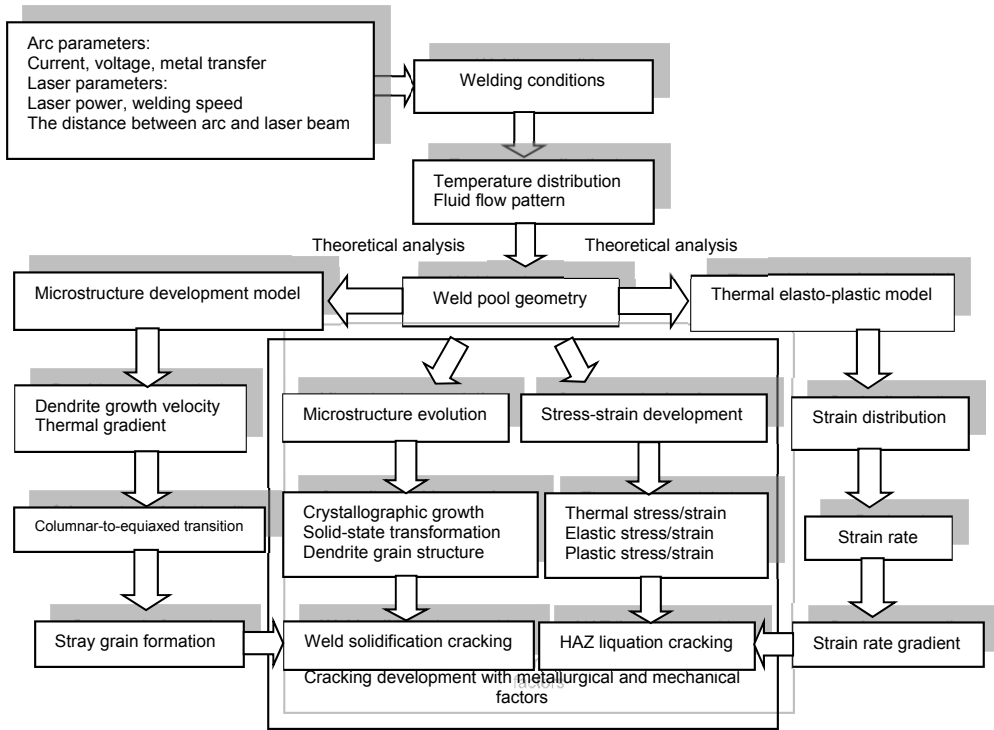


Figure 1. Schematic diagram of cracking development and theoretical analysis for the laser-GMA hybrid welding nickel-base superalloys

2.1. Solidification cracking modeling for single-crystal superalloys welding

2.1.1. Mathematical model description

To execute the analysis on the dynamic behavior and solidification of molten pool, three-dimensional essential governing equations, such as continuity, Navier-Stokes, energy and VOF method equations are iteratively solved with the assumption that the liquid flow is Newtonian, laminar and incompressible.

Continuity equation

$$\nabla \cdot V \rho_l = \dot{m}_s \tag{4}$$

Momentum equation

$$\rho_l \left(\frac{\partial V}{\partial t} + V \cdot \nabla V \right) = \mu \nabla^2 V - \nabla P + \dot{m}_s \cdot V + F - KV \quad (5)$$

Energy equation

$$\rho_l \left(\frac{\partial(U)}{\partial t} + V \cdot \nabla(U) \right) = \nabla \cdot (k_l \nabla T) + \dot{U}_s \quad (6)$$

$$U = \int_T c(T) dT + (1 - f_s) h_{st} \quad (7)$$

where V is the molten metal velocity, \dot{m}_s is a mass source term, P is the hydrodynamic pressure, μ is the dynamic viscosity, F is the body force, ρ_l is the fluid density, U is internal energy per unit mass, k_l is thermal conductivity, T is a local temperature, \dot{U}_s is an energy source term due to mass source term, K is the drag coefficient for the porous media model, f_s is the solid fraction, and $c(T)$ is specific heat.

According to the kinematic motion equation, the VOF function moves according to the velocity field in the fluid, as shown by Equation (8).

$$\frac{\partial F}{\partial t} + \nabla \cdot (VF) = \dot{F}_s \quad (8)$$

For a single fluid, incompressible problem F represents the volume fraction occupied by the fluid. Thus, fluid exists where $F=1$, and void regions correspond to locations where $F=0$. \dot{F}_s represents the change of volume fraction of fluid associated with the mass source .

The local temperature gradient G_{hkl} and dendrite growth velocity V_{hkl} can be calculated to predict the microstructure development across the entire solidification interface. The solidification front produced at the rear part of the weld pool is identified by a solidus curve. The effect of keyhole penetration on weld pool geometry is considered in the analysis of the microstructure development. Fig. 2 illustrates a schematic diagram of the weld pool and associated geometry variables, which illustrate the relationships among the welding velocity \vec{V}_b , the solidification front unit vector \vec{n} , and the dendrite growth velocity \vec{V}_{hkl} . Ψ is the angle between the solidification front normal \vec{n} and a particular dendrite growth direction $[hkl]$. θ is the angle between the surface normal \vec{n} and the welding direction, and ϕ is the angle between the y-axis and the projection of \vec{n} on the y-z plane. L_{al} is the distance between the laser beam and GMA, c_l and c_a are the penetration of laser and arc welds, respectively.

Based on previous analytical methods(Liu&DuPont,2004,2005; Rappaz et al.,1990), a mathematical model is extended for the calculation of stray grain fraction during solidification microstructure development in the hybrid weld pool. The 3-D melt-pool geometry on the rear part of the weld can be described in an ellipsoid formula.

$$\frac{x^2}{a^2} + \frac{y^2}{b^2} + \frac{z^2}{c^2} = 1 \tag{9}$$

where a , b and c are the half-axes of the ellipsoid in the x , y and z directions, respectively. As well, a is the length between the location of the maximum width and trailing point, b is the maximum width of the arc pool, c is the maximum depth and in consideration of the solidification history of weld pool penetration, c_1 is used in this model.

The relationship of the velocity of the dendrite tip, \vec{V}_{hkl} , along a specific $[hkl]$ direction is given by:

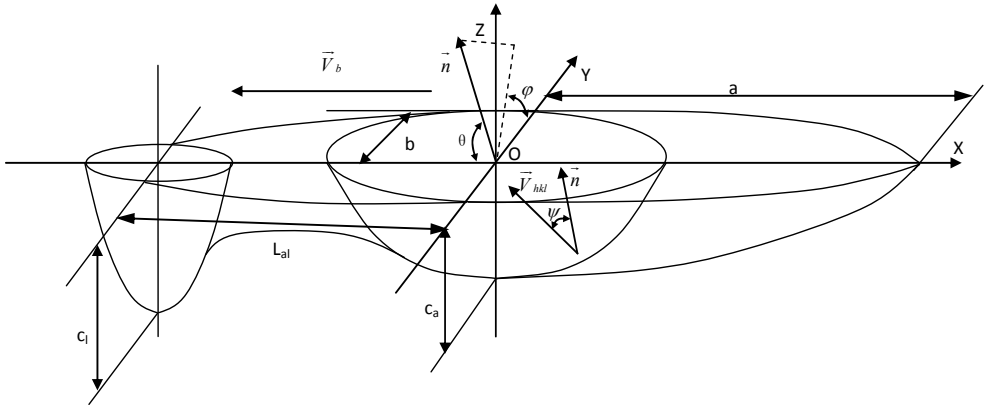


Figure 2. Schematic diagram of weld pool geometry mathematical model and associated variables (Gao&Ojo,2012a)

$$|\vec{V}_{hkl}| = \frac{|\vec{V}_n|}{\cos\psi} = |\vec{V}_b| \frac{\cos\theta}{\cos\psi} \tag{10}$$

where \vec{V}_n is the growth rate of the normal to the solidification front at the liquid-solid interface.

The unit component based on the weld pool normal in the x , y and z axes are determined by

$$\vec{n} = (\cos\theta, \sin\theta \cos\phi, \sin\theta \sin\phi) \tag{11}$$

In order to determine the growth velocity along the $[hkl]$ dendrite growth direction (one of the six $\langle 100 \rangle$ directions), the value of $\cos\psi$ can be determined from the relation:

$$\cos\psi = h \cdot \cos\theta - k \cdot (\sin\theta)(\cos\phi) + l \cdot (\sin\theta)(\sin\phi) \tag{12}$$

The thermal gradient along the dendrite growth direction, \vec{G}_{hkl} , is given by the expression:

$$|\vec{G}_{hkl}| = |\vec{G}_n| \cos\psi \tag{13}$$

where $\left| \overline{G}_n \right|$ is the total thermal gradient direction in the x, y and z directions.

The expression is solved for the volume fraction of stray grains Φ as a function of G_{hkl} and V_{hkl} which yields:

$$\Phi = 1 - e^S \tag{14}$$

$$S = \frac{-4\pi N_0}{3} \left(\frac{1}{(n+1)(G^n / aV)^{1/n}} \right)^3 = -2.356 \times 10^{19} \left(\frac{V_{hkl}}{G_{hkl}^{3.4}} \right)^{3/3.4} \tag{15}$$

The area-weighted average across the entire solidification interface, $\overline{\Phi}$, is given by the expression:

$$\overline{\Phi} = \frac{\sum_k A_k \overline{\Phi}_k}{\sum_k A_k} \tag{16}$$

where the variable k corresponds to the cross-section along the x axis, and A_k and $\overline{\Phi}_k$ are the areas and average Φ values for each cross-section, respectively. More information about this numerical model can be reviewed by the reference (Gao&Ojo,2012a).

Thermal properties of typical nickel-base alloy used in this model are directly taken from values produced in the previous literatures(Anderson et al.,2010; Banarjee&Overfelt,1999; Bonifaz&Richards,2009; Brooks et al.,1996; Luo et al.,2002; Pottlacher et al.,2002; Zeng,2006), and are presented in Table 1.

Material property	Value	Unites
Density of liquid	7578.9	Kg m ⁻³
Density of solid	7742.5	Kg m ⁻³
Viscosity of liquid	0.0074	Kg.s/m
Solidus temperature	1507	K
Liquidus temperature	1613	K
Specific heat of solid	430	J kg ⁻¹ K ⁻¹
Specific heat of liquid	700	J kg ⁻¹ K ⁻¹
Thermal conductivity of solid	11.4	Wm ⁻¹ K ⁻¹
Thermal conductivity of liquid	28.7	Wm ⁻¹ K ⁻¹
Coefficient of thermal expansion	1.33×10 ⁻⁵	K ⁻¹
Latent heat of fusion	1.45×10 ⁵	J kg ⁻¹
Latent heat of vaporization	6.4×10 ⁶	J kg ⁻¹
Surface tension	1.8	N m ⁻¹
Surface tension gradient	-1.37×10 ⁻³	N m ⁻¹ k ⁻¹

Table 1. Nickel-base alloy properties used in this model

2.1.2. Results and discussion

The material adopted for this simulation is a nickel-base superalloy with a thickness of 3 mm. The focal plane of the laser beam is placed on the top surface of the base metal. Arc droplets are assumed to be steadily generated through a certain wire feed rate at an initial speed of 1.5m/s, and initial temperature 1613K. The size of the droplet mainly depends on the diameter of the feeding wire, and the generation frequency is determined by the wire feed rate and wire diameter. The distance between the arc source and laser beam is 3 mm, and the different welding conditions are listed in Table 2.

	Current (A)	Voltage (V)	Laser power (W)	Welding velocity (m s ⁻¹)	Droplet frequency (Hz)	Arc heat distribution parameter(mm)
Weld1	120	21	3667	0.022	217	2.23
Weld2	150	21	3667	0.022	269	2.33
Weld3	180	21	3667	0.022	304	2.45
Weld4	120	21	3667	0.028	217	2.23
Weld5	120	21	3667	0.034	217	2.23
Weld6	120	21	4000	0.022	217	2.23
Weld7	120	21	4332	0.022	217	2.23

Table 2. List of Hybrid welding parameters used for Nickel-base superalloy (Gao&Ojo,2012a)

2.1.2.1. Role of welding parameters on microstructure development

The properties of weld metal are affected by solidification behavior parameters, such as growth rates, temperature gradients, undercooling and alloy constitution, which are often useful to determine the development of microstructures in weld zones (Farzadi et al., 2010; He et al., 2005; Roy et al., 2006). In this study, the effect of undercooling has been simplified and thereby the solidification parameters, such as cooling rate, thermal gradient, and solidification velocity, are computed by the weld pool geometry considering only the heat transfer and fluid flow.

Since the shape of the weld pool remains constant under a steady-state condition, the solidification rate can be calculated with position along the fusion boundary. The steady state solidification rate, V_n , is related to the welding velocity in the following formula relation:

$$V_n = V_d \cos \theta \quad (17)$$

where θ is the angle between the normal to the solid/liquid boundary and the welding direction, and V_d is the welding velocity. The solidification rate increases from the edge of the weld pool and pool bottom, where θ is nearly 90°, to the weld centerline, where the velocity equates V_d along the fusion boundary (Farzadi et al., 2010).

To remove the constitutional undercooling ahead of the growth front for columnar grain growth, a high thermal gradient is required and low solidification velocities are desired

(Bussac & Gandin, 1997; Dong, 2007). The values of the temperature gradient and solidification rate vary with position along the entire solidification interface of the weld pool. The density of temperature isotherm in the maximum width is greater than that of the trailing portion of the pool boundary, so the temperature gradient is higher at the fusion line than the centerline. The ramifications of cooling rates ($G \times R$) along the solid/liquid interface with different welding conditions are presented in Fig.3.

The cooling rate is higher at the maximum width of the fusion boundary and lower at the weld centerline for each case in Fig.3 (A). It is observed that the average range of the cooling rate is 4×10^3 - 2.4×10^4 K/s. The magnitude of the cooling rate decreases with an increase in the arc current and laser power, while an opposite effect will occur with a decrease in welding speed. In general, increasing the welding speed or decreasing welding heat sources power will increase the cooling rate, and the latter will result in an increase of residual stress and strain. In addition, the solidification velocities will be high and this may lead to more extensive non-equilibrium solidification and partitioning at high welding speeds (Rai et al., 2007; Vitek, 2005).

The cooling rate along the solid/liquid boundary of penetration in the conjoint zone is shown in Fig.3 (B). It is observed that the magnitude of the cooling rate is 10^5 - 7×10^5 K/s, which is approximate to the typical laser welding range of 10^4 - 10^6 K/s (Ral et al., 2009). It is higher at the bottom of the keyhole than that at the weld crown solid/liquid boundary. This distribution is consistent with higher convective heat transfer near the pool surface than the weld root. The Marangoni convection brings fluid from the weld center to the peripheral solid/liquid interface, which yields a lower thermal gradient on the weld pool surface. It can be further found that the value of the cooling rate near the bottom of the keyhole dramatically increases with increase in the arc current, welding speed and laser power, and the effect of laser power is the most obvious. Meanwhile, the magnitude of the cooling rate near the maximum depth of the weld pool is much higher than that of the rear part of the weld pool.

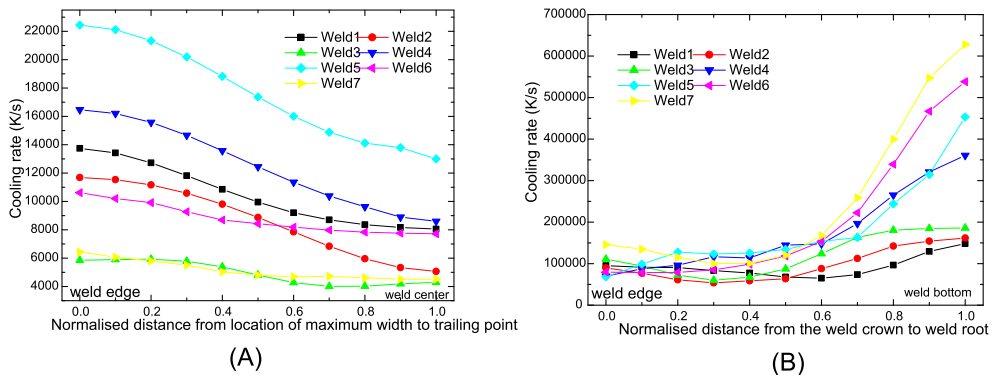


Figure 3. The calculated cooling rate along the solidification interface for different welding conditions, (A) Weld pool surface, (B) Weld penetration direction (Gao&Ojo, 2012a)

Secondary dendrite arm spacing (SDAS) is estimated from the cooling rates ($G \times R$). The dendrite arm spacing increases from the interface of maximum weld width to the weld centerline, and decreases from the weld crown to weld root, as shown in Fig.4. These explicate that the finer arm spacing is always found near the fusion boundary on the weld crown or part of the weld root, and the coarsest structure occurs in the center of the weld crown.

As the arc current and laser power were increased, the dendrite trunk spacing along the rear of the solid/liquid interface of the weld pool increases and the magnitude of the SDAS is between 2.88 and 4.2 μm . Dendrite arm spacing decreases with increasing velocity, more obvious for higher welding speed, and the characteristic magnitude of SDAS is between 2.18 and 3.2 μm . The calculated dendrite arm spacing along the solidification interface has the same tendency as the measured values, but the former is slightly greater than the latter, especially near the fusion boundary, see Fig.4 (A).

The SDAS near the solid/liquid boundary along the weld penetration is presented in Fig.4 (B). The dendrite trunk spacing near the root part of the weld gradually decreases with increase in the arc current, welding speed and laser power. The calculated dendrite arm spacing along the direction of weld penetration agrees reasonably well with the measured value near the lower region of the keyhole, and the experiment result is higher in value than that calculated on the weld crown. Hybrid welding allows for the weld metal to remain at a high temperature for a longer time and cool at lower rates compared to approximated laser power performed at the same welding speed (Moore et al., 2004). This results in a coarser dendritic microstructure region where the laser and arc beams simultaneously interact, which is at the weld crown center rather than the solidification boundary.

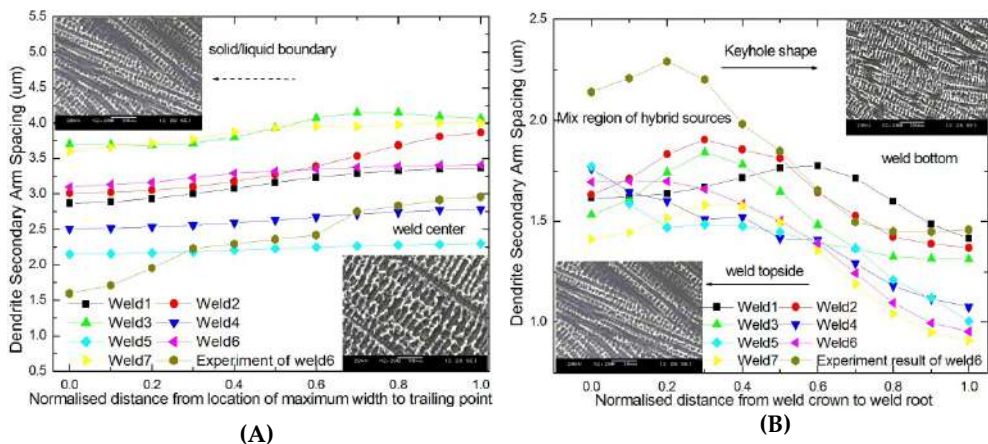


Figure 4. Predicted and experimental results of SDAS along the weld pool solidification interface, (A) Weld pool surface, (B) Weld penetration direction

Since the effect of the crystallographic orientation of the weld on the overall tendency to form stray grains is minimal, the weld direction [100] and sample surface plane (001) are specified for the sample orientation. The angles (θ , ϕ), which characterize the normal to the solidification front, are determined from three-dimension weld geometry, and dendrite growth pattern transitions can occur along the solidification interface. In consideration of the average growth velocity along the solidification interface front at each analysis cross-section, the dendrite orientation velocities of [100], [010] and [001] are presented in Fig.5. The θ , ϕ , ψ terms are used to calculate the dendrite growth velocity by Eqs. (10) and (12). The velocities of the [100] dendrites are always equal to those by welding, regardless of the weld pool shape for the (001) || [100] orientations (Rappaz et al.,1990), and average dendrite tip velocity in [010] and [001] is higher than that of the [100] orientation along the rear part of the solid/liquid interface. The average dendrite tip velocity of the [001] orientation is much larger than that of [010], and the latter is higher than that of [100] near the solidification interface. It can be underlined that $\psi > \theta$ and the dendritic orientation does not coincide with the solidification front for [010] and [001]. The discrepancy between ψ and θ is larger in [001] than [010]. At the weld center, the dendrite growth velocities of [010] and [001] are lower than those at the solid/liquid boundary. For case (A), there are obvious transition positions among the solidification interface with differences in the average dendrite velocity for the [001] orientation. The average dendrite growth velocity of the [010] and [001] orientations of weld2 are lower than the other cases near the solidification interface. For case (B), the solidification time is much less at high welding speeds, and dendritic arrays do not have sufficient time to establish steady state spacing. The average dendrite tip velocity in the [010] and [001] orientations are irregularly volatile along the solidification front at the highest welding speed. It is also observed that the welding speed affects the magnitude of the dendrite growth velocity for the [001] orientation near the solidification interface. For case(C), the average dendrite tip velocity for the [001] orientation monotonically increases with increase in laser power, and its magnitude is the largest near the fusion line with the highest laser power.

2.1.2.2. Role of welding parameters on stray grain formation

The area-weighted average values of stray grain formation tendency with different welding conditions is shown in Fig.6, and partial columnar growth with the value of Φ is below 0.5 and above 0.0066 with increase in arc current or welding speed. These welding parameters are beneficial for avoiding CET during the entire welding process. The effect of welding speed on Φ is more complex. The latter initially increases with increasing welding velocity before decreasing at higher speeds. This can be explained through the changes in temperature gradient transition with different welding speeds. As the welding speed is increased, the temperature gradient is generally affected by two opposing factors (Grong, 1997). Thus, the magnitude of Φ will subsequently decrease with a further increase in the welding speed. The results from Anderson et al. (2010) and Vitek (2005) are similar to those illustrated here, in which the fraction of stray grain formation is generally observed to reach the maximum at an intermediate speed, and then always decreases as the speed increases.

Hitherto, literature mainly focused on wide and shallow pool shapes and higher laser power conditions were omitted due to limitations in simulation and method (Anderson et al., 2010; Gäumann et al., 2001; Vitek, 2005). From the investigations of this model, the effect of higher laser power is slightly negative on SG formation. Laser power is the primary factor in weld penetration and weld pool geometry which determines the shape of the liquid/solid interface and the slope of the weld pool edges. The local angle ϕ along the solidification interface in the nail-head shaped weld contributes more to stray grain formation. Hence, the typical keyhole geometry in a hybrid pool is more prone to create CET in the weld pool

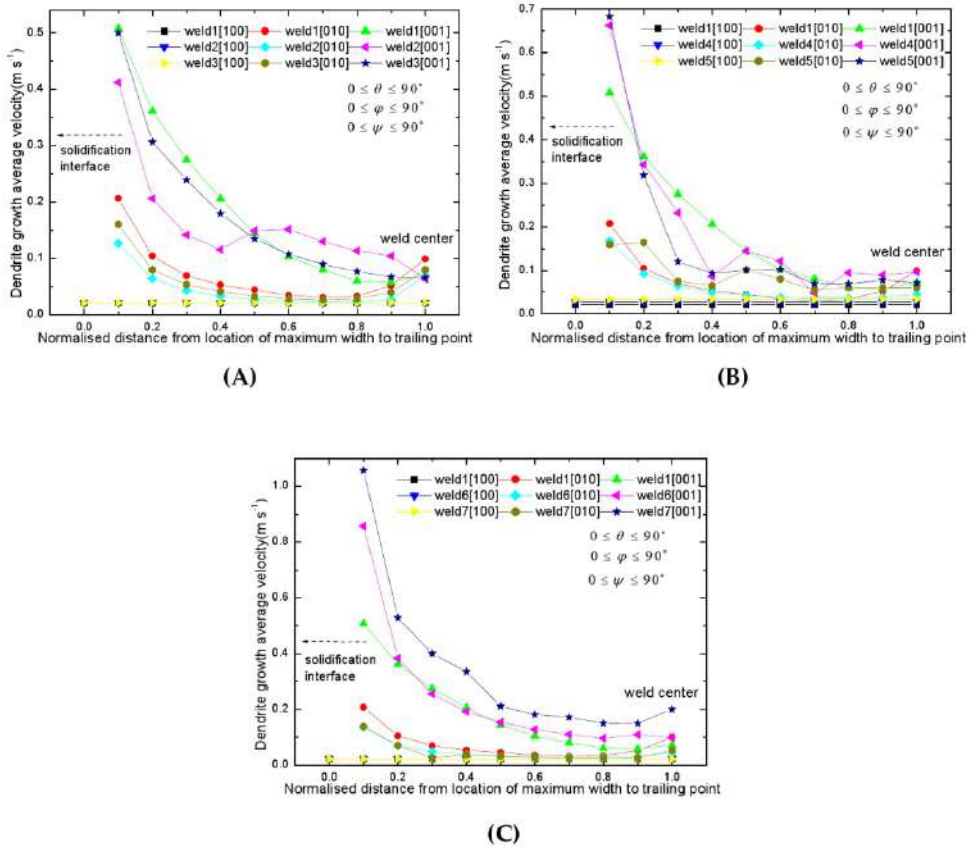


Figure 5. Dendrite tip velocity distribution around rear part of weld pool with different welding conditions, (A) variation of arc current, (B) variation of welding velocity, (C) variation of laser power (Gao&Ojo,2012a)

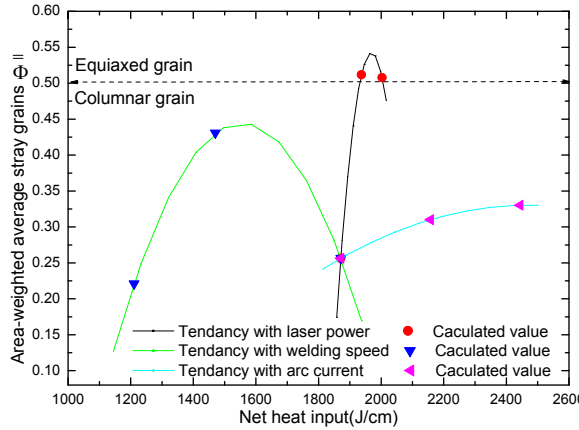


Figure 6. Area-weight average values of stray grain formation distribution as a function of heat input (Gao&Ojo,2012a)

when considering the distribution of Φ in the three directions from the above simulation, whereas the net effect of higher laser power on CET can be verified by the experimental work of Anderson et al. (2001), who used similar welding power intensity with an electron beam.

From the different tendencies of Φ summarized by the calculated value, higher welding speed and lower arc current or laser power ameliorate to minimize/avoid stray grain formation. In contrast, slower welding speed and higher arc current or laser power exacerbate stray grain formation, and abundant equiaxed dendrite will be yielded. Based on the above analysis, welding conditions should be optimized to minimize the overall likelihood of forming stray grains.

2.2. Liquation cracking modeling for polycrystalline superalloys welding

2.2.1. Mathematical model description

In consideration of tractable object symmetry, a 1/2 model including the weld metal, deposition filler material and base metal is adopted. A sequential thermal-mechanical finite element analysis is performed in present study based on ANSYS 13 code. Specifically, 2D thermal solid plane55 is used to simulate the temperature field and 2D structure element plane42 is then used to calculate the stress-strain field with the nodal temperature extracted from the thermal analysis as the load. All the material properties used in the model are displayed in Fig.7.

In this model, the laser-GMA hybrid process employs heating the base metal in a localized zone with sequent transient heat sources. The effect of the synergistic interaction between laser and GMA on the heat flux distribution is not considered in this simulation. The distribution of laser beam energy is assumed to be Rotary-Gauss body heat source, which is

suitable for nail-head shape with large depth to width ratio of molten pool along the workpiece thickness direction (Wu et al., 2004).The distribution of the GMA energy is assumed to be a Gaussian flux over the workpiece surface.

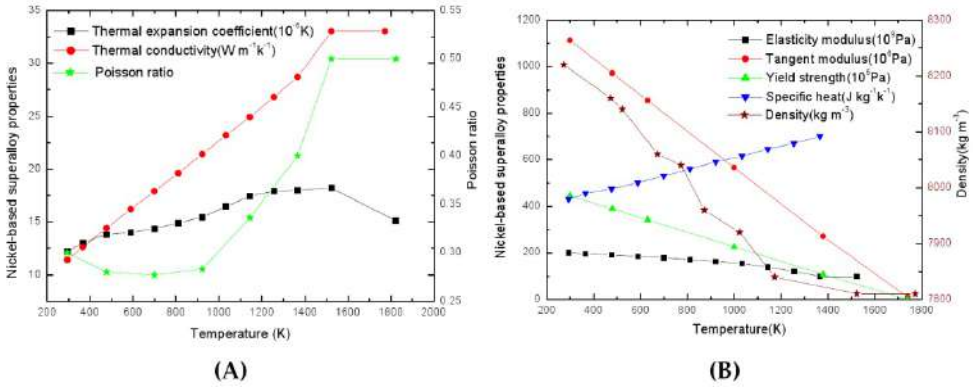


Figure 7. The physical and mechanical properties used for the simulation (Gao&Ojo, 2012b)

The crystallographic orientation of the dendrites is not taken into account and they are assumed to grow in a direction that is always perpendicular to the growth front. Local growth velocity of dendrite along the solidification front as a function of undercooling is represented by the following function (Hunziker et al., 2000):

$$v_{kin} \{ \Delta T \} = a \Delta T^n \tag{18}$$

where $n=3.05$, $a=1.2754 \times 10^{-7} \text{ms}^{-1} \text{K}^{-3.05}$ and the undercooled liquid is the region between the growth front and liquidus temperature. Using growth rate R and the temperature gradient G along the fusion boundary, the cooling rate ($G \times R$) can be calculated.

For the case of nonlinear material, the definition of total strain is given:

$$\{ \varepsilon \} = \{ \varepsilon^{el} \} + \{ \varepsilon^{th} \} + \{ \varepsilon^{pl} \} \tag{19}$$

where ε^{el} is the elastic strain vector, ε^{th} is the thermal strain vector, ε^{pl} is the plastic strain vector but the creep strain vector and swelling strain vector are ignored.

As mentioned above, the thermal elasto-plastic material model, based on von Mises yield criterion, temperature dependent mechanical properties and linear kinematic hardening rule, is considered. The incremental forms of stress-strain relation are described as (Akbari & Sattari-Far, 2009; Chang & Lee, 2009; Kong & Kovacevic, 2010):

$$[d\delta] = [D^{ep}] \{d\varepsilon\} - [D^{th}] dT \tag{20}$$

$$[D^{ep}] = [D^e] + [D^p] \tag{21}$$

where $d\delta$ is the stress increment, $d\varepsilon$ is the strain increment, $[D^e]$ is the elastic stiffness matrix, $[D^p]$ is the plastic stiffness matrix, $[D^h]$ is the thermal stiffness matrix and dT is the temperature increment. More information about this numerical model can be reviewed by referring to Gao (2012).

	Laser power (kW)	Arc power (kW)	Welding speed (m/min)	Time of laser heating (s)	Time of arc heating (s)	Time interval for hybrid (s)
Laser	2	-	3	0.012	-	-
Laser	4	-	3	0.012	-	-
Laser	6	-	3	0.012	-	-
Laser	4	-	2	0.018	-	-
Laser	4	-	4	0.009	-	-
Laser	4	-	6	0.006	-	-
Laser-GMA	2	4.75	3	0.012	0.05	0.02
Laser-GMA	4	4.75	3	0.012	0.05	0.02
Laser-GMA	6	4.75	3	0.012	0.05	0.02
Laser-GMA	4	4.75	2	0.018	0.075	0.03
Laser-GMA	4	4.75	4	0.009	0.0375	0.015
Laser-GMA	4	4.75	6	0.006	0.025	0.01

Table 3. Design laser and laser-GMA hybrid welding conditions (Gao&Ojo, 2012b)

Predictions for the cracking susceptibility have been estimated for a wide range of welding conditions. Two types of welding processing, three kinds of laser power and four kinds of welding speed have been investigated, which result in a total twelve laser fabrication conditions, as shown in Table 3. There is a time interval for laser-arc hybrid welding, which sequentially heats the base material due to the distance between laser beam and arc source.

2.2.2. Results and discussion

2.2.2.1. Weld pool solidification characteristics

The HAZ cracking in the waisted zone over the bead cross-section is attributed to the greater amount of grain boundary liquation during the cooling process. The solidification completion temperature of liquated grain boundary is around 1383K, which affects the Laves cluster dissolution and grain boundary liquid phase (Nishimoto et al., 2002). The shape of weld pool and cooling rate along localization fusion boundary derived from temperature isothermal are shown in Fig.8. The abscissa means the distance from the surface to the root of the weld bead along the fusion boundary. The left ordinate value indicates the weld geometry, which is the distance from the weld bead centerline and the right ordinate value is the cooling rate.

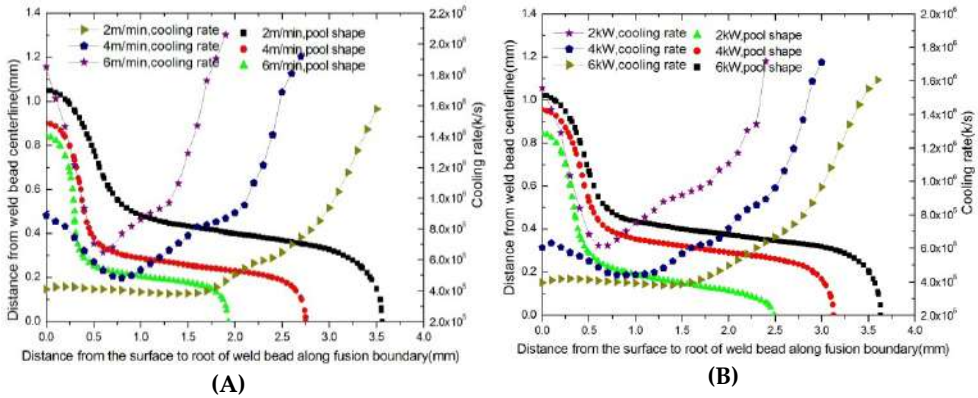


Figure 8. Correlation between the shape of weld pool and cooling rate with welding parameters for laser welding , (A) variation of welding speed, (B) variation of laser power

The results indicate that the cooling rate is a function of position along the fusion boundary among the weld fusion zone and varies simultaneously with the penetration shape. The shape decay of temperature in the surface region is attributed to the heat loss from the surface region due to heat transfer of conduction and convection in this region. Temperature decay in the initially high temperature region at the root of the keyhole during the laser beam moving away, which is due to the attainment of high temperature gradient in this region, results in faster solidification. The neck zone over the bead cross-section is more liable to heat stagnation than in other regions and undergoes lower cooling rates than other parts. That means that the maximum solidification time exists at the neck zone of the weld shape and the minimum solidification time occurs at the root of the keyhole. Thus, there is obvious solidification time transition region along the fusion boundary line. There is a steep cooling rate in the vicinity of the neck zone. With an increasing welding speed, the cooling rate in the neck zone gets steeper and weld pool geometry substantially decreases, respectively. Correspondingly, the shapes of weld pool synchronously enlarge with a laser power increase and the concomitant cooling rates considerably decrease.

Correlation between weld pool geometry and cooling rate of the hybrid pool characteristic are shown in Fig.9. The difference in these relationships between laser and hybrid laser arc welding are compared, and several conclusions can be drawn from the proposed study. First, with incorporating the effect of filler material on the weld bead cross-section, the weld pool geometry variation with welding speeds of laser hybrid welding are different from that of laser welding. Employing an additional heat and deposition metal lead to an extended region of weld width and increased neck zone radius of curvature. The volume of weld filler metal strongly depends on the welding speed and decreases with an increasing welding speed. Second, the rational link between cooling rate and weld pool geometry suggest that the neck zone over bead cross-section is more liable to heat stagnation and has larger solidification time, therefore, the minimized cooling rate occurs more readily at locations where it is underside of neck zone, which is especially observed in the neck-like waisted

zone of lower heat input of laser-GMA hybrid welding as well as laser welding. Third, laser-GMA hybrid welding alters the temperature distribution of the weld fusion zone and substantially enhances the cooling rate near the weld bead neck zone. The magnitude of cooling rate is lower than that of laser welding. Cooling rate attains low value in the region of neck zone due to higher solidification time, and obviously increases near the bottom of the keyhole. The relationship between the weld pool shape and the cooling rate elucidates clearly localized solidification behavior and enables the cause of liquation cracking to be explained.

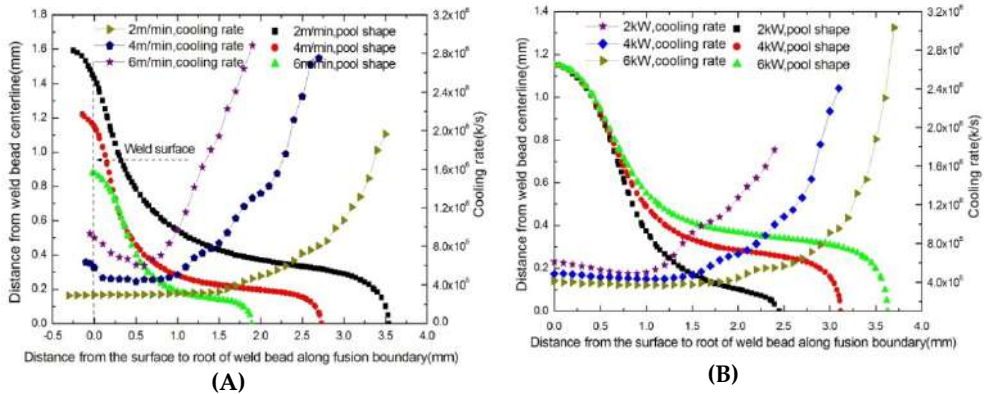


Figure 9. Correlation between the shape of weld pool and cooling rate with various welding conditions for laser-arc hybrid welding, (A) variation of welding speed, (B) variation of laser power

2.2.2.2. HAZ cracking analysis

Constitutional liquation theory and grain boundary segregation mechanism are associated with weld HAZ liquation cracking. Nishimoto et al (2002) explained the liquation cracking mechanism in laser welds of Inconel 718. The molten liquid of the Laves phase eutectically is liquated at a temperature below the solidus temperature of the matrix and infiltrates along the grain boundaries. Tensile plastic strain/stress induced by thermal shrinkage is imposed on the liquid film during the subsequent cooling process and cracking will occur with an attendant buildup of higher strain/stress across the grain boundaries.

Despite the fact that the HAZ cracking metallurgical mechanism of nickel-base alloy is revealed, the limited information is available in the literature about the explanation of the relationship between welding conditions and cracking susceptibility during the laser and hybrid laser-GMA welding.

For the purpose of comparison of crack susceptibility with various welding conditions and different welding types, von Mises stress and 1st principal strain are not sensitive to reflect these discrepancies (Gao, 2012). Quantitative evaluation of solidification crack with behavior of ductility near the solidification boundary can be calculated by crack susceptibility strain rate, which is represented:

$$\dot{\epsilon} = \frac{\epsilon_1}{t_s} \tag{22}$$

where ϵ_1 denotes total 1st principal strain along the fusion boundary, t_s denotes the lapse time of solidification boundary from liquidus temperature to crack sensitive temperature, 1383K.

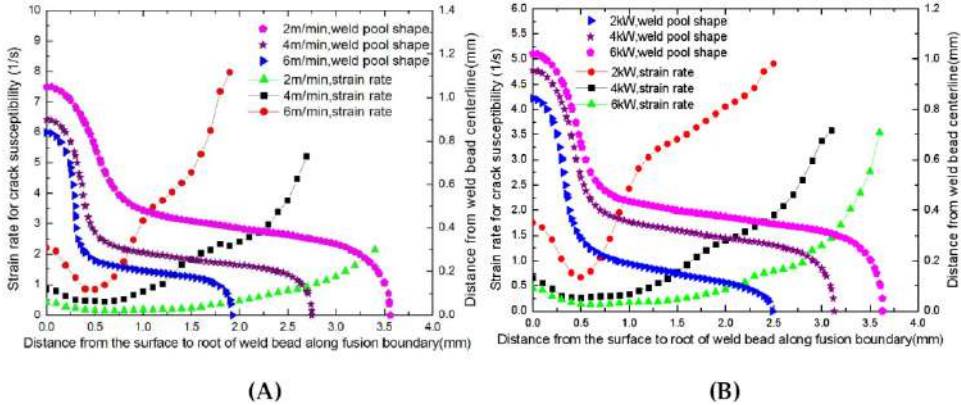


Figure 10. Correlation between the shape of weld pool and strain rate with various welding conditions for laser welding, (A) variation of welding speed, (B) variation of laser power(Gao&Ojo, 2012b)

Relations among crack susceptibility strain rate and pool shape of laser weld are shown in Fig.10. As a whole, it is worth noting that the value of the geometry of weld pool is nearly in the same order of the crack susceptibility strain rate, and the curve shapes of crack susceptibility strain rate conspicuously change with various welding conditions. It should be noticed that there is a concave shape, which suddenly decreases and then increases in the strain rate curve adjacent to the neck region of weld pool shape that means it is more susceptible to initiate crack in the stage of solidification. After the neck zone, strain rate increases until it is at the root of the keyhole and reaches a maximum value. The reason for this gradual increase in strain rate is thought to be due to the interaction between strain distribution and solidification characteristic within the weld pool. It can be estimated that greater welding speed and smaller laser power, namely less heat input results in the steeper curve of crack susceptibility strain rate, which is prone to engender and propagate cracks in the neck zone. Thus, the crack susceptibility strain rate itself is a major parameter determining the tendency of crack susceptibility.

As mentioned before, the effects of the welding conditions on the solidification crack susceptibility are interrelated. In contrast, laser-GMA hybrid welding can minimize the risk of variation of strain rate in the neck zone of the weld bead, and the value of these ductility curves are obviously smaller than that of laser welding, as shown in Fig.11. The strain rate becomes sharp near the neck region with an increasing welding speed or decreasing laser power.

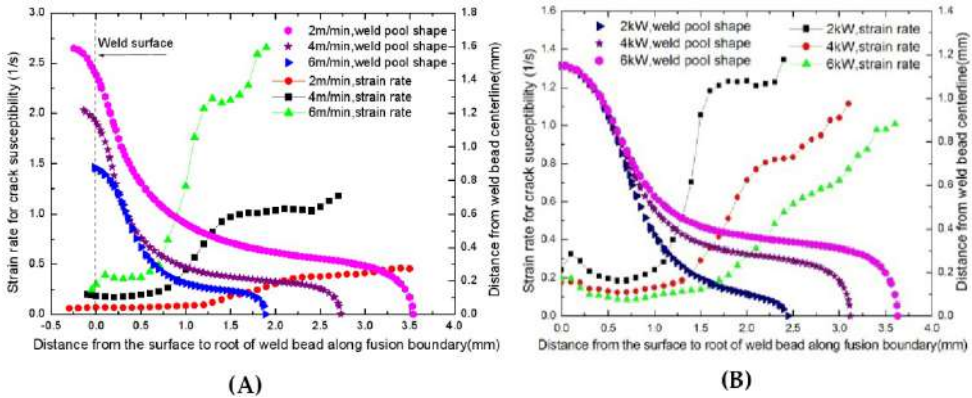


Figure 11. Correlation between the shape of weld pool and strain rate with various welding conditions for laser-arc hybrid welding, (A) variation of welding speed, (B) variation of laser power(Gao&Ojo, 2012b)

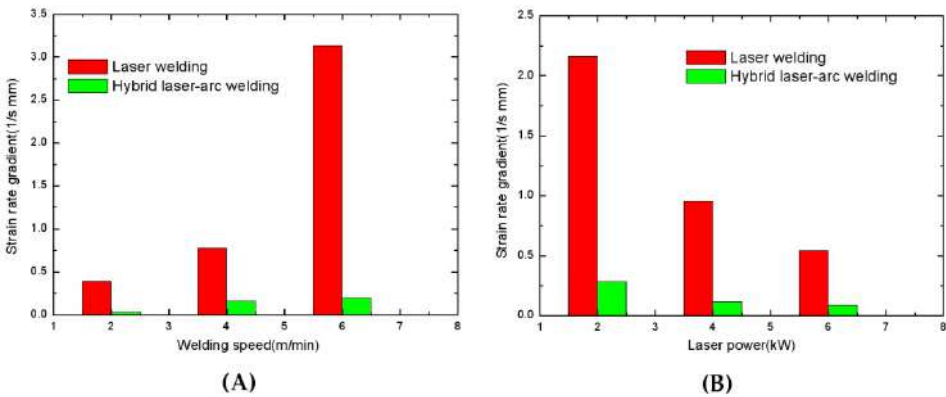


Figure 12. The strain rate gradient near the neck region with different welding conditions, (A) variation of welding speed, (B) variation of laser power

Comparison of strain rate gradient near the neck region under different welding conditions is illustrated in Fig.12. It is worth noting that the strain rate gradient decreases with heat input increase. The values of strain rate gradient of laser welding are on the whole higher than those of hybrid laser arc welding. It clearly reveals that laser welding is more susceptible to liquation cracking and the crack is located more in the neck region during low heat input. Therefore, the solidification cracking relating the liquid film stage in cracking sensitive temperature range can be explained from the view point of the contribution of strain rate gradient. From the above results, using strain rate gradient for evaluation of the susceptibility to HAZ liquation cracking provides theoretically understanding of how laser-arc hybrid welding produces less susceptibility to liquation cracking compared to laser welding as previous reported experiment results (Stelling et al., 2005).

3. Conclusions

These models provide valuable insight into the metallurgical and mechanical driving force for cracking. These results will be used to predict the effect of welding conditions on the potential for weld solidification cracking and HAZ liquation cracking and to interpret the experimental results during laser-GMA hybrid welding single-crystal and polycrystalline nickel-base superalloys. It should be noted that higher welding speed and lower laser power or arc current are beneficial for minimizing stray grain formation for laser-GMA welding single-crystal nickel-base superalloys, but generally lower heat input exacerbate HAZ liquation cracking for laser-GMA welding polycrystalline nickel-base superalloys. These promising results will also be used to identify preferred welding conditions that minimize stray grain formation, local stress-strain and associated cracking. For the future research, many efforts will focus on the different welding parameters on the cracking trend with optimized tactics and substantiate them by experiments.

For the solidification cracking modeling of welding of single-crystal nickel-base superalloys, there are some conclusions:

1. In almost all cases, the cooling rate is higher at the maximum width of the fusion boundary and at the bottom of the keyhole, while lower at the weld centerline and weld crown solid/liquid boundary. Meanwhile, it is shown that the finer arm spacing is always found near the solid/liquid boundary of the weld crown or the weld root, and the coarsest structure occurs in the center of the weld crown;
2. The average dendrite tip velocity of the [001] orientation is much greater than that of [010], and the latter is higher than that of [100] near the solidification interface for the (001) || [100] orientations. At the weld center, the average dendrite growth velocity of [010] and [001] is lower than that at the solid/liquid boundary;
3. Higher welding speed and lower laser power or arc current are beneficial for minimizing stray grain formation, when taking into consideration, on average, the tendency for stray grain formation over the entire weld pool;
For the HAZ liquation cracking modeling of welding of polycrystalline nickel-base superalloys, there are also some conclusions:
4. The neck zone radius of curvature in the laser hybrid pool is larger than that of the laser pool, which means the neck region is more liable to heat stagnation and has a smaller cooling rate. The minimized cooling rate occurs more readily at the underside of the neck zone, which is observed in the neck-like waisted zone of laser-GMA hybrid welding as well as laser welding;
5. Laser-GMA hybrid welding alters the temperature distribution of the weld fusion zone and substantially improves the cooling rate near the weld bead neck zone; the magnitude of cooling rate is lower than that of laser welding. The cooling rate attains low value in the region of neck zone due to higher solidification time and increases near the bottom of the keyhole;
6. The values of strain rate gradient near the neck region of laser welding are on the whole higher than those of hybrid laser-GMA welding. Laser welding is more susceptible to

liquation cracking and the crack is located more in the neck region during lower heat input compared to laser-GMA hybrid welding;

7. The weld pool shape has a strong influence on the stress-strain pattern, and a neck weld pool shape can have a detrimental effect on the HAZ cracking behavior. Adding the arc heat source alters the strain distribution, and strain rate gradient provides theoretically understanding of how laser-GMA hybrid welding produces less susceptibility to liquation cracking compared to laser welding.

Author details

Zhiguo Gao

University of Manitoba, Canada

Acknowledgement

Thanks a lot to the Journal of Acta Materialia, Journal of Materials Science Research and International Journal of Advanced Manufacturing Technology, the author makes reference to some previous works in this chapter.

4. References

- Akbari, D. & Sattari-Far, I. (2009). Effect of the welding heat input on residual stresses in butt-welds of dissimilar pipe joints. *International journal of pressure vessels and piping*, Vol.86, No.11, pp. 769-776
- Anderson, T.; DuPont, J. & DebRoy, T. (2010). Origin of Stray Grain Formation in single-crystal superalloy weld pools from Heat Transfer and Fluid Flow Modeling. *Acta Materialia*, Vol. 58, No.4, pp.1441-1454
- Banerjee, P. & Overfelt, R. (1999). Viscosity measurements of industrial alloys using the oscillating cup technique. *International Journal of Thermophysics*, Vol.20, No.6, pp.1791-1800
- Bonifaz, E. & Richards, N. (2009). Modeling cast IN-738 superalloy gas tungsten arc welds. *Acta Materialia*, Vol.57, No.57, pp.1785-1794
- Brooks, R.; Monaghan, B. & Barnicoat A. (1996). The Physical properties of alloys in the liquid and "Mushy" states, *International Journal of Thermophysics*, Vol.17, No.5, pp.1151-1161
- Bussac, A. & Gandin, C. (1997). Prediction of a process window for the investment casting of dendritic single crystals. *Materials Science and Engineering: A*, Vol.237, No.1, pp. 35-42
- Chang, K. & Lee, C. (2009). Finite element analysis of the residual stresses in T-joint fillet welds made of similar and dissimilar steels. *Int J Adv Manuf Technol*, Vol.41, No.3-4, pp.250-258
- Claus, B. & Flemming, O. (2005). Review of laser hybrid welding. *Journal of Laser Applications*, Vol.17, No.1, pp.2-13

- Dai, K. & Shaw, L. (2001). Thermal and stress modeling of multi-material laser processing. *Acta Materialia*, Vol.49, No.20, pp. 4171-4181
- Dong, H.(2007). Analysis of Grain Selection during Directional Solidification of Gas Turbine Blades, *Proceedings of the World Congress on Engineering 2007*, Vol.II WCE 2007, ISBN: 978-988-98671-2-6, London, U.K., July 2-4, 2007
- Egbewande, A.; Buckson, R. & Ojo, O. (2010). Analysis of laser beam weldability of Inconel 738 superalloy, *Materials characterization*, Vol.61, No.5, pp.569-574
- Farzadi, A.; Serajzadeh, S. & Kokabi, A. (2010) Investigation of weld pool in aluminum alloys: Geometry and solidification microstructure. *International journal of thermal sciences*, Vol. 49, No.5, pp.809-819
- Gao, Z.; Wu, Y. & Huang, J. (2009). Analysis of weld pool dynamic during stationary laser-MIG hybrid welding. *Int J Adv Manuf Technol*, Vol.44, No.9-10, pp.870-879
- Gao, Z. (2012). Numerical modeling to understand liquation cracking propensity during laser and laser hybrid welding (I). *Int J Adv Manuf Technol*, Doi:10.1007/s00170-012-3907-8, pp.1-13
- Gao, Z. & Ojo, O.(2012a) Modeling analysis of hybrid laser-arc welding of single-crystal nickel-base superalloys, *Acta Materialia* ,Vol.60,No.6-7,pp.3153-3167
- Gao, Z. & Ojo, O.(2012b) Numerical modeling of HAZ liquation cracking tendency during laser and hybrid laser-arc welding processes, *Journal of Materials Science Research* , Vol.1,No.2,pp.42-55
- Gäumann, M.; Bezençon, C.; Canalis, P. & Kurz, W. (2001). Single-crystal laser deposition of superalloys: processing microstructure maps. *Acta Materialia*, Vol.49, No.6, pp.1051-1062
- Grong, Ø. (1997). *Metallurgical Modeling of Welding*, The Institute of Materials, London, U.K.
- He, X.; Elmer, J. & DebRoy, T. (2005). Heat transfer and fluid flow in laser microwelding. *J. Appl. Phys.* Vol. 97, No.8, pp.084909-084909-9
- Hee, S.; Han, S.; You, C. & Sung, M. (2010). Analysis of residual stress on AH32 butt joint by hybrid CO₂ laser-GMA welding. *Computational materials science*, Vol. 49, No.2, pp.217-221
- Hong, J.; Park, J.; Park, N.; Eom, I.; Kim, M. & Kang, C. (2008). Microstructures and mechanical properties of Inconel 718 welds by CO₂ laser welding. *Journal of materials processing technology*, Vol.201, No.1-3, pp.515-520
- Hu, B. & Richardson, I. (2006). Mechanism and possible solution for transverse solidification cracking in laser welding of high strength aluminium alloys. *Materials science and engineering, A* ,Vol.429,No.1-2,pp.287-294
- Hunt J. (1984). Steady state columnar and equiaxed growth of dendrites and eutectic. *Materials Science and Engineering*, Vol.65, No.1, pp.75-83
- Hunziker, O.; Dye, D. & Reed, R. (2000). On the formation of a centerline grain boundary during fusion welding. *Acta Materialia*, Vol.48, No.17, pp. 4191-4201
- Kong, F.& Kovacevic, R. (2010). 3D finite element modeling of the thermally induced residual stress in the hybrid laser/arc welding of lap joint. *Journal of Materials Processing Technology*, Vol.210, No.6-7, pp.941-950
- Liu, W. & DuPont. J. (2004). Effects of melt-pool geometry on crystal growth and microstructure development in laser surface-melted superalloy single crystals.

- Mathematical modeling of single-crystal growth in a melt pool (part I). *Acta Materialia*, Vol.52, No.16, pp.4833-4847
- Liu, W. & DuPont, J. (2005). Effects of substrate crystallographic orientations on crystal growth and microstructure development in laser surface-melted superalloy single crystals. Mathematical modeling of single-crystal growth in a melt pool (Part II). *Acta Materialia*, Vol.53, No.5, pp.1545-1558
- Liu, F.; Lin, X.; Yang, G.; Song, M.; Chen, J. & Huang, W. (2011). Microstructure and residual stress of laser rapid formed Inconel 718 nickel-base superalloy. *Optics & laser technology*, Vol.43, No.1, pp.208-213
- Long, R.; Liu, W.; Xing, F. & Wang H. (2008). Numerical simulation of thermal behavior during laser metal deposition shaping. *Transactions of Nonferrous Metals Society of China*, Vol.18, No.3, pp.691-699
- Luo, X.; Shinozaki, K. & Kuroki, H. (2002). Analysis of temperature and elevated temperature plastic strain distributions in laser welding HAZ study of laser weldability of Ni-base superalloys. *Welding International*, Vol.16, No.5, pp.385-392
- Moore, P.; Howse, D. & Wallach, E. (2004). Microstructures and properties of laser/arc hybrid welds and autogenous laser welds in pipeline steels. *Sci Technol Weld Joining*, Vol. 9, No.4, pp.314-322
- Nishimoto, K.; Woo, I. & Shirai, M. (2002). Analyses of temperature and strain distributions in laser welds study of the weldability of Inconel 718 cast alloy. *Welding International*, Vol.16, No.4, pp.284-292
- Park, J.; Babu, S.; Vitek, J.; Kenik, E. & David, S. (2003). Stray grain formation in single crystal Ni-base superalloy welds. *Journal of Applied Physics*, Vol.94, No.6, pp.4203-4209
- Pottlacher, G.; Hosaeus, H.; Kaschnitz, E. & Seifert, A. (2002) Thermophysical properties of solid and liquid inconel 718 alloy. *Scandinavian Journal of Metallurgy*, Vol.31, No.3, pp.161-168
- Rai, R.; Roy, G & DebRoy, T. (2007). A Computationally Efficient Model of Convective Heat Transfer and Solidification Characteristics during Keyhole Mode Laser Welding. *J Appl Phys.*, Vol. 101, No. 05409, pp.1-11
- Ral, R.; Palmer, T.; Elmer, J. & Debroy, T. (2009). Heat Transfer and Fluid Flow during Electron Beam Welding of 304L Stainless Steel Alloy. *Welding Journal*, Vol. 88, No.3, pp.54-61
- Rappaz, M.; David, S.; Vitek, J. & Boatner, L. (1990). Analysis of solidification microstructures in Fe-Ni-Cr Single-Crystal welds. *Metallurgical Transaction A*, Vol.21A, No.6, pp.1767-1782
- Ribic, B.; Palmer, T. & DebRoy, T. (2009). Problems and issues in laser-arc hybrid welding. *International Materials Reviews*, Vol.54, No.4, pp.223-244
- Roy, G.; Elmer, J. & DebRoy, T. (2006). Mathematical modeling of heat transfer, fluid flow, and solidification during linear welding with a pulsed laser beam. *J. Appl. Phys.* Vol.100, No.3, pp.034903-034903-7
- Stelling, K.; Boellinghaus, Th.; Lammers, M. & Schobbert, H. (2005). Laser plasma power hybrid welding in vertical-up and vertical-down positions, *Proceedings of the 7th*

- international conference on trends in welding research*, pp. 121-126, Callaway gardens resort, Pine mountains, Georgia, USA, May 16-20, 2005
- Vitek, J. (2005). The effect of welding conditions on stray grain formation in single crystal welds-theoretical analysis. *Acta Materialia*, Vol. 53, No.1, pp., 53- 67
- Wang, N.; Mokadem, S.; Rappaz, M. & Kurz, W. (2004). Solidification cracking of superalloy single- and bi-crystals. *Acta materialia*, Vol.52, No.1, pp.3173-3182
- Wu, S.; Zhao, H.; Wang, Y. & Zhang, X. (2004). A new heat source model in numerical simulation of high energy beam welding. *Transactions of the china welding institution*, Vol.25, No.1, pp.91-94
- Yann, D.; Eric, L. & Corinne, A. (2010). Numerical modeling of Inconel 738LC deposition welding: prediction of residual stress induced cracking. *Journal of Materials Processing Technology*, Vol.210, No.14, pp.2053-2061
- Yilbas, B.; Akhtar, S. & Karatas, C. (2010). Laser surface treatment of Inconel 718 alloy: Thermal stress analysis. *Optics and Lasers in Engineering*, Vol.48, No.7-8, pp.740-749
- Zeng, D. (2006). Annular beam shaping and optical trepanning, In: *Doctor of Philosophy*, 22.02.2012, Available from http://etd.fcla.edu/CF/CFE0001333/Zeng_Danyong_200612_PHD.pdf

Development of a Comprehensive Process Model for Hybrid Laser-Arc Welding

Fanrong Kong and Radovan Kovacevic

Additional information is available at the end of the chapter

<http://dx.doi.org/10.5772/45850>

1. Introduction

Recently, a hybrid welding technique combining laser welding and arc welding has been finding broader applications in industry due to its unique advantages, such as higher welding efficiency and lower costs [1, 2] compared to the traditional arc welding or autogenous laser welding. Because of rapid melting and solidification occurring in the weld zone, a locally high thermal gradient inevitably exists and accompanies with the whole welding process, which really decides the final residual stress and distortion distributions of weld and affects the remained grain size in the fusion zone (FZ) and heat affected zone (HAZ). Also, the levels of residual stresses and distortions directly influence the weld quality [3]. In comparison with traditional arc welding and autogenous laser welding, the temperature field and residual stress distribution in hybrid laser-arc welding involve more variables because of the additional interaction between the laser and arc plasma [4] thus becoming much more complex and difficult to theoretically and experimentally analyze. Trial-and-error experiments are not able to fully describe those physical mechanisms involved in the hybrid laser-arc welding process. Therefore, the numerical tools have been widely used to help explain the complex welding mechanisms present in the hybrid laser-arc welding process [5, 6].

Up to now, numerical work on the welding process mostly concentrates on traditional electric arc welding, including gas tungsten arc welding (GTAW) [7 - 9], submerged arc welding (SAW) [10,11], gas metal arc welding (GMAW) [12-16], and partly on laser beam welding (LBW) [17-21]. These studies focused on the heat and mass transfer phenomena in the weld pool [8, 11-15], thermal-induced distortion and residual stresses [16, 17, 19, 20], solidification-induced dendrite growth in the FZ [21], and recrystallization in the heat affected zone (HAZ) [9]. Due to the locally rapid melting and solidification occurring in the welding process, a high temperature gradient—which inevitably exists in the weld zone—

causes a high-stress concentration in the weld zone and nearby HAZ [22], which usually exceeds the yield strength of the material. Large residual stresses presented in the welded structure can obviously reduce the fatigue strength of metal components, causing crack generation and shorten the lifetime of metal component [23], which could possibly have disastrous results. A number of mitigation procedures to reduce and/or eliminate the level of residual stress have been presented by researchers, mainly including enhancement of the material ductility of solidification zone (SZ) and HAZ, and improving the thermal and mechanical conditions in the welding processes [24].

Because of the complex physical mechanisms in the welding process—which are related to the heat source properties, material performance, and welding parameters, etc.—trial-and-error methods to optimize welding parameters takes a long time and is usually more costly. Also, understanding of the physics of the welding process is limited by only using an experimental approach. Numerical simulation as accompanied by theoretical analysis has been widely applied as a cost-efficient way to help explore the welding phenomena in different welding techniques. Eagar et al. [25, 26] spent a lot of time in developing theoretical models for GTAW processes. Dong et al. [27-29] developed numerical models to predict the residual stresses as well as fatigue life of weld obtained by the multi-pass welding process. Deng et al. [30-32] developed a series of numerical models to study the residual stress distribution in variable welding joints.

Compared to the traditional electric arc welding, laser welding has unique advantages such as high energy density, narrow HAZ, low heat input, and high energy efficiency. However, laser welding is also limited by its disadvantages like poor gap bridgeability and high equipment cost. In order to fully use the advantages of both laser and arc welding techniques, Steen et al. [33] introduced for the first time a hybrid technique by combining the laser beam and arc for welding and cutting in the late 1970s. Subsequently, researcher and engineers have presented a number of works on combining the laser and electric arc in the past decades. Considering that interaction between laser beam and arc plasma is complex, the hybrid laser-arc welding and cladding processes have not been understood fully. Most available literature on these approaches is limited at the level of the experimental study including hybrid laser-GTAW, hybrid laser-GMAW, and hybrid laser-plasma arc welding for steels, magnesium alloy, aluminum alloy, titanium alloy and dissimilar materials. In order to further study the welding mechanism of hybrid laser and arc, it is necessary to develop a comprehensive model to understand the heat and mass transfer, residual stress evolution, as well as microstructure formation in the hybrid laser-arc welding process. Zhou and Tsai [34, 35] presented heat transfer and fluid flow models to study the metal inert gas (MIG) welding and laser-MIG hybrid welding processes. Rao et al. [36] reviewed the modeling of hybrid laser-gas metal arc (GMA) welding and presented further studies on synergistic interaction between the laser beam and arc, the metal transfer features, and behavior of shielding gas. Ribic et al. [37] developed a three-dimensional (3-D) finite volume model to study heat transfer and fluid flow in the hybrid laser-GTA welding process. Considering that the microstructure formation of weld has a close relationship with the macro-scale heat transfer and fluid flow, and residual stress fields, it will be very

necessary to integrate the thermal, fluid flow and mechanical modeling with the microstructure evolution like grain growth in the fusion zone and HAZ. Multi-scale and multi-physics modeling is one of most interesting simulation trends in the laser-based heat processes, especially in the hybrid laser-arc welding process.

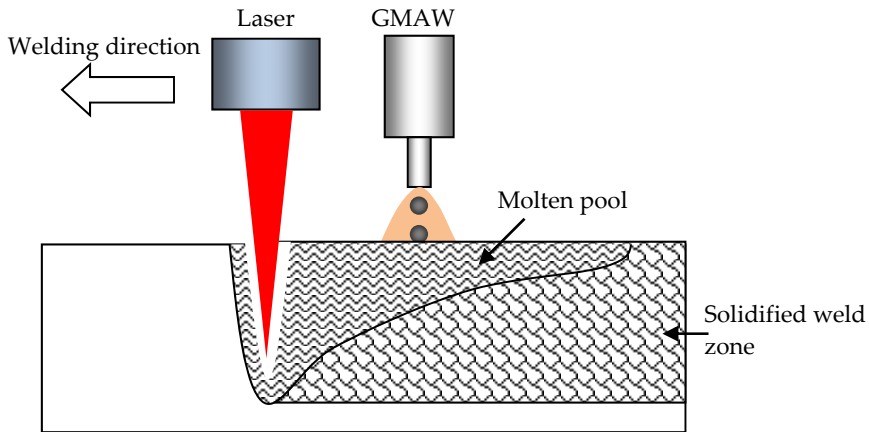


Figure 1. Schematic view of hybrid laser-GMA welding system

In this chapter, a 3-D mathematical model will be developed to numerically predict the transient temperature distributions and residual stresses in the hybrid laser-GMA welding of a thick plate of A514 steel in butt joint configuration, as shown in Figure 1. The numerical solution is achieved based on a finite element method by using a commercial numerical package, ANSYS. A Monte Carlo model is introduced to consider the grain growth and phase transformations in the HAZ. The laser and arc heat inputs and heat losses at the surface of coupons are considered by using ANSYS Parametric Designed Language (APDL). The influences of the processing parameters (including welding speed, laser power, wire feed rate, arc power, and stand-off distance from laser to arc) on the profile and geometrical size of the molten pool, residual stress distribution of the weld, and grain size in the HAZ are numerically studied. The numerically obtained results are experimentally verified.

2. Finite element modeling

2.1. Thermal analysis of hybrid laser-GMA welding

In the hybrid laser-GMA welding process, laser and GMA simultaneously heat the coupon surface in local area, which makes the thermal distribution of weld much more complex. In this study, a cylindrical volume heat-source model with a Gaussian distribution is assumed to simulate the heat input by laser, and a double-ellipsoidal volume heat source is selected to consider the heat input by GMA welding. The general thermal governing equation is shown below, in which thermal conduction-induced heat transfer is considered and temperature-dependent material properties are used [38].

$$\rho c_p \frac{\partial T}{\partial t} = \{L\}^T ([D]\{L\}T) + \ddot{q}_l + \ddot{q}_a \quad (1)$$

$$\text{where } [D] = \begin{bmatrix} k_{xx} & 0 & 0 \\ 0 & k_{yy} & 0 \\ 0 & 0 & k_{zz} \end{bmatrix}, \quad (2)$$

$$\text{and } \{L\} = \begin{Bmatrix} \frac{\partial}{\partial x} \\ \frac{\partial}{\partial y} \\ \frac{\partial}{\partial z} \end{Bmatrix}, \quad (3)$$

ρ is the density, c_p is the specific heat, T is the temperature, t is time, k_{xx} , k_{yy} , and k_{zz} are the thermal conductivity components along the x , y , and z axis, respectively; \ddot{q}_l and \ddot{q}_a are the volume heat generation rates due to the laser and GMA heat input, respectively.

So far, a number of heat source models have been developed to simulate the arc welding and laser welding processes. Laser welding usually consists of laser conduction welding or laser keyhole welding. The former one has lower energy density as compared with the latter one by which a keyhole is formed in the weld pool. A surface heat flux model is usually applied in the thermal analysis of laser conduction welding. However, a volume-distributed heat source model, like rotary Gaussian heat density distribution [39], is usually used for simulating a laser keyhole welding. Compared to the laser beam welding, electric arc welding has much lower energy density, and surface heat flux models with Gaussian distributions used to be applied to simulate the arc heat input in the arc welding process.

Considering that the enthalpy brought into the weld pool by melted wire in GMAW, volume-distributed heat source models are preferred, such as hemi-spherical power density distribution [40], ellipsoidal power density distribution [41], and double ellipsoidal power density distribution [42]. However, all of these heat source models are empirically derived based on the experimentally fitting data. Therefore, each heat source model mentioned above has a certain applicable range in the real production case. It is suggested that engineers in the welding process design should reasonably select a heat source model which matches well with the specific welding process. There are a limited number of publications available to numerically describe the hybrid laser and arc welding process because of lack of knowledge on complex interaction between the material, arc plasma, and laser beam [43]. Current heat source models of hybrid laser and arc including GTAW and GMAW were mostly developed with the help of experimental support [34-37].

In this study, a double-ellipsoidal heat source model is introduced to simulate the GMAW heat input, and a cylindrical heat source model with a sectional Gaussian distribution is used to consider the laser heat input. $q_{\text{arc}}^f(x, y, z, t)$ and $q_{\text{arc}}^r(x, y, z, t)$, depict heat input distributions inside the front and rear quadrants of the GMAW heat source, respectively, which can be expressed as follows [42, 44]:

$$\dot{q}_{arc}^f(x, y, z, t) = \frac{6\sqrt{3}f_f P_{arc}}{abc_f \pi \sqrt{\pi}} \exp\left(-\frac{3(x-x_0)^2}{a^2}\right) \cdot \exp\left(-\frac{3(y-L_w)^2}{b^2}\right) \cdot \exp\left(-\frac{3(z-vt)^2}{c_f^2}\right) \quad (4)$$

$$\dot{q}_{arc}^r(x, y, z, t) = \frac{6\sqrt{3}f_r P_{arc}}{abc_r \pi \sqrt{\pi}} \exp\left(-\frac{3(x-x_0)^2}{a^2}\right) \cdot \exp\left(-\frac{3(y-L_w)^2}{b^2}\right) \cdot \exp\left(-\frac{3(z-vt)^2}{c_r^2}\right) \quad (5)$$

where a , b , c_f , c_r are the characteristic parameters of heat sources, and a , b , c_f , and c_r are set at 4 mm, 3 mm, 3 mm and 7 mm respectively [44]. P_{arc} denotes the nominal power of the GMAW, and $P_{arc} = \mu UI$. Where μ is the energy efficiency of GMAW based on the welded metal, U denotes the arc voltage of GMAW, and I stands for arc current of GMAW. $\dot{q}_{laser}(x, y, z, t)$ denotes the laser radiation-induced volume heat input given by [45, 46]:

$$\dot{q}_{laser}(x, y, z, t) = \eta_l \frac{P_{laser} \cos \Phi}{2\pi R_l^2} \exp\left(-\frac{(x-x_0)^2 + [z + (L_w - y) \tan \Phi - vt - D_{la}]^2 \cos^2 \Phi}{2R_l^2}\right) \quad (6)$$

(y / L_w^2)

where η_l is laser absorption efficiency based on the welded material, P_{laser} stands for the nominal power of the laser beam, x_0 is the x -coordinate of the center point of laser spot at the coupon surface, L_w is the thickness of the butt joint, and R_l is the effective radius of the laser beam, Φ is the inclination angle of laser head, D_{la} is the laser-to-arc stand-off distance. Φ is set at 0° and D_{la} is set at 8 mm in this study, and v denotes the welding speed.

The boundary conditions at the sample surfaces are given by:

$$-k \frac{\partial T}{\partial n} = h_c (T - T_\infty) \quad (7)$$

where n is the normal outward vector to the surface of specimen, T_∞ is the room temperature, and h_c is the heat transfer coefficient of sample surface.

2.2. Mechanical analysis of hybrid laser-GMA welding

The mechanical analyses of hybrid laser and arc welding are similar to the previous studies on the electric arc welding and laser welding. The stress and distortion of weld are mainly caused by the thermally-induced expansion and shrinkage and the accompanying phase transformation-induced volume change. By considering the elastic-plastic material properties, stress and strain relationships in the hybrid laser-GMA weld are given by [38]:

$$\{\sigma\} = [D_e] \{\varepsilon^{el}\} \quad (8)$$

where $\{\sigma\}$ denotes the stress vector, $[D_e]$ denotes elastic stiffness matrix, and $\{\varepsilon^{el}\}$ denotes elastic strain vector expressed by [30]:

$$\{\varepsilon^{el}\} = \{\varepsilon\} - \{\varepsilon^{th}\} - \{\varepsilon^{pl}\} - \{\varepsilon^{\Delta V}\} - \{\varepsilon^{Trp}\} \quad (9)$$

where $\{\varepsilon\}$ is the total strain vector, $\{\varepsilon^{\text{th}}\}$ is thermal strain vector, $\{\varepsilon^{\text{pl}}\}$ is the plastic strain vector, $\{\varepsilon^{\Delta V}\}$ is strain vector due to phase transformed induced volume change, and $\{\varepsilon^{\text{TP}}\}$ is strain vector due to phase transformation plasticity which is ignored in this study. The boundary conditions taken into consideration in the mechanical analysis assume that one edge of the butt joint is fixed, and the other one is only transversely shrinkage free.

2.3. Grain size prediction model by Monte Carlo method

Grain size evolution and phase transformation play a critical role in deciding the final mechanical properties of weld, and it is necessary to involve those factors in the thermo-mechanical modeling of different welding processes. Many good trials have been performed to numerically predict the grain growth in the fusion zone and heat affected zone for solidification and re-crystallization, respectively, which includes Monte Carlo (MC) model [47-50], phase field (PF) method [51], and cellular automaton (CA) model [52] combined with finite element and finite difference analyses. Here a brief introduction of MC model to predict the grain growth in HAZ will be performed. The detailed description of phase field method and cellular automaton model-based numerical prediction of grain growth in welds can be found in literature [53].

Monte Carlo model-based grain growth prediction generally includes the following several steps: (1) The representation of the considered material in a two-dimensional (2-D) or 3-D of cells, as shown in Figure 2a. The content of each cell stands for its crystallographic orientation. A region consisting of a set of consistently distributed cells with the same orientation value denotes a grain. The grain boundaries are identified by a curve in 2-D matrix or a surface in 3-D matrix between the separate planes or volumes with different orientations. (2) After selecting the matrix type and defining it by an initially random number, the free energy of a cell in the matrix with its specific crystallographic orientation based on its surroundings will be identified. (3) Randomly selecting a new crystallographic orientation for each cell. (4) Calculating the free energy of the new coming element with the new crystallographic orientation, the two energy values and their difference are then calculated. A new grain orientation that will minimize the free energy is generated with the selected transition probability [54]. These four steps will be reiterated many times at random positions in the matrix. The ultimate product is a microscopic simulation of the free energy decaying in the system, which is in fact the main driving force for grain growth. The Hamiltonian demonstrates the interaction among the closest neighbors in a particular cell, which stands for the grain boundary energy and can be calculated as follows [54]:

$$G = -J \sum_{nm} (\delta s_i s_j - 1) \quad (10)$$

where, J is a positive constant that characterizes the scale of the grain boundary energy; s_i is one of the possible orientations, which is set between 1 and q , in the i^{th} cell of the matrix; s_j is the crystallographic orientation of one neighboring cell; nm is the amount of neighboring cells for each element. In the Monte Carlo model, a Moore neighborhood model is selected

(see Figure 2b); therefore, $nn=8$. δ_{ab} is the Kronecker-delta, which equals 1 when two elements in the matrix are equal, i.e., $a=b$, and 0 for others. As a consequence, neighboring cells with different orientations contribute a free energy J to the system and 0 with the same orientation. The total number of grain orientations, q is set at 40 in this model since it is known that the grain-growth exponent becomes almost independent of q when its value is larger than 30 [54].

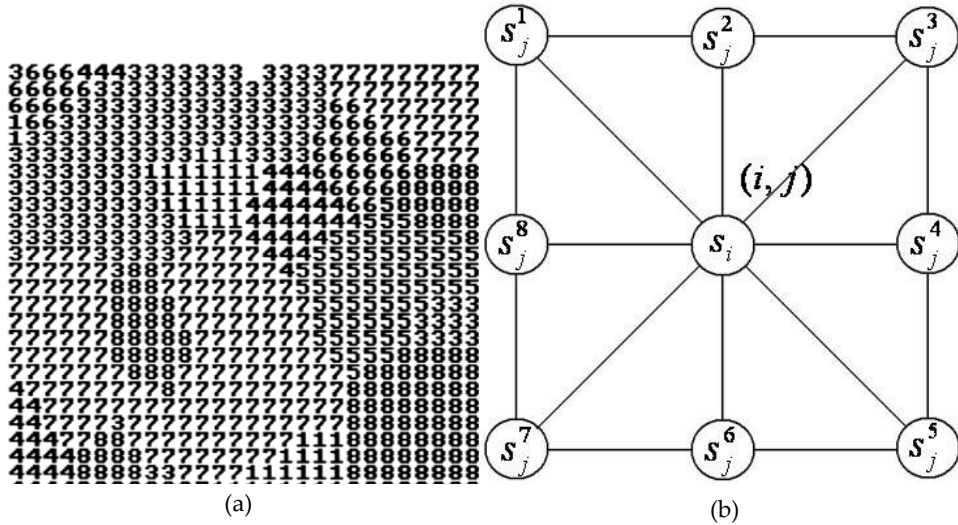


Figure 2. The grain structure in MC model with Moore neighborhood [51]
 (a) The grain structure represented by a 2D square (b) Moore neighborhood

The transition probability W is given by [55]:

$$W = \begin{cases} \exp(-\frac{\Delta G}{k_b T}), & \Delta G > 0 \\ 1, & \Delta G \leq 0 \end{cases} \quad (11)$$

where ΔG is the change of the free energy because of the orientation alteration, k_b is the Boltzman constant ($k_b=1.38 \times 10^{-23} \text{ m}^2\text{kg/s}^2\text{/K}$), and T is the temperature. Therefore, the speed of the moving segment can be calculated by [55]:

$$v_i = C_1 [1 - \exp(-\frac{\Delta G}{k_b T})] \quad (12)$$

where C_1 is the boundary mobility. For a continuous grain growth, the final grain size can be calculated by using the following equation [55]:

$$L^n - L_0^n = f(T)t \quad (13)$$

where L and L_0 are the final and initial mean grain sizes respectively calculated by the linear-intercept method, n is the grain growth exponent and set at 1.84 in this study [56]. $f(T)$ is usually computed as an Arrhenius-type equation [55], and its expression is shown as follows:

$$f(T) = K \exp\left(-\frac{Q}{R_g T}\right) \quad (14)$$

where K is the pre-exponential coefficient, Q is the activation energy for grain growth, and R_g is the universal gas constant. In this study, K is set at 3.01×10^{-2} , and Q is set at 1.7×10^5 J/mol [56].

The Monte Carlo method has been proven to be an effective way to simulate grain growth with slow and uniform temperature evolution such as metal casting [53]. In the hybrid welding by laser and arc, there exists a dynamic thermal process with rapid heating and cooling resulting in an abrupt temperature gradient in the HAZ and fusion zone. In the simulation of microstructure evolution, three techniques—such as the atomistic models, a grain boundary migration (GBM), and experimentally data-based (EDB) models—have been presented [53, 58-60]. The atomistic model used to be only applied to small numbers of atoms like nanocrystals [60], and it is not suitable for a large-scale FZ or HAZ simulation. The GBM model can be a good alternative for grain-growth simulation when the isothermal grain-growth kinetics is not accessible. However, the physical properties of the material in this model have to be known, and the grain size is assumed to be proportional to the square root of time. The EDB model can avoid these shortages and be applied to simulate the grain growth in HAZ when the isothermal grain-growth kinetics of metal are available. Therefore, it can be used to relate time and temperature to the Monte Carlo simulation-time step t_{MCS} [55]:

$$L = K_1 \lambda (t_{MCS})^{n_1} \quad (15)$$

where λ is the discrete grid-point spacing in the Monte Carlo model, and K_1 and n_1 are constants. Through the regression computation of t_{MCS} and the Monte Carlo model predicting the grain size, the values of K_1 and n_1 are obtained as 0.715 and 0.477, respectively [56]. In the EDB model, the relationship between the t_{MCS} and the real time-temperature $T(t)$ is further given by [60]:

$$(t_{MCS})^{m_{n_1}} = \left(\frac{L_0}{K_1 \lambda}\right)^n + \frac{K}{(K_1 \lambda)^n} \sum (\exp(-\frac{Q}{R_g T(t)}) \Delta t_i) \quad (16)$$

where n is the grain growth exponent, $T(t)$ is the mean temperature in a time interval Δt_i . Therefore, at any given monitoring location where the temperature is known as a function of time, t_{MCS} can be related to the real time t , which is $\sum \Delta t_i$. The t_{MCS} values at different locations calculated through Eq. (16) cannot be straightly applied to the Monte Carlo model since the selection of a grid point for updating the orientation number is stochastic in the Monte Carlo approach. Consequently, the probability of choosing each grid point is the

same as in the traditional MC calculations. However, grains usually grow at higher rates in the HAZ region of higher temperature, where a sharp temperature gradient is present. This fact has to be included in any practical grain-growth calculation scheme. One solution is to develop a scheme in which grain orientations at higher-temperature locations (higher t_{MCS} locations) are updated with a higher frequency by considering a probability gradient. In other words, the site-selection probability changes with location. The larger the t_{MCS} at a location, the higher the corresponding site-selection probability [57, 60]:

$$P = t_{MCS} / t_{MCSMAX} \tag{17}$$

where t_{MCSMAX} is the maximum of t_{MCS} in the simulation domain.

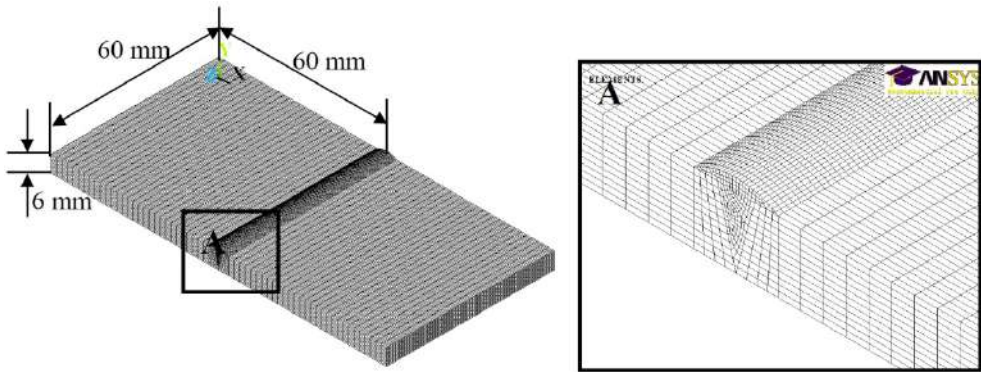


Figure 3. Finite element meshes for hybrid laser-GMA weld

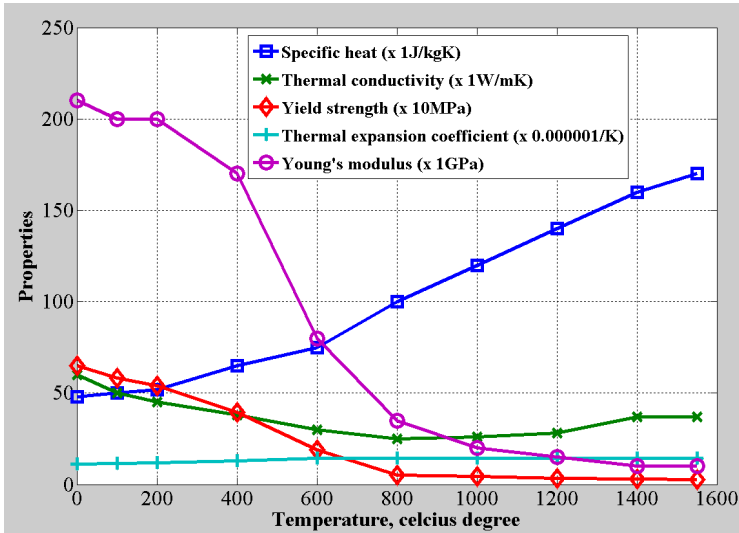


Figure 4. Temperature-dependent thermal and mechanical properties of A514 steel

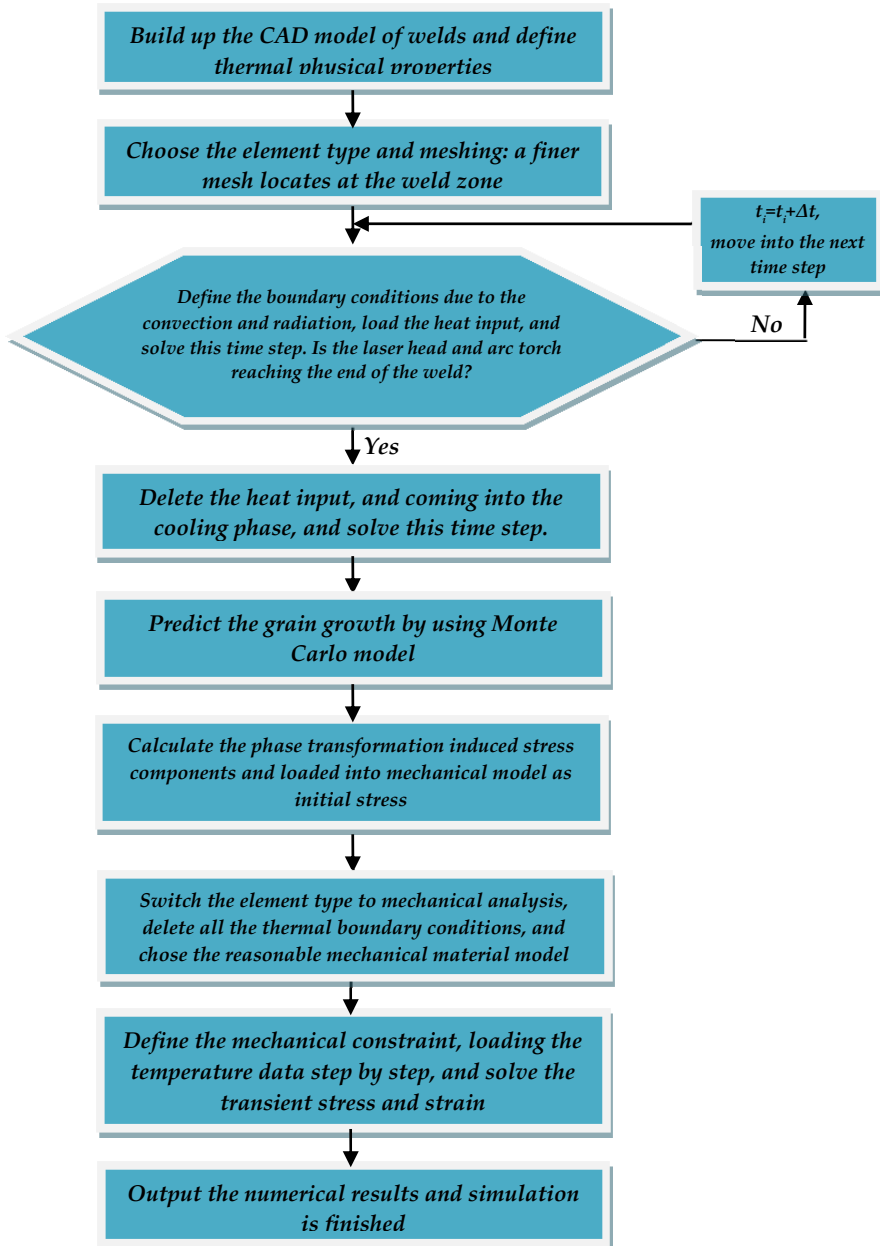


Figure 5. Numerical procedure performed in the thermo-mechanical FE analysis

2.4. Implementation of numerical procedure by using APDL

An uncoupled finite element thermo-mechanical model with considering the grain growth in the HAZ by Monte Carlo model is developed to study the temperature distribution and residual stress field in the hybrid laser-GMA welding process. A non-uniform mesh is selected in which a finer mesh is used in the weld bead and a course mesh is defined in the other region of the welded coupons (see Figure 3). A temperature-dependent material property is used in the numerical modeling, as listed in Figure 4. A thermal FE analysis is performed to achieve the temperature field of hybrid laser-GMA welding process. The wire feeding into the groove to form the weld bead has been simulated by using element kill-and-birth approach which is available in ANSYS software. The achieved geometrical size of the weld zone could be compared to the micrographs of the weld cross-section obtained by an optical microscope, by which the accuracy of thermal analysis can be verified. The numerical model is then transferred to mechanical analysis module in ANSYS by switching the element type from thermal to structural. The corresponding constraints are exerted into sample boundaries. The achieved temperature histories are subsequently loaded into the mechanical model step by step to calculate the displacement, stress/strain of the sample due to the thermal expansion or shrinkage during the welding process. A bilinear hardening principle is introduced in this study to simulate the material plastic behavior. Von Mises criterion is used for considering the yield behavior of the sample material. Figure 5 shows the numerical procedure used in this study.

3. Experimental set-up

A 4 kW fiber laser and a GMAW torch are mounted on a robotic arm to perform the hybrid welding of a thick plate for a butt joint configuration. The photo of an experimental set-up for welding is shown in Figure 6. In order to control the gap thickness, spot welding is performed at both ends of the joint before the formal welding starts. After the welding process is completed, the achieved sample will be cut into standard tensile coupon for tensile test, the left parts will be mounted for polishing, and etching to test the micro-hardness and microstructure. The base metal is high strength steel A514; its chemical composition is listed in Table 1. The wire material is ER100S-G. Its diameter is 0.9 mm, and its chemical composition is listed in Table 2. Residual stresses were measured by using the X-ray diffraction technique. Before performing the residual stress measurement, the measurement areas were cleaned by using polishing paper.

	C	Mn	P	S	Si	Cr	Mo	V	Ti	B
Min.	0.12	0.70			0.20	0.40	0.15	0.03	0.01	0.0005
Max.	0.21	1.00	0.035	0.008*	0.35	0.65	0.25	0.08	0.04	0.005

Table 1. Chemical composition of A514 [61]

Cu % max	Ni % max	Fe % max	Mn % max	Mo % max
<0.5	<5.0	Balance	<5.0	0.50

Table 2. Chemical composition of ER100S-G [62]

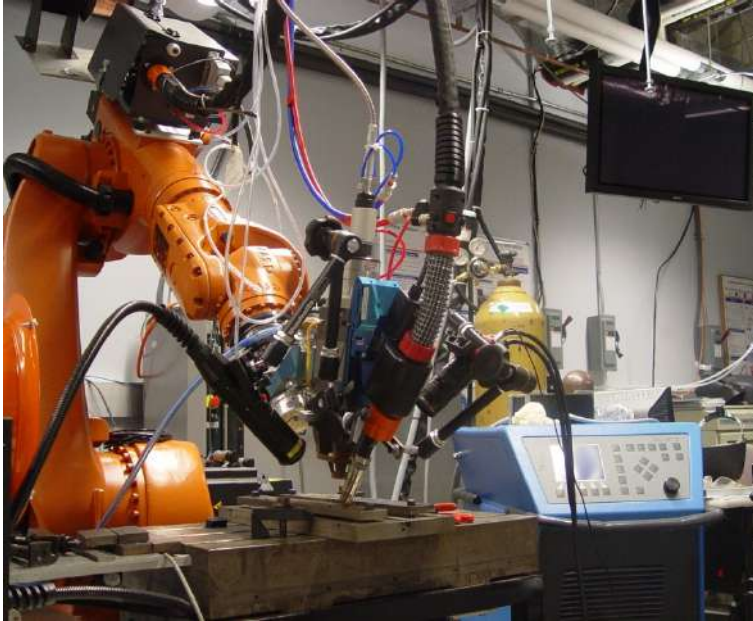


Figure 6. Photo of hybrid laser-GMA welding system used in this study

4. Results and discussion

4.1. Experimental results

Figure 7 shows the surface morphology of A514 weld obtained by hybrid laser-GMA welding, and Figure 8 presents the corresponding cross-sectional view of weld. It can be



Figure 7. A514 sample achieved by 3.8 kW laser and 159A×30.5V GMAW with a welding speed of 12 mm/s and 8-mm stand-off distance between the laser and arc

seen that a sound weld quality is achieved by using hybrid laser-GMA welding and the welding-induced cracks can be effectively mitigated by reasonably selecting filler wire matched with base metal. Also, a sound mechanical property can be obtained. Figures 9a and b show the hardness distribution in the weld obtained by hybrid laser-GMA welding.



Figure 8. Cross-sectional view of A514 weld sample achieved by 3.8 kW laser and 159A×30.5V GMAW with a welding speed of 12 mm/s and 8-mm stand-off distance between the laser and arc

4.2. Thermal results and grain size prediction in the HAZ of hybrid laser-GMA welding

Finite element analyses results show the temperature at the each location of weld with respect to the welding time. The temperature evolution curves at position A, B, and C are shown in Figure 10, where position A is located at the center of weld, position B is at the heat-affected zone, and position C is in the base metal, as shown in Figure 11b. Figures 11a and b show the top and cross-sectional views of weld obtained by hybrid laser-GMA welding, respectively. It is inevitable that material heating and cooling is accompanied by phase transformation and grain size change, especially in the HAZ of weld, which is the weakest zone of the weld. In this study, a Monte Carlo-based sub-model is introduced to numerically predict the grain growth in the HAZ combined with the finite element thermal analysis. Figure 12a shows the relationship of temperature versus Monte Carlo step at Position B, and Figure 12b presents the curve of Monte Carlo step versus real time at Position B. The corresponding predicted grain size distribution in the Position B is shown in Figure 12c. The numerically predicted grain size is compared to grain size shown in the micrograph of the cross-section of weld (see Figure 12d), and a qualitative agreement is achieved.

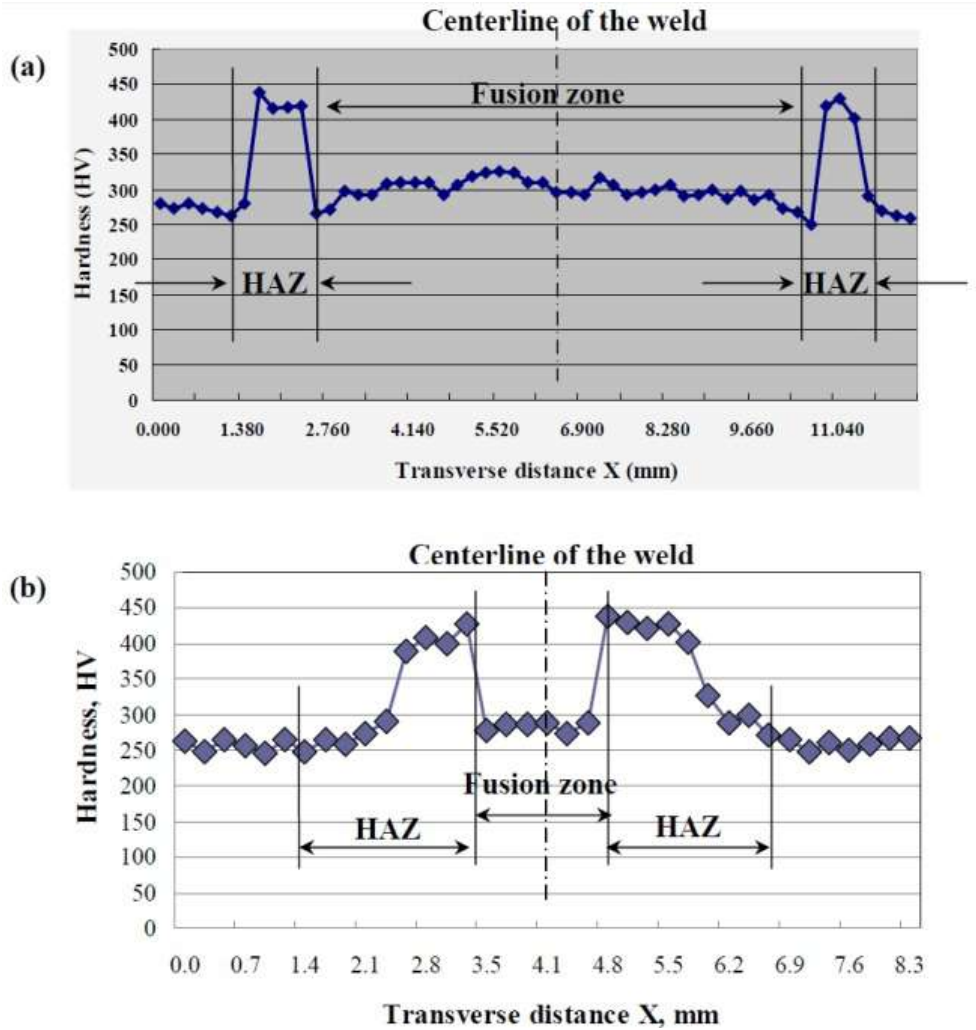


Figure 9. Hardness distribution transverse to the weld in A514 sample, (a) at the top surface and (b) at the bottom surface

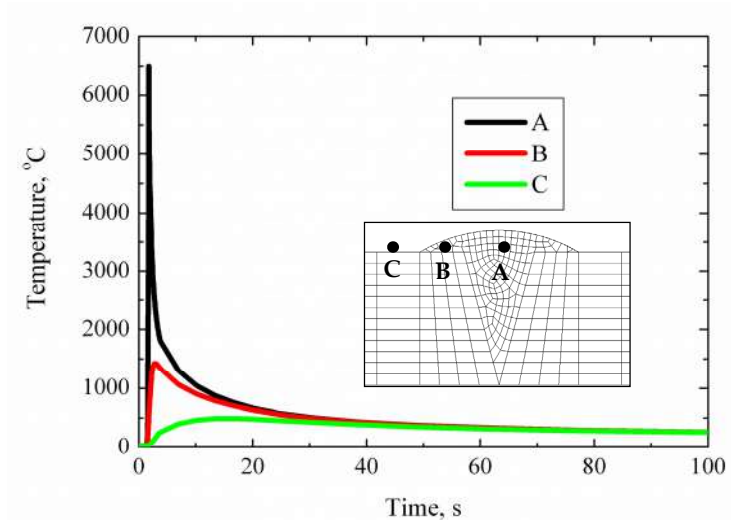


Figure 10. Temperature evolution curve at the FZ, HAZ and BM during the hybrid laser-GMA welding of A514 steel

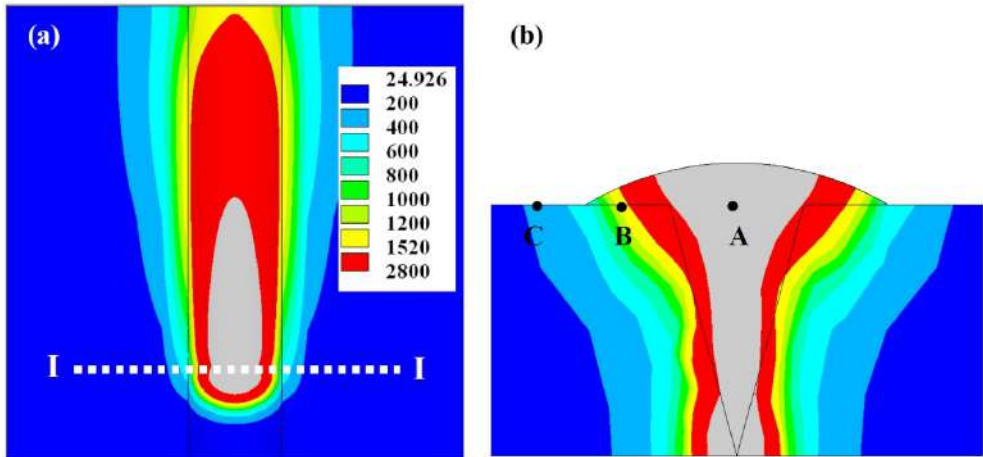


Figure 11. Numerically predicted isotherms at the top (a) and at the cross-section I-I of the weld (b) obtained by hybrid laser-GMA welding

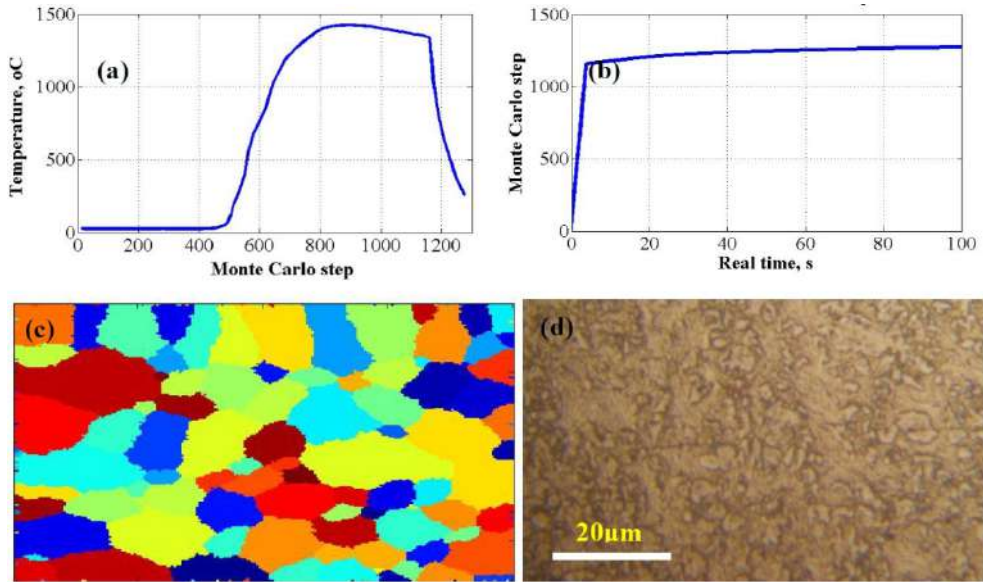


Figure 12. (a) Temperature versus Monte Carlo step, (b) Monte Carlo step versus real time, (c) numerical predicted and (d) experimentally measured grain size distributions at Position B in the HAZ of hybrid A514 weld by Monte Carlo sub-model

4.3. Thermally-induced residual stress in the hybrid laser-GMA welding

A finite element analysis is further performed to predict the thermally-induced residual stress distribution based on the previous thermal analysis results. The contours of transient stress, along thickness normal stress, longitudinal stress and equivalent residual stress of hybrid weld are shown in Figures 13a through d, respectively. It can be seen that the higher stress concentrations are located at the weld zone, which also indirectly verifies the previously experimentally obtained conclusions that the thermally induced cracks are usually generated at the weld zone, not in the base metal. The corresponding contours of stress distribution of the cross-section in the middle of weld length are shown in Figures 14a through d. A higher stress concentration is found to be located at the top region of cross-section

Figures 15a through c show residual stress distribution transverse to the weld bead at the different thicknesses in the middle of weld obtained by hybrid laser-GMA welding. It also validates the conclusion driven from Figure 14 that high tensile transverse and longitudinal stresses are located at the top and bottom regions of the weld center, high compressive transverse stresses are located at a half of the weld thickness. From the equivalent stress distribution point of view, the peak value of stress concentration is a little lower than that at the top and bottom of the weld. Figure 16 shows residual stress distribution transverse to the weld bead at the different locations along the top surface of weld obtained by hybrid laser-GMA welding. Figure 17 also shows residual stress distributions along the central line

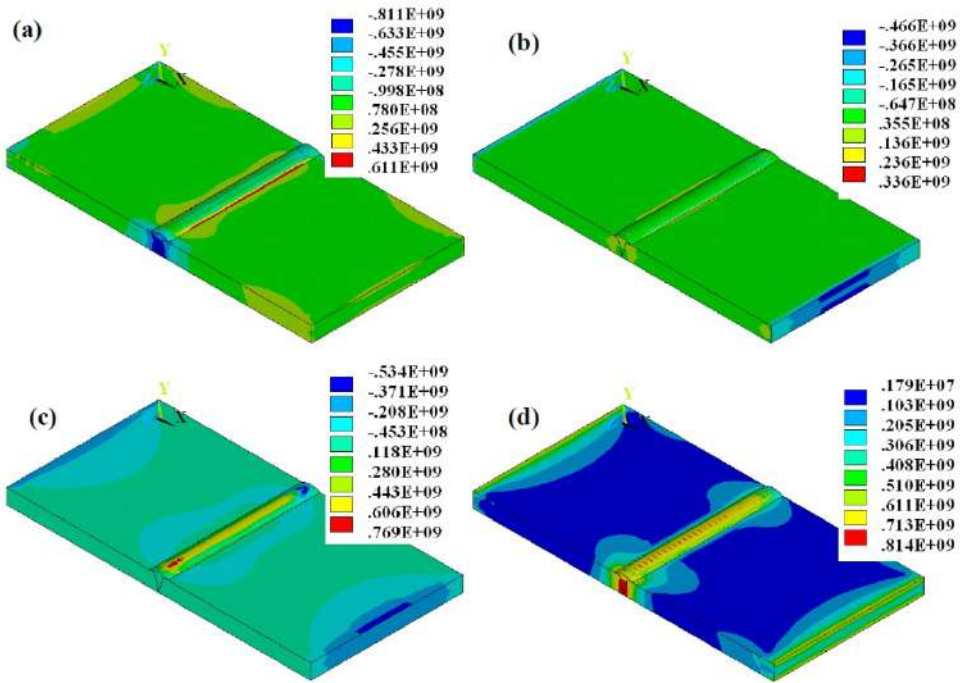


Figure 13. (a) Transverse stress SX, (b) along-thickness normal stress SY, (c) longitudinal stress SZ, and (d) von Mises equivalent residual stress SEQV mapping of weld by hybrid laser-GMA welding (unit of stress in the contour is Pa)

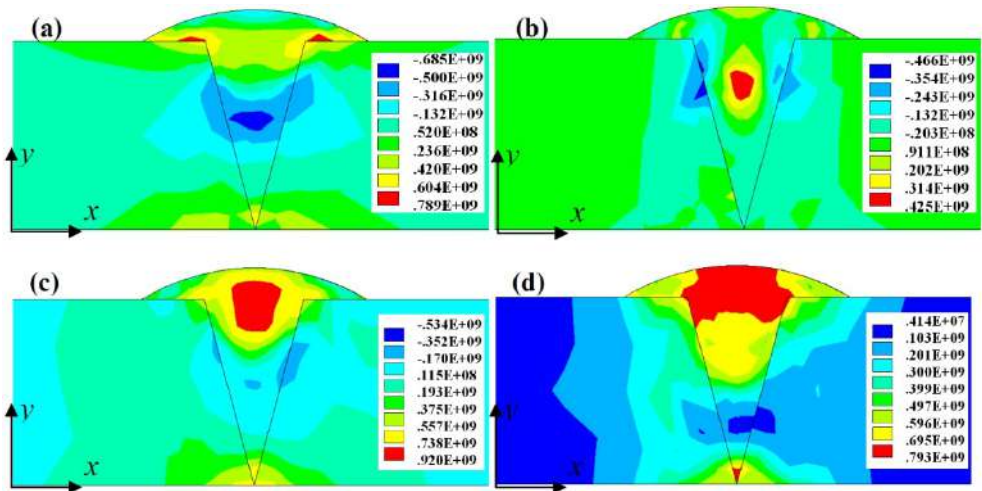


Figure 14. (a) Transverse stress SX, (b) along-thickness normal stress SY, (c) longitudinal stress SZ, and (d) von Mises equivalent residual stress SEQV mapping of cross-section of weld by hybrid laser-GMA welding (unit of stress in the contour is Pa)

at the top surface of weld centerline achieved by hybrid laser-GMA welding. It is clear that stress distribution across the weld bead is uniform along the weld; only a little drop in stress magnitude exists at the both ends of weld.

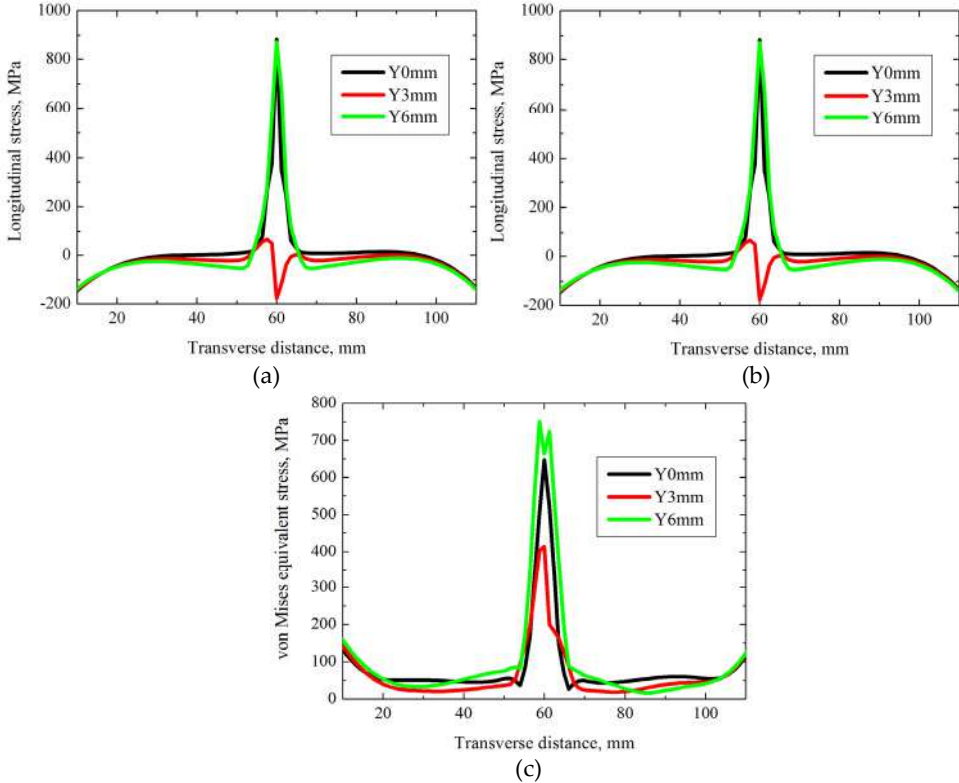


Figure 15. Residual stress distribution transverse to the weld bead at the different thicknesses in the middle of weld ($z=30$ mm) obtained by hybrid laser-GMA welding

Figure 18 shows a comparison of experimentally-measured and FE numerically-predicted residual stress distributions at the middle of weld length of top surface of weld by hybrid laser-GMA welding. There is a qualitative agreement between the developed numerical model and experimentally measured stress by an X-ray diffraction technique. Figures 19, 20 and 21 show the transverse, longitudinal, and equivalent stresses as well as temperature evolution with time at the positions A, B and C, respectively. It can be seen that the peak values of transient stresses at positions A, B, and C are sensitive to the temperature curve at the position A but not at the positions B and C.

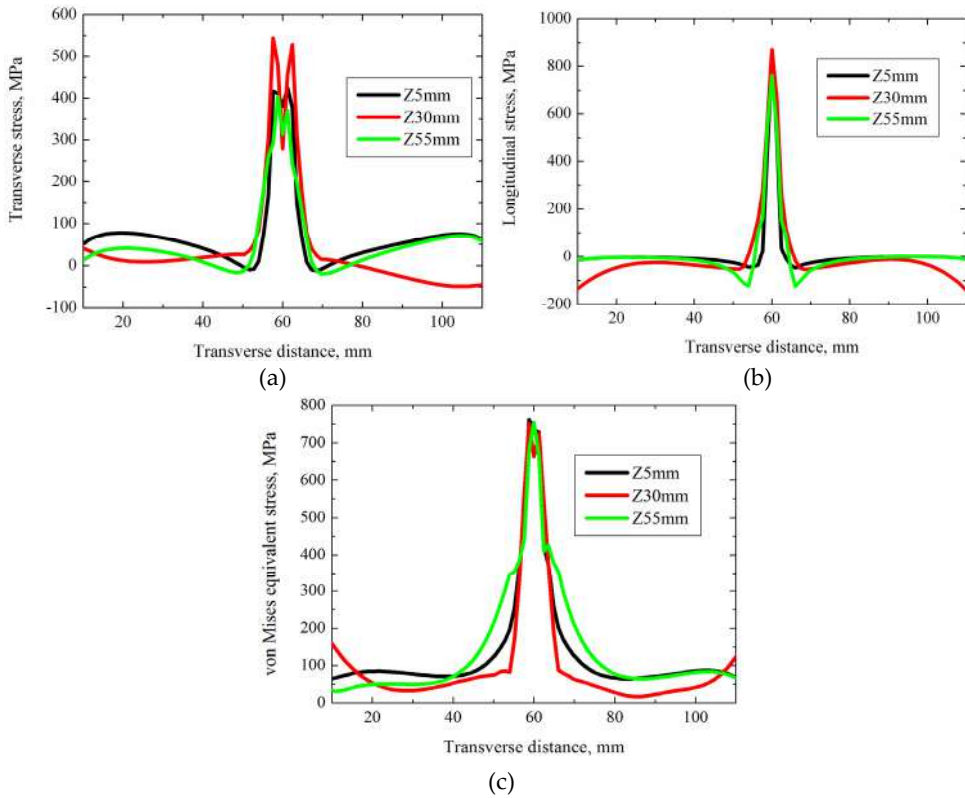


Figure 16. Residual stress distribution transverse to the weld bead at the different locations along the top surface of weld obtained by hybrid laser-GMA welding

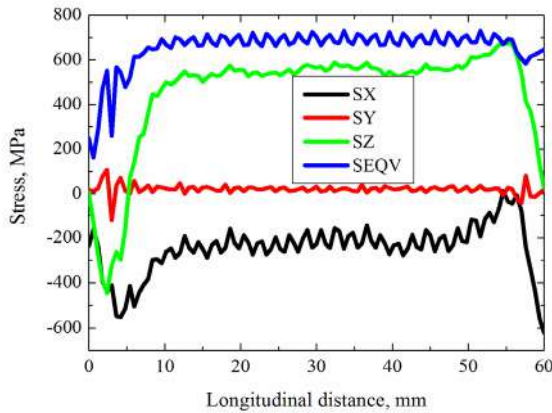


Figure 17. Residual stress distributions along the longitudinal direction of weld at the top surface of weld centerline achieved by hybrid laser-GMA welding

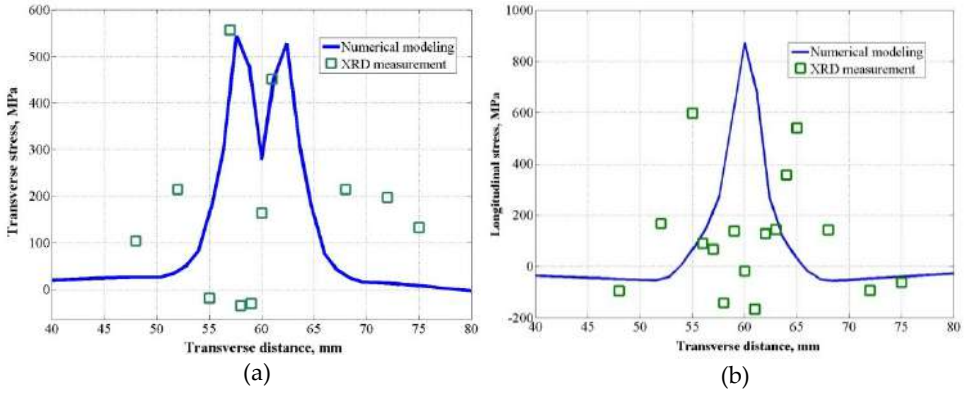


Figure 18. Comparison of experimentally-measured and FE numerically-predicted residual stress distribution at the middle of weld length of top surface of weld by hybrid laser-GMA welding

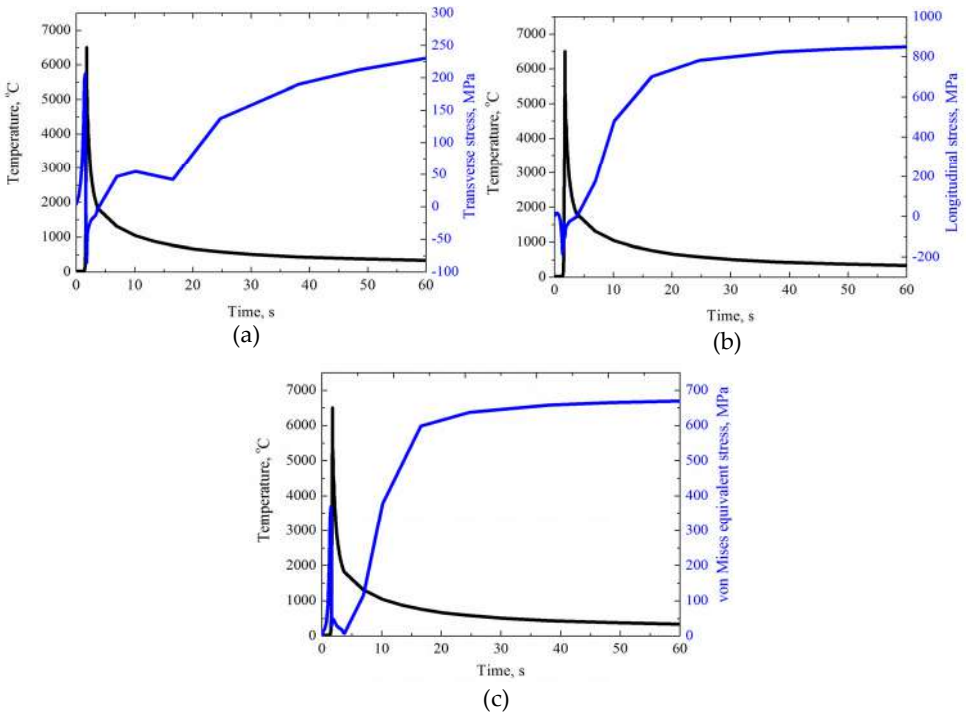


Figure 19. Stress and temperature evolution curves at the Position A in FZ of hybrid A514 weld

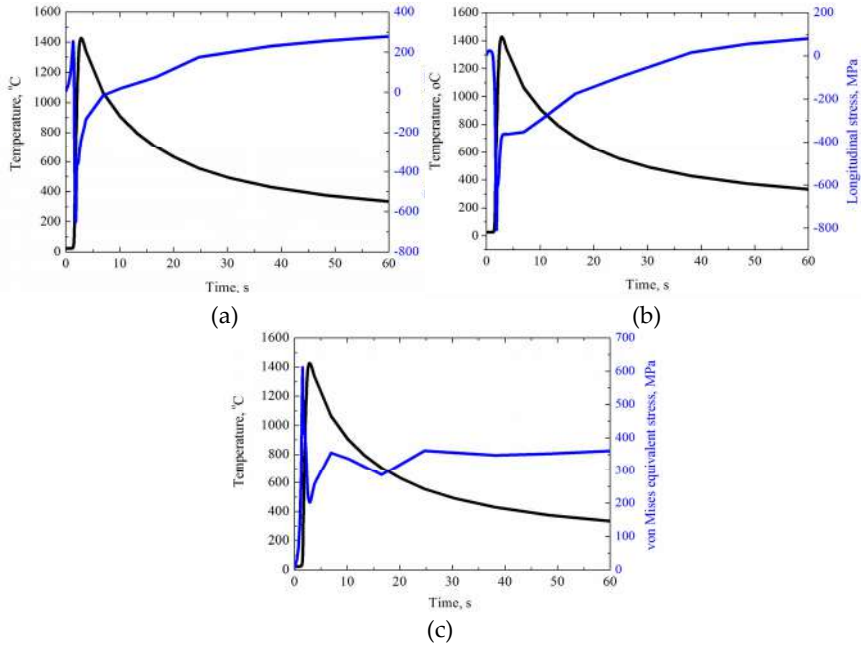


Figure 20. Stress and temperature evolution curves at the Position B in HAZ of hybrid A514 weld

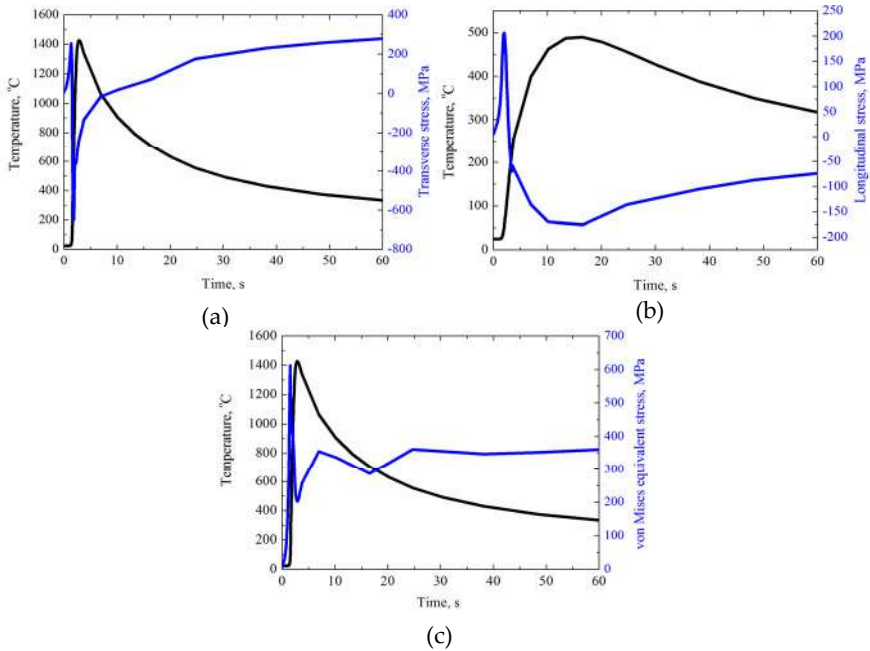


Figure 21. Stress and temperature evolution curves at the Position C in BM of hybrid A514 weld

5. Conclusions

The hybrid approach combining laser and arc has unique features which definitely help to achieve a better weld quality and to improve the production efficiency. A brief overview of modeling of hybrid laser-arc welding process has been presented in which heat transfer, fluid flow, residual stress and distortion, as well as phase transformation in the weld zone and heat affected zone, are involved. As a case study, a 3D thermo-mechanical finite element model is developed to study the thermally-induced residual stress in the hybrid laser-GMA welding process. A Monte Carlo model is introduced to numerically predict the grain growth in the heat affected zone of weld combined with finite element thermal analysis, which can be used to further understand the welding mechanisms of hybrid laser-GMA welding as well as other welding technology.

Author details

Fanrong Kong and Radovan Kovacevic*
*Research Center for Advanced Manufacturing, Lyle School of Engineering,
 Southern Methodist University, Dallas, TX, USA*

Acknowledgement

The authors would like to thank Ph.D. candidate, Mr. Junjie Ma for his valuable help in the experiment and technical discussions and Research Engineer, Mr. Andrew Socha for his support in the experimental set-up. This work was financially support by NSF's Grant No. IIP-1034652

6. References

- [1] C. Roepke, S. Liu, S. Kelly, and R. Martukanitz. Hybrid laser arc welding process evaluation on DH36 and EH36 steel. *Welding Journal*, 2010, 89: 140s-150s.
- [2] C. Bagger and F.W. Olsen. Review of laser hybrid welding. *Journal of Laser Applications*. 2005, 17(1): 2-14.
- [3] M. N. James, D. J. Hughes, Z Chen, H Lombard, D. G. Hattingh, D. Asquith, J. R. Yates and P. J. Webster, Residual stresses and fatigue performance, *Engineering Failure Analysis*, 2007,14: 384-385.
- [4] P. Kah. Usability of laser-arc hybrid welding processes in industrial applications. Ph.D. Dissertation, Lappeenranta University of Technology, 2011.
- [5] G. Turichin, E. Valdaytseva, I. Tzibulsky, A. Lopota, O. Velichko. Simulation and technology of hybrid welding of thick steel parts with high power fiber laser. *Physics Procedia*, 2011, 12: 646-655.
- [6] M.H. Cho and D.F. Farson. Simulation study of a hybrid process for the prevention of weld bead hump formation. *Welding Journal*, 2007, 86: 174s-179s.

* Corresponding Author

- [7] F.G. Lu, S. Yao, S.N. Lou, Y.B. Li. Modeling and finite element analysis on GTAW arc and weld pool. *Computational Materials Science*, 2004, 29:371-378.
- [8] H.G. Fan, H.L. Tsai, S.J. Na. Heat transfer and fluid flow in a partially or fully penetrated weld pool in gas tungsten arc welding. *International Journal of Heat and Mass Transfer*, 2001, 44: 417-428.
- [9] H.J. Aval, S. Serajzadeh, A.H. Kokabi. Prediction of grain growth behavior in HAZ during gas tungsten arc welding of 304 stainless steel. *Journal of Materials Engineering and Performance*, 2009, 18: 1193-1200.
- [10] L.J. Yang, M.J. Bibby, R.S. Chandel. Linear regression equations for modeling the submerged arc welding process. *Journal of Materials Processing Technology*, 1993, 39(1-2): 33-42.
- [11] D. V. Kiran, B. Basu, A.K. Shah, S. Mishra, and A. De. Three-dimensional heat transfer analysis of two wire tandem submerged arc welding. *ISIJ International*, 2011, 51 (5): 793-798.
- [12] J. Haidar. A theoretical model for gas metal arc welding and gas tungsten arc welding I. *Journal of Applied Physics*, 1998, 84: 3518-3529.
- [13] J. Haidar. Prediction of metal droplet formation in gas metal arc welding II. *Journal of Applied Physics*, 1998, 84: 3530-3540.
- [14] J. Haidar. An analysis of heat transfer and fume production in gas metal arc welding. III, *Journal of Applied Physics*, 1999, 85 3448-3459.
- [15] Z.H. Rao, J. Hu, S.M. Liao, H.L. Tsai. Modeling of the transport phenomena in GMAW using argon-helium mixtures. Part I- The arc. *International Journal of Heat and Mass Transfer*, 2010, 53: 5707-5721.
- [16] C. Heinze, C. Schwenk, M. Rethmeier. Numerical calculation of residual stress development of multi-pass gas metal arc welding. *Journal of Constructional Steel Research*, 2012, 72: 12-19.
- [17] A. Kaplan. A model of deep penetration laser welding based on calculation of the keyhole profile. *Journal of Physics D: Applied Physics*, 1994, 27(9): 1805-1814.
- [18] R. Spina, L. Tricarico, G. Basile, T. Sibillano. Thermo-mechanical modeling of laser welding of AA5083 sheets. *Journal of Materials Processing Technology*, 2007, 191: 215-219.
- [19] A.P. Mackwood, R.C. Crafer. Thermal modeling of laser welding and related processes: a literature review. *Optics & Laser Technology*, 2005, 37: 99-115.
- [20] P. Martinson, S. Daneshpour, M. Koçak, S. Riekehr, P. Staron. Residual stress analysis of laser spot welding of steel sheets. *Materials & Design*, 2009, 30(9): 3351-3359.
- [21] W. Tan, N.S. Bailey, Y.C. Shin. A novel integrated model combining cellular automata and phase field methods for microstructure evolution during solidification of multi-component and multi-phase alloys. *Computational Materials Science*, 2011, 50: 2573-2585.
- [22] K. Asim, J. Lee, and J. Pan. Failure mode of laser welds in lap-shear specimens of high strength low alloy (HSLA) steel sheets. *Fatigue & Fracture of Engineering Materials & Structures*. 2011, 35: 219-236.

- [23] Y. Arai, M. Kikuchi, T. Watanabe, M. Nakagaki. Residual stress due to welding and its effect on the assessment of cracks near the weld interface. *International Journal of Pressure Vessels and Piping*, 1995, 63(3): 237-248.
- [24] Y.P. Yang, P. Dong, J. Zhang and X. Tian. A hot-cracking mitigation technique for welding high-strength aluminum alloy. *Welding Journal*, 2000, 79(1): 9s-17s.
- [25] A.H. Dilawari, T.W. Eagar and J. Szekely. An analysis of heat and fluid flow phenomena in electros slag welding. *Welding Journal*, 1978, 57(1): 24s-30s.
- [26] L. A. Jones, T. W. Eagar, J. H. Lang. Magnetic forces acting on molten drops in gas metal arc welding, *Journal of Physics D: Applied Physics*, 1998, 31: 93-106.
- [27] P. Dong. Residual stress analyses of a multi-pass girth weld: 3-D special shell versus axisymmetric models. *ASME Journal of Pressure Vessel Technology*, 2001, 123: 207-213.
- [28] P. Dong, J.K. Hong, and P. Rogers. Analysis of residual stresses in Al-Li repair welds and mitigation techniques, *Welding Journal (London)*, 1998, 77 (11): 439-445.
- [29] P. Dong, J.K. Hong, J. Zhang, P. Rogers, J. Bynum, and S. Shah, Effects of repair weld residual stresses on wide-panel specimens loaded in tension. *ASME Journal of Pressure Vessel Technology*, 1998, 120: 122-128.
- [30] Dean Deng, Yu Luo, Hisashi Serizawa, Masakazu Shibahara, and Hidekazu Murakawa. Numerical simulation of residual stress and deformation considering phase transformation effect. *Transactions of Joining and Welding Research Institute (Osaka University)* 2003, 32(2): 325-333.
- [31] D. Deng, H. Murakawa. Numerical simulation of temperature field and residual stress in multi-pass welds in stainless steel pipe and comparison with experimental measurements. *Computational Materials Science*, 2006, 37: 269-277.
- [32] D. Deng. FEM prediction of welding residual stress and distortion in carbon steel considering phase transformation effects. *Materials and Design*, 2009, 30: 359-366.
- [33] W.M. Steen, and M. Eboo. Arc augmented laser welding. *Metal Construction*, 1979, 11(7): 332-335.
- [34] J. Zhou, H. L. Tsai. Modeling of transport phenomena in hybrid laser-MIG keyhole welding. *International Journal of Heat and Mass Transfer*, 2008, 51: 4353-4366.
- [35] J. Hu, H.L. Tsai. Heat and mass transfer in gas metal arc welding. Part I: The arc. *International Journal of Heat and Mass Transfer*, 2007, 50 (5-6): 833-846.
- [36] Z.H. Rao, S.M. Liao, and H.L. Tsai. Modelling of hybrid laser-GMA welding: review and challenges. *Science and Technology of Welding and Joining*, 2011, 16 (4): 300-305.
- [37] B. Ribic, R. Rai, and T. DebRoy. Numerical simulation of heat transfer and fluid flow in GTA/laser hybrid welding. *Science and Technology of Welding and Joining*. 2008, 13 (9): 683-693.
- [38] ANSYS Inc., ANSYS 11.0 Manual, 2007.
- [39] S. Wu, H. Zhao, Y. Wang, X. Zhang. A new heat source model in numerical simulation of high energy beam welding. *Transaction of China Welding Institute*, 2004, 25: 91-94.
- [40] V. Pavelic, R. Tanbakuchi, O.A. Uyehara, and P.S. Myers. Experimental and computed temperature histories in gas tungsten arc welding of thin plate, *Welding Journal Research Supplement*, 1969, 48: 259s-305s.

- [41] E.A. Bonifaz. Finite element analysis of heat flow in single-pass arc welds. *Welding research supplement*, 2000, May: 121s-125s.
- [42] J. Goldak, A. Chakravarti, and M. Bibby. A new finite element model for heat sources, *Metallurgical Transaction B*, 1984, 15B: 299-305.
- [43] P. Peyffarth, and I.V. Krivt. *Welding and Allied Processes Volume I. Laser-Arc Processes and Their Application in Welding and Material Treatment*. Taylor&Francis, London, 2002.
- [44] F. Kong, J. Ma, R. Kovacevic. Numerical and experimental study of thermally induced residual stress in the hybrid laser-GMA welding process. *Journal of Materials Processing Technology*, 2011, 211(6): 1102-1111.
- [45] C.S. Wu, Q.X. Hu, J.Q. Gao. An adaptive heat source model for finite element analysis of keyhole plasma arc welding. *Computational Materials Science*. 2009, 46: 167-172.
- [46] F. Kong, R. Kovacevic. 3D finite element modeling of the thermally induced residual stress in the hybrid laser/arc welding of lap joint. *Journal of Materials Processing Technology*, 2010, 210 (6-7): 941-950.
- [47] M. Nosonovsky, X. Zhang, and S.K. Esche. Scaling of Monte Carlo simulation of grain growth in metals. *Modelling and Simulation in Materials Science and Engineering*, 2009, 17: 025004 (13pp).
- [48] S.Mishra, T.Debroy. Measurements and Monte Carlo simulation of grain growth in the heat-affected zone of Ti-6Al-4V welds. *Acta Materialia* 2004, 52: 1183-1192.
- [49] S.Sista, Z.Yang, and T. Debroy. Three-dimensional Monte Carlo simulation of grain growth in the heat-affected zone of a 2.25Cr-1Mo steel weld. *Metallurgical and Materials Transactions B*, 2000, Volume 31B: 529-536.
- [50] F. Kong, S. Santhanakrishnan, D. Lin, and R. Kovacevic. Modeling of temperature field and grain growth of a dual-phase steel DP980 in direct diode laser heat treatment. *Journal of Materials Processing Technology*, 2009, 209 (18-19): 5996-6003.
- [51] A. Farzadi, M Do-Quang, S. Serajzadeh, A.H. Kokabi, and G. Amberg. Phase field simulation of weld solidification microstructure in an Al-Cu alloy. *Modelling and Simulation in Materials Science and Engineering*, 2008, 16: 165005 (18pp).
- [52] Ch.A. Grandin, J.L. Desbiolles, M. Rappaz, and Ph. Thevoz. A three-dimensional cellular automaton-finite element model for the prediction of solidification grain structures. *Metallurgical and Materials Transaction A*, 1999, 30A: 3153-3165.
- [53] Dierk Raabe, Franz Roters, Frédéric Barlat, Long-Qing Chen, *Continuum Scale Simulation of Engineering Materials: Fundamentals-Microstructures-Process Applications*, Wiley-VCH, Weinheim, 2004.
- [54] B. Radhakrishnan and T. Zacharia. Simulation of curvature-driven grain growth by using a modified monte carlo algorithm. *Metallurgical and Materials Transactions A*, 1996, 26(1): 167-180.
- [55] S. Sista, Z. Yang, and T. Debroy, Three-dimensional Monte Carlo simulation of grain growth in the heat-affected zone of a 2.25Cr-1Mo steel weld, *Metallurgical and Materials Transactions B*, 2000, 31: 529-536.
- [56] S. Mishra, T. Debroy, Measurements and Monte Carlo simulation of grain growth in the heat-affected zone of Ti-6Al-4V welds, *Acta Materialia*, 2004, 52: 1183-1192.

- [57] Y.H. Wei, Y.L. Xu, Z.B. Dong, and J.L. Xia, Three dimensional Monte Carlo simulation of grain growth in HAZ of stainless steel SUS316, *Key Engineering Materials*, 2007, 353-358: 1923-1926.
- [58] M.-Y.Li, E. Kannatey-Asibu, Monte Carlo simulation of heat-affected zone microstructure in laser-beam welded nickel sheet, *Welding Journal*, March 2002: 37-44.
- [59] Weibin Wang, Yaowu Shi, Yongping Lei, and Zhiling Tian, FEM simulation on microstructure of DC flash butt welding for an ultra-fine grain steel, *Journal of Materials Processing Technology*, 2005,161: 497-503.
- [60] J. H. Gao, R. G. Thompson, Real time-temperature models for Monte Carlo simulations of normal grain growth, *Acta Materialia*, 1996, 44: 4565-4575.
- [61] http://www.ssab.com/Global/SSAB/SSAB_Americas/A514%20Grade%20S%20Brochure%2006-25-08.pdf
- [62] http://www.midalloy.com/html/pdf/low_alloy/TB%20ER100S-G%20Weld.pdf

Principles and Thermo-Mechanical Model of Friction Stir Welding

Jauhari Tahir Khairuddin, Jamaluddin Abdullah,
Zuhailawati Hussain and Indra Putra Almanar

Additional information is available at the end of the chapter

<http://dx.doi.org/10.5772/50156>

1. Introduction

Friction stir welding (FSW) is a solid-state welding process that gained much attention in research areas as well as manufacturing industry since its introduction in 1991 [1, 2]. For almost 20 years, FSW has been used in high technology applications such as aerospace to automotive till high precision application such as micro welding. The main feature of a solid-state welding process is the non-melting of the work material which allows a lower temperature and a lower heat input welding process relative to the melting point of materials being joined. This is advantageous over the conventional fusion welding where excessive high heat input is required to melt the work material. Much less heat input required for FSW translates into economic benefits, safer and less complicated welding procedures. The friction stir welding make it possible to join light weight materials such as aluminium alloy, magnesium alloy, copper and titanium alloys which are very difficult to weld by conventional welding. These clear advantages have greatly increased the usage of these materials in structural applications [3, 4]. In addition, FSW also makes possible to produce sound weldment in 5000 and 7000 series aluminium alloys that are not possible to be welded using conventional method. FSW does not produce sparks or flames. Thus, safety, environmental and legislation issues are not of major concern. FSW process provides proven good quality and strong weldment with inexpensive and lesser number of equipment, eliminates the use of filler metal and improved weldability. Due to these factors FSW has successfully been employed in aerospace, automobile and ship building industries. The need to further understand and improve FSW process continues to propagate in many applications. Many researchers have looked into several methods including mathematical modelling of the process, aiming at understanding the physical-material interaction [8 – 14]. However, there is lack of recorded work in the literature on a system or method to quantitatively measure the welding parameter such as force and torque in FSW process.

This chapter aims to introduce FSW process, its parameters, the applications and a thermo-mechanical model of the process. From the mathematical model derived, a measurement apparatus was developed for force and torque determination during FSW process and experiments were performed to validate the model.

2. Friction stir welding process

FSW set up consists of (1) cylindrical rotational tool, (2) two or more work materials of similar or dissimilar material combinations (3) backing plate and finally (4) clamping or holding fixture as shown in figure 1.

The rotating tool design consists of a combination of two cylinders of a specific radius ratio known as shoulder and smaller radius pin or probe, where the height of the pin or probe is usually more than half of the work material thickness but not equal to its overall thickness. The work materials to be joined may be arranged as conventional welding method but the most common configurations used in FSW are abutted and lapped configuration. For any configuration, FSW has the capability to join thick plate without the need for special preparation prior to welding process. Meanwhile, the backing plate is to ensure the establishment of confine volume and it becomes a must when welding with a pin penetration approaching the bottom of the work materials. The most crucial part of the work materials set up is the clamping or holding fixture. Improper clamping may jeopardize the mated surfaces to be welded and will generate gaps leading to the formation of worm hole or cavities in the weldment. FSW is the non-filler process; hence no substitute material to fill in gaps created by the separation of the work materials is required.



Figure 1. Friction stir welding experimental set up [5].

2.1. Stages in friction stir welding process

FSW process involves four phases which are (1) plunging phase, (2) dwelling phase, (3) welding phase, and finally (4) exit or retract phase. Briefly, the process starts with rotating tool pin or probe thrusting onto the configured work materials under a constant axial load to generate friction heat. This process will continuously increase the temperature at the immediate contacting surface of the rotating tool and work material. The process continues until the temperature at the immediate contact of the rotating tool and the work material increased to a temperature which causes the work material to soften, plasticized and significantly lose its strength. Consequently, these conditions allow the rotating tool to penetrate to a certain depth usually almost to the thickness of work material. The plasticized material is subjected to displacement by the rotating tool pin plunge, effectively being flashed out with a portion of the generated heat, thus introducing new immediate lower temperature and harder surface of work material. This event explains the transient heat generated through pure mechanical friction work at the tool and work material interface. The end of the plunging phase is signified by the sound contact of the rotating tool shoulder with the immediate work material surface.

At this moment, the process enters the dwelling phase where the rotating tool is allowed to dwell for a period of time, causing the temperature to increase further, up to its hot working temperature. The heat generated from frictional work is greatly dependent on the relative increase of contact surface area as well as the relative speed. The heat generated causes the affected area under the shoulder to expand considerably. Phenomenally, the heat causes the work material close to the immediate contact to lose its strength and become plastic. Once this condition is reached, thin soft material layers are produced and would stick to the dynamic rotating tool surfaces (pin and shoulder) and being forced to be displaced along. Instantly the mechanical friction heat generation is partially turned into plastic dissipation heat generation. It is explained by the energy dissipated from the internal shearing of different velocity between the displaced softened work material layers to static more solid surface. Ideally, intermittent heat generation mechanisms due to friction work and plastic dissipation take place because of the transient heat transfer effect and the material ability to regain its strength as heat is lost to the ambient. In addition, the other role of these frictional work and plastic deformation mechanisms are to induce soft material displacement and causes the stirring action or severe material deformation which later produce the amalgamated joint.

The dwelling phase is followed by welding phase. After the local temperature of work material under the rotating tool approaches its hot working temperature and is soft enough to be stirred and displaced, the rotating tool is moved transversely along the welding line. This traverse motion caused the plasticized soft material at the leading edge of the rotating tool being squeezed and sheared through a small slit formed by the displaced soft material at the side or lateral of the tool, preferably in the direction of tool rotation. The displaced soft material is then deposited to the gap at the trailing edge left by rotating tool pin or probe. The soft plasticized material is forcedly displaced by the rotating tool along its rotating

direction under a closed encapsulation of harder solid work material wall and rotating tool shoulder. The soft material is forged to the trailing edge in layers, forming weld nugget. At each traverse increment of the rotating tool motion, the displacement of soft plasticized work material to the trailing edge will introduce new solid, lower temperature work material at the leading edge. Thus it reintroduces friction work heat generation mechanism prior to plastic deformation mechanism and continuously repeating the heat generation process all over again at each traverse displacement of the tool. This produces cyclic transient heat generation. This cyclic process takes part throughout the welding phase and strongly affected by the combination of the rotating tool's rotational and traverse speed. Recap, during the welding phase the plasticized material is subjected to displacement, extrusion and shearing mechanisms facilitated by the tool rotation, thrust and transverse movement under cyclic heat generation along welding line and finally consolidating welding nugget in the trailing side.

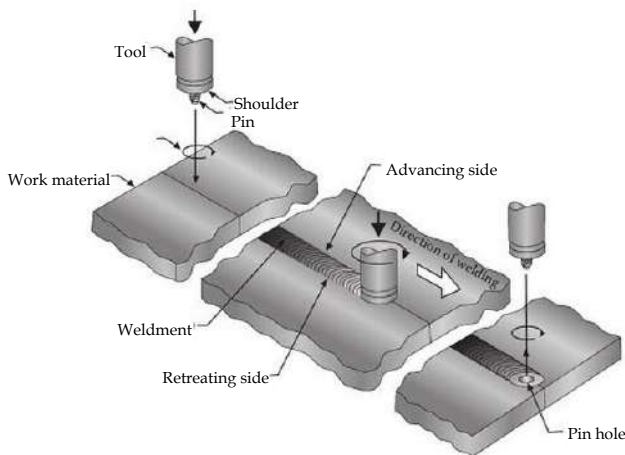


Figure 2. Friction Stir welding process phases of a butted work material configuration [6].

At the end or exit phase of FSW process, the rotating tool is retracted away from the work material leaving a cylindrical hole mark that once occupied by the tool pin. For cosmetic reason, the cylindrical hole may be filled with filler material at the end of the welding process but the most common method used is by introducing dummy material prior the exit phase. Dummy material is of the same material used for the work material to be weld and placed at the end of welding line where the rotating tool is allowed to traverse to and exit within it. The dummy material is later to be cut away leaving good surface finish. Though, this cosmetic issue would remain in the application of innovated friction stir spot welding.

These process phases in FSW are dependent to one another to produce a good amalgamated weldment and are strongly affected by the welding parameters. The assurance of good weldment is determined by proper control of varying measureable welding parameters such as rotational speed, axial plunge force and torque, traverse speed, tool geometry and

orientation in the form of heat energy. Similar to other conventional welding methods, heat energy notably determines the quality of the joint.

2.2. Thermo-mechanical dynamic of friction stir welding

To understand the working principle of friction stir welding, it is necessary to explore the physics related to heat generation. Friction stir welding process started with initial mechanical friction between tool and the surface to be welded which results in heat generation. Rotating tool rotates and advances in trust motion against the work material followed by heat generated through plastic dissipation or deformation of sheared and strained layers of soften material close to the rotating tool surfaces. The heat generation mechanisms occur intermittently or in cycle throughout the welding process.

2.2.1. Friction heat generation

Mechanical friction work is initiated when rotating tool surfaces are in contact with the immediate stationary surface of work material under a normal load. While the rotating tool is sliding, it introduces velocity difference between the dynamic rotating tool and the static work material surface and thus creates friction work and subsequently, heat. This mechanical friction work is described based on the Amonton's laws which firstly explain that the friction between two separate bodies is directly proportional to the normal load applied onto the bodies. In this law, coefficient of friction of static friction is a constant variable and temperature dependent but only to be considered as kinetic friction when the contact condition is non-sticking or sliding. Secondly, the friction force is independent on the apparent contact area [7].

In general application, friction work is assumed based on Coulomb's dry friction model between solid bodies, which is also at the same time conforms the aforementioned Amonton's law. In details, the mechanical work and heat generation relationship in the presence of sliding friction is explained by contact conditions between hard and soft metallic material interaction. It involves very small scale asperities at the contact surfaces of hard and soft material. As normal force is acting on the rotating tool, it is being distributed onto smaller area asperities at the contact surfaces which resulted in a very high pressure per unit force. Due to relative velocity difference, the normal force causes ploughing of the soft material by the hard materials' asperities. The soft material gets agitated, deformed and finally broken, releasing the stored energy in the form of heat [8].

The released energy which is a very high local thermal energy causes the temperature to rise. The heat energy is eventually transferred and stored into the rotating tool and the lump work material. The heat causes the work material to soften, reduces its strength, broken and deforms into soft material layer in between the rotating tool and the work material. This soft layer is gradually displaced by the rotating tool pin revealing new surface contact condition for another cycle of ploughing action by the rotating tool. The process promotes another cycle of mechanical friction heat generation.

2.2.2 *Plastic dissipation heat generation*

This phenomenon typically occurs at higher temperature resulting from friction heat mechanism but only significant during dwelling and actual welding phase where work material is confined under the rotating tool. Through friction heat mechanism, work material temperature under the rotating tool is increased to a degree where work material layer at rotating tool interface started to lose its strength, yielded, stick and move with the rotating tool. This phenomenon increases the thermal softening effect from friction heat and causes shears at the work material to work material layers interface. It reduces friction heat mechanism but at the same time introduces high strain rate plastic deformation. As a result, highly localized heat is generated internally within the work material itself away from the rotating tool to work material interface due to dynamic velocity differences and boundary sliding condition [9, 10, 11].

Due to the heat transfer within the process, the plastically deformed material tends to recover its strength thus establishing a new lower temperature level and reinitiate mechanical friction heat generation mechanism [12]. Furthermore, at the welding phase, heat generation from plastic dissipation mechanism is increased at the cost of the travelling rotating tool and the shearing of the work material to higher extent toward trailing edge. It further increases the process temperature as the rotating tool is reintroduced to new contact condition at the leading edge and reinitiates the mechanical friction heat generation mechanism [13].

These heat generation mechanisms throughout the FSW process occur in cycles due to the instance of slip and stick contact conditions and the alternating boundary conditions at the material-rotating tool interface [14]. In this regard, heat generation mechanism has most influential effects on the process introducing high strain rate and thermal effect which softens work material adjacent to the tool to work material interface, to be encompassed at the trailing edge and produces welding nugget which is the main characteristic of the joint [15].

2.2.3 *Heat transfer*

Simultaneously, heat generated is constantly being transferred within the system; portions of heat are distributed within the work material, the rotating tool, the holding fixture or backing plate and finally to the ambient. In depth, heat generated is subjected to three-dimensional (3-D) heat flows away from the heat source under boundary conditions. Heat input and heat transfer at the rotating tool are indirectly coupled at the rotating tool to work material interface into the work material through heat conduction and incorporated with convective heat transfer effect around the pin in the deformation zone [12, 13, 16, 17]. For the work material, convective and radiative heat transfers are considered for heat exchange at the top work material surface, past the shoulder peripheral while at the same time only convective condition is considered for the bounding surfaces of work material [18, 19]. For the case of backing plate, appropriate variable gap conductance is considered for work material to backing plate interface depending on specific thermal contact resistance condition; of temperature dependent or contact pressure dependent or surface contour of work material or any of the combinations [13, 18, 20].

Ultimately 100% energy generated from mechanical work throughout the process is converted to heat and physical deformation with approximately 88% of heat is conducted and distributed globally through to the lump work material, backing plate and else to the rotating tool [12]. Heat plays a very significant role not only toward the physical success of the joint but also towards the process temperature profile, heat transfer and the work material internal strain and stress distribution. It causes direct influences on the final weldment microstructure and residual stress resulting properties which are strongly correlated to the welding variables and temperature-dependent material properties [21].

2.2.4. Friction stir welding mechanism

Weldment is produced in the course of welding phase where layers of materials are forced to move along with and around the rotating tool surfaces at a specific contact condition; fully sliding or sliding and sticking or fully sticking. The soft material layers motion are heavily deformed and driven by the tool rotational direction. It is forced through the retreating side toward trailing edge and downward closed to the pin before finally being forged and deposited at the once occupied volume of the rotating tool pin at the trailing edge under severe plastic deformation [17, 21, 22, 23].

The mechanical torque of the rotating tool causes mechanical shearing to the immediate work material close to the rotating tool and work material interface, forcing soft work material layers to motion and strained, creating flows of fine layers of materials prior progression into weldment. The flow motion or velocity is visually estimated through the grain size and shape, correlated to internal strain rate [24]. The material flow and joining mechanisms are described by the region formed by the FSW process known as the flow zones. It describes the zones where shear layers are visibly distinguished by material characteristics and exhibit the evident of non-melting but severely deformed soft material deposited into amalgamated weldment in layers and flowing manner.

2.2.5. Welding characteristics

Temperature profile and history of FSW process are resembled by the distinct regions at the weldment. These regions are characterized by discrete microstructure sizes, shapes and varying properties, produced by the significant thermal effect and mechanical deformation. Under the heat generation, lump effect and heat transfer of the process, thermal profiles are being distributed from the crown shaped heat source around the rotating tool to work material interface toward the peripheral work materials surfaces and edges [22, 25]. These regions are known as; 1) weld nugget, the product of plastic deformation due to the stirring effect deposited behind the rotating tool pin at the trailing edge, 2) thermo-Mechanically Affected Zone (TMAZ) of internally sheared plastic deformation within the work material away from rotating tool to work material interface, 3) heat Affected Zone (HAZ) of structurally altered and thermally affected region due to intense temperature different between TMAZ and base metal temperature region, and 4) base metal of work material which is not physically affected by the thermal effect [26].

Temperature profile within the FSW process portrayed direct relationship of the heat generation, torque generated through the rotating tool, loads exerted throughout the work material and power consumed by the welding process. Both thermal and mechanical effect from heat generation and stirring effect engender welding characteristic in term of stresses, tensile and hardness properties. For which, the rotating tool rotational and traverse speed interchangeably influenced the temperature profile and affectively manipulate the material flow behaviour, weld material chemical composition, microstructure orientation, strain, residual stress, thermal stress, material hardness and strength of the weldment [27, 28, 29]

2.3. Applications of friction stir welding

Recently, FSW won attractive attention by manufacturing industries because of the ability that outperformed other welding technique such as tungsten inert gas (TIG) to weld aluminium. Besides, it has the ability to be adapted in advanced automation system such as robotic which is very predominant in aluminium components and panel fabrications of highly rated technology readiness level [30]. For example, it is an applicable technique adapted for rail cars for fabrication of floor panel part of a Type 700 Shinkansen or bullet train, as well as the aluminium roof, side wall and floor panel for suburban train and other more recent commuter or express rail cars [31]. This is due to its low distortion and its suitability to produce large welded products including prefabricated panels as well as tailored blanks and joints. These advantages are also shared in marine application when it is first commercially used for ship building in 1996 with the ability to joint thick panels, sandwiched, honeycomb panels and corrosion resistance material panels [32]. FSW is well favoured for performing butt joint in comparison to conventional arc welding application which also turns out to be significantly viable in terms of low labour cost and shorter welding cycle time [33].

The other important application of friction stir welding is in aeronautical and aerospace industries where aluminium alloy is used as primary material for their construction. The welding process enables manufacturers to completely replace the riveted joints and assemblies of lapped and abutted configuration that are used mainly for fuselage sections, propellant and fuel tanks of commercial air craft as well as space launch vehicle [34]. Thus, the process allows total elimination of the use of thousands of rivets. This has resulted in better quality, stronger and lighter joints at reduced assembly cost for aviation industry. Meanwhile in automotive application, FSW and its recently innovated process of friction stir spot welding (FSSW) are introduced to replace conventional resistive spot welding (RSW) in the transition when aluminium alloy application is ready and becoming ideal to be used for panels in passenger and commercial vehicle bodies. Aluminium application in automotive industry are sought for its prefabricated and tailored panel, good strength-to-weight ratio, potential for reducing fuel consumption, its ease of recycling as well as marked reduction in production cost. This has compelled car manufacturers to use the same concept not only for the body panels, but for other parts as well [35].

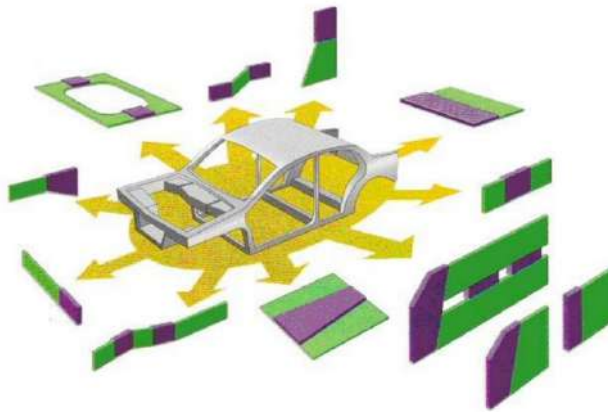


Figure 3. Tailored welded blanks in a passenger vehicle [36].

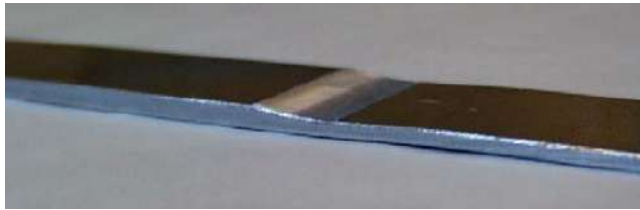


Figure 4. A component of friction stir tailored welded blank [36].

Since its introduction, friction stir welding has matured significantly with widespread use of wide range aluminium alloys for structural applications with its compatibility to be used in ferrous, stainless steel, nickel, copper and titanium alloys. However, only a small percentage of world welding and joining market has implemented the process. It is still relatively underutilised and this is varied among industries, university researches, collaborations and other niche applications. With all the challenges to joints wide variety hard to weld materials, the motivation of the application and adaptation of this noble technology in manufacturing not only to meet quality joints, but for the potential economic value and also for its environmental friendliness.

2.4. Recent development & future outlook

Since the last two decades, there are considerably vast lab and industrial work done on FSW process which leads to the emerging advancement of new materials application and combinations, process improvement, tool designs, welding configurations, tailored blank application and adaptation to automation. Though, the most important innovation in the process itself is its variations; (1) high speed FSW (HS-FSW), (2) ultrasonic stir welding (USW), (3) thermal stir welding (TSW), (4) friction stir spot welding (FSSW), (5) friction stir joining (FSJ), (6) friction stir processing (FSP), (7) friction bonding (FB) [37].

The recent advancement shows the introduction of HS-FSW aiming at reducing the process forces by means of increasing heat generation rate. This reduction in forces is to realize the idea of permitting manual handheld welding work. HS-FSW process is also designed to achieve lighter and portable device or equipment. This will make possible manual handheld welding and eliminates the need for rigid fixturing of the work material and rotating tool.

USW is another variation of the process where ultrasonic energy is used to assist in initial heat generation. The objectives are to reduce process forces and welding time. The major boost of USW is it reduces dependency on the tool shoulder to generate heat and instead, make use of the coupled ultrasonic vibration to further agitate the rotating tool at the contact interface, amplifying the mechanical friction effect.

Different from USW that utilize ultrasonic energy to generate heat, TSW decouples heat generation from mechanical friction of conventional FSW and instead, utilizes external induction heating to increase work material temperature at the welding spot or welding line. Though induction heating may ultimately increase the rate of heat generation but it reduces strain rate of plastic deformation, a prevalent characteristic in FSW. Reduced strain rate will significantly affect the final welding properties [38].

The most common variation of all is the FSSW, which is well known to be used in transportation industries to replace rivet and as well as adhesive joining method. Though this method produces cosmetic defect in the form of pin hole created by the rotating tool, the weldment has sufficient mechanical strength for joining method [39].

While the other FSW variants are dedicated for metallic materials, FSJ method is dedicated for joining thermoplastic materials. It has been used for polypropylene, polycarbonate and high density polyethylene materials [40]. The advancement of FSJ method may possibly makes way for mechanical joining method involving plastic matrix composites.

FSP is a unique non-joining method variant of FSW where it utilizes the stirring process to alter microstructure derived from FSW method to be super fine, modified with improved physical properties and at the same time suppressed defects such as porosity and short crack [34]. The introduction of foreign particle into base material during FSP creates new near quality to metal matrix composite or MMC structure and thus improving the material properties. This provides a new platform to produce improved future materials.

The consequent of FSP method emerges as a modified method of FB that allows bonding of overlapping thin plates through locally modified microstructure. The process utilizes less stirring effect due to the short pin geometry and thus differs from common FSW method.

The majority of these FSW variants stress on their ability to increase welding time and at the same time to reduce forces exerted from the welding process. The other purpose of these methods is to provide means of producing joining method involving different type of materials and configurations. More or less, these method share the same mechanism of mechanically manipulating soften work material and formation of fused material at the trailing edge.

3. Friction stir welding parameters

Independent process variables play significant effect on the welding process and the process control. The process variables entail the axial force for plunging, rotating tool rotational speed, rake angle, welding speed and tool geometry. The aforementioned variables strongly affect the heat generation rate, temperature profile within the work material, mechanical power required by the process, material evolution of the weldment and also loads distributed within the work material. These variables are extensively discussed in this chapter to understand the mechanics of joining, process and final weld properties optimizations, where direct measurement can be done experimentally and predicted numerically.

3.1. Effect of welding parameters on joint quality

It has been reported that rotational and traverse speeds have both direct and indirect influence to the final weldment. Its direct influences to the mechanics of joining suggesting the degree of stirring based on the contact condition and multi component loads. Whilst, it's indirect influences to mechanical properties of the weldment is heavily derived from the combination of temperature exposure and tool design [41]. Low rotational speed induces low stirring effect and finally low heat generation rate. At low traverse speed, it increases exposure to heat source, facilitate more material flow and reduced multi component loads, vice versa to high traverse speed but only to an extent. Extreme high rotational speed results too much heat while extreme high traverse speed results less heat, low stirring effect and increase travel resistance due to heavy loads on the rotating tool and hard work material at the leading edge. At this moment, the material is sheared to the lateral side instead of moving around the rotating tool direction [42]. Excessive heat which is generated from either high rotational speed or low traverse speed, or combination of both conditions, significantly reduces the mechanical properties of joint due to microstructure evolution of the regions exposed to excessive heat [43]. Albeit, the appropriate traverse and rotational speed below critical speeds might result optimum heat generation rate and reduced thermal exposure that produce good strength and hardness of weld joints [44, 45].

Torque produced during the welding process depends heavily on the contact conditions which are determined by the rotating tool rotational speed, degree of softness of work material or plasticity at the rotating tool to work material interface, axial load exerted and the tool design [22, 46, 47]. Any changes in the traverse speed at a constant tool rotational speed do not significantly affect the temperature profile compared to changes done in the rotational speed. These make the torque to be insensitive to the traverse speed. In addition, optimum rotating tool design influences torque produced through the effect of sum of contact areas and contact conditions at the interface where it plays major role in plastic deformation or strain work distribution, material transportation or flow and toward process loads and work material temperature [41, 48, 49, 50]. As temperature increases, work material temperature dependent shear stress plump and no longer display full solid properties thus reduces the torque at the rotating tool to work material interface and further reducing power and energy required to produce heat within the process.

3.2. Optimizing process parameters

Considerably vast works has been made in pursue to understand and optimize the physical process of FSW that influenced by the associated variables using both empirical as well as numerical models for the heat generation, material interaction and flow.

3.2.1. Thermal modelling

Heat generation is modelled based on the torque required to rotate a circular shaft relative to the material surface. The model is made by assuming a constant coefficient of friction, pressure distribution and 100% conversion of the shearing work to heat. It is also assumed that the net power required is directly proportional to the tool rotational speed and the tool shoulder radius i.e. $q \approx \omega R$ [51].

Friction work principle used for heat generation model is coupled with plastic work principle to model three-dimensional heat and material flow based on temperature dependent coefficient of friction and temperature dependent pressure distribution for aluminium alloys [26]. In detail, three-dimensional visco-plastic flow and heat transfer have been investigated through solving the equations of conservation of mass, momentum and energy by considering the heat source at two separate conditions. Firstly, visco-plastic flow and heat transfer at the tool to work material interface due to the mechanical friction or due to the plastic dissipation heat generation mechanisms and secondly, the visco-plastic flow and the heat transfer within the layers of soft work material away from the tool to work material interface under the combination of both friction and plastic dissipation heat generation mechanisms [11, 52, 53, 54].

The model is defined by the contact area, the radial distance of the rotating tool pin and shoulder, the material shear stress or the spatially variable coefficient of friction or their combinations, the angular velocity and the exerted normal pressure acted on the work material surface. Then, the model is validated through comparison of the computed heat generation, peak temperature and the total torque exerted on the tool with the experimental results. Contact conditions at the interface are described as sliding, sticking or partial sliding or sticking, known as slip factor is also being adapted. The slip factor is derived experimentally, determined by the plunge force and torque from the welding process. The slip factor yield a proportional relationship between plunge force and heat generation where Coulomb's law of friction is applied to describe the shear forces at the interface [10, 55]. Slip factor is also used to evaluate the welding energy and temperature, utilizing torque based heat input [53]. These works allow the prediction of the welding temperature from the transverse speed, tool rotational speed and the applied force. Ultimately, fully coupled thermo-mechanical model with adaptive boundary condition which applied both thermal and mechanical model is used to predict transient temperature profile, active developed stresses as well as the three-dimensional force components [13].

3.2.2. Model validation

The force and temperature measurement experiments are conducted under different welding parameters for model verification by differing the transverse and the tool rotational speed whilst maintaining the constant vertical force. The result is later used for the calculation of the heat input into the tool and workpiece. In relation, numerical model is developed to take account the process effects on the work material such as the material plasticity properties, thermal expansion and stress, cooling effect, stress stiffening, stress distribution, material strain, residual stress as well as the thermal history of the welding process [56, 57, 58].

The mechanical effect is visualised and simulated as material flow model to describe the process parametric effects on the soft work material flow and the welding mechanisms [59, 60]. The physical material flow highlights the particular material strain, its distribution and flow motion around the rotating tool, at the leading edge of advancing and retreating sides and at the trailing edge as well as the actual bond that might occur in the FSW process. Thus, thermo-mechanical model is required to exhibit the importance of the three-dimensional loads and torque exerted by the rotating tool material to determine the best and optimized parameter for the welding process of any materials which is greatly related to the joint and process properties such as residual stresses, process temperature, joint strength and productivity. The parameter optimization is related to variables such as welding speed, rotating tool rotational speed as well as rotating tool design. Proceeded, welding power has been modelled to determine the overall heat input for FSW process based on the traverse speed and tool rotational speed as well as its effect on the material properties. The model has been derived based on the relationship between the rotating tool rotational speed and the represented rotating tool torque with association to the key parameters aforementioned [61, 62].

Significantly all of these works and models represent the correlation of the mentioned independent variables of the associated welding parameters as well as material properties serve the heat generation, temperature distribution and joining mechanism that contribute to the success of the welding process. In summary, the relationship between the independent process variables and the dependent process output to the heat generation mechanisms is best described as in a closed and correlated system, explained by the interaction of process welding variables and key process conditions; physical, metallurgical, heat generation and heat transfer effect [63].

4. Mathematical modelling of welding forces & torque

FSW is not widely available in general application rather than conventional fusion joining methods especially in automotive industry due to shorter process and heat generation cycle. Thus, the true understanding of FSW process is still in far-reaching; understanding the physics and nature of the process, lacking of standards guideline and practice, optimization of the process for typical material usage or application as well as still typically not suitable for small scale robotic or manual handling. The mathematical model on the welding forces

and torque is proposed for optimizing FSW process and to study the effects of varying its parameters. The model is to be compared with experimental work [64, 65].

4.1. Model development & assumption

Initial heat generation takes place at the first contact of the rotational tool pin surface and continue throughout the plunging phase where the temperature distribution of the work material is asymmetrical at the leading, trailing edge as well as advancing and retreating side. It is based on the assumption that the interface heat generation is constant with the consideration of the constant rotating tool angular speed, ω , temperature-dependent pressure distribution function, $P(T)$, heat capacity, ρc_p , thermal conductivity, k and constant coefficient of friction, μ_k . Based on Fourier's 2nd law [66];

$$\rho c_p \frac{\partial T}{\partial t} = k \left(\frac{\partial^2 T}{\partial x^2} + \frac{\partial^2 T}{\partial y^2} + \frac{\partial^2 T}{\partial z^2} \right) + \dot{q} \quad (1)$$

Where ρc_p is the heat capacity, x , y , and z are the space coordinate and is the heat source term correspond to heat generated from the welding process. The function of the heat generation is directly related to friction work of the contacting surface thus accounts the sum of contact surface area of the tool. The sum or contact area is represented as function of rotating too plunge depth, h . The data used is as in table 1. Given;

$$A_{(h=0)} = \pi r_p^2 \quad (2)$$

$$A_{(0 < h < 5)} = A_{(h=0)} + \pi \left[\left(\frac{R_p}{h_p} h_{(0 \rightarrow 5)} + r_p \right) \left(\frac{R_p - r_p}{\sin 2} \right) - r_p s_2 \right] \quad (3)$$

$$A_{(h=5)} = A_{(0 < h < 5)} + \pi (R_s - R_p)^2 \quad (4)$$

For A is the contacting surface between the rotating tool and the work material surface, r_p is the bottom pin radius, R_p is the top pin radius, h_p is the total height of the pin and $\pi r_p s_2$ is the minor cone area.

Furthermore, the torque required to rotate the rotational tool relative to the static workpiece surface under $P(T)$ represents the conversion of mechanical work of the rotating tool. Given;

$$M = \int_0^{M_R} dM = \int_0^R \mu P(T) 2A(h) r dr = \mu P(T) A(h) R^2 \quad (5)$$

Or by simplification of the sum of contact area through cylindrical approximation, given [67, 68];

$$M = \int_0^{M_R} dM = \int_0^R \mu P(T) 2\pi r^2 dr = \frac{2}{3} \mu \pi P R^3 \quad (6)$$

Where M is the interfacial torque of the in contact workpiece surface and rotating tool surface, μ_k is the coefficient of friction, R is the contact surface radius, and $P(T)$ is temperature dependent pressure distribution across the interface.

For fully sliding contact condition and with assumption of all the friction work is converted into frictional heat, the average heat input per unit area and time becomes;

$$q_0 = \int_0^{M_R} \omega dM = \int_0^R \omega \mu P(T) 2\pi r^2 dr = \frac{2}{3} \omega \mu \pi P R^3 = \frac{4}{3} \mu \pi^2 n P R^3 \quad (7)$$

Where q_0 is net power in Watt (Nms^{-1}) and ω is rotational speed (rads^{-1}). Apparently, in equation 7, heat input depends on the normal pressure distribution function, contact surface radius, temperature dependent function of coefficient of friction and the rotational speed of the rotating tool which produce transient heat generation, distributed into the work material and thus characterized the process variables for the friction stir welding process.

In order to understand the physics of the welding process in the expression of the mechanical loading associated to the welding process, a mathematical representation is derived based on figure 5;

$$r_1 = -(x_1 + x)i + y_1j - z_1k \quad (8)$$

$$r_2 = -(x_2 + x)i - y_2j - z_2k \quad (9)$$

$$r_3 = (x_3 - x)i - y_3j - z_3k \quad (10)$$

$$r_4 = (x_4 - x)i + y_4j - z_4k \quad (11)$$

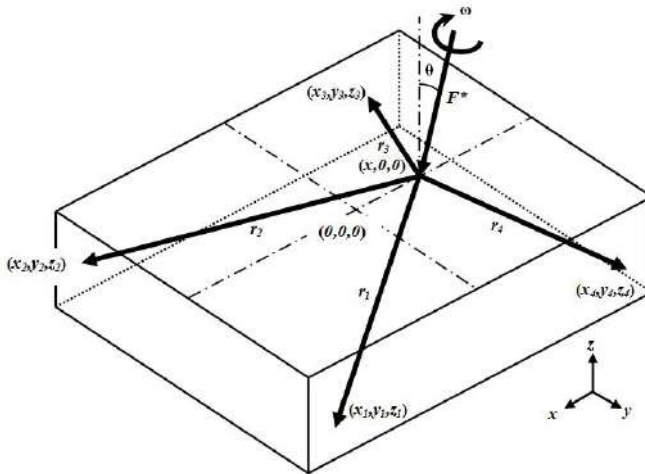


Figure 5. Free body diagram of multi-component load measuring device [65].

$$\sum F = 0 \quad (12)$$

$$F_{x,y,z}^* = \sum_{n=1}^4 Fn_{x,y,z} \quad (13)$$

$$F^* \sin \theta i + F^* \cos \theta k = (F_{1x}^* + F_{2x}^* + F_{3x}^* + F_{4x}^* - F_{1x} + F_{2x} + F_{3x} - F_{4x})i + (-F_{1y} - F_{2y} + F_{3y} - F_{4y})j + (F_{1z}^* + F_{1z} + F_{2z}^* - F_{2z} + F_{3z}^* - F_{3z} + F_{4z}^* + F_{4z})k \quad (14)$$

Where F^* , is the plunge force as the function of contact surface area and under the temperature dependent pressure distribution $P(T)$ for a desired depth of penetration. The torque exerted on the work material by the rotating tool mechanical friction work is calculated based on equation 6 and coupled by the moments reacted at each of the measuring references on the workpiece as in figure 5;

$$\sum M = 0 \quad (15)$$

$$M_{x,y,z}^* = \sum_{n=1}^4 rn_{x,y,z} \times Fn_{x,y,z} = 4(Rn_{x,y,z} \times Fn_{x,y,z}) \quad (16)$$

$$M_{x,y,z}^* = \frac{2}{3} \mu F_{x,y,z}^* R \quad (17)$$

Where;

$$M_1 = M_2 = M_3 = M_4 \quad (18)$$

$$r_1 \times F_1 = r_2 \times F_2 = r_3 \times F_3 = r_4 \times F_4 \quad (19)$$

In figure 5, the moment exerted on the measuring references is in equilibrium and the acting forces exerted by the rotational tool mechanism are determined from equation 18, generally;

$$\frac{1}{4} M_{x,y,z}^* = Rn_{x,y,z} \times Fn_{x,y,z} \quad ; n = 1, 2, \dots, 4 \quad (20)$$

$$r_n \times F_n = (y_n Fn_z + z_n Fn_y)i - (-x_n Fn_x)j + (-x_n Fn_y - y_n Fn_x)k \quad (21)$$

The general equation can be presented in a matrix form as;

$$\begin{bmatrix} \frac{1}{4} M_x^* \\ 0 \\ \frac{1}{4} M_z^* \end{bmatrix} = \begin{bmatrix} 0 & z_n & y_n \\ -z_n & 0 & x_n \\ -y_n & -x_n & 0 \end{bmatrix} \begin{bmatrix} Fn_x \\ Fn_y \\ Fn_z \end{bmatrix} \quad (22)$$

At any static equilibrium where the slip contact condition between the rotating tool and the workpiece surface remain constant, the moment at each of the measuring references remain

the same but dependent on the radius of the rotating tool and the function of pressure distribution $P(T)$ for the respective rotating tool position. The values for the moment are also remained constant at any Cartesian coordinate (x, y) location of the rotating tool on the surface of the workpiece. Although the basic assumption for the constant contact condition for the function of pressure distribution $P(T)$ in modelling the process is not physically correct but appropriate to be acceptable in the context of numerical model as average value used throughout the investigation.

Properties/parameter	Value
Work material dimension, mm	200 X 200 X 7
Shoulder radius, mm	9
Tool radius, mm	3
Pin radius, mm	2.852
Pin height, mm	5
Pin conical angle, °	2
Tool angle, °	2
Workpiece material	6061 T-6
Tool material	M42
Coefficient of friction	Figure 7
Plunge forces	Figure 8

Table 1. Summary of data used for loads and torque calculation [5].

4.1.1. Co-planar analysis

A closer approximation is made on the geometry of the work material is to measure the reaction forces and moment caused by the rotating tool from the friction welding process. Equation 22 is reduced by performing co-planar analysis at measuring points of the workpiece as in figure 6 for the initial heat generation until the full penetration of the stirrer tool.

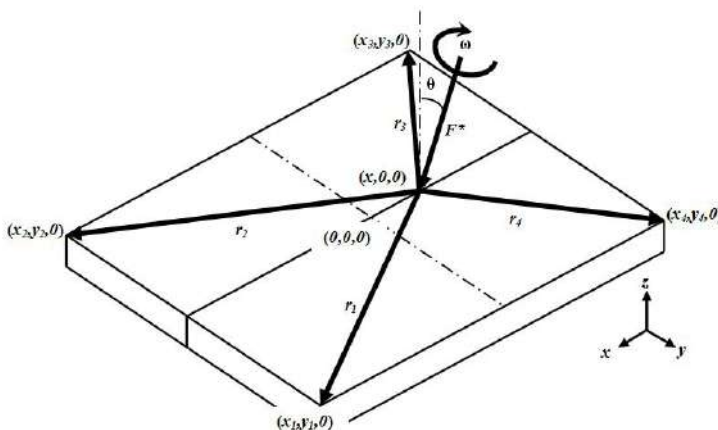


Figure 6. Co-planar analysis of the workpiece material during welding process [65].

Parametric analysis are carried out based on the work material temperature dependent tensile, yield and shear strengths properties, welding configuration, work material dimension and also tool design to investigate loads and torque distributed within the work material. The temperature dependent material properties data used in the calculation are as in figure 7 and 8 used to determine the theoretical plunge forces for the FSW process. In addition, a constant plunge force is proposed as to simulate the experimental work as comparison to numerical analysis.

Theoretically in this work, the mechanical properties suggest the controlling parameters of the welding process especially regarding the plunge force which is based on the contact area and controlled pressure parameter on the tool, heat energy consumed and the mechanical loads applied.

The details of the parametric analysis are explained based on the case studies as carried as;

Case 1: Theoretical plunge force based on temperature dependent tensile strength. This approach is based on the assumption that contact condition is fully sliding follows the temperature dependent coefficient of friction curve as in figure 7.

Case 2: Theoretical plunge force based on temperature dependent yield strength. This approach is also based on the assumption that contact condition is fully sliding.

Case 3: Theoretical plunge force based on temperature dependent shear strength. The assumption for fully sticking contact condition is that the rotating tool which is trusting and work material is separated by a thin layer of plasticised material at the contact interface.

Case 4: Experimental plunge force based on manual force and plunge depth control method [5]. Force and plunge depth control methods are common control method for FSW process [69, 70].

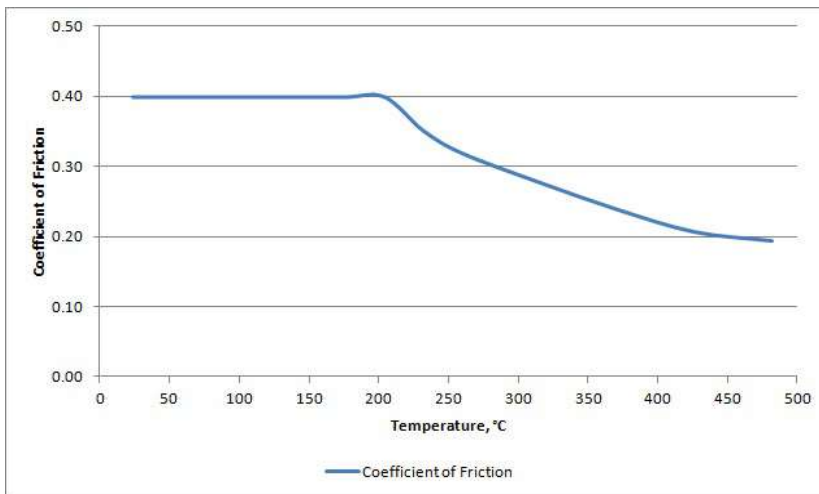


Figure 7. Temperature dependent coefficient of friction [5].

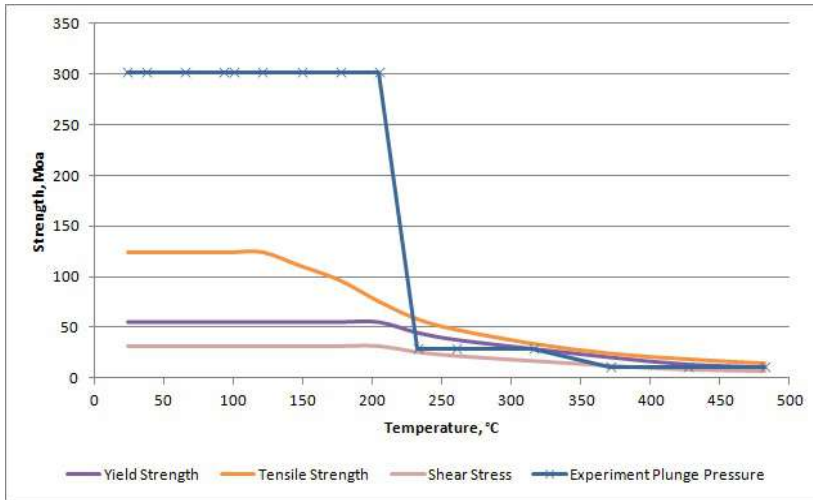


Figure 8. Variable temperature dependent material properties of aluminium alloy 6061 and plunge pressure variation for FSW process cases 1 – 4 [5, 6].

Though in this work, only case 1, 3 and 4 are being considered to visualize the maximum and minimum limits of the parametric effect in comparison to the experimental work. Case 1 encompasses the maximum strength value of the work material prior failure due to the mechanical effect of the FSW process. As for case 3, it represents the minimum requirement of the FSW process to initiate mechanical or physical effect on the work material. Finally, case 4 is the corresponding load suggested based on the work holding fixture as in figure 1 [5, 65].

4.2. Model validation with experimental data

The plunge variation profiles in FSW processes based on the temperature dependent work material properties and experimental plunge pressure value are as exhibited in figure 8. It is noticeable that the cases are significant at temperature range approximately 120°C to 220°C, where the theoretical plunge pressure started to decrease. The work material becomes soft and lost its strength, allowing the rotating tool to displace axially into the work material. The corresponding rotating tool plunge force theoretical calculation based on the plunge pressures schemes aforementioned are compared to experimental result and exhibited in figure 9.

During the plunging phase, the rotating tool thrusting under the plunge pressure profiles and constant rotational speed produces mechanical torque. It acts on the work material and initiates the mechanical friction work thus results the friction heat. The variations of mechanical torque exerted at the rotating tool and the work material interface during the plunging phase are as in figure 10.

Sticking and sliding contact conditions referred as case 1 and 3, exhibit significant torques built up beyond 300°C. For case 4, high torque exerted at initial plunge phase abruptly

decrease as the temperature approaches 220°C before it increase back at temperature beyond 300°C. The decrease in torque indicate the softening effect of the work material while the immediate increase of the torque values are due to the rotating tool shoulder surface comes into contact to the work material.

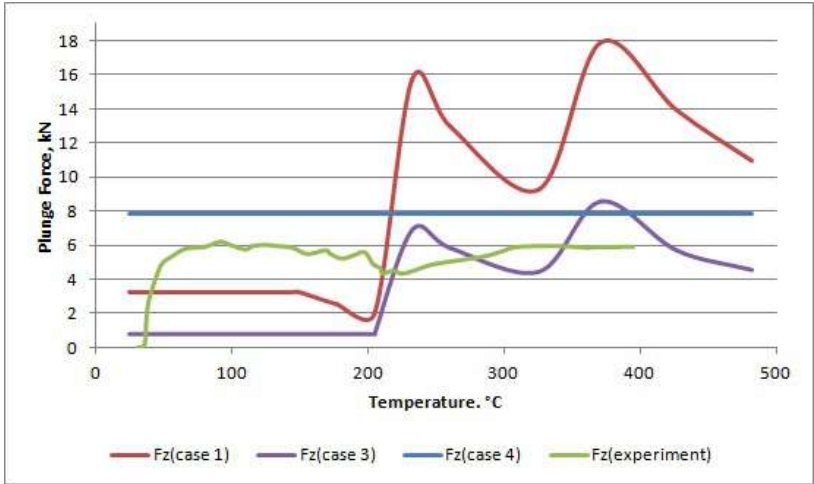


Figure 9. FSW plunge forces as controlling parameters [5].

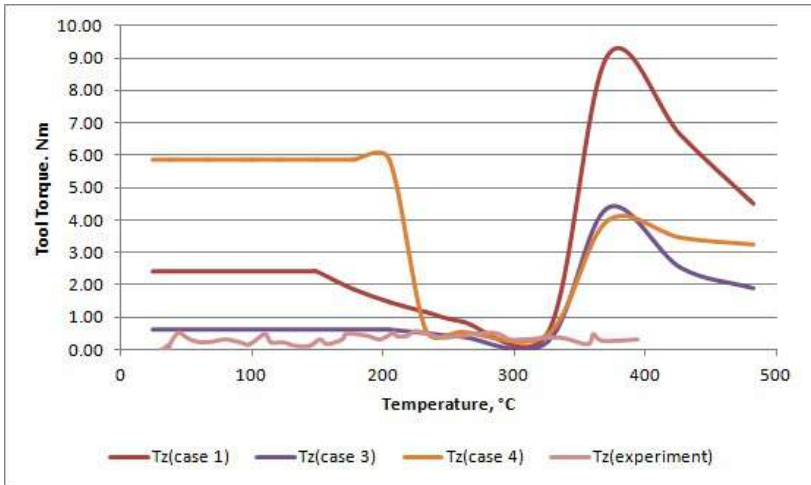


Figure 10. Tool torque exerted at the tool - work material interface for case 1, 3 & 4 [5].

An approximation of the process is based on case 4 where plunge pressure is based on manual control of constant plunge force. The comparison of the theoretical plunge forces and experimental work of the FSW process reveal distinct variation based on the assumption used. However, the values act as references for the actual FSW process that agree to the experimental result as shown in figure 9. The experimental result shows that its